

Iowa Research Online

Monte Carlo simulations and phantom measurements towards more quantitative dosimetry and imaging in nuclear medicine

Tiwari, Ashok

https://iro.uiowa.edu/esploro/outputs/9984271452102771/filesAndLinks?institution=01IOWA_INST&index=null

Tiwari, A. (2023). Monte Carlo simulations and phantom measurements towards more quantitative dosimetry and imaging in nuclear medicine [University of Iowa]. <https://doi.org/10.17077/etd.006424>

**Monte Carlo Simulations and Phantom Measurements towards more Quantitative
Dosimetry and Imaging in Nuclear Medicine**

by

Ashok Tiwari

A thesis submitted in partial fulfillment of the
requirements for the Doctor of Philosophy
degree in Physics
in the Graduate College of
The University of Iowa

May 2022

Thesis Committee:

John J. Sunderland, Thesis Supervisor
Vincent Rodgers
Wayne Polyzou
Craig Pryor
Ryan Flynn

Copyright by

Ashok Tiwari

2022

All Rights Reserved

This work is dedicated to my parents, without whom I would be nothing and nobody. Their love, encouragement, patience, and kindness mean a lot to me.

ACKNOWLEDGEMENTS

I would like to take this opportunity to thank all the people that have made it possible for me to complete my Ph.D. degree at the University of Iowa. I would like to express my sincere gratitude to Prof. John Sunderland for suggesting the problem and for his constant guidance throughout this work. His encouragement and assistance always have been of immense value. I am very grateful for all the help and advice that Prof. Sunderland has given me as well as his willingness to always take the time to help me, no matter how busy or where in the world he was. Working with Prof. Sunderland has given me the necessary rigor that one needs to solve the problem. Thank you for managing financial support throughout the work, including the full-time summer support. I also want to thank Prof. Wayne Polyzou, Prof. Vincent Rodgers, Prof. Craig Pryor, and Prof. Ryan Flynn for being my committee members.

I had the great pleasure of working with Prof. Stephen A. Graves. I appreciate his valuable co-operation throughout this work. He helped me with many things, such as checking my Monte Carlo simulation results, preparing radionuclide solutions for experiments, film irradiations using the linac, and making my concepts clear of the medical physics field. I am also grateful for the methodologies that I have learned from Prof. Graves, particularly the courage not to back away from examining problems in as much detail as required.

My sincere thanks go to all respected faculty members of the Department of Physics. I acknowledge the Department of Physics and the Department of Radiology at the University of Iowa for providing graduate research assistantship and travel support to attend the meetings or conferences for me to carry out this thesis work. I also want to thank Colbin Erdahl, Benjamin Bender, Lisa K. Dunnwald, and all staff at the PET Center in the Department of Radiology for all

their help. In addition, I want to thank the Graduate College University of Iowa for their trust in me by providing a prestigious Ballard and Seashore Dissertation Fellowship 2022.

It is impossible to list here the name of all my friends who have given me help, encouragement, and advice. I wish to express my sincere thanks to all my colleagues. I could not remain without giving thanks to my wife, Sadiksha Poudel, for her help and support through the toughest times, and I am forever grateful to her. I would also like to thank my brother Prabin Tiwari, and my sister, Suchana Tiwari, for all the support during the many years.

Thank you to my parents, Pampha and Homnath Tiwari, for always being there, encouraging and motivating me through these years away from everyone and everything I knew. Nothing would have been possible without your support. I would like to dedicate this Ph.D. thesis to my parents as a small token of gratitude for the beautiful life they gave me.

ABSTRACT

Targeted radiopharmaceutical therapy (TRT) is an explosively growing and evolving cancer treatment approach that uses therapeutic levels of biochemically targeting radioactive molecules to attach to cancer cells and subsequently irradiate them with toxic levels of radiation. This approach is currently being used clinically to treat neuroendocrine tumors, and a new drug to treat prostate cancer is likely to be approved in the coming months. In TRT, molecules that are chemically engineered to seek out and attach to proteins highly specific to a particular tumor type are labeled with a particle-emitting (beta or alpha) radionuclide and injected intravenously. Over a period of several hours, the radioactively-tagged molecules (radiopharmaceuticals) chemically bind with high specificity to cancer cells, where they typically remain for several days until the radionuclide decays and emits its high-energy particulate radiation. These particles, through Coulombic interaction with molecules in the cells, break critical molecular bonds, inflicting biological damage in its wake. The mass quantity of these therapeutic radiopharmaceuticals is small, typically 1-10 micrograms, but the number of potentially therapeutic molecules injected number on the order of 10^{15} .

Currently, clinical use of these therapeutic radiopharmaceuticals uses a “one dose fits all” approach, where regardless of patient size, sex, age, the same quantities of radioactivity are administered (the dose that was used in the clinical trial that resulted in the drug’s approval). Although this single-dose approach has been demonstrated to be clinically useful, it is by no means optimized; in fact, most patients are substantially and systematically under-dosed, and do not receive the full potential therapeutic benefit of TRT, as the clinical trials often emphasize safety over potential efficacy.

There is a growing interest in personalizing TRT using quantitative imaging techniques like positron emission tomography (PET) and Single Photon Emission Computed Tomography (SPECT) to quantitatively measure the spatial and temporal biological distribution of the therapeutic radiopharmaceutical. From the *in vivo* imaging data, where we estimate the number of radioactive decays per second in each voxel of the image, we can calculate the amount of energy deposited both in the tumor, to determine whether therapeutic levels of radiation are being achieved, and in normal organs, to be assured that we are not inadvertently delivering toxic levels of radiation to the normal organs. Using this information, it should be possible to tailor a radiotherapeutic dosing approach that is tuned to a patient's own tumor and normal tissue uptake, as measured by imaging that both optimizes dose to tumor, while assuring that healthy organs are not over-dosed.

Several methods are under-study for absorbed dose calculations post radiopharmaceutical therapy. The current gold standard for 3D voxel-wise dosimetry is patient-specific Monte Carlo calculations using the quantitative nuclear imaging activity distributions over time (SPECT or PET) as the input data for the absorbed dose deposition map. Monte Carlo simulations are, however, highly computationally intensive if one wants to achieve low statistical noise at the voxel level. The dose point kernel (DPK) method is a more computationally efficient approach, which uses pre-calculated, radionuclide- and tissue-specific DPKs and image-based patient specific radionuclide distributions as input data to generate patient-specific absorbed dose maps. This method relies on convolving pre-calculated isotope-specific energy deposition kernels with the cumulative activity distribution, obtained from patient imaging, such that the absorbed dose map is obtained.

The first project of this thesis generated Monte Carlo-based dose point kernels for clinically relevant radionuclide beta decays and monoenergetic electrons in various tissues to understand the impact of tissue type on dose point kernels. One fundamental limitation to using this DPK method in clinical dosimetry is that the dose kernels are based on analytic or numerical calculations, or Monte Carlo simulations of beta absorbed dose deposition, yet these probabilistic physics-based energy deposition calculations have not been experimentally validated. The lack of experimental validation work in the literature is primarily due to the challenge of accurately measuring absorbed dose deposition along the relatively short beta range of therapeutic radionuclides (1–10 mm) with sufficient spatial resolution to meaningfully compare with Monte Carlo simulations. As a second project of this work, physical measurements were performed using radiochromic film to measure the beta absorbed dose distributions of ^{90}Y and ^{177}Lu . Excellent agreement was observed between the experimental beta absorbed doses in the linear region of the radiochromic film and the GATE Monte Carlo simulations, demonstrating that radiochromic film dosimetry has sufficient sensitivity and spatial resolution to be used as a tool for measuring beta decay absorbed dose distributions. It also demonstrated, for the first time, that Monte Carlo simulations appear to be accurate to within several percent, as compared with careful physical measurements.

There is increasing evidence that the use of alpha-emitters as radiolabels on some of these therapeutic radiopharmaceuticals results in even more effective treatment than beta-emitters. This is an emerging and promising cancer treatment procedure that is fundamentally different from all other cancer treatments due to the very highly localized nature of energy deposition. Monte Carlo simulations suggested that the alpha-emitters travel $< 100\ \mu\text{m}$ (only several cell diameters) in the tissue and they are highly potent because their ionization density is 100-1000x greater compared to therapeutic beta-emitters. This dense ionization track is highly damaging to DNA and extremely

effective in tumor killing. Another project of this thesis work was to study clinically relevant therapeutic alpha-emitters energy deposition details in several tissues. This project provides a comprehensive study on α -emitting radionuclides for the purposes of its micro-dosimetric calculations for the DPKs generation and to study the impact of their Bragg peaks on overall dose distribution. Since the voxel sizes used in nuclear imaging modalities are > 1 mm, and the range of therapeutic α -emitters are substantially less than 1 mm, so the image-based dosimetry using alpha DPKs are not feasible at this point. However, these kernels may be useful to study the micro metastasized tumor dosimetry in the context of pathology slides demonstrating the microscopic distribution of cancer cells in a tumor.

In nuclear imaging there has been a great excitement in the research and development of the PET scanners for monitoring radiopharmaceutical therapy especially for neuroendocrine tumors and prostate cancer. Total-body PET, where the PET detection ring is extended to multiple rings such that extend nearly fully from head to toe is a new scanner design. New prototype scanners have been designed and built by academia and now industry are demonstrating 20-30X increases in photon detection sensitivity. Major PET scanner manufacturers are beginning to offer new versions of PET systems with unprecedentedly large axial fields of views from 1-2 meters. This could be an ideal tool for both identifying patients eligible to TRT, as well as evaluating the results of these therapies in late-stage metastatic cancers. There has been recent significant interest in the development of a total-body PET scanners in academia for research such as uEXPLORER (United Imaging Healthcare), PennPET EXPLORER (University of Pennsylvania) and the Siemens Vision Quadra for a commercial production. However, GE Healthcare, a prominent PET system manufacturer, yet seems undecided whether to enter the TB-PET market. The latest generation of PET scanners manufactured by GE Healthcare is the Discovery MI (DMI) scanner with an AFOV

up to 25cm and a crystal thickness of 25 mm. This crystal thickness is more than 20% longer than the crystals used in other commercial PET systems. As a next project, we assessed the DMI's potential as a total-body scanner using Monte Carlo simulations. This work investigated the imaging properties of a large extended AFOV DMI scanner by looking at the performance gain with increasing AFOV through simulation. We have found that the AFOV of 2 meters with its 25 mm thick LYSO crystals resulted in ~(28-60)-fold performance gain relative to the current 4-ring DMI architecture, and interestingly, even a potential 2X sensitivity enhancement over other similarly configured TB-PET systems.

PUBLIC ABSTRACT

Cancer is a leading cause of death worldwide, accounting for nearly 10 million deaths in 2020. There are different treatment options available for this disease such as chemotherapy, surgery, radiation therapy, and most recently radiopharmaceutical therapy. Radiopharmaceutical therapy is emerging as a safe and effective targeted method to treating numerous types of cancers in clinics. Pharmaceuticals are radiolabeled with radioisotopes such that it binds very specifically to cancer cells, and not normal tissues, and deliver the radiation dose locally to tumors or cancer cells. This approach of treating cancer has shown efficacy with minimal toxicity to the peripheral healthy cells compared with all other cancer treatment procedures. This current non-optimized approach uses the same amount of radiopharmaceutical dose to all patients; however, every human being is different, their tumor burdens are different, and the biological washout system is different. Therefore, there is a critical opportunity to optimize this cancer treatment method for individual patients through the use of quantitative nuclear imaging. This Ph.D. thesis has developed the utilities that may help to optimize the radiopharmaceutical injection dose for each patient.

In this work, we employed computer simulations to generate the dose point kernels (DPKs) of therapeutic beta- and alpha-emitting radionuclides. These radionuclides are used in radiopharmaceuticals and are a combination of radionuclide and a targeting molecule. The DPKs are useful to calculate the radiation absorbed dose post radiopharmaceutical therapy, thus helpful in personalizing the injection dose. The PET scanners used in nuclear medicine is used for cancer imaging. We have developed a virtual total-body PET scanner using the front-end architecture of current clinical PET scanner, which can image the patient in less time and/or using a lower injected dose. Results of this computer simulations work could be useful in manufacturing a real total-body PET scanner.

TABLE OF CONTENTS

LIST OF TABLES	xvi
LIST OF FIGURES	xvii
PREFACE.....	xxiii
CHAPTER 1: INTRODUCTION	1
1.1. Radiopharmaceutical Therapy	5
1.1.1. Radionuclides used for RPT	7
1.2. Radiopharmaceutical Dosimetry.....	12
1.2.1. MIRD dosimetry	14
1.2.2. Voxelwise dosimetry	16
CHAPTER 2: FUNDAMENTALS OF NUCLEAR MEDICINE IMAGING	22
2.1. Molecular Imaging.....	22
2.1.1. Positron Emission Tomography.....	22
2.1.1.1. Basic Physics of PET Imaging.....	23
2.1.1.2. PET Scanner Architecture.....	25
2.1.1.3. Total Body PET	26
2.1.1.4. PET Radiopharmaceuticals	28
2.1.2. Single Photon Emission Computed Tomography.....	30
2.1.2.1. Physics of SPECT Imaging.....	32
2.1.2.2. Clinical applications.....	33
CHAPTER 3: MONTE CARLO SIMULATIONS IN NUCLEAR MEDICINE.....	35
3.1. Introduction.....	35
3.2. Introduction of GATE Monte Carlo toolkit.....	38
3.2.1. Simulation architecture	41
3.2.1.1. PET simulation setup	41

3.2.1.2. Dosimetry simulation setup	45
CHAPTER 4: DOSIMETRY OF THERAPEUTIC BETA-EMITTERS.....	47
4.1. Introduction.....	47
4.2. Methodology	50
4.2.1. Monte Carlo Simulation using GATE	50
4.2.1.1. Electron step size	51
4.2.1.2. Energy Thresholds	52
4.2.2. Monoenergetic electron dose point kernels	53
4.2.3. Therapeutic beta emitter radionuclides dose point kernels.....	55
4.3. Results.....	56
4.3.1. Monoenergetic electron dose point kernels	56
4.3.1.1. Literature comparison of electron dose point kernels.....	58
4.3.2. Tissue specific beta emitting radionuclide dose point kernels.....	60
4.3.2.1. Literature comparison of beta dose point kernels	65
4.4. Discussion and Conclusions	66
CHAPTER 5: EXPERIMENTAL VALIDATION OF BETA ABSORBED DOSES	71
5.1. Background.....	71
5.2. Methodology	73
5.2.1. Film and Phantom Preparation.....	74
5.2.2. Film Calibration and Scanning Protocol.....	74
5.2.3. Line Source Preparation.....	75
5.2.4. Film Exposure.....	76
5.2.5. Absorbed Dose Calculations.....	77
5.2.6. Sources of uncertainty in measurement of absorbed dose	78
5.2.6.1. Uncertainty in calibration irradiations and curve fitting parameters	78

5.2.6.2. Uncertainty propagation in experimental irradiations	79
5.2.6.3. Uncertainty propagation in activity concentration measurement	80
5.2.6.4. Monte Carlo Simulation and Experimental Setup	80
5.2.6.5. Quantification of absorbed dose distributions: the gamma index test	81
5.3. Results	82
5.3.1. Film Calibration	82
5.3.2. Experimental films exposure with line sources: experiment	84
5.3.3. Absorbed dose uncertainty estimates	85
5.3.4. Experiment vs. Monte Carlo simulations	86
5.3.5. Comparison of measured and simulated dose distributions	90
5.4. Discussion and Conclusions	92
CHAPTER 6: MONTE CARLO SIMULATIONS OF THERAPEUTIC ALPHA-EMITTERS..	96
6.1. Introduction	96
6.2. Materials and Methods	98
6.2.1. Dose Point Kernels	99
6.2.2. Monoenergetic α -particles simulations	99
6.2.3. Simulations of α -emitting radionuclides	100
6.2.4. Application of alpha dose point kernels	101
6.3. Results	102
6.3.1. Monoenergetic α -particles simulations	102
6.3.1.1. Dose point kernels of mono-energetic α -particles and comparison against different tissues	105
6.3.2. α -Emitting radionuclides in different tissues	106
6.3.2.1. Comments on multiple Bragg-peaks	109
6.3.3. Dose point kernels comparison against different tissues	110
6.3.4. Convolution of dose point kernels with histological slides for microdosimetry ..	115

6.4. Discussion and Conclusions	115
CHAPTER 7: MONTE CARLO SIMULATION OF GE DISCOVERY MI PET SCANNER AND EVALUATION OF LONG AXIAL FIELD-OF-VIEW SCANNER USING ITS FRONT-END ARCHITECTURE	119
7.1. Introduction.....	119
7.2. Methodologies.....	122
7.2.1. Monte Carlo simulations.....	122
7.2.2. Discovery MI 4-ring scanner geometry	122
7.2.3. GATE Modelling of Discovery MI scanner	123
7.2.3.1. Intrinsic Activity in LYSO crystals	125
7.2.4. System Performance	126
7.2.4.1. Spatial resolution	126
7.2.4.2. Sensitivity	127
7.2.4.3. Count rates, scatter fraction, and Noise Equivalent Count Rates	128
7.3. Results.....	130
7.3.1. Quantification of contribution from Intrinsic Activity from LYSO crystals.....	130
7.3.2. Spatial resolution	131
7.3.3. Sensitivity	133
7.3.4. Count rate performance.....	136
7.4. Discussion and Conclusions	139
CHAPTER 8: PET PHANTOM DEVELOPMENT.....	144
8.1. Introduction.....	144
8.2. Methods.....	151
8.2.1. Modified NEMA phantom.....	152
8.2.2. Large anthropomorphic phantom design	153
8.2.3. Phantom fill and image acquisition.....	156

8.3. Results.....	158
8.3.1. Imaging of modified NEMA phantom.....	158
8.3.2. Imaging of large anthropomorphic chest phantom	165
8.4. Discussion and Conclusions	169
CHAPTER 9: DISCUSSION.....	172
CHAPTER 10: CONCLUDING REMARKS AND FUTURE DIRECTIONS	177
APPENDIX.....	184
A. Dose point kernels GATE simulation scripts.....	184
A.1 50 keV monoenergetic electrons.....	184
A.2 Simulation scripts of ^{186}Re β -emitter	187
B. Validation experiment simulation setup in GATE using ^{177}Lu line source	190
C. Decay chains of simulated α -emitting radionuclides.....	195
D. Dose point kernels simulation scripts of ^{225}Ac α -emitter	196
E. Simulation scripts of Discovery MI 4-ring scanner with a scatter phantom.....	199
F. List of publications	206
G. List of peer reviewed abstracts	207
REFERENCES	209

LIST OF TABLES

Table 1: Representative list of diagnostic PET radiopharmaceuticals.....	29
Table 2: The densities and effective atomic numbers of tissues used in simulations.....	51
Table 3: The CSDA range of electrons in different tissues used for dose point kernel scaling ...	53
Table 4: The electronStepLimiter parameters for monoenergetic electrons in simulation.....	54
Table 5: The electronStepLimiter parameters for the beta radionuclides in simulation.....	56
Table 6: X_{90} values calculated from simulated dose point kernels. The indicators (a), (b), (c) and (d) in the table are references [126], [145], [148], and [149] respectively.	61
Table 7: Various uncertainty components in the experimental work to absorbed dose measurements.....	85
Table 8: Summary of radionuclides simulated in this work. Full decay chain was simulated for all radionuclides.	100
Table 9: Number of Brags peaks observed in simulations.	109
Table 10: Specifications of the Discovery MI used in the simulation for 4-ring scanner.	123
Table 11: Spatial resolution results for different radial, tangential and axial positions for simulated and measured point sources at two radial positions: (0, 1, 0) cm and (0, 10, 0) cm within the scanner FOV. The mean values of the three different reconstructed images are reported. Measurement performed at Stanford University from Hsu et al.[206] are also reported for comparison.....	132
Table 12: Comparison of NECR peak values for 4 - 40 ring scanners. The NECR peak value for 4-ring scanner using a 200 cm long scatter phantom is compared to 8, 20, 30, and 40-ring scanner configurations.	139
Table 13: Comparison of different phantoms.	146
Table 14: PET/CT acquisition and reconstruction parameters.	157
Table 15: Visual comparison of reconstructed images using three different reconstruction algorithms with variable filter (6, 5, 4, 3, and 2 mm) and penalization factors ($\beta = 450, 400, 350, 300, \text{ and } 250$).	159
Table 16: Comparison of three different reconstructed images of large andromorphic chest phantom.....	166

LIST OF FIGURES

Figure 1: Illustrative IMRT treatment plan for the prostate and proximal seminal vesicles. The image shows the radiation dose distribution in the (A) axial (B) coronal and (C) sagittal orientations. The treatment plan includes seven beam angles and uses beam energy of 10 MV [4]...... 1

Figure 2: Images shows (a) pretherapy image and follow up after (b) 2 cycles (c) 4 cycles (d) after 6 cycles. Patient was treated with 6.0 GBq of ¹⁷⁷Lu-PSMA-617 radiopharmaceutical [5].... 2

Figure 3: (A, B) shows the image pretherapy and post therapy image of the patient. (A) is ⁶⁸Ga-PSMA-617 PET/CT image shows intense PSMA uptake was detected in supra-infra diaphragmatic metastatic lymph nodes (B) post therapy image taken after 4 cycles of ¹⁷⁷Lu-PSMA-617 therapy, PSA decline of 95% was observed and image shows a complete metabolic response [6]. However, figures (C and D) is an example of therapy of a different patient where RPT was failed. After 3 cycles of ¹⁷⁷Lu-PSMA-617 therapy tumor spreads throughout the body [7]. In both example a similar level of activity (~6 GBq) was administered..... 3

Figure 4: Schematic diagram of the workflow for the patient-specific dosimetry using the DPKs and the patient quantitative imaging data [50]. Only one imaging time point is shown in the figure. 17

Figure 5: Maximum intensity projection images of PSMA ligands commonly used for PET imaging. Image show typical biodistribution of different radiopharmaceuticals as well as different number of positive lesions. Specific tumor uptake is shown by red arrows [66]. 23

Figure 6: (A) Schematic drawing of PET imaging principle and (B) schematic shows how PET measures the activity using the lines of response (LOR)..... 24

Figure 7: (A) GE Discovery 4-ring (20 cm AFOV) PET/CT clinical scanner and (B) total body uEXPLORER PET scanner with 196 cm AFOV..... 25

Figure 8: (A) Schematics of SPECT dual head camera with parallel hole collimators and (B) SPECT/CT clinical camera. 32

Figure 9: ^{99m}Tc-MIBG SPECT/CT imaging for the diagnosis of pheochromocytoma. (A) planar image showing intense focal lesion in left suprarenal area (B) section of SPECT imaging slice (C) corresponding CT imaging slice (D) fused SPECT and CT slices shows the lager uptake in adrenal gland, indicating pheochromocytoma. (E) SPECT slice shows the right adrenal gland (F) CT slice and (G) both adrenal glands show the higher uptake [86]. 34

Figure 10: Modeling of Discovery MI 4-ring scanner in GATE. The scanner system has a total of 34 rsectors, 4 axial and 4 transaxial modules (blocks)..... 43

Figure 11: Dose point kernels simulations in GATE. Tracks in green are photons whereas tracks in red are electrons. 46

Figure 12: Beta spectra of radionuclides simulated in this work; spectra were taken from RADAR website.	56
Figure 13: Dose point kernels of (A) 15 keV, (B) 50 keV, (C) 100 keV, (D) 500 keV, (E) 1 MeV, (F) 2 MeV, (G) 4 MeV, and (H) 10 MeV monoenergetic electrons in water, bone, blood, adipose, red marrow, and lung.	58
Figure 14: Comparison of DPKs of monoenergetic electrons with published kernels (A) 50 keV, (B) 100 keV, (C) 1 MeV in water and (D) 1 MeV in bone.	59
Figure 15: Mean percentage deviation from other published works for (A) monoenergetic electrons in water 50 keV, 100 keV, 1 MeV, and 1 MeV monoenergetic electrons in bone and (B) ^{177}Lu and ^{90}Y beta dose point kernels in water and bone with literature values.	60
Figure 16: (A) Beta DPKs for ^{177}Lu in bone, blood, red marrow, water, adipose, and lung (B) the beta DPKs of ^{177}Lu and ^{90}Y in water compared with other tissues.	62
Figure 17: Dose point kernels of the beta emitters (A) ^{90}Y , (B) ^{188}Re , (C) ^{186}Re , (D) ^{32}P , (E) ^{153}Sm , and (F) ^{89}Sr nuclides in water, bone, blood, red marrow, adipose and lung as a function of scaled distance (r/X_{90}).	63
Figure 18: DPKs of beta radionuclides plotted with scaled distance and radial distance in (A) & (B) lung, (C) & (D) water, (E) & (F) blood, and (G) & (H) bone. The abscissa and ordinates are scaled to be same so that one can easily make a comparison.	64
Figure 19: Comparison against literature kernels for ^{177}Lu in (A) water and (B) bone.	65
Figure 20: Comparison against literature kernels for ^{90}Y in (A) water and (B) bone.	66
Figure 21: (A-C) GATE Monte Carlo simulation set-up with the line source and EBT3 film and (D) experimental setup.	80
Figure 22: Scanned images of calibration films irradiated with 6 MV photon beams.	83
Figure 23: Sensitometric response curves for the red, green, and blue channels of scanned EBT3 film irradiated by 6MV photons to absorbed dose from 0 to 13.4 Gy using the Equation (8).	83
Figure 24: Scanned images of the ^{90}Y exposed experimental films in low-density polyethylene (first row), cortical bone (second row), and lung equivalent (third row) phantom material.	84
Figure 25: Scanned images of the ^{177}Lu exposed experimental films in lung equivalent phantom material.	85
Figure 26: (A-C) Experimental vs. Monte Carlo absorbed dose measurements of ^{90}Y in polyethylene, cortical bone and lung equivalent phantoms and (D) ^{177}Lu in lung equivalent phantom for different exposure times. The shaded area corresponds to error bars in simulated	

and measured absorbed doses. Significant disagreement at small radii is due to delamination of films at the line-source interface. 87

Figure 27: Monte Carlo simulation of absorbed dose distribution from beta and bremsstrahlung radiation of the decay scheme of ^{90}Y as a function of distance from a line source of activity 5.18 MBq in a plastic cylinder of wall thickness of 0.21 mm and internal diameter of 0.42 mm using the same line source and similar Monte Carlo setup but with the larger low-density polyethylene geometry of radius of 42 cm. Acquisition time in simulation was 4 hr. The voxel size used for betas simulation was 0.05 mm, whereas for bremsstrahlung simulation was 1 mm. The yellowish shaded region in the plot represents the sensitive region of the EBT3 film. 89

Figure 28: 1D gamma analysis calculations for ^{90}Y simulation and experimental absorbed dose comparisons in (A) lung and (B) cortical bone for 16-hour exposures. The dashed line in plot is the boundary of the pass-fail region..... 90

Figure 29: Simplified decay chains of ^{225}Ac and ^{213}Bi radionuclides. 100

Figure 30: Histological slides showing the FAP (A) uniform expression and (B) irregularly shaped expression. 101

Figure 31: Simulation of mono-energetic α 's in several tissues. (A, C, E, G, I, K) Plot of absorbed dose per decay vs the radial distance and (B, D, F, H, J, L) plot of Bragg peak at different energies. Plots are arranged in terms of decreasing density of tissues for ease of comparison..... 104

Figure 32: (A, C, E, G) Dose point kernels of mono-energetic α 's (5-8) MeV in several tissue types. (B, D, F, H) Comparison of tissue-specific dose point kernels of mono-energetic α 's in several tissues..... 106

Figure 33: (A-L) α -Emitting radionuclides ^{227}Th , ^{224}Ra , ^{223}Ra , ^{225}Ac , ^{211}At , ^{212}Pb , ^{212}Bi and ^{213}Bi in compact bone, blood, red marrow, water, adipose and lung tissues. 109

Figure 34 (A-P): Dose point kernels of α -emitting radionuclides ^{227}Th , ^{225}Ac , ^{224}Ra , ^{223}Ra , ^{212}Pb , ^{211}At , ^{212}Bi , and ^{213}Bi in several tissues and their DPKs comparisons. 113

Figure 35: (A) and (B) are inverted images of the original images, (C) and (D) are ^{225}Ac dose point kernels, and (E) and (F) are the results of convolution, i.e., the dose map..... 115

Figure 36: Count rates estimation using the NEMA protocol [236]. The activity of 800 MBq was used in the scatter phantom to generate this figure using the 4-ring scanner. (A) Sinograms of coincidences obtained from GATE root output (B) Sinogram after inserting Gaussian filter and setting pixels farther than 12 cm from the center of FOV to zero (C) Sinogram after alignment according to maximum values for each projection angle (D) Sum of all projection angles of the sinogram (E) Selecting the central 40 mm strip to estimate the scatters and randoms (F) plot of count rates curves and NECR. A sinogram-based analysis was performed to estimate the coincidence event rates. 130

Figure 37: (A) Spatial resolution along the axial and transverse (average of radial and tangential) direction for different scanner rings (B) Transverse resolution for six-point sources with varying radial offsets (at 0, 1, 5, 10, 15, and 20 cm) in the center of the axial FOV for five scanner geometries..... 132

Figure 38: (A) Figure shows a comparison of simulated and measured absolute attenuation free sensitivity for the DMI 4-ring scanner. There is a 6.41% difference between simulation and measurement [206] data points. Exponential regression of the true count rates was used for attenuation-free sensitivity estimation. (B) Comparison of attenuation-free sensitivities for 4, 8, 20, 30, and 40-ring scanners..... 133

Figure 39: (A) Axial sensitivity profile of contiguous axial slices from the center of the scanner for 4-ring scanner. (B) Axial sensitivity profiles for 4, 8, 20, 30, and 40-ring scanner configurations. Acceptance angles were not restricted for these profiles as the Discovery MI scanner accepts all oblique lines. Sensitivity profiles were obtained using simulation of a 200 cm long 3.2 mm diameter line source with 4 MBq ¹⁸F activity..... 134

Figure 40: Relative sensitivity profiles for a line source of 200 cm length in a 30 cm diameter, 200 cm long cylindrical phantom, for scanners with 4-ring, 8-ring, 20-ring, 30-ring, and 40-ring configurations. Line source had a same diameter as in NEMA sensitivity phantom. Similar sets of sensitivity profiles were seen in simulations performed by Surti et al [75]...... 135

Figure 41: Count rates comparison between simulation with and without intrinsic activities (IA). The volume of the scatter phantom was considered for the activity concentration calculations. The impact of intrinsic activities was found to be < 1% in the clinical activity range. Therefore, intrinsic activities in LYSO crystals are not included in all simulations performed herein to save the computation burden..... 136

Figure 42: Comparison of count rates curve between simulation and measurement performed at Stanford University for DMI 4-ring scanner [206]. The volume of the scatter phantom (~22 L) was considered for the activity concentration calculations. The maximum deviation in activity concentration measurements was 2.43%. 137

Figure 43: Count rate curves and NECR for 4-ring (AFOV 20 cm) and 20-ring (1 m AFOV) scanner. Count rate curves for the 4-ring scanner lies at the bottom of the plot. For comparison with 4 and 20 ring scanner NECR, a 200 cm long scatter phantom was simulated in both ring configurations. A gain of 15 times can be expected when comparing the NECR peak values..... 138

Figure 44: Count rate curves and NECR for 4-ring (AFOV 20 cm) and 40-ring (2 m AFOV) scanner. Count rate curves for the 4-ring scanner lies at the bottom of the plot. For comparison, 200 cm long scatter phantom was simulated in both ring configurations. A gain of 28 times can be expected when comparing the NECR peak values..... 138

Figure 45: The increase in NECR as a function of axial length for 4, 8, 20, 30, and 40-ring scanners. Note that for this comparison, all scanners were simulated with 200 cm long scatter phantom with an activity concentration range of (0.02 – 12.74) kBq/mL..... 139

Figure 46: Commonly used phantoms in nuclear medicine PET and SPECT applications. (A) Cylindrical (B) Jaszczak (C) NEMA image quality and (D) CTN chest phantom.....	145
Figure 47: The ACR PET phantom (A) side view of the phantom shows upper faceplate, middle portion with spheres (for use in SPECT), and lower part with six different sizes of rods arranged in a 6 pie-shaped pattern (B) top view of the phantom.....	149
Figure 48: (A) NEMA phantom with 6 spheres. (B) CAD drawing of modified NEMA spheres with 12 spheres.	152
Figure 49: (A) Drawing of the inner platform support of the phantom. (B) Inner tubing circuitry path.	154
Figure 50: (A-D) CAD drawings of the large CTN chest phantom showing its interior parts...	155
Figure 51: (A) Final product of large CTN chest anthropomorphic phantom. (B) PET MIP image of the final product showing the different sized spheres.....	155
Figure 52: PET/CT maging of modified NEMA phantom with 12 spheres showing the spheres in the upper and lower part of the phantom (A) CT scan (B) PET scan and (C) fused PET and CT slices.....	158
Figure 53: ROIs based (A) recovery coefficient calculations and (B) the background activity calculations of modified NEMA 12 spheres phantom. 3D spherical ROI were drawn for analysis.....	159
Figure 54(A-D): VPFX reconstructions with different iterative updates and post reconstruction filter.....	160
Figure 55: Impact of iterative updates on the recovery coefficients of spherical lesions.....	161
Figure 56: Impact of post-reconstruction filter size is shown for two different combinations...	162
Figure 57: VPFXS (SharpIR) reconstructions using 4 iteration and 16 subsets (A) using post filter of 5 mm (B) 6 mm filter (C) RC max values using different filters and (D) RC mean values with variable filter sizes.....	163
Figure 58: RC curves (A) RC max and (B) RC mean values obtained using QCFXS (Q.Clear) reconstructions for different penalization factors.	163
Figure 59: Comparison of percentage contrast recovery (mean) using three different reconstructions.	164
Figure 60: Comparison of recovery coefficients using three different reconstructions.....	164
Figure 61: PET/CT imaging of large anthropomorphic chest phantom. Transverse, sagittal, and coronal slices of the phantom are shown. (A) CT scan (B) PET scan and (C) fused PET/CT slices.	165

Figure 62: Recovery coefficient curves of the large anthropomorphic chest phantom spherical lesions using (A) VPFX and (B) VPFXS (Sharp IR) reconstructions.	166
Figure 63: RC curve using the Q.Clear reconstruction using $\beta = 350$	167
Figure 64: Comparison of recovery coefficient curves of three reconstructions using (A) RC max and (B) RC mean values.	168
Figure 65: Comparison of recovery coefficient (RC max) curves for two different phantoms developed in this work.	168
Figure C1: Simplified decay chains of ^{227}Th and ^{223}Ra radionuclides.	195
Figure C2: Simplified decay chains of ^{224}Ra , ^{212}Pb and ^{212}Bi radionuclide.	195
Figure C3: Simplified decay chain of ^{211}At radionuclide.	195

PREFACE

The basis for this research originally stemmed from my passion for understanding the physics of radiopharmaceutical therapy, with a goal of developing new and more accurate tools for quantitative radiation dosimetry. Targeted radiopharmaceutical therapy is a rapidly growing therapeutic approach to treat widely metastatic cancers of various types. However, optimized treatment planning requires that the administered radioactive dose be tailored to the particular patient; there is a critical need to personalize the treatment. As the physics associated with therapy and imaging go hand in hand, this work necessarily integrates a combination of computational dosimetry (energy deposition) and imaging. All the work presented henceforth was conducted in the Department of Radiology and Radiation Oncology at the University of Iowa. All projects and associated methods were approved by the dissertation committee.

Chapter 1 introduces the radiopharmaceutical therapy and dosimetry methods of radiopharmaceutical therapy such as the MIRD schema and voxel-wise dosimetry. Chapter 2 presents the overview of nuclear medicine imaging, including PET and SPECT imaging. Chapter 3 describes the Monte Carlo simulations and their uses in nuclear medicine imaging and therapy. The brief overview of Monte Carlo simulation setup used in this thesis work is also presented in chapter 3.

The work presented in Chapter 4 has been published in the journal *Radiation Research* [1]. The work targeted demonstrating the importance of including tissue type in dosimetry calculations. I was the first author, responsible for all major work, including the Monte Carlo simulations and data analysis, and manuscript composition. Stephen Graves was integrally involved in this work. John Sunderland was the supervisory author on this project and was involved throughout the project in concept formation and manuscript preparation.

Chapter 5 consists of a Monte Carlo simulation of the therapeutic alpha-emitters for the purposes of their dose point kernels generation, and their utilization for the absorbed dose calculations. The summary of chapter 4 will be submitted for publication.

The work discussed in Chapter 6 describes carefully performed experiments measuring the spatial radiation absorbed dose (energy deposited per unit mass) distribution for few medically relevant beta-emitters, and comparisons with radiation absorbed dose Monte Carlo simulation. This work represents the first time that careful high-resolution measurements radiation absorbed dose of clinically important beta emitters have been made and compared with Monte Carlo calculations. This work has recently been published in the journal *Medical Physics* [2]. I was the first author, responsible for all major areas of concept formation, experimental measurements, Monte Carlo validation and data analysis, and the manuscript composition. Stephen Graves, Ryan Flynn, and Sarah Strand were involved in the early stages of concept formation and contributed to manuscript edits. Stephen Graves and Sarah Strand contributed to the calibration of the films. Stephen and John helped to prepare the radionuclide sources for the experiment. Thanks to Stephen for his radiochemistry expertise. John Sunderland was the supervisory author and was involved in conceptualization and manuscript edits.

Chapter 7 presents the Monte Carlo simulations of a clinical PET scanner for the purpose of studying a hypothetical long axial field-of-view (LAFOV) total-body PET scanner. This work presents the first Monte Carlo model of the GE Discovery MI scanner. With the help of computer simulations, we evaluated the performance of the LAFOV scanners in terms of scanner sensitivity, counts rates, and NECR. The summary of this work has been published in *Medical Physics* [3]. I was the first author, responsible for all major areas of concept formation, Monte Carlo simulation, data analysis, and most of the manuscript composition. Michael Merrick and Stephen Graves

contributed to manuscript edits. John Sunderland was the supervisory author and involved in concept formation and manuscript edits throughout the project.

Chapter 8 consists of the PET phantom development project, including an anthropomorphic adult chest phantom and modified NEMA phantom. Such phantoms aid in the characterization of quantitative performance of PET and SPECT imaging systems – necessary input for quantitative dosimetry. The large chest phantom was developed to simulate the clinical scanning situation of male adult chest. The phantoms were imaged and performed visual and quantitative measurements of the PET scan. Discussion of this thesis work is included in Chapter 9 and Chapter 10 discusses the conclusion of this work and future remarks.

CHAPTER 1: INTRODUCTION

External beam radiotherapy (EBRT) is based on a well-studied relationship between radiation absorbed dose to tissue, and its associated toxicity. Cancer cells have a tendency to be more radiation-sensitive than normal tissues, as the cancer cell's ability to repair itself from radiation damage is typically substantially less than normal human tissue. External-beam radiation therapy planning is prospective in nature, and typically based upon a physician's prescription of a quantitative therapeutic radiation dose delivered to the targeted tumor(s) from a well-calibrated linear accelerator. A maximum radiation dose to normal nearby organs is often also specified as in **Figure 1**. Together, the radiation therapy physicist and the radiation therapy physician are in complete control of how much radiation dose is delivered to the tumor and normal tissue through control of the linear accelerator output, and carefully controlled targeting. **Figure 1** shows the Intensity Modulation Radiotherapy (IMRT) treatment plan encompasses the prostate (red outlined region) and proximal seminal vesicles and avoids nearby regions such as bladder, rectum, and femoral heads.

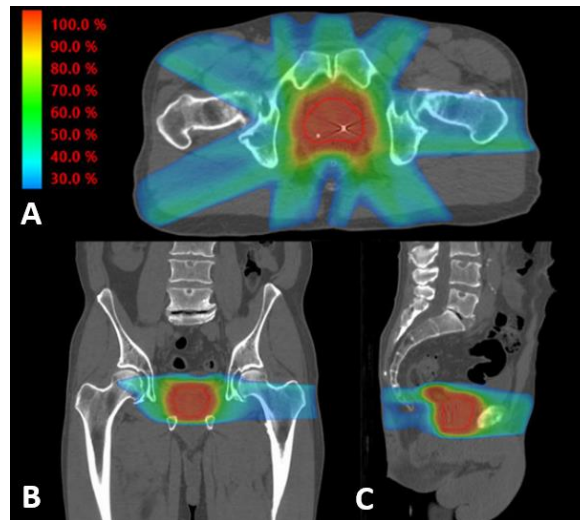


Figure 1: Illustrative IMRT treatment plan for the prostate and proximal seminal vesicles. The image shows the radiation dose distribution in the (A) axial (B) coronal and (C) sagittal orientations. The treatment plan includes seven beam angles and uses beam energy of 10 MV [4].

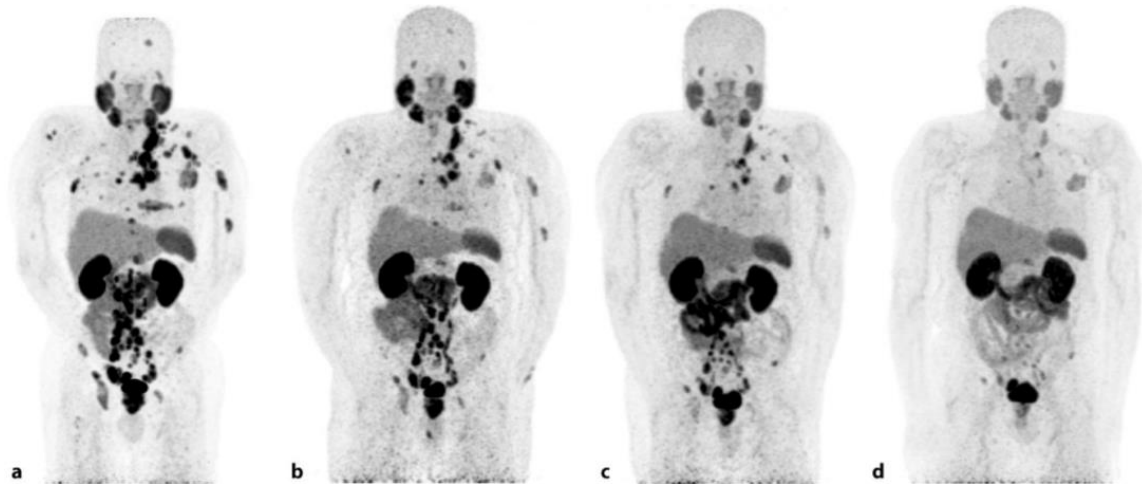


Figure 2: Images shows (a) pretherapy image and follow up after (b) 2 cycles (c) 4 cycles (d) after 6 cycles. Patient was treated with 6.0 GBq of ^{177}Lu -PSMA-617 radiopharmaceutical [5].

However, in targeted radiopharmaceutical therapy (RPT) localization of the radiation dose is largely outside of the direct control of the physicist and physician, as its spatial distribution in the body is entirely dependent upon the pharmacokinetics of the radiopharmaceutical after injection, and its chemical binding characteristics to both tumor and normal tissues. It remains very difficult to predict its effectiveness or toxicity without direct measurements of distribution being performed. Further, dosimetry in RPT is more complex and subtle than for EBRT as it requires multiple time point imaging as shown in **Figure 2**. The ability to predict treatment response based solely on image-based dosimetry in RPT has to date been inconsistent, presumably because the binding of the radiopharmaceuticals at the cellular level is typically non-uniform, and the low-dose-rate of the treatment radiation from the radiopharmaceutical allows for cellular repair during the prolonged day and week-long internal irradiations. Biological effective dose (BED) and Equivalent uniform BED have been unevenly introduced to account for the protracted and non-uniform irradiation delivered by RPT. **Figure 2** (a) shows the activity uptake in metastasized prostate cancer using the diagnostic PET imaging agent ^{68}Ga -PSMA prior to ^{177}Lu -PSMA therapy and (b-d) after subsequent therapeutic treatments with ^{177}Lu -PSMA. With ^{177}Lu -PSMA

treatment, the tumor cells are irradiated directly from the beta particles from ^{177}Lu for several weeks (the half-life of ^{177}Lu is 6.7 days). Each [^{177}Lu]-PSMA treatment serves as a fresh source of exposures and emit particulate and photons radiations to kill the cancer cells over the course of a several month treatment regimen.

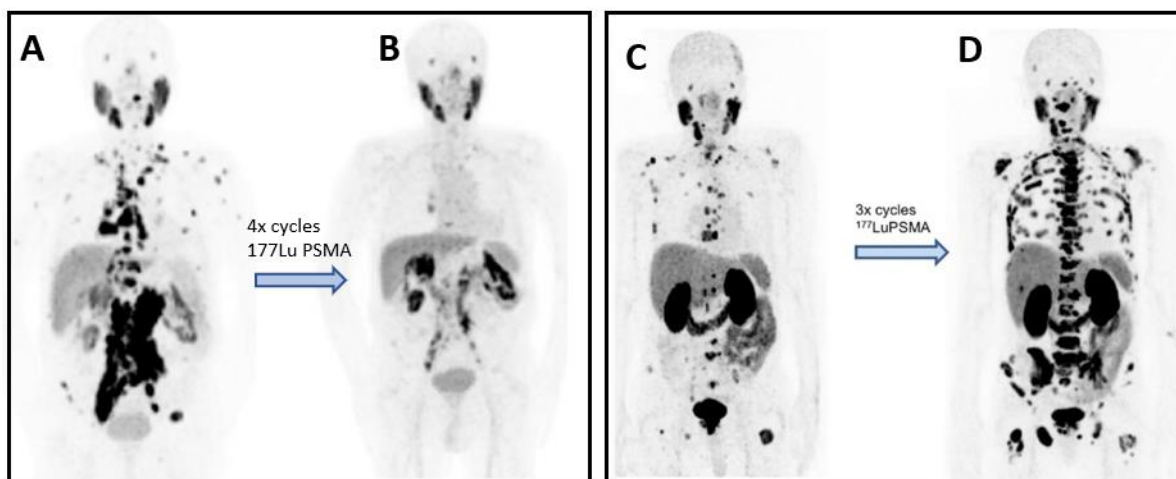


Figure 3: (A, B) shows the image pretherapy and post therapy image of the patient. (A) is ^{68}Ga -PSMA-617 PET/CT image shows intense PSMA uptake was detected in supra-infra diaphragmatic metastatic lymph nodes (B) post therapy image taken after 4 cycles of ^{177}Lu -PSMA-617 therapy, PSA decline of 95% was observed and image shows a complete metabolic response [6]. However, figures (C and D) is an example of therapy of a different patient where RPT was failed. After 3 cycles of ^{177}Lu -PSMA-617 therapy tumor spreads throughout the body [7]. In both example a similar level of activity (~ 6 GBq) was administered.

To help move the field forward and better understand and optimize clinical RPT, we aim to perform in-depth dosimetric calculations of therapeutic beta and alpha emitters in various tissue types. There has been a significant interest in personalizing the RPT because the current clinical practice utilizes the “one-dose-fits-all” approach. However, every individual is different, and their biology and washout systems are different. Thus patient-specific administered activity needs to be optimized for effective therapeutic treatment. This can be done by using imaging to estimate the dosimetry in both tumors and normal organs.

Patient-specific dosimetry calculations can be performed in multiple ways. One of the conventional methods is by utilizing the MIRD schema [8]. Other methods such as direct Monte Carlo simulations exploiting the patient pharmacokinetics data and anatomy, is considered the gold standard for absorbed dose calculations. Although the Monte Carlo simulations results are likely more accurate, they are an excessively computationally inefficient method. Another image-based approach, called as dose point kernel convolution or voxel S values method, is gaining traction because this method is computationally efficient. The dose point kernels, or voxel S values are radionuclide-specific Monte Carlo derived data. This method is currently used in commercial dosimetry software applications, such as MIM, DOSIsoft, and Velocity. Using this approach, once we make the pre-tabulated data ready; we don't have to perform additional Monte Carlo simulations each time to be used for absorbed dose calculations. Efforts have been made by some investigators to simulate and generate a database of radionuclides of interest in RPT [9-11]. However, as of writing this thesis, not all radionuclide-specific Monte Carlo generated dose point kernels data are available in the literature.

One aim of the thesis was therefore to simulate and generate DPKs database of several important radionuclides of interest in RPT. We generated the dose point kernels of 7 therapeutic beta and 8 alpha-emitting radionuclides. In addition, the impact of tissue types on dose point kernels were studied carefully to investigate the dose point kernel in water and kernels in other tissues that have been scaled to account for density; however, tissue density predictably demonstrated itself to be a significant variable in dose point kernel distribution.

Although dose point kernels data are available in the literature, only a few photons absorbed dose distributions have been experimentally validated, and up until now, the beta component has not yet been experimentally validated. Thus, an additional aim of this thesis was

to experimentally measure the beta absorbed dose distributions to compare with the theoretical predictions. We experimentally measured the ^{90}Y beta absorbed doses in low-density polyethylene, cortical bone, lung, and ^{177}Lu doses in the lung using radiochromic EBT3 film and tissue-equivalent phantoms. Measured absorbed doses using the film were assessed by comparing them to the corresponding Monte Carlo simulations. The result of this work provides (1) experimental evidence regarding the accuracy of existing Monte Carlo codes and (2) an upper bound on the systematic error from Monte Carlo calculations in the context of radionuclide dosimetry.

In nuclear medicine, PET/CT scanners are used to image the disease staging, and to monitor the therapy response. There are ongoing efforts in making total-body PET systems to maximize imaging, hence the image quality and minimize patient scanning time and injection activity. The next aim of the thesis was to simulate a hypothetical long total-body PET scanner of 2 m AFOV by exploiting the SiPM based GE Discovery MI clinical PET scanner to study the performance evaluation of the total body scanner based on its front-end geometry.

1.1. Radiopharmaceutical Therapy

Radiopharmaceutical Therapy (RPT) is the process of targeted delivery of radioactive atoms to tumor-associated or cancerous targets. It is a novel therapeutic approach for the treatment of cancer, providing several advantages over other treatment options, particularly in the situation of widely metastatic disease. A radiopharmaceutical is composed of a radioisotope (radioactive tag) bound to a targeting agent such as organic or inorganic small molecule that it designed to bind to particular cancer types or features (for example, Fibroblast Activation Protein Inhibitor (FAPI) for a variety of solid tumors, Prostate Specific Membrane Antigen (PSMA) for prostate cancer, a peptide (Somatostatin Receptor type 2 (SSR2)) for neuroendocrine tumors, a protein including antibodies (CD20, CD37, CD45), antibody fragments, or a nanoparticle with associated

biochemical targeting. The targeting agents can have a high specificity and affinity for different types of targets, such as receptor and transporter systems, enzymes, antigens, or misfolded proteins. The labeled molecule conveys the radioisotope to specific organs, tissues, or cells according to the inherent pharmacokinetics of the radiopharmaceutical. Once a radioisotope reached to cancer or tumor site, it delivers a high radiation dose to cancer or tumor while minimizing the dose to healthy organs or tissues due to its high target specificity and low background tissue uptake. Unlike external beam radiotherapy (EBRT), the radiation is not administered from outside the patient's body, but is internally administered through intravenous or intraarterial injection, and localizes to the tumor or its microenvironment systemically, similar to chemotherapy or biologically targeted therapy [12]. The principle of "theranostics" in nuclear medicine uses a pair of radiopharmaceuticals for therapeutic and diagnostic purposes. The pharmaceuticals bind to the same target and can be radiolabeled with either a therapeutic (longer lived with high activity) or diagnostic radionuclide (shorter half-life and lower activity). For therapy, beta and alpha-emitting radionuclides are used, while for diagnostic imaging, gamma or positron-emitting radionuclides are used. There are several theranostic pairs that have been used in clinics such as Ga-68 DOTATATE and Lu-177 DOTATATE, Ga-68 DOTATOC and Y-90 DOTATOC, Ga-68 PSMA11 and Lu-177 PSMA617, Ga-68 FAPI and Lu-177 FAPI, F-18 PSMA and Ac-225 PSMA, etc. The concepts of the theranostics are the foundation of nuclear medicine and new tools soon to be achieved may help increasing precision and tailored medicine.

Radioisotopes such as ^{131}I , ^{90}Y , ^{177}Lu , ^{153}Sm , and ^{223}Ra have been used in RPTs. For the treatment of thyroid cancer, ^{131}I is administered. ^{90}Y microspheres have been used for the treatment of liver cancer. ^{223}Ra is used for the treatment of bone metastases. And ^{177}Lu -DOTATATE (LUTATHERA; Advance Accelerator Applications) is used for the treatment of neuroendocrine

tumors (NET). To assure that new RPT radiopharmaceuticals are being optimally implemented, advances in targeting need to be matched with advances in quantitative imaging and dosimetry methods. RPT pharmacokinetics are measurable by quantitative imaging and are known to vary across patients, both in tumors and normal tissues. Therefore, fixed or weight-based activity prescriptions are not currently optimized to deliver a cytotoxic dose to targets while remaining within the tolerance dose of organs at risk. Methods that provide absorbed dose estimates to individual patients rather than to reference geometries are needed to assess and personalize the injected dose to achieve optimal effect. Accurate doses to targets and organs at risk will benefit the individual patients and decrease uncertainties in clinical trials. PET or SPECT imaging can be used to measure activity distribution in-vivo and image-based activity information can be used to determine patient-specific treatment plans where the absorbed dose to the targets and organs at risk can be calculated. The development and adoption of imaging-based dosimetry methods are particularly beneficial in early clinical trials. For the image-based dose calculations, several methods can be utilized, such as the MIRD organ-based approach, voxel-wise dosimetry, and full Monte Carlo simulations. However, the full Monte Carlo simulations using the patient activity distribution and anatomical geometry, is highly computationally intensive. On the other end of the spectrum, the MIRD method gives only a crude approximation of the absorbed dose estimate. Therefore, the voxel-wise dosimetry using the dose point kernels (DPKs) method may be the most pragmatic approach to facilitate the treatment planning for radiopharmaceutical therapy.

1.1.1. Radionuclides used for RPT

Three different types of radiations are relevant for RPT, they are electrons (β -particles, Auger electrons, internal-conversion electrons and Coster-Kronig electrons), alpha particles, and photons (x-rays and gamma rays). These radiations are emitted from the decay of the radionuclides.

In RPT the activity distribution of the radionuclides may be visualized and quantitated in both space and time by PET or SPECT imaging techniques to examine targeting of the agent. This provides a significant advantage over other therapeutic methodologies like chemotherapies and immunotherapies where drug delivery is unmeasurable. The ability to quantitative image and measure the distribution of therapeutic radiopharmaceuticals enables a precision medicine approach to RPT delivery [12]. It is the radionuclide photon emissions that are used for imaging the distribution of RPT using PET and SPECT. The photon energy range of 100 to 200 keV are optimal for imaging using the SPECT and gamma-camera, however a wide range of photons energy can be imaged. In PET, the 511 keV annihilation photons are used for imaging. From the quantitative radioactivity information from these nuclear imaging techniques, absorbed dose (energy deposited per unit mass) deposited by the radionuclides can be calculated using several computational approaches.

Radionuclides that decay by electron capture emit Auger electrons, very low energy electrons, that have a range of 1-1000 nm, depending on their emission energy. Auger emitting radionuclides with appropriate half-lives are candidate radionuclides for RPT and can be attached to highly targeting molecules for RPT applications. Due to its very short range of energy deposition, Auger electrons emitted in cascade offer potential for a highly focal irradiation for cancer treatment while sparing normal tissues. Radionuclides such as ^{111}In , ^{67}Ga , $^{99\text{m}}\text{Tc}$, $^{195\text{m}}\text{Pt}$, ^{125}I , and ^{123}I emit Auger electrons [13]. This short-range radiation could be highly cytotoxic, if the RPT drug localizes within a cell nucleus [14-16]. Preclinical studies using the Auger electrons were first performed by Kassis and Adelstein using ^{125}I in mammalian cells [17, 18]. Following the preclinical studies, a small number of human investigations were performed but that did not lead to clinical efficacy [19, 20]. However, the human study using the locoregional administration

of Auger electrons emitters showed promise in terms of tumor cell incorporation of the Auger emitters and they remain viable options for therapeutic applications [14, 21] but are not investigated further in this work.

β -radiation are electrons emitted from the nucleus. Typically, the beta particles ranges are in the order of (0-5) mm, but the beta range is highly radionuclide dependent. For example, the maximum range of a β -particle from the decay of ^{90}Y is ~ 11 mm in soft tissue ($E_{\text{max}} = 2.28$ MeV) [1]. The most commonly used therapeutic beta-emitting radionuclides in nuclear medicine clinics are ^{131}I , ^{90}Y , ^{177}Lu and ^{153}Sm . ^{177}Lu emitted β -particles have a range of ~ 2 mm in soft tissues that is currently considered to be close to ideal, as the dose stays highly localized within the 2 mm radius of its deposition. Other radionuclides including ^{32}P , ^{186}Re and ^{188}Re have a suitable range to treat the cancer nodules of size (1 mm – 1 cm), but the longer betas ranges result in a “crossfire” effect that can kill non-targeted non-cancerous cells within the range of the β -particles. Early theoretical evaluations of radionuclides back in 1984 (^{67}Cu , ^{77}Br , ^{82}Br , ^{90}Y , $^{99\text{m}}\text{Tc}$, ^{111}In , ^{131}I , ^{186}Re , ^{211}At) predicted that ^{186}Re and ^{90}Y were likely the best candidate therapy radionuclides as they possess sufficiently long half-lives necessary for tumor localization, are almost pure beta-emitters, possessed intermediate beta energies, resulted in stable daughter products, and had a reasonable chance to form a stable chelate with an antibody system [22]. But more recent work in understanding radiobiology (absorbed dose rates and effective therapeutic dose levels) and development of better chelation methodologies (allowing for easier chemical incorporation of radionuclides), and the development of more sensitive image techniques (to visualize and measure distribution) has since dramatically altered this list.

^{131}I is currently the most used therapeutic radionuclide in nuclear medicine; it is used to treat thyroid cancer. RPT began in 1941 with the efforts and insight of Saul Hertz and Arthur Roberts.

They used ^{131}I for the treatment of benign and malignant thyroid disease. Currently, this radionuclide is used in hyperthyroidism and in differentiated thyroid cancer. In 2018, I-131 iobenguane was approved for treatment of pheochromocytoma and paraganglioma. The radionuclides used in RPT often emit photons and photons emissions may be imaged with quantitative imaging techniques such as SPECT/CT or PET/CT. Imaging is used to assess the absorbed dose distribution of the RPT in patients.

^{90}Y (almost a pure beta emitter), a RPT radionuclide, was previously thought not to be imageable, have been imaged using SPECT via Bremsstrahlung photons emissions and by PET via a low positron yield of ^{90}Y [23, 24]. In early days (1970s) ^{90}Y was used in colloidal form to mainly treat rheumatoid conditions [25]. Currently, it is available in the form of $^{90}\text{YCl}_2$ and ^{90}Y -impregnated microspheres. ^{90}Y -microspheres are commonly used in radioembolization therapy, which has been shown to be safe and efficacious treatment for patients with hepatocellular carcinoma. This requires the ^{90}Y glass (or plastic) microspheres injection into a branch of the hepatic artery where the microspheres, due to their size being slightly larger than capillary diameters, are lodged in the microvasculature proximal to liver metastases to irradiate liver tumors internally [26]. However, the major challenges are the lack of reliable dosimetry methods for the absorbed dose prediction and dose verification. This radionuclide used in RPT can also be imaged, because ^{90}Y emitted the high energy beta emission (E_{max} 2.28 MeV). When these high energy β -particles interact with the nuclei of atoms in tissues, the phenomena called as Bremsstrahlung will occur generating a Bremsstrahlung x-ray spectrum that results in imageable photons. However, this approach requires a high amount of injected activities (more than 300 MBq) to achieve and imageable photon count [27].

Another radiopharmaceutical ^{177}Lu -DOTATATE has been recently approved by FDA for the treatment of neuroendocrine tumors (2018) and is of high interest because it emits photons [$E_\gamma = 113 \text{ keV}$ (6.6 %), 208 keV (11 %)], with $E_{\beta(\text{max})}$ of 497 keV (78.6 %), 384 keV (9.1 %) and 176 keV (12.2 %). The 176 keV photon is highly imageable with SPECT. Although it has only recently been introduced into the therapeutic realm, ^{177}Lu has established a strong foothold at the forefront of RPT. In a relatively short time, ^{177}Lu has virtually pervaded all areas of in-vivo RPT and may be poised to become a key therapeutic radionuclide of choice for RPT. ^{177}Lu -labelled compounds are used for Neuroendocrine tumors [28] or mCRPC [29] (Metastatic Castration-Resistant Prostate Cancer) treatments. For NETs, [^{177}Lu] Lu-oxodotreotide has been approved by regulatory agencies to be used with a fixed activity of 7.4 GBq as the only option [30]. Recently, Sartor et al. (2021) reported the results of VISION phase III trial using ^{177}Lu -PSMA-617 for mCRPC. They observed that the PSMA based ^{177}Lu therapy resulted in improvements in both progression-free (5-mo delay in disease progression) survival and overall survival (4-mo gain in life) when given in combination with standard of care in patients with mCRPC [31]. Recently, in 2021, ^{177}Lu -PSMA-617 receives FDA breakthrough therapy designation for metastatic castration-resistant prostate cancer (mCRPC). As mentioned before, both the ^{177}Lu -DOTATE and ^{177}Lu -PSMA-617 both generate significant survival benefit, but they did not exploit the patient-specific injection dose while injecting the patients under treatment. So questions have recently arisen, how much better clinical performance might be achieved with dosimetry-guided optimization [32]? Recently, the Society of Nuclear Imaging and Molecular Imaging (SNMMI) launched a ^{177}Lu dosimetry challenge program internationally to understand the variability and its various sources (calibration, imaging, reconstruction methods, noise) in image-based absorbed dose calculations [33].

α -particles are helium nuclei (${}^4_2\text{He}$), two protons and two neutrons, that are emitted from the nucleus of a radioactive atom. These particles carry more energy per disintegration than β -particles and deposit the energy in a relatively short distance and thus are considered a high LET (linear energy transfer) radiation. Depending on their emission energy, they can travel 50-100 μm in tissue, which is about 3-5 cell diameters, assuming a cell average diameter of 20 μm . They are positively charged and are orders of magnitude larger and more massive than electrons. A single α -particle traversal in a cell nucleus can cause multiple double-strand breaks and likely lead to cell irreparable death [34]. Unlike other forms of radiations, α -particles are more likely to interact directly with the DNA [35]. In RPT, radionuclides such as ${}^{227}\text{Th}$, ${}^{227}\text{Ac}$, ${}^{223}\text{Ra}$, ${}^{224}\text{Ra}$, ${}^{212}\text{Pb}$, ${}^{211}\text{At}$, ${}^{212}\text{Bi}$, and ${}^{213}\text{Bi}$ are being investigated. The α -particle-emitting drug radium-223 dichloride (Xofigo) was approved by the FDA in May 2013 for treatment of bone metastases. The very encouraging clinical trial results and the subsequent FDA approval were instrumental in the renewed interest in RPT, in general. Subsequently, individual-patient demonstrations of α -emitter potency have reinforced the interest in α -particle-emitting RPT [12].

1.2. Radiopharmaceutical Dosimetry

Dosimetry in an EBRT is a standard practice, but is not yet routinely performed in RPT. There has been a significant interest in personalization of RPT with the help of quantitative imaging to enhance the patient outcomes and overall survival rate. Personalizing treatment for optimized outcome has two potential benefits. First it promises to reduce normal organ toxicity by being able to predict and monitor absorbed dose to normal organs. On the flip side, physicians would like to be more certain that they are giving enough radiation dose to the tumors, to assure the patient is, in fact, benefitting from the treatment. Treatment optimization and personalization through individual planning of injected activity and absorbed doses delivered to target organs,

taking into account the absorbed doses delivered to healthy organ or tissue, is a challenge. Usually, the oncologic patients often have progressive disease and poor clinical condition, thus efficient and effective treatment is of vital importance. Therefore, the dosimetry-guided dose prescriptions should not delay the start of the treatment procedures [36].

Quantitative nuclear imaging plays a major role in personalizing treatment planning and dose verification in RPTs [37]. Personalized absorbed dose assessment potentially facilitates optimizing treatment response by delivering the maximal possible dose to cancerous targets while simultaneously monitoring the radiation absorbed dose to healthy organs or tissues and keeping them below toxic thresholds. Serial quantitative SPECT/CT or PET/CT imaging after therapy permits the determination of the activity distribution in patients' organs or tissues and manual drawing of multiple regions of interest is necessary for the absorbed dose calculations. Most current dosimetry procedures use 4 time point imaging over the course of a week; however, this is very time-consuming process, and puts burden on patients and clinic resources. Therefore, dosimetry using a single time point imaging is gaining a traction and could offer a compromise between the accuracy and resources needed for dosimetry [38]. This is an evolving space. Several studies published recently have suggested the use of a single imaging time point in combination with population based pharmacokinetic data to estimate the time-integrated activity and the absorbed dose to a target is achievable with acceptable accuracy [39-41].

To date, RPT in nuclear medicine clinics is usually performed by administering the same activity for each therapy cycle. This means that this approach does not account for patient-specific differences such as patient's height and weight in metabolic clearance or uptake of the radiopharmaceutical. Furthermore, imaging and subsequent dosimetry is not routinely performed

as the dosimetry require more time and effort, availability of trained personnel, and is not currently well reimbursed.

In 2009, the MIRD committee published a generalized framework for the RPT dosimetry at whole organs, tissue subregions, voxelized tissue structures and cellular levels [42]. Several guidelines to perform the dosimetry using planar imaging, SPECT multi time point imaging, and hybrid SPECT-planar imaging approaches are also available [43]. In addition, with the combined efforts of MIRD and EANM, guidelines for image quantification of ^{177}Lu using SPECT/CT has also been published in 2016 [44].

The ultimate objective of RPT dosimetry is the estimation of organ or tumor absorbed doses since biologic effects will be better predicted by absorbed dose than by injected or administered activity. As of now, regardless of RPT type there are two methods exists for patient-specific absorbed dose calculations post RPT: (1) MIRD (organ based) dosimetry and (2) 3D voxel-wise dosimetry. The MIRD dosimetry uses an absorbed fraction calculations whereas 3D voxel-wise dosimetry is generation of 3D voxelized dose map within patient anatomy. These are described below:

1.2.1. MIRD dosimetry

One of the most widely used approaches at the organ level dosimetry is the MIRD schema. In this method, the source and target volumes are defined, in which cumulated activity distributions and absorbed dose are assumed to be isotropic and homogeneous. Several computer software incorporating the MIRD formalism have been developed, including MIRDOSE [45], OLINDA/EXM (Organ Level Internal Dose Assessment/ Exponential Modeling) [46], IDAC Dose (MATLAB based) [47], and MIRDcalc (Excel spreadsheet based) [48].

According to the MIRD schema, the mean absorbed dose to a target tissue is calculated by multiplying the number of disintegrations, i.e., the cumulated activity distributed within a source tissue, and absorbed dose in target tissue per nuclear transformation in source tissue, is given by **Equation (1)** [42]:

$$D(r_T, T_D) = \sum_{r_S} \tilde{A}(r_S, T_D) S(r_T \leftarrow r_S) \quad (1)$$

where, $\tilde{A}(r_S, T_D)$ is the cumulated activity or time-dependent activity in source region r_S over a dose-integration period T_D and $S(r_T \leftarrow r_S)$ is the mean absorbed dose in target region r_T per nuclear transformation in r_S and defined mathematically as:

$$S(r_T \leftarrow r_S) = \sum_i \Delta_i \Phi(r_T \leftarrow r_S, E_i) \quad (2)$$

where, Δ_i is the product of E_i and yield Y_i , called as the mean energy of the i^{th} nuclear transition of the radionuclide in units of joules and $\Phi(r_T \leftarrow r_S, E_i)$ is the specific absorbed fraction (SAF), defined as the fraction of the energy E_i emitted in source region r_S to the target region r_T divided by mass of the target tissue in kilograms of the i^{th} emitted radiation of the radionuclide [49].

The time-dependent activity in the source region or tissues of the patient may be obtained directly from the quantitative imaging (SPECT, PET), including planar imaging, or by tissue sampling using a blood or urine collection. The parameter $S(r_T \leftarrow r_S)$ in **Equation (2)** is a radionuclide-specific value simply called as S values (mGy/MBq.s). Different radionuclide-specific S values are available for organ-based dosimetry, where S values were estimated using the computational anthropomorphic phantoms representing reference individuals [46]. MIRD pamphlet no. 17 reported the tabulations of voxel S values for several voxel dimensions (6 mm, 3

mm, and 0.1 mm) calculated with Monte Carlo code for five radionuclides, namely ^{32}P , ^{89}Sr , ^{90}Y , $^{99\text{m}}\text{Tc}$, and ^{131}I [8].

Organ level dosimetry applications based on standard reference phantoms are inadequate for 3D absorbed dose calculations in targeted RPT because they do not account for patient-specific or tumor dosimetry. However, OLINDA can model simple tumors in the form of unit density spheres of different sizes based on the absorbed fractions by assuming uniform activity distributions. Because it is not always possible to model the size, shape, and location of every unique tumor with the reference phantoms used in OLINDA, this approach does not provide information about the 3D absorbed dose distribution in tumors.

Drawbacks of this approach are that spatial variations of the activity distribution, tissue composition, and thus of absorbed dose inside the macroscopic source and target volumes are not considered. The concept of DPKs extends the MIRD formalism, which estimates absorbed dose in entire organs, to smaller source and target volumes. Therefore, in the limit of smaller spatial scales, DPKs ultimately could be regarded as approximating a continuous spatial distribution of point sources.

1.2.2. Voxelwise dosimetry

Voxel-wise or voxel level dosimetry is generated on a voxel-by-voxel basis from SPECT or PET quantitative images of radionuclide concentration and can be efficiently performed by using (a) the dose point kernels (DPKs) convolution or using voxel S values and (b) full Monte Carlo simulations. The activity distributions in an image can be quantified on a voxel level. These techniques make it possible to estimate absorbed dose with individual patient anatomy, including tumors, rather than using an average reference phantom geometry. This method is not yet clinically adopted because of challenges associated with the requirement of multiple imaging using

SPECT/CT, new tumor and organ segmentation challenges that require a huge time commitment, and dosimetry processing requirements. These problems are exacerbated by the fact that these procedures are not commonly reimbursed.

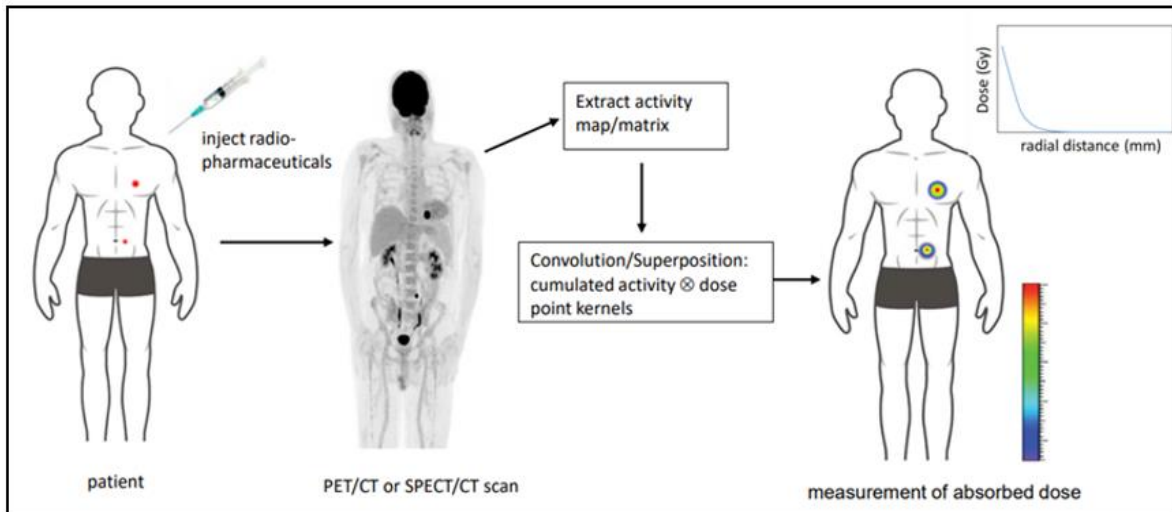


Figure 4: Schematic diagram of the workflow for the patient-specific dosimetry using the DPKs and the patient quantitative imaging data [50]. Only one imaging time point is shown in the figure.

DPKs are the radial absorbed dose profile as a function of the radial distance. These kernels are derived from the Monte Carlo simulations and are radionuclide and tissue specific. Literature also tends to use another terminology of DPKs, i.e., dose voxel-kernel (DVK), which is the discretized version of continuous DPKs. A convolution of pre-simulated DPKs with the patient activity map obtained from the quantitative imaging using either SPECT/CT or PET/CT imaging results the spatial 3D absorbed dose distribution, where tissue compositions can be derived from x-ray CT. The generic process is illustrated in **Figure 4**. With the advancement of computing power and availability of more plentiful memory and computing resources, convolution can be performed within a few minutes. Specifically, the convolution of patient activity map and DPKs results in the absorbed dose rate images. Subsequently, using the absorbed dose rate (Gy/s or Gy/h)

vs time (s or h) curve, one can obtain absorbed dose in units of (Gy) by performing the integration of absorbed dose rates.

The absorbed dose calculations using the DPKs involves the following steps. First step in dosimetry workflow is the patient quantitative imaging that allow for the accurate measurement of the activity distribution in the patient over time – usually several days. Usually, quantitative SPECT imaging, planar images, or a combination of planar and SPECT images are acquired at multiple time points (typically 3-4) after the administration of the radiopharmaceutical. The goal is to measure the biodistribution of the radiotracer as a function of time. Quantitative imaging modalities such as SPECT/CT or PET/CT allow us to measure this. However, the image acquisition and reconstruction parameters needed for accurate quantification is a topic of ongoing research. For accurate quantification in SPECT imaging, the image degrading effects such as scatter and attenuation need to be corrected. However, the scatter correction remains a challenging task in SPECT reconstruction.

As the multiple time point imaging puts a burden on patients and clinic resources, some investigators have assessed the possible reduction of time points for kidneys and tumors [39, 40] and perhaps other organs. However, the reliability of this approach requires validation and the observed variable biology among tumors makes it unlikely to be translatable to lesion dosimetry.

In the second step, image registration and segmentation of the tissues and organs of interest are performed. Various image registration and segmentation methods are available. After this step, we can extract the activity map, either a whole map or a segmented, to define volumes of interest for further quantitative dose analysis.

In the third step, the activity map from the patient imaging is convolved with dose point kernels or voxel S values. The DPKs (in units of MeV/g per decay) or VSV values are Monte

Carlo-derived quantities. If the DPKs data are not in a suitable format, this step requires the DPKs to be resampled. DPKs can be resampled to SPECT image resolution to be used in the convolution algorithm. The convolution of these quantities yields the absorbed dose rate maps, i.e., the 3D images of the absorbed dose deposited per unit time in each voxel. The Fourier-based approach can be implemented in convoluting the activity map and DPKs to save computation time. Using these methods, organ level absorbed dose rates to tumors or organs can be calculated by averaging over tissues of interest.

The next step is to plot of absorbed dose rate vs. time. The x-axis of the plot, i.e., time represents the multiple time points in imaging if multiple time point imaging techniques were used. Usually, a total of 3-4 time point imaging is performed. Time-integration of the absorbed dose rate vs. time results in the total absorbed dose. A simple method would be the trapezoidal integration of the time-integrated absorbed dose rate curve. However, the integration process more typically involves the use of multi-exponential curve fitting.

Voxel-wise dosimetry using the direct or full Monte Carlo (MC) simulations is considered a gold standard in 3D dosimetry because it considers the tissue heterogeneity within the patient body regarding both activity distributions and tissue compositions. Recently, the GATE toolkit [51] based on Geant4 [52], has been used frequently for both clinical and preclinical dosimetry applications. By using GATE, we can simulate the electromagnetic interactions of photons, electrons, hadrons, and ions with matter down to the electron volt energy scale [53]. Various studies have been performed to validate the reliability and accuracy of GATE MC for dosimetry [2]. Many other MC simulation platforms are available such as MCNP, EGSnrc, PENELOPE, and FLUKA. In direct MC simulations, the CT and PET or SPECT images of the preclinical or human subject can be used as a voxelized phantom and voxelized source, respectively. Thus, using the

direct MC simulations using CT and nuclear imaging data, patient specific heterogeneous tissue compositions and activity distributions are taken into account.

Recently, GATE has been used in many preclinical studies for the full Monte Carlo simulations with the aim of voxel-wise dosimetry. Taschereau and Chatziioannou [54] calculated absorbed dose distributions from ^{18}F -FDG PET imaging of mice using GATE simulations and using MOBY phantoms. Mauxion et al. performed a study with GATE and MCNP Monte Carlo codes to assess the impact of organ mass on absorbed dose from ^{18}F -FDG using MOBY phantoms [55]. Parach et al. [56] calculated organ doses from the digital geometry of a Snyder mathematical phantom using the GATE toolkit and compared the results with the MIRD data previously published by Snyder et al. [57]. In addition, PET/CT images of mice were used to estimate the absorbed doses in sensitive organs at the voxel-level to evaluate the suitability of GATE for preclinical dosimetry by Gupta et al. [58].

Although Monte Carlo simulations calculations are more robust and produce accurate internal 3D dosimetry estimations at the voxel level because of (1) the inclusion of inhomogeneous activity distributions and tissue heterogeneity, (2) complex geometries, and conditions where charged particle equilibrium is not fulfilled (near the tissue interfaces), it requires extensive computational resources to minimize the simulation time, therefore it is not usually feasible to apply in daily clinical practice.

The 3D voxel-wise dosimetry methods suffer from several limitations because the activity value in individual voxels can be influenced by image noise and artifacts. In addition, the limited resolution of SPECT imaging leads to a spill-over of reconstructed activity between structures. Therefore, the reconstructed 3D activity distribution may not fully represent a purely physiological activity uptake and must be interpreted with care. Therefore, the development and potential

improvement to handle spill-over and partial volume compensation techniques should be subject to future investigations. Well controlled and designed phantom studies are generally used to provide data to models that inform these partial volume correction techniques. These will be discussed later.

Methods for determining patient-specific absorbed dose vary in complexity and accuracy, however, there are an increasing number of software tools to facilitate absorbed dose calculation from radiopharmaceuticals. Commercially available dosimetry software's are QDOSE (ABX-CRO advanced pharmaceutical services), PLANET DOSE [59], GE Dosimetry Toolkit [60], MIM SurePlanTM MRT [61], Stratos (Philips) [62], Hermes Medical Solutions (OLINDA) [46], PMOD, RAPID, Simplicity90Y, Voximetry Torch, and RapidSphere Dosimetry Navigator. A detailed description of these tools is provided in a paper by Capala et al. [63].

In summary, radiopharmaceutical therapy is a rapidly growing therapeutic approach for treating cancer, but it is early in development. There is potential for substantial improvement in patient outcome through the implementation of quantitative imaging-based radiation dose methods. This thesis focuses on development of technologies and approaches that will enhance and fortify downstream developments in quantitative imaging and dosimetry.

CHAPTER 2: FUNDAMENTALS OF NUCLEAR MEDICINE IMAGING

2.1. Molecular Imaging

2.1.1. Positron Emission Tomography

Positron Emission Tomography (PET) is a powerful diagnostic tool in the armamentarium of modern healthcare that uses radiopharmaceuticals labeled with positron-emitting radionuclides. PET imaging is used in a variety of medical conditions including neurology, cardiology and oncology. Its most common use is in the detection of molecular alterations suggestive of tumor tissues. Different radiopharmaceuticals are tuned to a variety of molecular targets and biochemical mechanisms such as glucose metabolism, fatty acid metabolism, amino acid metabolism, prostate-specific membrane antigen (PSMA), androgen receptors, and osteoblastic bone activity. In contrast to alternative imaging modalities such as ultrasound or Magnetic Resonance Imaging (MRI), PET uses ionizing radiation – positron-emitting radionuclides and their associated 511 keV annihilation photons for imaging. Functional imaging with PET plays an increasingly important role in diagnosing and staging of malignant disease, image-guided therapy planning, and treatment monitoring. PET with the radiolabeled glucose analog fluorine-18 fluoro-deoxyglucose (FDG) has gained widespread acceptance in clinics the world over for cancer imaging. FDG PET complements the more conventional anatomic imaging modalities of computed tomography (CT) and magnetic resonance imaging. CT is complementary because it provides accurate anatomic images of organs and lesions, while PET maps normal and abnormal tissue function through expression of glucose metabolism. When PET and CT imaging modalities are combined, it can help both identify and localize both anatomical and functional abnormalities, most commonly tumors. As the name suggests, PET radiopharmaceuticals are radiolabeled with suitable positron-emitting radioisotopes such as ^{11}C , ^{13}N , ^{15}O , ^{18}F , ^{64}Cu , ^{68}Ga , ^{76}Br , ^{82}Rb , ^{86}Y , ^{89}Zr , ^{124}I , and ^{152}Tb

[64, 65]. These isotopes used in medical imaging are relatively short-lived with half-lives ranging from minutes to days, which enables optimal use of imaging photons while keeping patient radiation doses low. Several use cases of these radioisotopes in diagnostic radiopharmaceuticals are shown in **Figure 5**. Furthermore, many of these isotopes can be incorporated into biological substrates (glucose, H₂O, NH₃, CO₂, O₂, etc.) and pharmaceuticals without changing their biological activity.

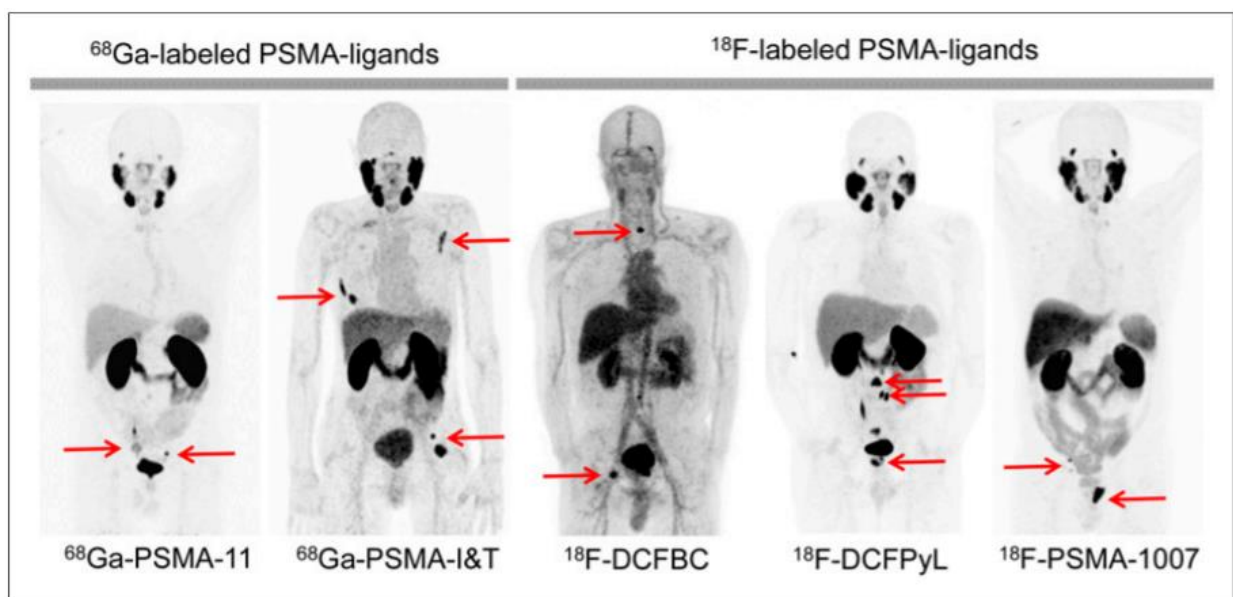


Figure 5: Maximum intensity projection images of PSMA ligands commonly used for PET imaging. Image show typical biodistribution of different radiopharmaceuticals as well as different number of positive lesions. Specific tumor uptake is shown by red arrows [66].

2.1.1.1. Basic Physics of PET Imaging

Positrons (β^+) are positively charged beta particles. They are emitted when the nucleus is proton enriched. A positron has only a transient existence. After losing its kinetic energy, generally in less than a millimeter or so, it interacts with a surrounding electron and is annihilated. Both the mass of positron and electron are converted to energy ($E = mc^2$) during the annihilation process, and two 511 KeV annihilation photons are emitted at an angle of 180° to each other (**Figure 6**).

The PET imaging schema is based on the coincidence detection of the two oppositely directed photons. Coincidence detection is a powerful method for localization of positrons position in the body. The PET system consists of a ring of small scintillation detectors (typically 4-5 mm on a side, and approximately 20 mm in depth) that encircle the patient. After accumulating and localizing millions of coincidence lines (lines of response), the line integral of activity is calculated, and computed tomography reconstruction methods are applied to derive the three-dimensional distribution.

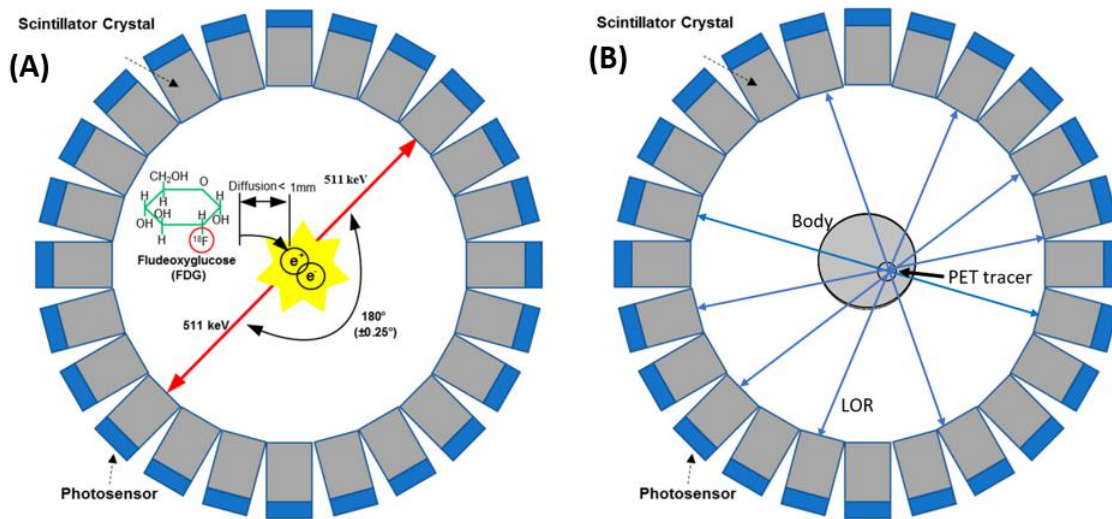


Figure 6: (A) Schematic drawing of PET imaging principle and (B) schematic shows how PET measures the activity using the lines of response (LOR).

Compared to CT, PET images are generally noisier and/or blurrier due to the relatively limited number of photons that are typically collected during the imaging study, the physical size of the scintillation crystals used in the PET scanner (typically 4 mm x 4 mm x 20 mm deep), positron range, and small divergences from non-collinearity of the 511 keV annihilation photons. X-ray CT scanners can easily resolve anatomies less than 1 mm in size, while PET scanners cannot reliably resolve point sources smaller than about ~ 4 mm in the best commercial whole-body PET

scanners. However, this limited resolution does not substantially impair their clinical utility, which lies primarily in allowing physicians and researchers to image and quantitate the biological function at the source of the disease. PET, even with limited resolution allows physicians to visualize clinically relevant disease completely invisible to CT and MRI.

2.1.1.2. PET Scanner Architecture

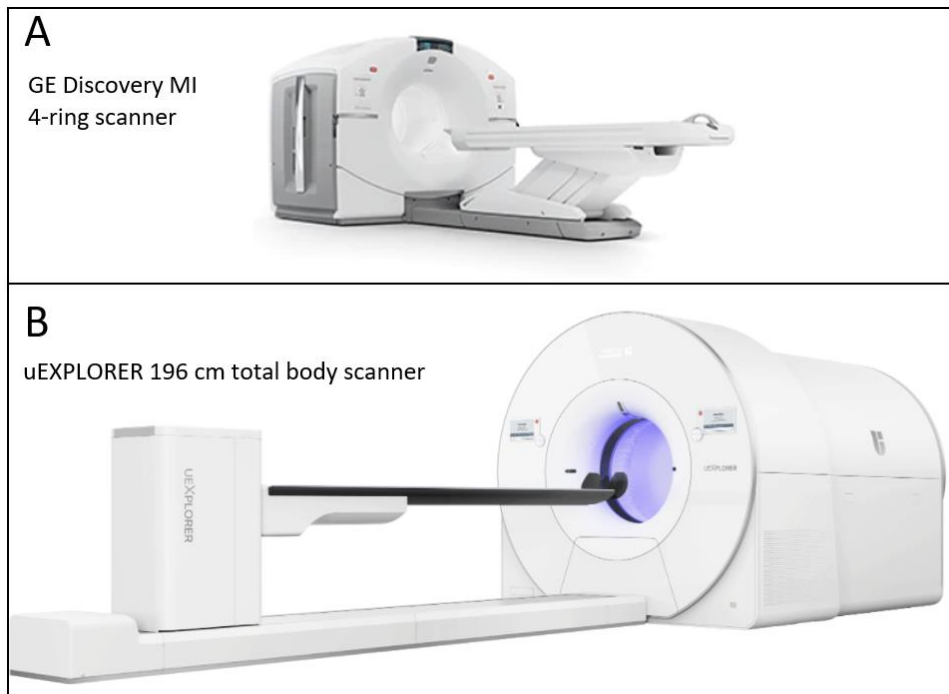


Figure 7: (A) GE Discovery 4-ring (20 cm AFOV) PET/CT clinical scanner and (B) total body uEXPLORER PET scanner with 196 cm AFOV.

Current clinical PET scanners have an axial field of view (AFOV) of ~15-30 cm. This AFOV covers only ~10-20% of the human body in one-bed position. This means that there will a need to image multiple bed positions to cover the majority of the organs in the body, which takes a longer time. However, the AFOV of ~20 cm is usually sufficient for acquiring brain or cardiac PET scans in a single bed position. That being said, the sensitivity of the commercial PET systems have a photon detection sensitivity of only ~1% of the emitted radiation from the patient. The

majority clinical PET imaging performed is oncologic applications and requires scanning with a 5-6 bed position scan, which typically covers from head to thigh of the patient, where the majority of the body organs are located. This is usually performed in a so-called step and shoot mode, and this scanning usually takes about 10-30 min (one-bed position takes ~2-3 min) [67].

2.1.1.3. Total Body PET

A total-body PET scanner is a system with many more detectors in the axial direction to increase the sensitivity of the PET system by a significant factor [67]. New total body systems have axial extents ranging from 1-2 meters in length and boast a photon detection sensitivity of greater than 20X that of conventional PET systems. A rapidly developing area of clinical application is the use of PET for monitoring radiopharmaceutical therapy, especially for neuroendocrine tumors and prostate cancer. Total-body PET is an ideal tool for evaluating the results of these therapies in multiple metastases spread through the body in a short period of time.

Total body PET also has important applications in monoclonal antibody imaging applications where kinetics are slow, and localization in the body takes days rather than minutes. In these cases, longer-lived positron emitters like ^{89}Zr ($t_{1/2} = 78$ hours) are used, but only a fraction of the activity can be injected (10x less), to reduce absorbed radiation dose, and a positron branching ratio of only 20% reduces photon flux by another factor of 5. In these low count scenarios, the enhanced photon detection sensitivity of long axial field of view systems shines.

PET is also a valuable scientific tool in understanding the pharmacokinetics of drugs. Labeling a drug with a positron emitting radionuclide allows us to quantitatively image its time course through the body. But a standard PET scanner's limited axial extent of approximately 20 cm and limited photon detection sensitivity makes it difficult to have the ability to image with a

time resolution on the order of seconds (statistics limitations) and to image more than 20 cm at a time. Total body PET systems remedy all of these problems.

As the writing of this dissertation, three total-body PET scanner models have been developed and marketed. They hold potential to become transformative for molecular imaging in humans. These systems are the United Healthcare Imaging uEXPLORER [68-70], PennPET EXPLORER [71, 72], and the Siemens Biograph Vision Quadra [73, 74]. The uEXPLORER is based on the United Imaging Healthcare's uMI 550 and 780 PET/CT scanners, while the PennPET Explorer is based on the Philips detector technology and detector geometry used in the Vereos scanner [75]. The Biograph Vision Quadra uses the same technology as digital Biograph Vision PET/CT systems (Siemens Healthineers) [73]. All these scanners use a modern silicon photomultiplier (SiPM) technology instead of traditional PMTs. First human studies on the uEXPLORER total-body PET scanner have already been performed using substantially lower injected doses of 25 MBq and a short total acquisition time of ~1 min [76, 77]. The first human imaging results using the uEXPLORER have been published [76, 78]. Results of the work demonstrate images of high statistical quality, reduced scan time, reduced injected dose, and total body dynamic imaging [76]. The PennPET EXPLORER group recently reported their development of a “whole-body” imager currently with a 64 cm active AFOV and indicated that the optimal axial length of the scanner could be in the range of (1.0 -1.4) m [71]. The PennPET EXPLORER is gradually adding additional detector rings and will likely call the scanner complete once it tops the 1.0 meter axial extent.

Monte Carlo simulations of a total body PET scanner with a 2 m AFOV with 20 mm thick detectors using Siemens Biograph mCT geometry suggested that the total body imaging geometry could provide gains up to 40-fold in effective count rate for total-body applications compared to

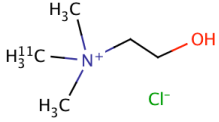
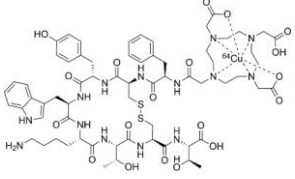
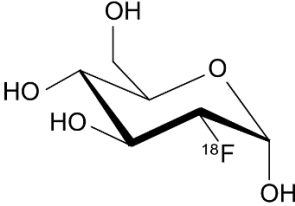
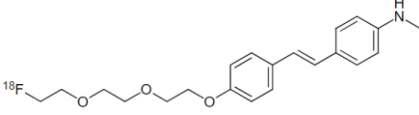
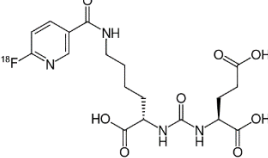
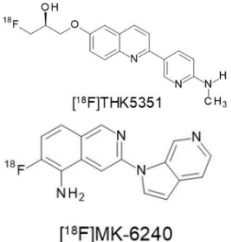
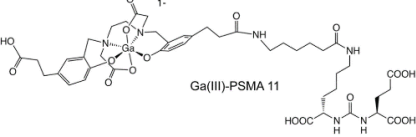
conventional ~20 cm AFOV scanner [79]. This means that using the same protocols i.e., injected activity, imaging time as those we currently use, we can increase the signal to noise ratio (SNR) in the reconstructed image by a factor of ~6. It was these Monte Carlo simulations that led to the NIH to invest more than \$10 million into the design and construction of the first prototype system. Our simulation work, using the PET front-end architecture of GE Discovery MI PET scanner resulted in a sensitivity gain up to 60-fold [3]; please refer to chapter 6 for further details of this work.

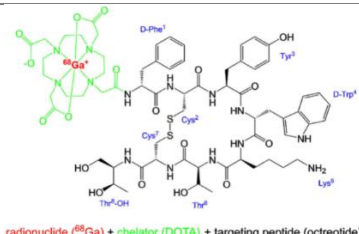
The total-body PET scanner can image better (6-7 times higher SNR compared to existing scanners), faster, with a low injection radiopharmaceutical dose. However, there are challenges associated with the developments of these systems. Major challenges are big data handling (sinogram sizes are about 100x larger), scanner cooling, and fast image reconstruction [80]. In addition, the cost for a total-body PET scanner (2 m AFOV) is about ~8-times compared to the current clinical PET scanner of 20 cm AFOV [67]. Our simulations suggest that if we want to image major organs, from head to pelvis, with the peak sensitivity, then the AFOV of 1.5 m seems sufficient because we can have a relatively uniform profile in the central 80 cm using this AFOV and that covers most of the major organs [3]. Efforts have also been made to lower the cost of the scanner by reducing the scintillator thickness [81], utilizing a plastic scintillator [82], and using sparse axial coverage of the detectors [83-85].

2.1.1.4. PET Radiopharmaceuticals

As of now, there are more than 10 PET radiopharmaceuticals officially approved for clinical use by FDA. They are summarized in **Table 1** below:

Table 1: Representative list of diagnostic PET radiopharmaceuticals.

	Radiopharmaceutical	Uses	Chemical structure
1	C-11 choline	imaging of patients with suspected prostate cancer recurrence	
2	Cu-64 DOTATATE	for localization of somatostatin receptor positive neuroendocrine tumors (NETs) in adult patients	
3	F-18 FDG	currently the most widely used PET radiopharmaceutical for glucose metabolism and primary and metastatic malignant diseases, in addition to its clinical applications in cardiology and neurology	
4	F-18 sodium fluoride	bone imaging agent to delineate areas of altered osteogenesis	$\text{Na}^+ \text{}^{18}\text{F}^-$
5	F-18 Florbetaben, (Flutemetamol, Florbetapir)	for amyloid imaging	
6	F-18 Fluciclovine (amino acid analog)	tumor metabolism/prostate cancer imaging	
7	F-18 DCFPyL (Piflufolastat)	PSMA imaging agent for prostate cancer	
8	[18F] THK 5351, [18F] MK-6240	For <i>in vivo</i> Tau protein imaging in dementia, Alzheimer's disease	
9	Ga-68 DOTATATE, Ga-68 PSMA	PET imaging for localization of somatostatin receptor-positive neuroendocrine tumors	

		(NETs) in adult and pediatric patients, Prostate Cancer	
10	Ga-68 DOTATOC	PET imaging for localization neuroendocrine tumors (NETs) in adult and pediatric patients.	 <p>radionuclide (⁶⁸Ga) + chelator (DOTA) + targeting peptide (octreotide)</p>
11	¹³ NH ₃ ammonia	lung perfusion imaging	$\begin{array}{c} ^{13}\text{N} \\ \\ \text{H} - \text{N} - \text{H} \\ \\ \text{H} \end{array}$
12	Na ¹⁸ F	bone imaging	Na ⁺ F ⁻
13	⁸² RbCl rubidium chloride	assessment of regional myocardial perfusion in the diagnosis and localization of myocardial infarction	⁸² Rb ⁺ Cl ⁻

The application of PET in clinical oncology is increasing as we continue to identify cancer specific molecular targets that can be labeled with positron emitting radionuclides.

2.1.2. Single Photon Emission Computed Tomography

Single-photon emission computed tomography (SPECT) is a widely available and flexible imaging technique capable of visualizing and quantifying changes in cerebral blood flow, neurotransmitter systems, and assessing the perfusion and functionality of specific tissues. Like as in PET, SPECT requires the use of radiopharmaceuticals, and the acquisition of projection data, which are then reconstructed into transaxial image slices. This imaging method also requires computed tomography reconstruction procedures. However, SPECT utilizes standard gamma-emitting radiopharmaceuticals such as ⁶⁷Ga, ⁶⁷Cu, ^{99m}Tc, ¹¹¹In, ¹²³I, ¹³¹I, ¹⁵³Sm, ¹⁵³Ga, and ¹⁷⁷Lu. Radioisotopes used for SPECT are typically radiometals, requiring complexation chemistry. The predominant isotope used in SPECT imaging is the metastable form of technetium (^{99m}Tc, t_{1/2} = 6 h).

Just as in PET imaging, radiopharmaceuticals labeled with relatively short-lived gamma-emitters are typically injected intravenously and localize in the body according to the pharmacokinetics of the radiopharmaceutical. Following *in vivo* radioactive decay, photons will be isotropically emitted and exit the body. That small fraction of gamma photons that are emitted through the body orthogonal to the camera face will make it through the thick lead collimators and strike the large planar SPECT scintillator crystals that are on opposite sides of the patient for detection. Since in SPECT, there is not a contiguous ring of detectors surrounding the patient, the two parallel detector heads must slowly rotate around the patient to collect the necessary projection angles 180° around the patient. Using the projection data, the reconstructed images reflect a three-dimensional mapping of the radiopharmaceutical's distribution in the body, reflecting the functional information specific to the radiopharmaceutical. The radiopharmaceuticals used in SPECT imaging usually have a longer half-life.

SPECT requires a calibration factor to convert count/sec (i.e., reconstructed image voxel value unit) to activity concentration (Bq/mL). The absolute quantitative activity measure Bq/mL requires a calibration or scaling factor to convert reconstructed image unit counts/sec to activity. This calibration factor, in units of cps/MBq, may be estimated from a reconstructed SPECT image of a uniform phantom or from a planar sensitivity measurement and must be applied to the reconstructed images (counts) for quantitative analysis. Some modern SPECT/CT systems come with in-built calibration support and the reconstructed images are available in activity (Bq/ml), similar to PET imaging.

As in PET, the goal of SPECT is to determine accurately the 3D radioactivity distribution resulting from the radiopharmaceutical uptake inside the patient. SPECT utilizes non-positron-emitting radiopharmaceuticals rather than those that emit positrons with the generation of two 511-

keV annihilation photons, as is the case with PET. This modality thus requires instrumentation and image reconstruction methods that differ from those used in the PET modality.

2.1.2.1. Physics of SPECT Imaging

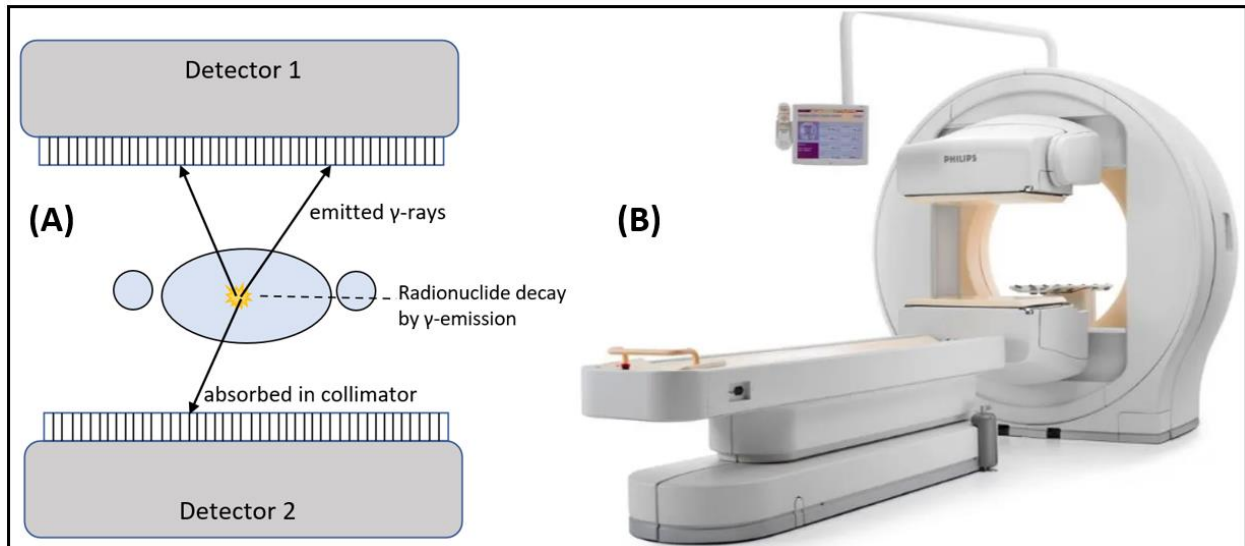


Figure 8: (A) Schematics of SPECT dual head camera with parallel hole collimators and (B) SPECT/CT clinical camera.

Unlike PET systems, SPECT incorporates collimators that are located at the front face of the detector to collimate the incoming photons as shown in **Figure 8**. A collimator is a thick sheet of metal of high atomic numbers such as lead tungsten, gold, or platinum, pierced by an array of holes. Only the photons that pass these holes without hitting the septa between them can be detected. Only a small fraction of emitted photons $\sim 10^{-4}$ pass through the holes and are detected. Making collimator holes bigger increases the sensitivity but degrades the spatial resolution of the system. Thus, the collimators are used for creating the projection, and different collimators have been used in different studies such as pinhole, multiple pinhole, parallel-hole, and converging and diverging hole, but they all exhibit a trade-off between resolution, efficiency, and FOV. The spatial resolution achieved in SPECT system is 7.5 - 15 mm FWHM. Resolution depends on the crystal

thickness, collimator, radionuclide being imaged, the geometry of the patient (distance from the collimator), and the reconstruction and compensation methods (attenuation and scatter corrections) chosen.

SPECT/CT imaging can be performed image the distribution of radiopharmaceutical therapy drugs. The SPECT/CT images are corrected for count losses due to dead time, partial volume effects, attenuation and scatter. Calibration factors are determined to convert the number of photons actually detected to activity concentrations (Bq/ml). Calibration factors (cps/MBq) are then used to convert the counts/ml to activity per voxel (Bq/ml). It is worth mentioning that these factors depend on the acquisition and reconstruction protocol. Fully calibrated and corrected, images can then be used to assess patient-specific dosimetry. It has been shown that the spatial resolution in SPECT imaging with medium-energy gamma photons ~200 keV associated with radionuclides used in RPT such as ^{177}Lu and ^{67}Cu of ~ 20 mm FWHM severely limits the recovery of accurate radioactivity concentrations *in vivo* due to the partial volume effect and leads to underestimation in radiation dose delivered to small metastasized tumors in RPT. Estimating the dose delivered to small lesions in RPT using conventional SPECT reconstruction methods is therefore challenging. Thus, partial volume correction is essential for accurate RPT treatment planning, monitoring therapeutic dose, and establishing the relationship between RPT and treatment outcome.

2.1.2.2. Clinical applications

SPECT/CT imaging is used to image the breast cancer, benign and malignant skeletal diseases, infectious diseases, differentiated thyroid cancer, parathyroid tumors, sympathetic nervous system, adrenocortical tumors, neuroendocrine tumors, and cardiac perfusion imaging. In addition, SPECT/CT have been used to evaluate the pain of spinal origin, postoperative spine, hip

pain, knee pain, image the pain in extremities such as ankle joint pain and infection and inflammation. **Figure 9** shows an example of usefulness of SPECT/CT system for the diagnosis of pheochromocytoma, which is the tumor derived from the sympathetic nervous system [86].

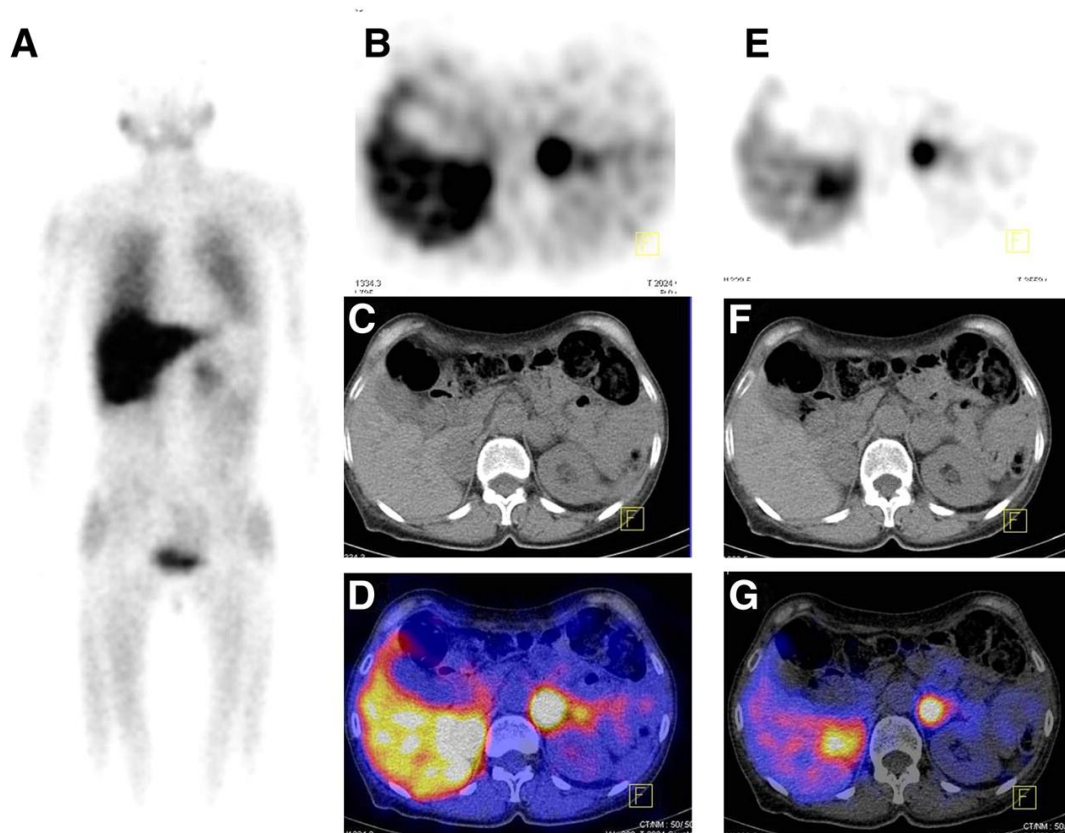


Figure 9: ^{99m}Tc -MIBG SPECT/CT imaging for the diagnosis of pheochromocytoma. (A) planar image showing intense focal lesion in left suprarenal area (B) section of SPECT imaging slice (C) corresponding CT imaging slice (D) fused SPECT and CT slices shows the larger uptake in adrenal gland, indicating pheochromocytoma. (E) SPECT slice shows the right adrenal gland (F) CT slice and (G) both adrenal glands show the higher uptake [86].

CHAPTER 3: MONTE CARLO SIMULATIONS IN NUCLEAR MEDICINE

3.1. Introduction

Monte Carlo (MC) simulations are an essential tool for solving statistical problems that require random sampling, particularly where system properties cannot be determined experimentally. The field of Nuclear medicine has used Monte Carlo techniques for over 50 years [87]. Interestingly, the very first utilization of these simulations in nuclear medicine goes back to the early days of the Medical Internal Radiation Dosimetry (MIRD) Committee of the Society of Nuclear Medicine in the 1960s. Now, 50 years later, more sophisticated MC simulations are being used again, generating a solid foundation for next-generation radiation dosimetry that is standing at the heart of the radiopharmaceutical therapy revolution. MC simulations are considered the gold standard for macroscopic 3D absorbed dose distribution calculations because of their vast experimental benchmarking, but they are currently even making headway into simulating microdosimetry at the cellular level.

Monte Carlo simulations have been employed for dosimetry estimations and for the validation and performance prediction of PET and SPECT imaging systems. In addition, simulations have been increasingly used in nuclear medicine to develop new medical imaging devices, treatment planning systems, shielding and radiation protection systems, optimizing reconstruction algorithms and scatter correction methods, and in radionuclide dosimetry calculations. These simulations are increasingly gaining popularity following the development and utilization of powerful computing resources. Given all these varied uses, it is popular tool and source of great research interest in the whole medical physics community. These simulation techniques help better understand the physics of complex radiation transport mechanisms in medical physics. For accurate results, the Monte Carlo techniques require the well-defined and

accurate modeling of the system under investigation and incorporation of the accurate model of the fundamental physics interactions associated with photons (x-ray and gamma-ray), electrons, beta particles, and alpha particles emitted by the radionuclides. In particular, Monte Carlo simulation has proven itself over the years to be a valuable tool for simulation of nuclear medicine imaging and therapy applications.

The statistical nature of radionuclide decay and emission tomography makes them perfect candidates for the application of Monte Carlo simulations. Radioactive decay, positron annihilation, photon attenuation and scattering, and photoelectric absorption are some of the more common physical phenomena foundational to nuclear medicine imaging and therapeutic applications of radioactivity that can be easily simulated with current Monte Carlo tools. These processes can be described analytically, but we cannot construct and analytically predict the history of each generated particle from its birth to its detection. This is where Monte Carlo techniques are invaluable. The primary downside of the Monte Carlo simulation is the long simulation or computation times associated with transporting the tens of thousands to tens of millions radiation events through complex materials and geometries. The computational burden is still the bottleneck for their widespread use in clinical and research environments. However, efforts have been made to improve simulation efficiency by utilizing either the parallel simulations [51] or using high performance graphics processing units (GPUs), including GPUMCD [88], gDPM [89], and GMC [90]. However, the thread divergence remains a major hurdle since those GPU codes are adapted from the CPU counterparts that exploit the acceptance-rejection method.

Available Monte Carlo codes that have been useful for the radiation transport are divided into two categories: general-purpose codes such as Geant4 [52], MCNP [91], EGSnrc [92], and PENELOPE [93] developed for high-energy physics and dosimetry and dedicated codes such as

GATE [51], SIMIND [94], SimSET etc that are optimized for prototyping novel nuclear imaging geometries, materials, and equipment. The general-purpose MC codes have a long history of applications in radiotherapy, where accurate patient-specific dose calculation play a crucial role in the practice of radiation therapy [95]. All these packages include well-validated physics models and provide a mechanism for geometry modeling and efficient visualization. In general, results from these simulations have been experimentally validated through careful energy deposition experiments. The optimal choice of these simulation codes for a given application depends on various factors such as the computer system type and configuration, and the user's ability or skills.

GATE, Geant4 Application for Tomographic Emission [53, 96], is a Monte Carlo simulation toolkit currently available for nuclear medical imaging and radionuclide dosimetry. It is based on the Geant4 source code (Geant4 was designed to study the high energy physics at CERN) used for (1) nuclear imaging simulations such as positron emission tomography (PET) and single-photon emission computed tomography (SPECT) devices and has advantages for tracking and predicting scattered photons (2) dosimetry simulations and (3) radiotherapy simulations.

Despite the increased use of MC simulations, there are several limitations or challenges to be faced in order to increase the accuracy of MC calculations. In addition, currently available MC packages are quite complex and involve a steep learning curve. Some of the major limitations are as follows:

- (1) Simulation statistics: Only a finite number of histories or radioactive decays can be simulated given the limitations and costs associated with computation time; otherwise, the computation time (CPU time) becomes too high for many routine clinical applications. The lower the number of histories in Monte Carlo simulations, the higher the associated statistical errors. That said, the statistical errors in MC simulation depend

not only on the total number of primaries or histories simulated but also on the number of particles in a given region of interest. This means that MC fluctuations increase by decreasing the dose scoring voxels, for example, in dosimetry simulations.

- (2) Energy cut-offs: Cuts are the value below which the particles are not tracked in simulations and is very helpful in saving the computation time. Low energy cut-offs are desirable in the simulation setup; lower-energy interactions with minimal impact on the metric under study increases the simulation time substantially, without enhancing accuracy of the simulation result. High-energy cuts typically yield an inaccurate result. Finding a balance is critical for a good simulation.
- (3) Modeling of radiobiology – Although efforts have been made to simulate the radiobiological processes in MC simulations, challenges have been exits for the reliability of modeling radiobiological factors in simulations.

3.2. Introduction of GATE Monte Carlo toolkit

GATE, the Geant4 Application for Tomographic Emission, is an open-source Monte Carlo toolkit developed by OpenGATE collaboration and dedicated to numerical solutions in medical imaging, dosimetry, and radiotherapy. In medical imaging - it supports the Monte Carlo simulations of PET, SPECT, CT, and Optical imaging. GATE now plays an important role in designing new medical imaging devices, optimizing and assessing imaging protocols, performance projection of imaging systems, development of image reconstruction algorithms, and image reconstruction techniques. In therapy – it can be used for simulations of radiotherapy experiments, brachytherapy related experiments and radiopharmaceuticals absorbed dose distributions [53, 96]. This toolkit encapsulates the Geant4 cross-section libraries to achieve a modular, versatile and scripted macro mechanism toolkit adapted to the field of nuclear medicine. GATE simulation

allows the source decay kinetics and an accurate description of time-dependent phenomena such as source or detector movement. It is possible to perform realistic simulations of the time-dependent phenomenon in GATE because of its ability to synchronize all time-dependent components allows a coherent description of the acquisition process.

This toolkit was initially focused on nuclear imaging, including PET and SPECT [51, 53]. Since its inception, GATE has been used for simulating preclinical and clinical imaging systems. In nuclear imaging, primarily GATE is used for simulation of PET systems and, to a lesser degree, SPECT systems. The first simulation of SPECT system – dual-headed AXIS camera, Philips Medical systems – was performed in GATE by Staelens et al. in 2003 [97]. Also, a scintillation camera of CsI(Tl) system dedicated to the animal imaging was also simulated [98]. Validation of GE Advance/Discovery LS PET scanner was performed by Schmidlein et al. in 2006 [99]. In addition, many other PET scanner simulations such as simulations of Phillips Allergo/GEMINI systems [100], Siemens Inveon LSO based scanner [101], Siemens Biograph mCT LSO system [79], preclinical Argus PET scanner [102], Biograph mMR model (PET/MR) [103], GE eXplore 120 micro-CT [104], J-PET plastic scintillators based PET system [105], Philips Vereos SiPM based scanner [106], GE Discovery MI scanner [3, 107] and many others. Moreover, GATE simulations have been used to project the performance of total-body PET scanners using Siemens Biograph mCT [79], PennPET Explorer geometry [108], GE Discovery MI scanner up to 2 m AFOV [3], and other systems.

GATE has been used for various aspects of dosimetry using DPKs [1, 10, 50, 109, 110] and radioembolization simulations [26]. In addition, many preclinical dosimetry studies, including the energy deposition from ^{18}F -labeled radiopharmaceuticals in mice, were simulated in GATE. A voxelized MOBY phantom [54] and PET imaging of mice [58] data were inserted as an input in

simulations. Furthermore, Kostou et al. used GATE to simulate the S values of commonly used radionuclides including ^{18}F with whole-body heterogeneous activity distribution as the source organ [111]. GATE is also a major contributor to the OpenDose project, which aim to provide a large range of dosimetric data and tools, including radionuclide S values and specific absorbed fractions (SAFs) [112].

Brachytherapy simulations have also been performed in GATE. Low energy ^{125}I photon brachytherapy dosimetry reported results agree within 2% [113]. The GATE has also been used for the evaluation of clinical intensity-modulated radiotherapy (IMRT) treatment planning by performing absolute and relative dosimetry [114]. In addition, GATE simulation has been used in intraoperative radiation therapy (IORT) using a low-energy x-ray source [115]. GATE simulation has also been used to simulate the pencil beam scanning model for proton treatment plans [116]. Furthermore, a 6 MV Elekta Linac photon beam simulation was also performed in GATE [117, 118].

Recently, efforts have been made to write a GATE output data in Python '*NumPy*' file format with an extension of '*.npy*'. Previously, up to GATE version 9.0, GATE supported a ROOT file format including ASCII for virtually all simulations. However, the output files are bigger than ROOT files using the '*NumPy*' array as a simulation output. Even though the file sizes are larger, mechanisms exist to save the desired variables using the '*NumPy*' array. In addition, the ROOT files obtained from the GATE simulation can also be processed in Python with the *uproot* library [119]. The PyTorch machine learning library has been integrated into GATE since version 9.0 [120]. This integration likely opens the door to developments exploiting Artificial Intelligence methods.

The GATE toolkit provides a collection of pre-written Geant4 code to make simulations more user-friendly. Developers at the OpenGATE collaboration originally developed the customizable code for PET and SPECT systems so that users can simulate these systems without the detailed knowledge of the C++ programming language [51]. The use of GATE is based on the execution of scripting macro mechanisms. A macro script is an ASCII file with a *.mac* extension that consists of command scripts. Several macro files can be linked in a single macro file, called a main macro file that needs to be submitted for a simulation job. Thus, the main macro file consists of the definition of the simulation volume, the geometry of the detectors, the physics models, the source, the data digitization process, the definition of random number generator, and finally, the simulation execution commands. The main macro file is then executed in the command-line interface.

3.2.1. Simulation architecture

The simulation macro code starts from defining a simulation volume called as world volume. This volume can be of a 3D volume of any size, but it should be large enough to include all simulation volumes. All other volumes are defined inside the world, called daughters' volumes. Based on need, we can define the daughters of daughter's volumes. In GATE, we can only track the particles inside the world volume. The style of defining world volume is the same for all simulations, including imaging or dosimetry simulations. The following sub-sections define how we can set up simulations in GATE for imaging and dosimetry simulations.

3.2.1.1. PET simulation setup

1. First, we define a world volume then start defining the materials of the world volumes. For this, we need to include or link *GateMaterials.db* database file by using a */control/execute*

command. This file should contain the atomic or elemental compositions and materials definitions, including their density.

2. The second step is to define a detector or scanner geometry. GATE offers a wide range of predefined scanner templates to simulate the scanners, which can be adapted to model virtually all existing PET and SPECT systems. This thesis simulated GE Discovery MI PET scanner for PET imaging, a cylindrical scanner with a variable AFOV (15 – 25) cm or 3-5 ring systems. Thus, '*CylindricalPET*' system was chosen as a PET system to model this scanner. This system consists of 5 hierarchy levels – *rsector* (depth 1), *module* (depth 2), *submodule* (depth 3), *crystal* (depth 4), and *layer* (depth 5). Although it has 5 levels, *module* and *submodule* can be made optional. Inside these hierarchic levels, ring repeaters (to repeat rsectors), cubic array repeaters (to repeat module, submodules, and crystals) can be used to define the complete scanner system. The detector material is specified in the *layer* of the system. **Figure 10** shown below, is a model of the Discovery MI 4-ring scanner system simulated in this work; please refer to chapter 6 for complete modeling and results of the simulations.
3. Third step is to define a phantom geometry under investigation. Geometric primitives can be easily defined in GATE. In addition, we can also insert the stereolithographic (STL) files in GATE as a phantom. The complex geometry of STL files can be created elsewhere, such as in AutoCAD or other 3D modeling software. This addition in GATE can be useful to simulate an irregular shape geometry, such as tumors, kidneys, or other organs.

- Physics lists can be inserted in the fourth step. To insert the physics list in simulation, *'addPhysicsLists'* command is used. Customizing the physics lists, including enabling and disabling the physics processes, is also possible. For accurate simulation of PET imaging system, the *emStandard_opt4* physics list should be used in the recent versions of GATE [52, 106]. This list is the most accurate physics constructor for standard and low energy physics modeling.

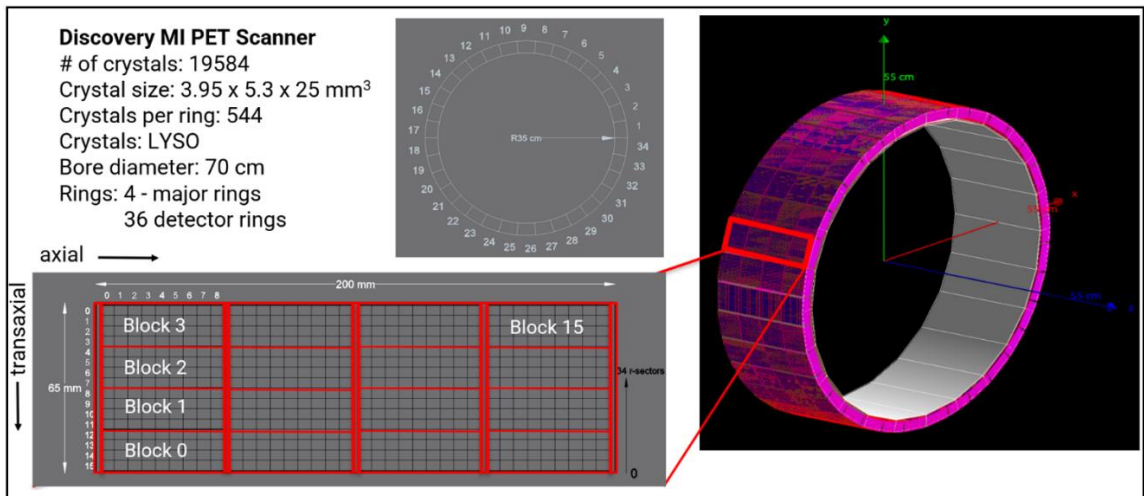


Figure 10: Modeling of Discovery MI 4-ring scanner in GATE. The scanner system has a total of 34 rsectors, 4 axial and 4 transaxial modules (blocks).

- The fifth step is to set up the digitizer module. The digitizer converts the photons interactions in the crystal into digital counts. The digitizers processes are common to PET and SPECT systems and may be used either during the simulation (online) or after the end of the simulation (offline). Several parameters such as energy resolution of the crystal, time resolution, scanner dead time, energy window (upholder and threshold), coincidence timing window, and multiples policy are inserted in the digitizer for an accurate simulation. Furthermore, the delayed window can also be set in the digitizer module if randoms are needed to be estimated from the delayed window method.

6. The sixth step is to define a source. Based on the simulation goal, the source can be defined by either the 'ion' source or the 'particle' type source (e^+).
7. The seventh step is to define a simulation output. Several types of output file formats are available in GATE, such as ROOT, NumPy (.npz) or ASCII file format. The NumPy and ASCII output files are bigger than the ROOT file format. It should be noted that the output should be written after the initialization command.
8. The eighth step is to define a Random number generator as GATE is a Monte Carlo toolkit. The CLHEP libraries used in GATE provide random number generators, the Ranlux64, the James Random, and Mersenne Twister. The default one is the Mersenne Twister generator.
9. The final step is to start a simulation. However, before running a large simulation, it is always good to check the simulations by defining a few primaries.

In GATE, we can 3D visualize the simulation geometry with the help of QT software. However, visualization consumes more memory; thus, best practices are to turn off the visualizations during the final simulation. In addition, setting the verbosity of '0' in the final simulation would be helpful to minimize the simulation time. The job splitting mechanism is also available in GATE, which allows us to make many parallel simulations of a single job, but at the end of simulations, the data need to be merged for analysis.

Details of the simulation, including scanner geometry, phantom geometries, and all other simulation macros, are available in the GitHub repository link below. Additionally, other post-processing data analysis tools written in MATLAB and ROOT scripts used in this simulation work are also available in the repository: <https://github.com/ashok-tiwari/PET-scanners-simulations>

3.2.1.2. Dosimetry simulation setup

In this work, in addition to the PET imaging, a large number of simulations were performed for dosimetric calculations of therapeutic β - and α -emitters for their DPKs generation in several tissue types. Following is the dosimetry simulation architecture that we used in virtually all dosimetry related simulations performed in this work:

1. First, we defined a world volume then the materials database file was inserted. This step is the same for all simulations.
2. Simulation verbosity levels were defined in a single macro file and linked to the main macro file. We can print the related information on-screen during the simulation by setting verbosity values. Verbose values of 0 to 2 are allowed in GATE.
3. The simulation phantom geometry was defined, and its material definitions were assigned to it. Phantom is a solid sphere of homogeneous tissues (**Figure 11**). The radius of the phantom geometry should be larger than the *DoseActor* size definition.
4. For absorbed dose tally, the *doseActor* tool was used in all simulations. This actor is used to calculate the energy and dose deposition in a voxel-level as a 3D matrix. While defining the *doseActor*, voxel size, position, or resolution of the matrix can be specified. We can tally dose, energy deposition (edep) and associated statistical uncertainty using this actor. This actor needs to be attached to the phantom geometry where dose or energy deposition is to be tallied.
5. In the next step, physics lists can be defined. For dose point kernels simulations of β -emitting radionuclides, *emStandard_opt3* option was exploited. After the physics list definition, the electron *Steplimiter* parameter and energy cuts were defined.

6. The source was defined after the initialization command. In dosimetry simulations, it can be defined either as ‘ion’ source, discrete spectrum, or histogram type source can be used. The ion source is very slow compared to the spectrum type source.
7. To check the simulation, visualization commands can be inserted after the source definition.
8. In the next step, a random number generator was defined. The default Mersenne Twister generator was used in all simulations.
9. The final step is to start a simulation.

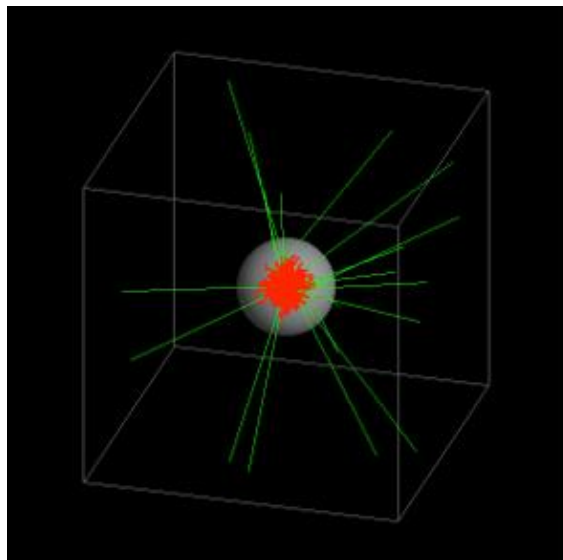


Figure 11: Dose point kernels simulations in GATE. Tracks in green are photons whereas tracks in red are electrons.

Simulation details are described in **chapters 4 and 5**. For details of the dose point kernel simulations, including phantom geometry, *doseActor* definition, source definition, and all other simulation macros are available in the GitHub repository link below: https://github.com/ashok-tiwari/Beta_dose_point_kernels

CHAPTER 4: DOSIMETRY OF THERAPEUTIC BETA-EMITTERS

4.1. Introduction

Radioisotopes and their associated decay products play a central role in both imaging and therapeutic nuclear medicine applications. Radionuclides such as ^{90}Y , ^{32}P , ^{131}I , ^{111}In , and ^{89}Sr have been used for several decades in both radiotherapy and single photon imaging applications, whereas ^{18}F , ^{11}C , ^{13}N , ^{15}O , ^{68}Ga , ^{64}Cu and ^{89}Zr are widely used in the PET imaging. In addition, ^{177}Lu and ^{223}Ra have recently attracted considerable attention and demonstrated great promise in clinical targeted radionuclide therapy applications in FDA approved therapeutic radiopharmaceuticals. Regardless of whether the radionuclides are tagged to imaging or therapy radiopharmaceuticals, irradiated molecules/atoms within cells absorb energy from the charged particles and photons emitted from radionuclide decay as well as with secondary charged particles. This energy deposition can promote direct macromolecular damage as well as generate reactive oxygen and/or nitrogen free-radical species that have proven to be responsible for the majority of molecular and cellular damage [121].

The field has amassed some data on how much radiation dose (energy absorbed per unit mass) different organs and tissues can tolerate before resulting in toxic effects. Different organs have different sensitivities. In general, the more cellular division that routinely occurs in the organ, the more radiosensitive it is. So it is critical for physicians and physicists to monitor and predict organ-specific radiation doses so as to avoid potential toxic effects.

If one knows the distribution of radioactive decays in the body, the absorbed dose to tissues can be estimated by several techniques. The Medical Internal Radiation Dosimetry (MIRD) approach is perhaps the simplest and most widely used approach to calculate organ-specific internal radiation dose. The traditional MIRD formalism is an organ-based dosimetry technique,

which uses pre-tabulated organ-based S-values. The S-value is a radionuclide-specific quantity representing the mean absorbed dose rate to a target organ per unit activity in a source organ [42]. The drawbacks of this approach are severalfold. First, activities in organs are assumed to be uniformly distributed in the source organ, which is a gross oversimplification. Second, the MIRD “standard man” that is used in these calculations assumes standard organ shapes and sizes with rigid geometric relationships and distances between organs, which does not take into account the somewhat varied geometry found between individuals. This methodology was the one primarily used for several decades due to the lack of computing power to perform more accurate calculations.

However, the MIRD method has evolved over recent years. The latest MIRD/ICRP update includes scalable voxel-based anthropomorphic phantoms, however, tissue composition heterogeneity are still not accounted and patient-specific organ geometries are not yet feasible [122-124].

Intra-organ dosimetry with nonuniform activity distributions has been addressed by development of voxel-based dosimetry, including the voxel S-value (VSV) and the dose point kernel (DPK) methods. These methods rely on convolving isotope-specific kernels with the cumulative activity distribution of interest, such that a dose map is obtained. Dose kernels used for this process often follow the nomenclature ‘VSV’ for kernels that are in voxelized coordinate space, and ‘DPK’ for kernels that are tabulated as a function of radius from a point source - although this convention is not universally followed. Converting a DPK to a VSV map involves resampling the DPK into Cartesian coordinates and convolving with the uniform activity of a source voxel.

Empirical measurement of beta dose point kernels is challenging due to the limited range of electrons in matter (typically on the order of millimeters) and spatial limitations of conventional

dosimeters. As such, many authors have calculated kernels analytically [125] or simulated them using Monte Carlo (MC) methods [10, 126-133]. Monte Carlo codes that have been used for this purpose include ETRAN, SMOOPY, EGSnrc, FLUKA, PENELOPE, MCNPX, Geant4DNA and GATE. All of these MC codes attempt to approximate a solution to the Boltzmann transport equation by employing different treatments of stochastic transport processes.

The simulation of interactions between electrons and their secondary particles with matter is one of the main tasks of Monte Carlo simulations. The resulting energy deposition is relevant to a wide variety of applications. GATE, previously introduced in Chapter 3, incorporates the Geant4 cross-section and stopping power data libraries [134]. The GATE software has been extensively used in imaging applications since its release in May 2004 [135]. Visvikis et al. [136] were the first to study the potential of GATE in dosimetric applications; similar dosimetric uses of GATE have been the subject of additional manuscripts [10, 96, 113, 137-139]. In this study, we exclusively used the GATE Monte Carlo simulation toolkit (GATEv8.1) to simulate the dose distribution of monoenergetic electrons and the beta spectra of several medically relevant radionuclides in several tissue types.

The simulation of beta-emitting radionuclides and monoenergetic electrons in different materials is essential to understanding the impact of tissue type on the spatial distribution of energy deposition. In this work, we simulate electrons and betas in different tissues — water, compact bone (hereafter bone), blood, red marrow, adipose, and lung. Monoenergetic electrons dose point kernels were simulated for energies (0.015-10 MeV). Variability of scaled kernels may inform of the utility of multi-kernel dosimetry methods, so comparison of kernels generated in different tissues was a priority within this work. In addition to monoenergetic electrons, dose point kernels were simulated for common therapeutic radionuclides - ^{90}Y , ^{188}Re , ^{32}P , ^{89}Sr , ^{186}Re , ^{153}Sm , and

^{177}Lu . The beta emitters ^{90}Y , ^{188}Re , ^{186}Re , and ^{177}Lu are isotopes which are used in targeted radiopharmaceutical therapy, whereas the isotopes ^{153}Sm , ^{89}Sr , and ^{32}P are useful for the treatment of metastatic bone pain [140]. Finally, a comparison of the dose point kernels in water and bone against other MC codes were performed. The novel dataset of all GATEv8.1 generated dose point kernels in mediums as mentioned above are included as supplementary material.

4.2. Methodology

4.2.1. Monte Carlo Simulation using GATE

DPKs were simulated in a spherical phantom assuming a homogeneous spherical system with a point source at its center, emitting isotropically. Dose deposition was tabulated in spherical concentric shells placed around the source at fixed radial distances. The thickness of the concentric shells was made to be equal to the voxel size of the 3D dose matrix. The dose scoring voxel volume has been defined as the dosel [134]. In all simulations, the radius of the phantom was greater than the range of electrons in the homogeneous medium.

Electrons, in passing through the matter, undergo physical interactions and lose energy primarily by ionization, although other processes (multiple scattering, bremsstrahlung, Cerenkov radiation, backscattering, and Moller scattering losses) contribute. In this simulation using GATE, the electromagnetic (EM) constructor called *emstandard_opt3* was implemented for the physics list. This EM constructor is useful for applications that require higher accuracy of electrons, hadrons and ion tracking [52].

The following parameters in GATE were used for all simulations: $E_{\text{Min}} = 0.1 \text{ keV}$, $E_{\text{Max}} = 10 \text{ GeV}$, $\text{DEDXBinning} = 220$, and $\text{LambdaBinning} = 220$. These parameters specify the kinetic energy range for all physical processes, the number of bins for the mean energy loss (default = 84), and the number of bins for the mean free path table (default = 84). Variance reduction techniques

were not used in any of the simulations performed in this work.

In GATE, *doseActor* was used to calculate the energy deposition. The deposited energy EDep was scored at the voxel level, and associated uncertainties were calculated in each dosel with the *doseActor* UncertaintyEDep. The output of the simulation, i.e., 3D energy deposition matrices and its statistical uncertainties were stored in the MetaImage format, i.e., mhd, as it is recommended by GATE [134]. A Matlab in-house code was developed, which converts the cartesian coordinates to the polar coordinates, to obtain the relevant dosimetric quantities from the results. In this simulation work, deposited energies were scored into bins of size equal to the thickness of the concentric shells. To ensure at least one physical interaction in each bin, the bin width was set equal to the *electronStepLimiter* parameter called as StepMax. The effective atomic number (Z_{eff}) and densities of simulated tissues are tabulated in **Table 2**. The atomic composition and densities of these materials were obtained from ICRU 46 [141].

Table 2: The densities and effective atomic numbers of tissues used in simulations

Materials	ρ (g/cm ³)	Z_{eff}
bone	1.85	11.87
blood	1.06	7.78
lung	0.26	7.74
water	1.00	7.42
red marrow	1.03	7.21
adipose	0.92	6.47

4.2.1.1. Electron step size

During simulation electron trajectories were divided into sub-steps, all of equal length, regardless of electron energy. The fixed step-size scheme used herein also permits efficient implementation of Goudsmit-Saunderson theory. The step length is usually chosen so that the energy loss along a step is constant. The MCNP [91] and ETRAN code [132] have a default value

of 8.3% average energy loss per step. However, in Geant4, the recommended value of fractional energy loss per step is 10% set by the parameter called as `dRoverRange` during a step for particle [52, 142].

Electron step size is a user-controlled parameter in simulation; the `electronStepLimiter` parameter was used to set the electron step. It was fixed by the corresponding percentage energy loss of the electrons in different mediums. To get more accurate results very small steps are optimal; however, simulation becomes computationally intensive as the step-size decreases. The step size is calculated using the stopping power and energy of the electron. The fractional energy loss for each step is $\frac{\Delta E}{E} = \text{constant}$, where $\Delta E = E_n - E_{n-1}$ is given by **Equation (3)**,

$$\Delta E = - \int_{S_{n-1}}^{S_n} \frac{dE}{dS} dS \quad (3)$$

where dE/dS is the total stopping power for the energy and material medium of interest. The stopping power values were taken from the ESTAR database [143] to calculate the step length parameter. Electron step sizes were equal to the voxel sizes in all simulations performed herein.

4.2.1.2. Energy Thresholds

An energy threshold was set, below which the particle transport assumed local energy deposition, using the range cut parameter. This energy threshold is necessary to avoid the infrared divergences that appear in electromagnetic processes [134]. In this work, where electrons energy is greater than 1 MeV, energy thresholds of ~10 keV were set, for 100 keV to 1 MeV energy range, energy thresholds of ~5 keV were set, and for 15 keV to 100 keV, the energy thresholds used were ~2 keV. For instance, the associated range thresholds at the energy threshold of 5 keV was 3.1 μm in bone, 5.2 μm in blood, 5.3 μm in red marrow, 5.4 μm in water, 5.76 μm in adipose, and 21 μm in lung.

4.2.2. Monoenergetic electron dose point kernels

The dose point kernels (DPKs) can be defined as energy deposition kernels from point isotropic sources. DPKs can also be described as the dose deposition profile as a function of radial distance. For monoenergetic electrons, the scaled absorbed dose can be written as [125, 144],

$$J\left(\frac{r}{R_{CSDA}}\right) = 4\pi r^2 D(r) \frac{R_{CSDA}}{E_0} \quad (4)$$

where, r is the radial distance from the center of the sphere, $D(r)$ is the absorbed dose per source particle a distance r and R_{CSDA} is the range of electrons in the continuous slowing down approximation (CSDA) with source energy E_0 . The nominal CSDA range (R_{CSDA}) tabulated in **Table 3** for all energies was obtained from NIST ESTAR database (accessed May, 2019) [143]. The values of R_{CSDA} tabulated in **Table 3** are the ranges of electrons scaled with corresponding density of the material medium in g/cm^2 and demonstrate a differential range of approximately 10%.

Table 3: The CSDA range of electrons in different tissues used for dose point kernel scaling

e ⁻ energy (MeV)	R _{CSDA} range (g/cm ²)					
	water	adipose	blood	red marrow	bone	lung
0.015	5.147×10^{-4}	4.940×10^{-4}	5.198×10^{-4}	5.095×10^{-4}	5.627×10^{-4}	5.189×10^{-4}
0.05	4.320×10^{-3}	4.175×10^{-3}	4.362×10^{-3}	4.290×10^{-3}	4.681×10^{-3}	4.355×10^{-3}
0.10	1.431×10^{-2}	1.387×10^{-2}	1.445×10^{-2}	1.423×10^{-2}	1.545×10^{-2}	1.443×10^{-2}
0.50	1.766×10^{-1}	1.720×10^{-1}	1.781×10^{-1}	1.761×10^{-1}	1.898×10^{-1}	1.780×10^{-1}
1.00	4.367×10^{-1}	4.275×10^{-1}	4.413×10^{-1}	4.369×10^{-1}	4.711×10^{-1}	4.388×10^{-1}
2.00	9.875×10^{-1}	9.621×10^{-1}	9.895×10^{-1}	9.820×10^{-1}	1.056	9.719×10^{-1}
4.00	2.037	2.010	2.061	2.049	2.191	2.000
10.0	4.975	4.933	5.031	5.014	5.293	4.842

Use of the scaled kernel formalism given by **Equation (4)** facilitates inter-kernel comparison by (i) normalizing the domain to R_{CSDA} , (ii) normalizing the range to the total electron

energy, and (iii) removing the inverse-square dependence of energy deposition about an isotropic point source. The dimensionless quantity (J), defined by **Equation (4)**, represents the fraction of dose deposited in a spherical shell of scaled radius r/R_{CSDA} to $r/R_{\text{CSDA}} + d (r/R_{\text{CSDA}})$.

Twenty million primaries were simulated for each monoenergetic electron simulation. The dose point kernels for monoenergetic electrons with energies 15 keV, 50 keV, 100 keV, 500 keV, 1 MeV, 2 MeV, 4 MeV, and 10 MeV were simulated in mediums of water, bone, blood, red marrow, adipose, and lung and compared our work with published literature [10, 126, 127, 144, 145].

The voxel sizes for each simulation were calculated using **Equation (3)** and were also used with preliminary simulations to check whether the calculated values are in good agreement with the results of other MC codes. All the voxel sizes for each simulation are provided in **Table 4** and **Table 5**. Moreover, the voxel sizes for 50 keV, 500 keV and 2 MeV monoenergetic electrons in water were made to match with Papadimitroulas et al. [10] for comparison with his work.

Table 4: The electronStepLimiter parameters for monoenergetic electrons in simulation

e ⁻ energy (MeV)	<i>electronStepLimiter (voxel size) (mm)</i>					
	water	adipose	blood	red marrow	bone	lung
0.015	1.065×10^{-4}	1.158×10^{-4}	9.999×10^{-5}	1.034×10^{-4}	5.323×10^{-5}	4.096×10^{-4}
0.05	6.227×10^{-4}	6.768×10^{-4}	5.875×10^{-4}	6.045×10^{-4}	3.374×10^{-4}	2.395×10^{-3}
0.10	2.730×10^{-3}	2.730×10^{-3}	2.730×10^{-3}	2.650×10^{-3}	2.730×10^{-3}	1.050×10^{-2}
0.50	1.909×10^{-2}	2.074×10^{-2}	1.799×10^{-2}	1.854×10^{-2}	1.034×10^{-2}	7.342×10^{-2}
1.00	4.734×10^{-2}	4.446×10^{-2}	4.791×10^{-2}	4.601×10^{-2}	2.532×10^{-2}	1.816×10^{-1}
2.00	1.058×10^{-1}	1.150×10^{-1}	9.981×10^{-2}	1.027×10^{-1}	5.719×10^{-1}	4.070×10^{-1}
4.00	4.032×10^{-1}	4.732×10^{-1}	3.803×10^{-1}	3.913×10^{-1}	2.714×10^{-1}	1.500
10.0	5.400×10^{-1}	5.870×10^{-1}	5.099×10^{-1}	5.243×10^{-1}	2.919×10^{-1}	2.070

4.2.3. Therapeutic beta emitter radionuclides dose point kernels

All simulation parameters were maintained when moving to beta spectra, however a different scaled kernel formalism was used. The absorbed scaled dose for beta kernels can be written as **Equation (5)** [125, 144],

$$J(r/X_{90}) = 4\pi\rho r^2 D(r) \frac{R_{\text{CSDA}}}{E_{\text{ave}}} \quad (5)$$

where, ρ is the density of the medium, r is the radial distance from the center of the sphere, $D(r)$ is the absorbed dose per source particle at radius r , X_{90} is the radius of the homogeneous sphere in which 90% of the emitted energy is absorbed, and E_{ave} is the average energy of the beta spectrum. The beta radionuclide's dose point kernels are usually scaled by using the X_{90} parameter. In this work, these parameters were calculated from the simulations themselves. The numerical value of X_{90} for each simulating material-energy combination can also be calculated using **Equation (6)**,

$$4\pi\rho \int_0^{X_{90}} r^2 \Phi(r) dr = 0.90 \quad (6)$$

where $\Phi(r)$ is the fraction of energy deposited per unit mass at a distance r from a point source.

Beta spectra (**Figure 12**) were simulated using the histogram option in GATE, and energy spectra of radionuclides tabulated in **Table 5** were obtained from the RADIATION DOSE ASSESSMENT RESOURCE (RADAR, accessed May, 2019) [146]. The average energy and the endpoint energy of the betas were obtained from NNDC (accessed June, 2019) [147]. In this simulation, only beta spectra are used for source input for the simulations for all isotopes.

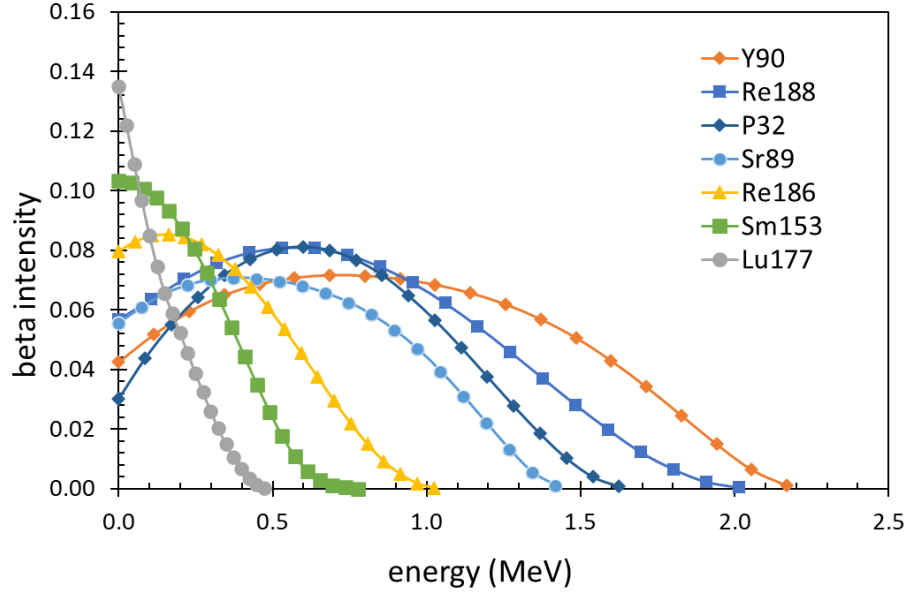


Figure 12: Beta spectra of radionuclides simulated in this work; spectra were taken from RADAR website.

Table 5: The electronStepLimiter parameters for the beta radionuclides in simulation

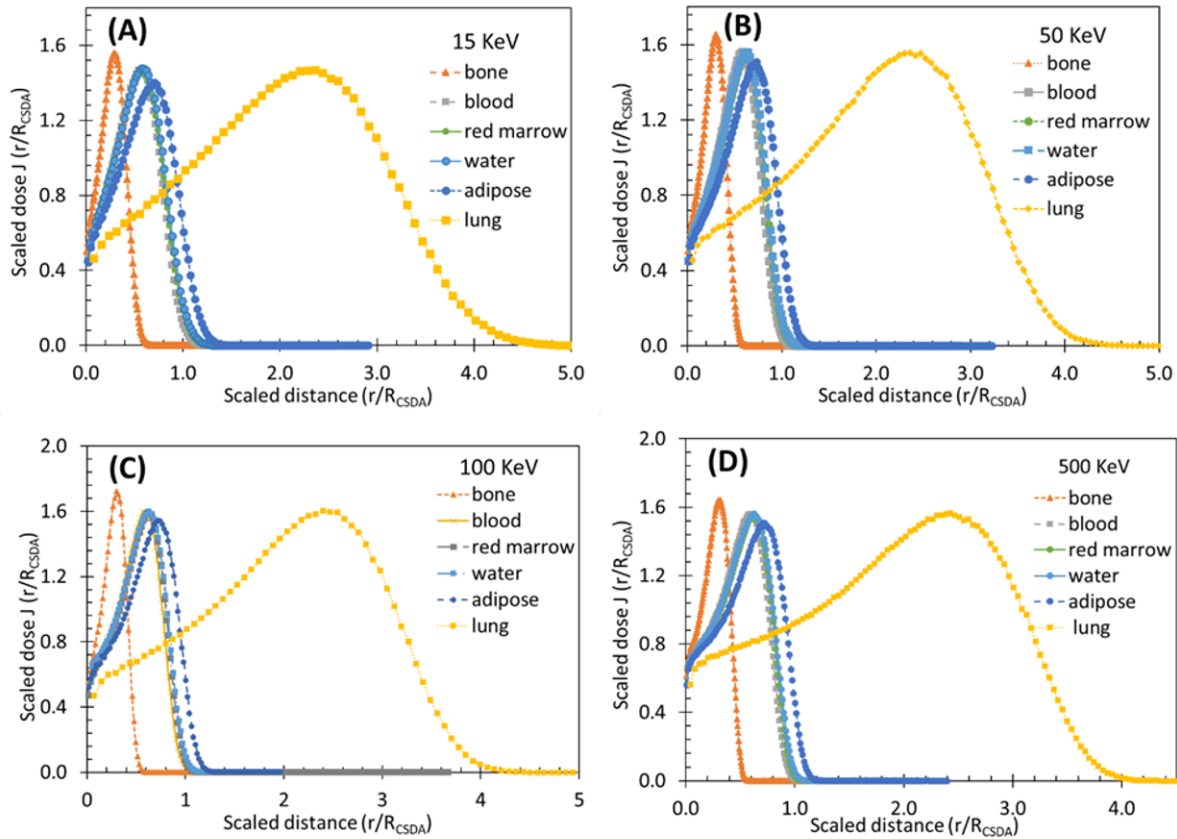
radio-nuclide	<i>electronStepLimiter (voxel size) (mm)</i>					
	water	adipose	blood	red marrow	bone	lung
^{90}Y	1.106×10^{-1}	1.202×10^{-1}	1.045×10^{-1}	1.074×10^{-1}	5.979×10^{-2}	4.250×10^{-1}
^{188}Re	9.550×10^{-2}	1.040×10^{-2}	9.009×10^{-2}	9.300×10^{-2}	5.160×10^{-2}	3.670×10^{-1}
^{32}P	7.672×10^{-2}	8.320×10^{-2}	7.220×10^{-2}	7.444×10^{-2}	4.137×10^{-2}	2.949×10^{-1}
^{89}Sr	6.400×10^{-2}	6.956×10^{-2}	6.037×10^{-2}	6.210×10^{-2}	3.456×10^{-2}	2.460×10^{-1}
^{186}Re	3.860×10^{-2}	4.208×10^{-2}	3.640×10^{-2}	3.750×10^{-2}	1.937×10^{-2}	1.150×10^{-1}
^{153}Sm	2.300×10^{-2}	2.500×10^{-2}	2.050×10^{-2}	2.223×10^{-2}	1.150×10^{-2}	6.440×10^{-2}
^{177}Lu	1.210×10^{-2}	1.354×10^{-2}	1.147×10^{-2}	1.175×10^{-2}	6.500×10^{-2}	4.549×10^{-2}

4.3. Results

4.3.1. Monoenergetic electron dose point kernels

The results of the simulations of dose point kernels for monoenergetic electrons are presented in **Figure 13**. The DPKs have slightly different peaks in different tissues. This is because

the DPKs are associated with the effective atomic number (Z_{eff}) of the medium. The medium that has a greater value of Z_{eff} has the highest peak (bone) in **Figure 13**, and vice-versa. This is in accordance with the stopping power theory, i.e., the proportionality of the stopping power with the ratio of atomic number and the mass number (Z/A) of the material medium. The complete set of scaled dose point kernels obtained in this work for electrons energies 15, 50, 100, and 500 keV, 1, 2, 4, and 10 MeV, in water, bone, blood, red marrow, adipose, and lung, are available as supplementary material 1 in our published paper [1].



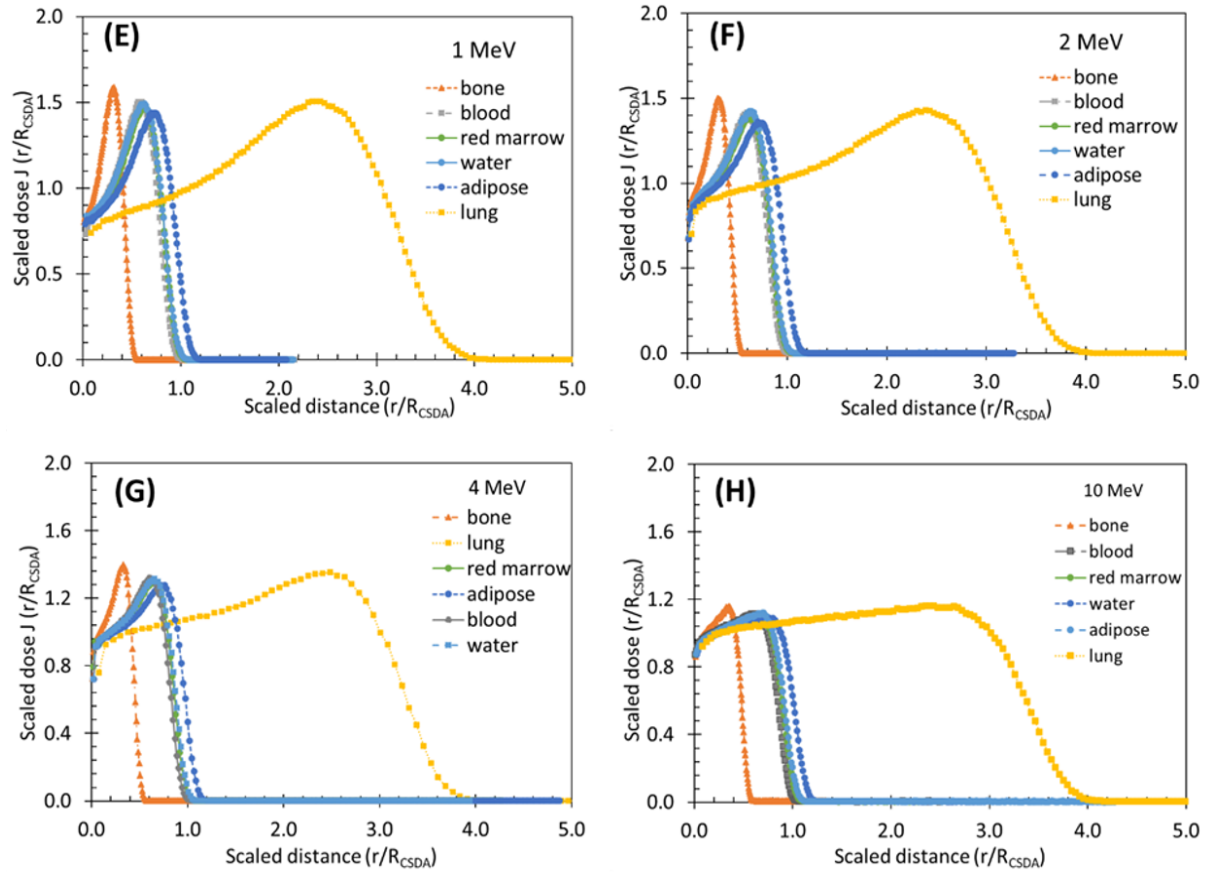


Figure 13: Dose point kernels of (A) 15 keV, (B) 50 keV, (C) 100 keV, (D) 500 keV, (E) 1 MeV, (F) 2 MeV, (G) 4 MeV, and (H) 10 MeV monoenergetic electrons in water, bone, blood, adipose, red marrow, and lung.

4.3.1.1. Literature comparison of electron dose point kernels

The simulated monoenergetic electrons dose point kernels were compared with the published kernels as shown in **Figure 14**. The dose point kernels generated with different Monte Carlo codes were generally in good agreement. **Figure 14(A)** shows the dose point kernels for 50 keV monoenergetic electrons in water compared with other published codes. The greatest differences occur near the maxima of the energy deposition. The maxima of dose kernels for 50 keV monoenergetic electrons generated with GATEv8.1 is at $r/R_{CSDA} = 0.650$, i.e., 65% of the R_{CSDA} range. Other codes such as Geant4DNA and MCNPX [127] also appear to have maxima at

$r/R_{\text{CSDA}} = 0.650$. However, for remaining codes PENELOPE [127], and ACCEPT [144] kernels shows a peak at $r/R_{\text{CSDA}} = 0.600$. The largest point-to-point percentage difference between GATEv8.1 and other codes at $r/R_{\text{CSDA}} = 0.650$ is 1.5 % (PENELOPE), 3.5 % (ACCEPT), 2.1% (EGSnrc), 3.8% (Geant4DNA) and 21.3% (MCNPX) respectively. However, the mean point-to-point percentage differences are 1.5% (PENELOPE), 3.1 % (ACCEPT), 1.7% (EGSnrc), 2.4% (Geant4DNA) and 6.9 % (MCNPX) as shown in the **Figure 14(A)**.

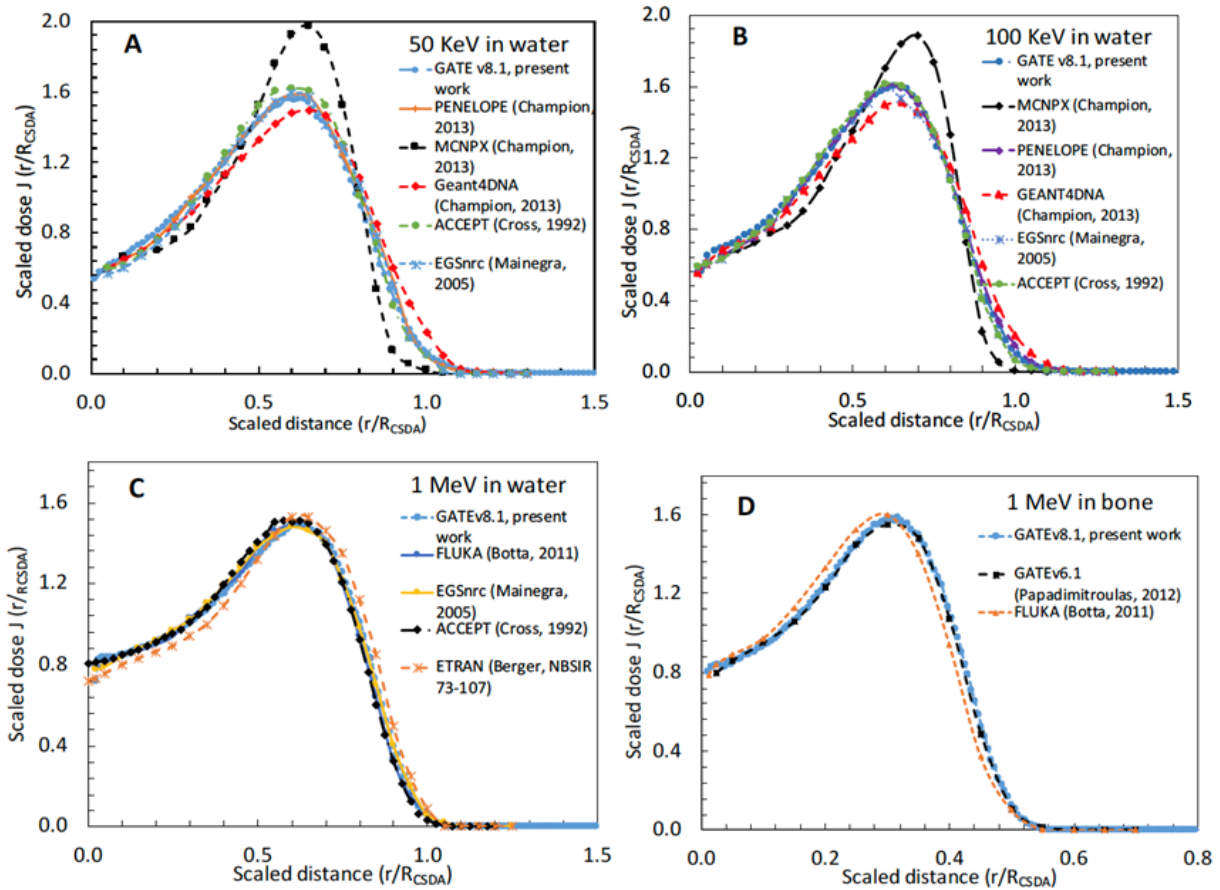


Figure 14: Comparison of DPKs of monoenergetic electrons with published kernels (A) 50 keV, (B) 100 keV, (C) 1 MeV in water and (D) 1 MeV in bone.

For the 100 keV monoenergetic electrons as shown in **Figure 14(B)**, similar shapes of kernel distributions have been observed. The most significant differences obtained at the maxima of the kernel distribution, where they amount to less than 6% for the PENELOPE, ACCEPT,

EGSnrc, Geant4DNA codes and ~21 % for MCNPX code respectively. However, the mean percentage differences are slightly less than that of 50 keV monoenergetic electrons as shown in **Figure 14**. For the 1 MeV electrons in water, similar discrepancies were observed and are comparable to the variations between other Monte Carlo codes. Overall, there is a good agreement between the codes.

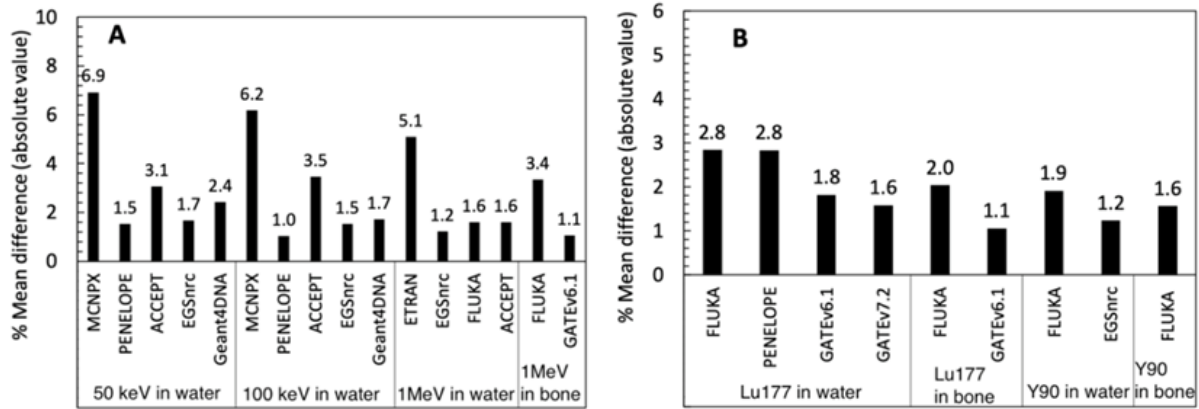


Figure 15: Mean percentage deviation from other published works for (A) monoenergetic electrons in water 50 keV, 100 keV, 1 MeV, and 1 MeV monoenergetic electrons in bone and (B) ^{177}Lu and ^{90}Y beta dose point kernels in water and bone with literature values.

Dose point kernels in bone are not available in literature for all electron energies simulated herein, so comparisons were only made for 1 MeV monoenergetic electrons. Comparison between the results of our study with FLUKA [126] and GATEv6.1 [10] are favorable with 3.4% and 1.1% differences.

4.3.2. Tissue specific beta emitting radionuclide dose point kernels

The numerical values of X_{90} were calculated based on the 90% total energy deposited by all the primary events. The corresponding radius of the concentric spheres at 90% total energy deposited value gives the X_{90} metric. The X_{90} values simulated herein are included in **Table 6**. The simulated values in water agree with values reported in the literature. The large differences in X_{90} values in **Table 6** as a function of tissue type are primarily driven by the density of tissue. The

results of the simulation of beta dose point kernels for ^{90}Y , ^{32}P , ^{188}Re , ^{186}Re , ^{89}Sr , ^{153}Sm , and ^{177}Lu isotopes in water, bone, blood, red marrow, adipose, and lung are presented in the **Figure 16**, **Figure 17** and **Figure 18**. The complete data are available as supplementary material 2 in our manuscript [1].

Table 6: X_{90} values calculated from simulated dose point kernels. The indicators (a), (b), (c) and (d) in the table are references [126], [145], [148], and [149] respectively.

radio-nuclide	X_{90} values (mm)						Literature X_{90} water (mm)
	bone	blood	red marrow	water	adipose	lung	
^{90}Y	2.93	5.09	5.33	5.39	5.85	20.36	5.40 (a), 5.43 (b)
^{188}Re	2.60	4.43	4.65	4.71	5.15	18.05	4.57 (a), 4.89 (c)
^{32}P	2.13	3.68	3.81	3.86	4.25	14.95	3.66 (b), 3.74 (d)
^{89}Sr	1.81	3.21	3.24	3.28	3.62	12.36	3.21 (d)
^{186}Re	1.24	2.14	2.23	2.25	2.47	8.71	1.91 (a)
^{153}Sm	0.65	1.15	1.19	1.20	1.32	4.65	1.15 (a)
^{177}Lu	0.36	0.63	0.65	0.66	0.73	2.57	0.62 (a)

In **Figure 16** and **Figure 17**, we observe that the beta dose point kernels in different mediums do not differ significantly when normalized to X_{90} . To quantify the differences between kernels, the mean percentage difference between the point to the point comparison of dose point kernels for ^{177}Lu has been calculated by using **Equation (7)** for all tissue types. The point-to-point comparison of the two-dose point kernel profiles at the same scaled distance from the source can be calculated using the following equation,

$$\% \text{ mean difference} = \frac{1}{N} \left[\frac{\sum_{i=1}^N (J_{w,i}(r/X_{90}) - J_{t,i}(r/X_{90}))}{\max(J_{w,i}(r/X_{90}), J_{t,i}(r/X_{90}))} \right] \times 100\% \quad (7)$$

where, $J_w(r/X_{90})$ is the dose point kernel in water at the scaled distance (r/X_{90}) and $J_t(r/X_{90})$ is the dose point kernel at the same scaled distance (r/X_{90}) in other tissues; namely bone, blood, adipose, lung, and red marrow, and N represents the total number of points in calculation.

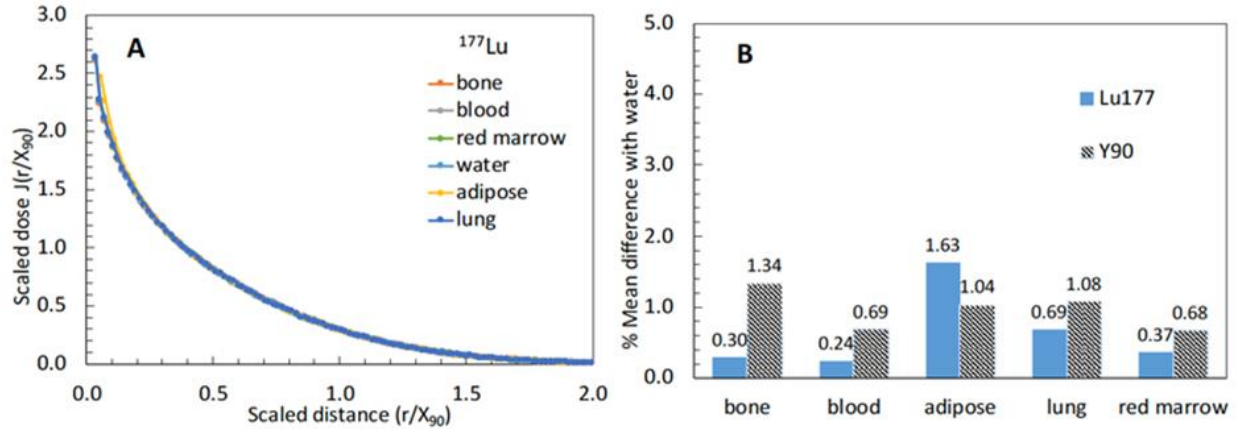


Figure 16: (A) Beta DPKs for ^{177}Lu in bone, blood, red marrow, water, adipose, and lung (B) the beta DPKs of ^{177}Lu and ^{90}Y in water compared with other tissues.

The average statistical uncertainties in all beta simulations are less than 5% for $0.1 < (r/X_{90}) < 1.0$. The beta DPKs of ^{177}Lu and ^{90}Y in different mediums as shown in **Figure 16** and **Figure 17**. The mean percentage difference between the beta DPKs in water to the bone, blood, lung, adipose, and red marrow are less than 2% are shown in **Figure 16(B)**. The calculated discrepancies are not statistically significant.

The **Figure 18** depicts the beta radionuclide dose point kernels plotted with the scaled distance and the radial distance in water, bone, blood, and lung. All the DPKs plotted with the scaled distance (**Figure 18 A, C, E, G**) and the radial distances (**Figure 18 B, D, F, and G**) in different tissues are found to be similar in shape and magnitude.

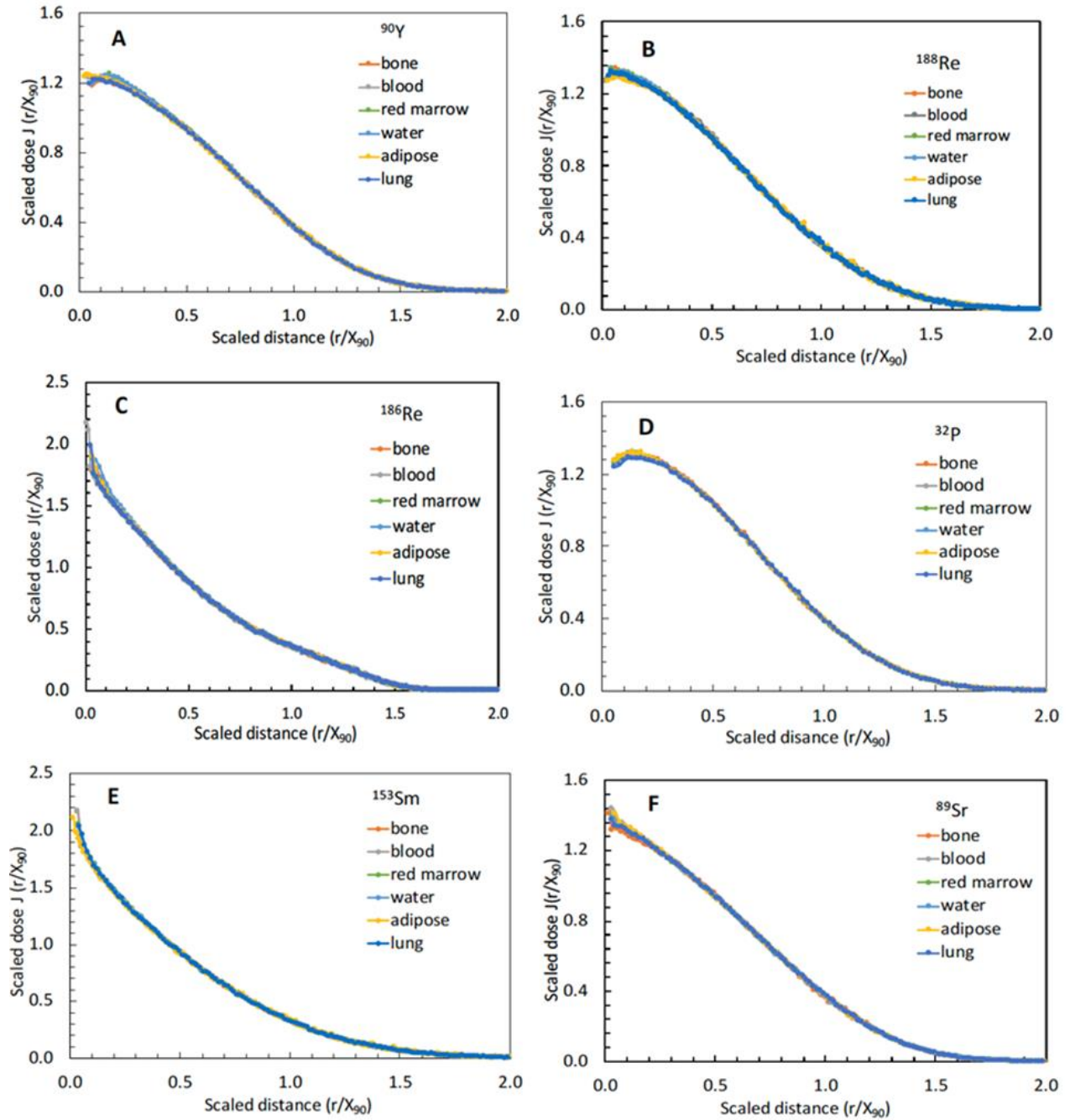


Figure 17: Dose point kernels of the beta emitters (A) ^{90}Y , (B) ^{188}Re , (C) ^{186}Re , (D) ^{32}P , (E) ^{153}Sm , and (F) ^{89}Sr nuclides in water, bone, blood, red marrow, adipose and lung as a function of scaled distance (r/X_{90}) .

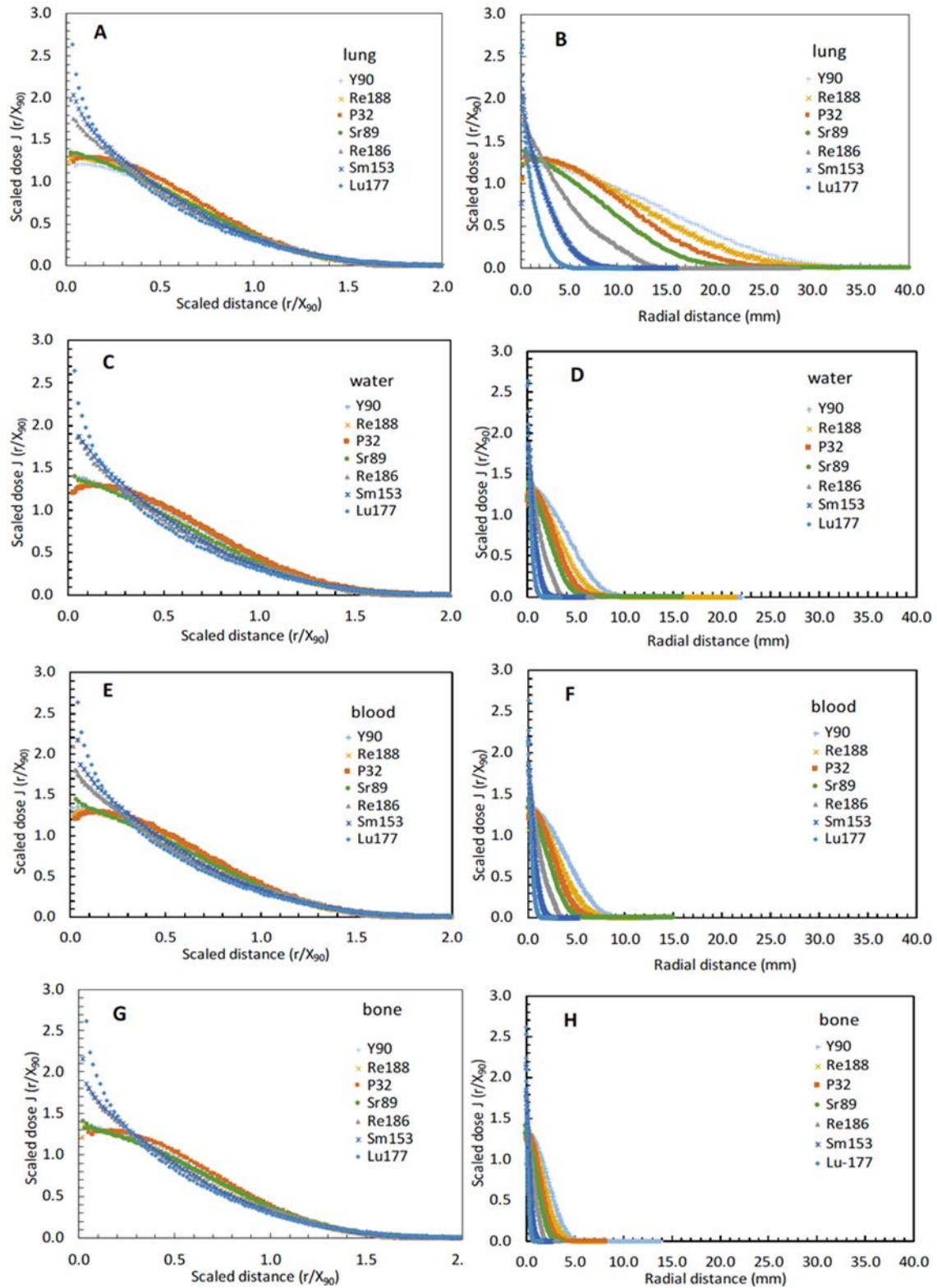


Figure 18: DPKs of beta radionuclides plotted with scaled distance and radial distance in (A) & (B) lung, (C) & (D) water, (E) & (F) blood, and (G) & (H) bone. The abscissa and ordinates are scaled to be same so that one can easily make a comparison.

4.3.2.1. Literature comparison of beta dose point kernels

Although beta kernels were generated for water, bone, blood, red marrow, adipose, and lung, comparison against literature data is only possible for water and bone. These comparisons are shown in **Figure 19** and **Figure 20**. This work with GATE version 8.1 and 7.2 shows an excellent agreement with the dose point kernels calculated with FLUKA and PENELOPE Monte Carlo codes.

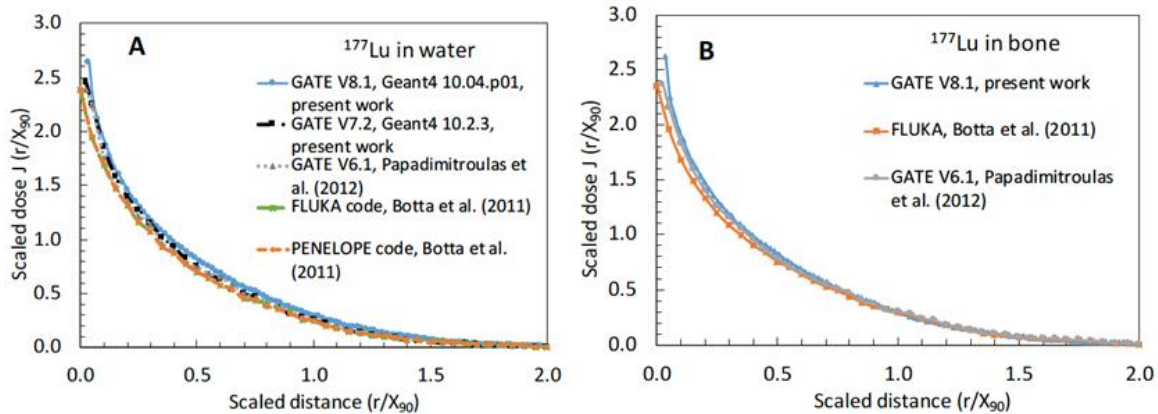


Figure 19: Comparison against literature kernels for ^{177}Lu in (A) water and (B) bone.

Discrepancies among kernels were quantified for scaled distances $(r/X_{90}) < 1$. The beta dose point kernels of ^{177}Lu were compared to those of FLUKA [126], PENELOPE [126] and GATE earlier versions GATEv6.1 [10] and GATEv7.2 (present work) in water and bone medium. Similarly, the beta kernels of ^{90}Y were compared with FLUKA [126] and EGS4 [145] in water and bone. The small deviations between dose kernels in **Figure 19** and **Figure 20** are likely caused by different values for the X_{90} parameter in addition to differences between Monte Carlo codes. The mean percentage difference between the dose kernels obtained by this work to other authors has been calculated and presented in **Figure 15(B)**. The results show the excellent agreement between the codes, and the mean differences between the GATE and other codes range between 1% and 3%.

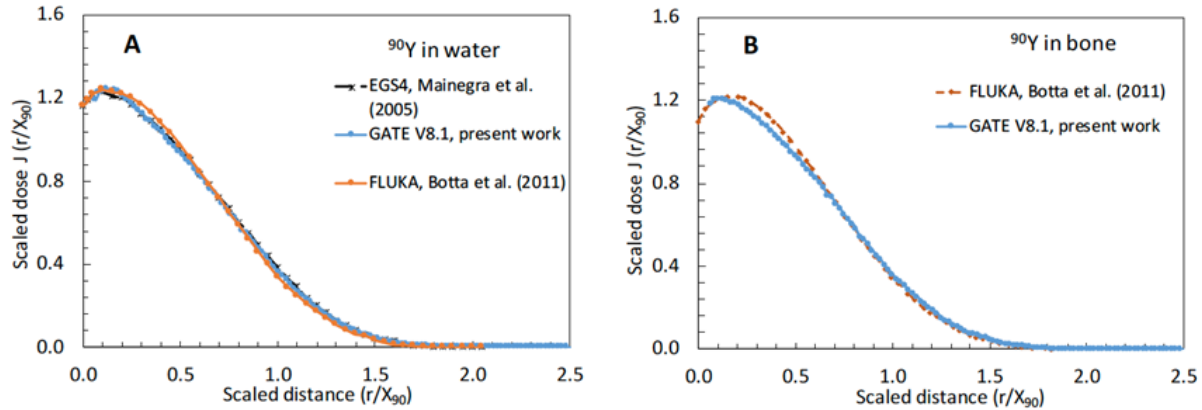


Figure 20: Comparison against literature kernels for ^{90}Y in (A) water and (B) bone.

4.4. Discussion and Conclusions

There has been significant interest in developing new 3D dosimetry tools for targeted radionuclide therapy. This interest is motivated by the shortcomings of utilizing pre-tabulated energy transfer coefficients generated from virtual anthropomorphic phantoms. So-called “voxel-wise dosimetry” aims to provide a dose or dose-rate estimate for each voxel within a nuclear medicine image volume. The most straightforward approach using dose point kernel voxel-wise dosimetry involves convolving an isotope-specific energy deposition kernel with the activity map derived from a quantitative SPECT image. However, this approach neglects the impact of tissue type and density heterogeneity within the patient. The purpose of this work was to (i) improve the availability of electron and beta kernels in literature and (ii) to assess the importance of utilizing tissue-specific electron kernels for voxel-wise dosimetry.

GATE is a validated MC simulation toolkit for tomographic emission, radiotherapy and dosimetric applications. During recent years, GATE has been widely implemented for different studies on the radiation transport field [10, 96, 137, 138]. It has been gaining popularity because of its versatility, its scripting mechanism, powerful visualization, and 3D rendering tools. Ferrer et al. [137] were the first to use GATE for monoenergetic electron dose point kernels simulations

in water using Geant4 4.8.1. In addition, Maigne et al. [138] simulated monoenergetic electrons in water by employing GATEv6.0. Further, Papadimitroulas et al. [10] implemented GATEv6.1 to simulate the beta radionuclides and monoenergetic electrons in water, bone, lung, and soft tissue. As the currently available voxel-wise approaches to radionuclide dosimetry ignore tissue composition and do not account for density heterogeneities, the study on impact of tissue type on dose point kernels is deemed necessary. This motivated us to study the impact of tissue types on dose point kernels for radionuclides that are widely used in nuclear medicine.

In this work, dose point kernels have been simulated with GATE Monte Carlo code for both monoenergetic electrons and beta radionuclides in water, compact bone, blood, red marrow, adipose, and lung. The resulting dose point kernels are in excellent agreement with published data. The maximum discrepancy observed in this work is 7% compared with MCNPX and ETRAN code. The observed discrepancies in the dose point kernels are due to the superposition of multiple factors. The significant contributions are from the following: (i) X_{90} values used in scaling of kernels, (ii) differences in the average energy of the radionuclides in literature, (iii) beta spectra used in the radionuclide simulation, and (iv) different treatment of charged particle transport among MC codes.

The X_{90} value reported by Mainegra-Hing et al. [145] for ^{90}Y does not greatly differ from the value calculated in this work, however, Botta et al. [126] reported a slightly higher value as tabulated in Table 5. In addition, for ^{188}Re , Mainegra-Hing et al. [145] reported a smaller value whereas Botta et al. [126] reported a higher value than the calculated value. Similar discrepancies were observed for all other radionuclide dose kernel simulations.

Differences among Monte Carlo codes are expected due to differences in their treatment of electron transport. The MC codes MCNPX and ETRAN utilize the condensed history algorithm,

and PENELOPE makes use of a mixed simulation algorithm that combines both the detailed and condensed history algorithm. In addition, EGSnrc exploited the Molière multiple scattering model with an exact boundary crossing algorithm and FLUKA code based on the multiple scattering model. However, GATE used in this work incorporates Geant4 source code and employs the revised electron multiple scattering algorithm along with the physics list mechanism; in GATE, a physics list is a mandatory user input.

For the beta radionuclide simulations, all beta energy spectra were obtained from the RADAR website [146]. Only beta spectra were included in radioisotope simulations, which excludes internal conversion electrons, Auger electrons, x-rays and gamma contribution of the radionuclide decay process. Simulation of beta spectra is sufficient to understand the impact of tissue type on dose point kernels. With that said if one wants to use these kernels in clinical dosimetry, they should be supplemented with the missing decay modes.

Results of the beta dose kernels simulations show a discrepancy of 3.0% when comparing with results in literature from FLUKA [126]. This is likely due to inclusion of Auger electrons, conversion electrons, and photons within the FLUKA simulations. In addition, deviation from results obtained by [10] is likely due to the fact they derived the beta spectra from the LBNL database in their study and implemented an earlier version of GATE. The observed discrepancy in this study, compared to GATEv6.1 [10] is less than 2.0%.

In this work, we did not include x-ray generation during charged particle transport. Therefore, the resulting dose point kernels include only the collisional electron stopping power. Based on the elemental composition of tissues, GATE calculates the mean excitation energies. The calculated mean excitation energies for the adipose, red marrow, water, lung, blood, and bone are respectively 61.75 eV, 66.21 eV, 68.99 eV, 69.73 eV, 69.80 eV, and 86.00 eV. Note that these

calculated values differ slightly from values reported in the NIST online database [143]. According to the Bethe-Bloch theory of electron stopping power, the collisional mass stopping power varies linearly with the ratio of atomic number and the mass number (Z/A). The Z_{eff} values of the simulated tissues are; bone (11.87), blood (7.78), lung (7.74), water (7.42), red marrow (7.21), and adipose (6.47) respectively. As the Z_{eff} and the mean excitation energy (I) values do not greatly differ from each other except for the bone, stopping power will have similar values for the same radionuclide. However, for the bone, a slightly larger value of the mean excitation energy serves to counteract the increase in average atomic number yielding dose point kernels that are comparable to water.

Mean percent deviation of tissue-specific kernels compared with water was less than 2% for all comparisons. This result is supported by stopping power theory and suggests that tissue composition heterogeneity is a second-order effect with regard to energy deposition. As expected, tissue density, appears to be a more critical variable that dramatically impacts DPK shapes. Based on this, we feel that water kernels alone can adequately describe energy deposition in tissue from electron-emitting sources as long as density heterogeneity, particularly in the lung and bone, is handled appropriately.

In summary, we report the generation of dose point kernels for medically-relevant radioisotopes in water, compact bone, lung, adipose, blood, and red marrow. The impact of tissue types on dose point kernels has been studied using the GATEv8.1 MC toolkit and also discussed the major contributing factors that result in uncertainties in dose point kernels simulations. Previously unreported kernels that have been generated herein include ^{90}Y , ^{188}Re , ^{32}P , ^{89}Sr , ^{186}Re , ^{153}Sm , and ^{177}Lu , and monoenergetic electrons (0.015-10 MeV) in blood, red marrow, lung, and adipose. The impact of tissue type has been found to be minimal for purposes of dosimetry

suggesting that the use of a single kernel generated in water may be suitable for voxel-wise calculations, provided tissue-specific density corrections are implemented.

However, these are all admittedly theoretically based computations. To have a better comfort-level in the implementation of DPKs for dose calculations in actual human studies, experimental verification would be useful. The following chapter describes methods and results for precision energy deposition measurements designed to experimentally validate the theoretical DPKs presented in this chapter.

5.1. Background

Targeted radionuclide therapy (TRT) is a rapidly developing area in nuclear medicine that is demonstrating paradigm shifting treatment efficacy across a number of cancers [150]. It is becoming increasingly clear that effectiveness of TRT could be substantially enhanced through the implementation of image-based personalized dosimetry, which would allow modulation of treatment doses designed to optimize treatment to tumors, while keeping absorbed doses to critical organs below toxicity thresholds [44, 151]. The dose point kernel (DPK) method has recently gained considerable attention because of its potential to use image-based information for the calculation of absorbed dose in patient-specific targeted radionuclide therapy [152]. Using the radionuclide specific DPKs, one can perform voxel level dose calculations for estimation of critical organ absorbed dose to avoid patient toxicity, or tumor absorbed dose to better estimate efficacy [153]. However, for multiple reasons, this method is not yet routinely implemented in clinical settings [154].

The current gold standard for 3D voxel-wise dosimetry is personalized, patient-specific Monte Carlo calculations using the quantitative nuclear imaging distributions (SPECT or PET) as the input data for the absorbed dose deposition map. Monte Carlo simulations are, however, highly computationally intensive, if one wants to achieve low statistical noise at the voxel level [152, 155]. The DPK method [156] is a more computationally efficient approach and is more typically used in dosimetry software applications, such as MIM, DOSIsoft and Velocity. This method uses pre-calculated, radionuclide- and tissue-specific DPKs and image-based patient specific radionuclide distributions (over time) as input data to generate patient-specific absorbed dose maps. In each of these cases, the pre-tabulated DPKs are also based upon Monte Carlo-based

calculations. To assess a patient's absorbed dose rate, the radionuclide distribution, as determined by imaging, is convolved with the radionuclide specific DPK to achieve a patient specific dose map. DPKs can be defined as energy deposition kernels from point isotropic radioactive sources. DPKs have been generated by many authors analytically as well as using different Monte Carlo codes [10, 11, 50, 125, 157-160].

Over the last few decades, there has been growing interest in the measurement of absorbed doses from internal emitters such as ^{90}Y , ^{177}Lu , ^{111}In , and ^{131}I radionuclides in molecular radiotherapy. First measurement of absorbed dose by beta-emitting radionuclides were performed in 1986 by using miniature thermoluminescent dosimeter (TLD) [161]. TLDs have been used in phantoms for the absorbed dose contribution from gamma radiation in the β^- decay of ^{131}I absorbed dose measurements [162, 163] and ^{111}In gamma absorbed dose [164] where submillimeter resolution is not critical. Polymer gel has also been utilized to test the suitability for ^{131}I absorbed dose measurements [165]. In the last few years, radiochromic film has been used for verification of external beam dosimetric accuracy [166], for IMRT dose verification [167], feasibility of alpha-particle dosimetry [168] and dose calibration for Ir-192 brachytherapy [169]. In addition, radiochromic film has been employed for the measurement of the absolute activity for high-energy beta emitters [170]. The dosimetric approach of using radiochromic film may be suitable for our aim of measuring beta absorbed doses due to its inherently high spatial resolution, minimal absorbed dose-rate and energy independence, and its near tissue equivalence from an atomic composition standpoint.

One fundamental limitation to using this DPK method in clinical dosimetry is that the dose kernels are based upon analytic or numerical calculations, or Monte Carlo simulations of beta absorbed dose deposition, yet, these probabilistic physics-based energy deposition calculations

have not, to date, been experimentally validated. The lack of experimental validation work in the literature is primarily due to the challenge of accurately measuring absorbed dose deposition along the relatively short beta range of therapeutic radionuclides (1 – 10 mm) with sufficient spatial resolution to meaningfully compare with Monte Carlo simulations.

The goal of this work was to validate Monte Carlo-based dosimetry estimates in different tissue types for the commonly used therapeutic radionuclides – ^{90}Y and ^{177}Lu . In this work we describe an innovative technique for high-resolution dosimetry of β^- particles using radiochromic film. The significance of this work is that it will provide direct, experimentally-derived evidence regarding the accuracy of Monte Carlo-based dosimetric calculations and provide a range of experimental uncertainty in radionuclide film-based dosimetry.

5.2. Methodology

Gafchromic EBT3 radiochromic film offers sensitivity in the 0.1–10 Gy dose range [171]. The film is comprised of an active layer, nominally 28 μm thick, sandwiched between two 125 μm polyester substrates. When EBT3 film is exposed to ionizing radiation, it reacts to form a blue colored polymer with absorption maxima at approximately 635 nm [172]. The effective atomic number (Z_{eff}) of the active layer of this film is 7.26, which is close to the Z_{eff} of water (7.42). The spatial resolution is sub-mm when read-out by conventional flatbed scanners [166]. As a self-developing film, EBT3 film requires no post-processing to develop or fix the image. Film handling protocols provided by AAPM Task Group 55 were meticulously followed in this work [173]. Powder-free latex gloves were used while handling film to minimize surface contamination. Light exposure was minimized by handling the films in opaque envelopes before and after exposure. Films were stored in a temperature and humidity-controlled environment. The orientation of films during scanning was held constant for all experimental and calibration films.

5.2.1. Film and Phantom Preparation

Calibration films were prepared by cutting EBT3 film into square pieces of dimension $\sim 3.8 \times 3.8 \text{ cm}^2$ using a guillotine cutter. With this cutting technique, the film layers separate near the cut edges. For our purposes this is acceptable, as we were able to avoid the measurements near the edges. Experimental films used for beta absorbed dose measurements were prepared by laser-cutting square pieces of dimension $4 \times 4 \text{ cm}^2$ with a central hole of diameter 0.88 mm. The central hole was precisely sized to snugly insert the cylindrical line source of diameter 0.84 mm. Laser cutting was performed using a KERN laser cutting system with the following settings: black vector color enabled with the laser speed of 2 inches/second, 10 % power, 7500 Hz frequency, EMF import with $\pm 4\%$, and tool offset of $\pm 3.5\%$. All films used in this work were prepared from a single lot number to mitigate potential changes in film sensitivity. A CNC milling machine was used for the phantom drilling processes with the drill size of 0.88 mm diameter. The same drill size was used for all phantom slabs drilling.

The tissue-equivalent materials used for the phantoms were designed to be larger than the maximum β^- range within each material. Three different tissue-equivalent materials were utilized – low-density polyethylene ($\rho = 0.940 \text{ g/cm}^3$), cortical bone tissue equivalent ($\rho = 1.898 \text{ g/cm}^3$) and lung equivalent material ($\rho = 0.307 \text{ g/cm}^3$). The low-density polyethylene cylindrical disk employed in this work had a thickness and radius of 2 cm. Cortical bone and lung equivalent materials had a thickness of 2 cm and dimensions of $5 \times 5 \text{ cm}^2$. Tissue-equivalent materials (cortical bone, 05750107 - 19F2 -212; lung tissue, 05750111- LG3 -145) were purchased from CIRS (Computerized Imaging Reference Systems, Inc. 2019).

5.2.2. Film Calibration and Scanning Protocol

The same lot number of Gafchromic EBT3 film that were used in the β^- absorbed dose

experiments were separately calibrated using standard techniques. Specifically, the 3.8 x 3.8 cm² square films were irradiated individually by a 6 MV photons beam by using a calibrated linear accelerator (Siemens Oncor). The photons irradiations were performed at a source-to-surface distance (SSD) of 100 cm, with a 10×10 cm² field (defined at the surface), and at a depth of 10 cm in a solid water. Solid water phantom was added below the EBT3 film to provide the necessary back-scatter. The number of monitor units (MU) used during irradiation were 0, 10, 20, 30, 50, 70, 100, 150, 200, 250, 300, 400, 500, 600, 800, 1000, 1400 and 2000 MU. The reference absorbed doses corresponding to these MUs were 0, 0.07, 0.13, 0.20, 0.34, 0.47, 0.67, 1.01, 1.34, 1.68, 2.01, 2.68, 3.35, 4.02, 5.36, 6.70, 9.38 and 13.40 Gy. Optical scanning of calibration films was performed 24 h post-exposure in order to let the polymerization process stabilize and have all films scanned at the same level of post-exposure growth [173]. Films were scanned (Epson 12000XL: 508 dpi, RGB format, 48-bit, TIFF image format, reflective mode, no color corrections) one at a time using a positioning jig with consistent orientation as recommended for radiochromic film dosimetry [174, 175].

Film measurements were fit to a rational function to obtain the calibration curves. Dose-response curves were obtained by using the three-parameter function given by **Equation (8)**,

$$X(D) = \frac{b + D}{a + Dc} \quad (8)$$

where X(D) is the scanner response, D is absorbed dose, and a, b, and c are constants. The fitting parameters a, b, and c are different for different each color channel, which are necessary to convert the film response to the dose map.

5.2.3. Line Source Preparation

Typically, the dose point kernels are calculated using an isotropic point source in a homogeneous media. However, the difficulty of reproducibly creating a point source of known

absolute activity, coupled with the point source having the concentration necessary to achieve linear absorbed doses (0.1-10 Gy) was prohibitive. The line sources consisted of the plastic capillary tube of length 13 ± 0.1 cm, having a 0.42 mm internal diameter with a wall thickness of 0.21 mm. Attenuation in the tubing wall, regardless of how thin, will impact the beta spectra seen by the film, however, the tubing geometry and material was precisely simulated in the Monte Carlo simulations. A 27-gauge syringe needle was used to inject the activity solution in the capillary tube that was sealed at both ends to prevent the leakage during the experiment.

^{90}Y line sources were prepared by dissolving the ^{90}Y -SIR microspheres as described by Lourenco et al [176]. First, a 30 ml 0.03 M Fe^{3+} stock solution in 1.5 M HNO_3 was prepared. The supernatant was removed from a vial of SIR-Spheres leaving a reduced volume of ~ 1 mL. $38 \mu\text{L}$ of the iron stock solution was added. The vial was left for 15 min to allow for binding of Fe^{3+} to sulfonated functional groups. $200 \mu\text{L}$ of H_2O_2 (30 wt%) was then added to the microsphere solution to reach a final concentration of $\sim 6\%$ H_2O_2 . The vial was heated to 80°C for 60 min and was left to cool for 15 min. Subsequently, $30 \mu\text{L}$ Fe^{3+} in 8 M HNO_3 was added to the mixture to reach 1 M HNO_3 in the solution. Sphere digestion was complete, with a final concentration of 316 MBq/ml concentration and was used to fill the line sources, resulting in a final activity in the tube of (0.336 ± 0.015) MBq/cm at the beginning of the experiment.

For ^{177}Lu , a suitable volume of activity was taken from a vial of ^{177}Lu -DOTATATE. An activity concentration of 333 MBq/ml was used to fill the line sources, and the final activity per unit length in the tube was (0.355 ± 0.014) MBq/cm prior to irradiating the films.

5.2.4. Film Exposure

Film was sandwiched between two pieces of phantom material and the line source was placed along the central axis of the phantom (**Figure 21**). Films were exposed for different

durations (10 minutes – 38 hours) to assure that we had films with exposures in the linear dose range of the film 0.1 - 10 Gy at different radii. Experimental films were scanned using identical methods matching that of the calibration films, and images were converted to a dose map for each color channel using the calibration curves. ^{90}Y exposures were performed for 10 minutes to 24 hours in three different tissue types. Experiments with ^{177}Lu were only performed using the lung equivalent material for 6 to 38 hours because of its short range in low-density polyethylene and cortical bone.

5.2.5. Absorbed Dose Calculations

Absorbed dose in films was calculated using the calibration function. The calibration function was inverted, and absorbed doses were calculated using the fitting parameters for different channels. The background reading in beta-exposed films was calculated by comparing the mean optical density against that of three unexposed films. This measured background was subtracted from resultant beta absorbed dose distribution measurements. Origin of the images, i.e., the center of each line source, were picked by using the MATLAB *getpts* function. Coordinates of the origin of these images were obtained by using the weighted mean of set of six different measurements. The 1D absorbed dose distribution was then obtained by using the volume averaging of the pixel values with cumulative bin sizes. The mean value of the absorbed dose deposition on the red and the green channel were used to calculate the beta absorbed dose.

The red channel is usually used to ensure dosimetric quality using a conventional fraction dose because the red channel is more accurate at absorbed doses within 4 Gy than the green channel [177]. However, the red channel is prone to rapid degradation of sensitivity at higher absorbed doses, while degradation of the green channel is slow. In this study, the dual channel method using the red and green channel was used for the beta absorbed dose calculations in the range of 0.1 - 10

Gy.

5.2.6. Sources of uncertainty in measurement of absorbed dose

Clinically, an overall standard uncertainty of <10% is desirable. Therefore, to calculate whether the measured absorbed doses are in a legitimate window, the uncertainty budget in experimental measurement of absorbed doses were analyzed. A complete portrait of primary sources of uncertainty in absorbed dose measurement are provided. Overall uncertainties in absorbed dose were calculated based on the following components:

5.2.6.1. Uncertainty in calibration irradiations and curve fitting parameters

The uncertainty budget due to calibration of the films comprised of the uncertainties in background measurement of the film, scanner/film response, curve fitting parameters and due to the uncertainties in irradiation process during the film calibration. The clinical linac employed for the film calibration had an uncertainty in output within 2% ($k = 1$) of absolute truth [178]. To measure the uncertainties in fitting parameters the equation (8) was used, where the quantity $X(D)$ represents the net optical density. **Equation (8)** can be re-written as,

$$D = \frac{b - aX(D)}{cX(D) - 1} \quad (9)$$

Let us now express the net optical density mathematically as:

$$\begin{aligned} X(D) &= OD_{\text{exposed_film}} - OD_{\text{unexposed_film}} \\ &= \log_{10} \frac{I_{\text{unexp}} - I_{\text{bckg}}}{I_{\text{exp}} - I_{\text{bckg}}} \end{aligned} \quad (10)$$

Now, the uncertainty propagation associated with the net optical density is [179],

$$\sigma_{X(D)} = \frac{1}{\ln 10} \sqrt{\frac{\sigma_{I_{\text{unexp}}}^2 + \sigma_{I_{\text{bckg}}}^2}{(I_{\text{unexp}} - I_{\text{bckg}})^2} + \frac{\sigma_{I_{\text{exp}}}^2 + \sigma_{I_{\text{bckg}}}^2}{(I_{\text{exp}} - I_{\text{bckg}})^2}} \quad (11)$$

where, I_{unexp} is intensity value of unexposed films, I_{exp} is intensity value of exposed films i.e., scanner-read out of exposed films, I_{bckg} is the zero-light transmitted intensity value measured with the opaque piece of film, and $\sigma_{I_{unexp}}$, $\sigma_{I_{exp}}$ and $\sigma_{I_{bckg}}$ are corresponding standard deviations in unexposed, exposed and background intensity measurements. It should be noted that all quantities in **Equations (10)** and **(11)** were calculated over the same ROI drawn on the film. For simplicity, cross-correlations between fit parameters and the uncertainty on measured optical density were ignored. A simple expression for uncertainty propagation can now be written as:

$$\sigma_y^2 = \sum_i \left(\frac{\partial y}{\partial x_i} \right)^2 \sigma_{x_i}^2 \quad (12)$$

where, $i = a, b, c$ for three fitting parameters and σ_{x_i} represents the uncertainties in fitting parameters. After calculating the partial derivatives of each term using the **Equation (8)** and substituting in **Equation (12)** we can get the variance in absorbed dose:

$$\sigma_{D_{fitting}}^2 = \frac{X(D)^2}{(c X(D) - 1)^2} \sigma_a^2 + \frac{1}{(c X(D) - 1)^2} \sigma_b^2 + \frac{X(D)^2 (b - a X(D))^2}{(c X(D) - 1)^2} \sigma_c^2$$

Therefore, the total absorbed dose uncertainty due to curve fitting becomes,

$$\sigma_{D_{fitting}} = \sqrt{\frac{X(D)^2 \sigma_a^2 + \sigma_b^2 + X(D)^2 (b - a X(D))^2 \sigma_c^2}{(c X(D) - 1)^2}} \quad (13)$$

5.2.6.2. Uncertainty propagation in experimental irradiations

Uncertainty in exposure time and film irradiation contributes the uncertainties propagation in experimental irradiations. Exposure time uncertainties were minimized by quick changing and loading a new film after exposure and clock was used to keep record of the exposures. For (4-38) hours of exposure, exposure time had a maximum permissible uncertainty of ± 2 minutes. Films take out after the exposure and loading a new film are accounted by the uncertainty in the film

exposure. Absolute propagated uncertainty in absorbed dose (D) can be calculated by taking the derivative both sides in **Equation (8)** with respect to X(D) and simplifying, we get,

$$\frac{dD}{dX(D)} = \frac{-bc}{(cX(D) - 1)^2} + \frac{a}{(cX(D) - 1)^2} = \frac{a - bc}{(cX(D) - 1)^2} \quad (14)$$

Therefore, uncertainty in measured absorbed dose given by equation (8) is,

$$\sigma_{D_{exp}} = \sigma_{X(D)} \left| \frac{a - bc}{(cX(D) - 1)^2} \right| \quad (15)$$

where, $\sigma_{X(D)}$ is the uncertainties in net optical density.

5.2.6.3. Uncertainty propagation in activity concentration measurement

A Dose calibrator was used to measure the activity of ^{90}Y and ^{177}Lu sources. Activity measurements were assigned an uncertainty of ~5%. First, the source vial was weighed, and the activity was transferred to the syringe. The vial was re-weighed to calculate the mass difference to determine volume. The residual vial activity was re-assayed to calculate the activity difference. The activity and volume data were utilized to calculate the activity concentration. Uncertainties in concentration associated with activities and volumes were propagated in quadrature.

5.2.6.4. Monte Carlo Simulation and Experimental Setup

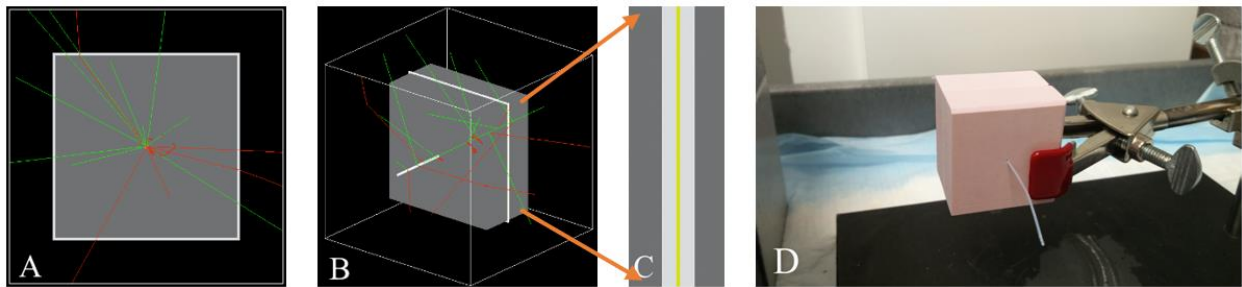


Figure 21: (A-C) GATE Monte Carlo simulation set-up with the line source and EBT3 film and (D) experimental setup.

Experimental irradiations, including the exact phantom geometry with the Gafchromic film, were simulated in the Monte Carlo platform to determine the energy deposition by the beta

decay of radionuclides. All layers of the film were simulated using the density and atomic compositions of the film active layer and matte-polyester layer available in the Appendix of our published paper [2]. GATE is the Monte Carlo simulation toolkit which encapsulates the GEANT4 libraries [53]. In this work, GATE version 8.1 was used for all simulations. The Geant4 “ion” source was used to generate the β^- decay spectrum of ^{90}Y . For ^{177}Lu , the beta spectrum including the conversion electrons were simulated using the spectra from MIRD data [180]. Using the ion source of ^{90}Y , ~1 million events were simulated in 1 hour, while using ^{177}Lu spectrum source, ~2.4 million events were simulated. Absorbed dose deposition was tabulated in cylindrical concentric shells with height of voxel size in the longitudinal axis around a line source at fixed radial distances. The thickness of the tally shells was made to be equal to the voxel size (0.05 mm) of the 3D simulation matrix. The origin of the polar coordinate system (r, θ) was positioned at the center of the experimental films. The electromagnetic (EM) constructor called *emstandard_opt3* was implemented for the physics list within GATE. This EM constructor is useful for applications that require higher accuracy of electrons, hadrons, and ion tracking [52]. In GATE, *doseActor* was used to calculate the energy deposition. The deposited energy *EDep* was scored at the voxel level, and associated uncertainties were calculated in each voxel with the *doseActor* Uncertainty *EDep* [96].

5.2.6.5. Quantification of absorbed dose distributions: the gamma index test

To quantify the observed level of agreement between the measured and simulated absorbed dose distributions, the γ -index dose comparison method was implemented [181, 182]. Instead of using the dose difference (DD) and distance-to-agreement (DTA) criteria separately, this method combines both metrics into a single γ -index. In this work, the dose-difference distribution was computed, point-by-point to co-locate the measured absorbed dose distribution and the simulated

distribution. To perform this gamma function test, the absorbed dose and distance criteria were fixed using preselected values. In practice, the values can be set as functions of space or absorbed dose value. In this work, an acceptable tolerance of 10% as a dose-difference (ΔD) and 1mm distance-to-agreement (Δd) criterion was set. The selection of gamma criteria was based on the measurement uncertainty, and beta particles range in different tissues under consideration. However, the DTA of 1 mm is not quite adequate for comparison of ^{177}Lu emitted beta absorbed dose distribution because of its small range, but it is best from a measurement perspective. Using this method points with $\gamma < 1$ are defined as passing preset tolerances and vice versa. The gamma index at a point r_s is defined by **Equation (16)**:

$$\gamma(r_s) = \min(\Gamma(r_s, r_m)) \forall \{r_m\} \quad (16)$$

where,

$$\Gamma(r_s, r_m) = \sqrt{\frac{\delta^2(r_s, r_m)}{\Delta D^2} + \frac{r^2(r_s, r_m)}{\Delta d^2}} \quad (17)$$

where $\delta(r_s, r_m)$ is the dose difference between simulated and measured absorbed doses at point r , ΔD is the dose difference criterion, $r(r_s, r_m)$ is euclidean distance between simulated and measured absorbed dose points, and Δd is the distance-to-agreement criterion. The gamma index method implemented in this work used the local gamma normalization where the ΔD is normalized to the local maximum value.

5.3. Results

5.3.1. Film Calibration

The scanned calibration films (**Figure 22**) were decomposed into red, green, and blue channels for data analysis. For each calibration film, an ROI of 5 x 5 mm² in the center of the film was analyzed to determine the mean pixel value vs. the delivered dose. Calibration was performed

for each color channel separately. The fitting function given by **Equation (8)** was found to best fit the calibration data, showing an R^2 coefficient > 0.999 for all three channels with the expected absorbed dose. Uncertainties in fitting parameters were found to be less for the red channel at $(2.20 \pm 1.02) \%$, whereas errors were comparable for the green and blue channel at $(4.32 \pm 1.28) \%$.

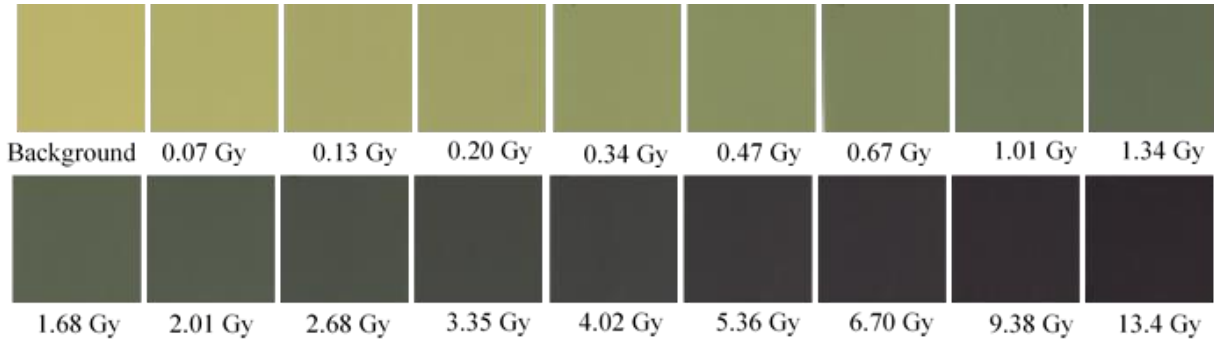


Figure 22: Scanned images of calibration films irradiated with 6 MV photon beams.

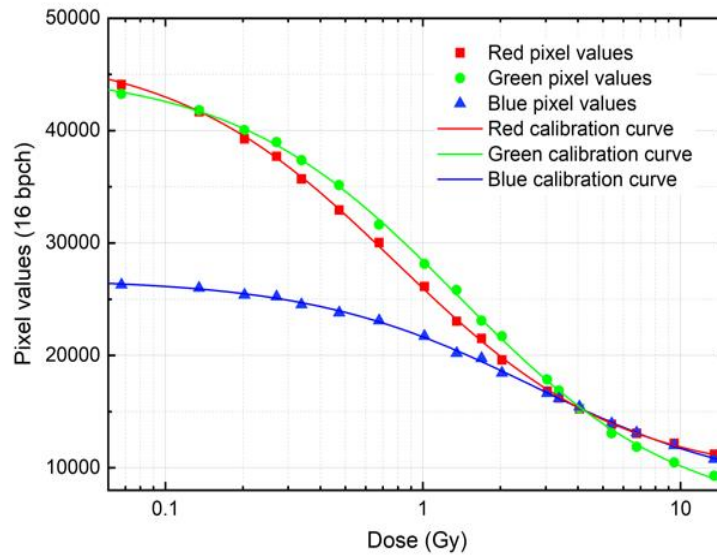


Figure 23: Sensitometric response curves for the red, green, and blue channels of scanned EBT3 film irradiated by 6MV photons to absorbed dose from 0 to 13.4 Gy using the Equation (8).

The correlation between the intensity of the three-color channels RGB of the scanned image and the absorbed dose represents the calibration curve. Pixel values were plotted as a function of absorbed dose and fitted by a rational function defined by **Equation (8)**. The calibration

curves are shown in **Figure 23**. Clearly the dynamic range of the film was observed in the calibration curve. The red and green channels exhibited the highest sensitivity, i.e., the net optical density per unit dose, whereas the blue color channel was found to be least sensitive in terms of dose-response. Consequently, the blue channel dose was excluded in all calculations throughout the analysis. The average uncertainty in absorbed dose was $(2.80 \pm 0.52) \%$, $(3.62 \pm 1.26) \%$, $(4.91 \pm 1.51) \%$ for the red, green, and blue channels, respectively. The dual (red and green) channel dosimetry algorithm was implemented in an in-house MATLAB R2016a code. Uncertainties due to the curve fitting process were $(2.20 \pm 0.86) \%$, $(3.61 \pm 1.27) \%$, and $(4.22 \pm 1.58) \%$, for red, green, and blue channels, respectively.

5.3.2. Experimental films exposure with line sources: experiment

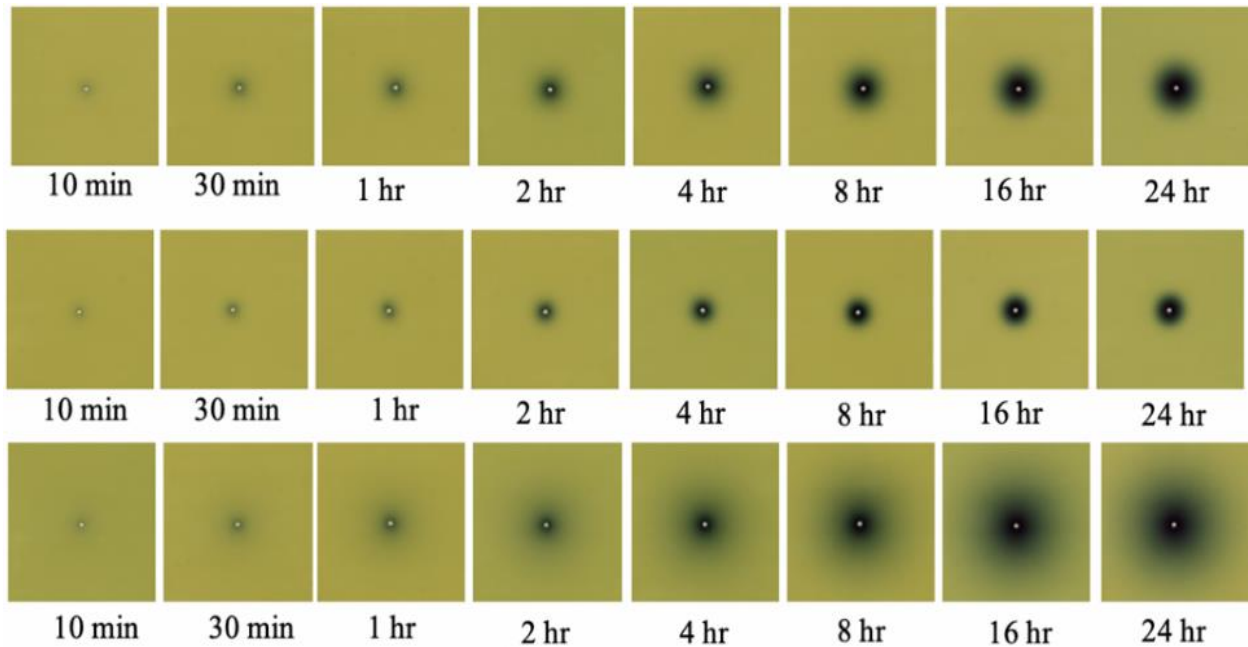


Figure 24: Scanned images of the ^{90}Y exposed experimental films in low-density polyethylene (first row), cortical bone (second row), and lung equivalent (third row) phantom material.

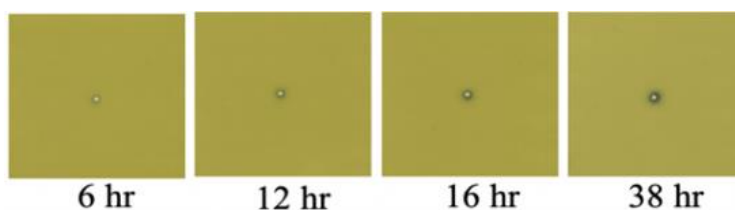


Figure 25: Scanned images of the ^{177}Lu exposed experimental films in lung equivalent phantom material.

Three sets of 8 EBT3 experimental films were exposed to ^{90}Y line source with exposures of 10, 30 minutes, 1, 2, 4, 8, 16, and 24 hours using the low-density polyethylene, cortical bone and lung equivalent phantoms. Using ^{177}Lu , films were exposed only in lung equivalent slabs with exposure times of 6, 12, 16 and 38 hours.

5.3.3. Absorbed dose uncertainty estimates

Table 7: Various uncertainty components in the experimental work to absorbed dose measurements.

Uncertainties source	Calculated uncertainties	Evaluation\comments
Optical density measurements	0.78%, 0.80% and 1.12%	Uncertainties in red and green channels and combined uncertainty
Exposure time: (4-38) hours	<1.00%	Clock was used to keep record of exposures
Activity measurements	5.82%	Combined uncertainty of activity concentration and dose calibrator uncertainty
Curve fitting	2.20%, 3.61% and 4.22%	Uncertainties in red and green channels calculated and combined uncertainty
Measurement of absorbed dose	4.56%	Combined uncertainty resulted from the red and green channels
Overall uncertainty	8.64%	Combined uncertainty from all individual components

The primary components of uncertainty in an absorbed dose measurement has been examined. The total uncertainties in optical densities for red, green, and blue channels were $(0.78 \pm 0.62) \%$, $(0.80 \pm 0.73) \%$, and $(0.94 \pm 0.76) \%$ respectively. For the absorbed dose measurements using the red and green channel at absorbed doses ranging from (0 - 10) Gy, a combined total

uncertainty of (4.56 ± 1.35) % was obtained, but the red channel exhibited a lower total uncertainty of (2.80 ± 0.52) %. The experimental uncertainties were comparable to the combined uncertainty arising due to the fitting process. Uncertainties propagated in calibration and experimental procedures are summarized in **Table 7**.

5.3.4. Experiment vs. Monte Carlo simulations

We were able to measure the absorbed dose in the range of (0.1-10) Gy as a function of radial distances using discrete radial measurements every 0.05mm, as shown in plots presented in **Figure 26**. Although we irradiated the films for eight different exposure times, only plots belonging to the absorbed dose values that lie in the dynamic range of the film in each tissue type are presented in **Figure 26**. Above the 16-hours exposure, the beta absorbed dose was saturated and below 4 hours, the absorbed dose was below 0.1 Gy, and therefore not in the linear range of the film. These plots are sufficient to obtain a qualitative assessment of the dose linearity and the absorbed doses in the sensitive region of the EBT3 film. Monte Carlo simulations were performed using the experimental exposure durations as explained in **section 5.2.6.4**. Higher discrepancies were observed proximal to the line source due to the film delamination around the laser-drilled hole, so these data were excluded from the analysis. The average statistical uncertainties in all simulations were less than 4.5% for the absorbed dose range of (0.1–10) Gy. For the beta absorbed dose, the mean point-to-point absolute percentage difference between the MC results and experimental measurements was 5.04% using ^{90}Y and 7.21% when using the ^{177}Lu line sources. The percentage difference was calculated down to an absorbed dose value of 0.1 Gy for all exposures, which is the lowest sensitive region of the EBT3 film. Higher deviations were observed for the region that is close to the film and line-source interface, and the lower dose regions, especially close to 0.1 Gy. These disagreements in the lower dose region between the experiment

and Monte Carlo simulations are due to the lower signal to noise ratio. The density and atomic composition of the tissue equivalent slabs are needed to reproduce Monte Carlo results described herein, and thus we have included these values in Appendix of our published paper [2].

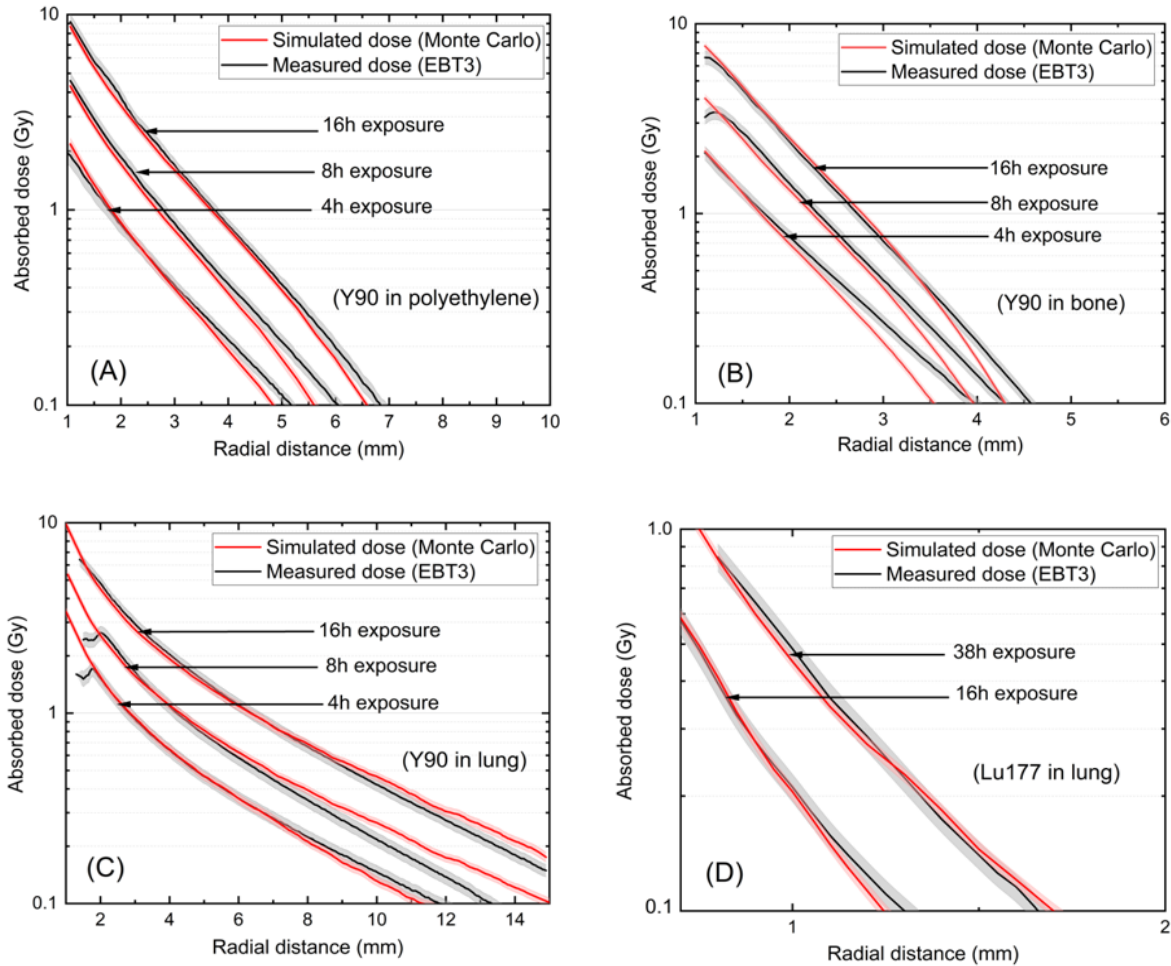


Figure 26: (A-C) Experimental vs. Monte Carlo absorbed dose measurements of ^{90}Y in polyethylene, cortical bone and lung equivalent phantoms and (D) ^{177}Lu in lung equivalent phantom for different exposure times. The shaded area corresponds to error bars in simulated and measured absorbed doses. Significant disagreement at small radii is due to delamination of films at the line-source interface.

The ^{90}Y irradiations, as presented in **Figure 26(A-C)** give the β^- absorbed dose as a function of radial distances for different exposure times. The measured absorbed dose shown in **Figure 26(A-C)** is the sum of beta and bremsstrahlung component of absorbed doses. As the bremsstrahlung photon range is substantially longer than the size of our phantom, the experimental

geometry used in this work does not include all the bremsstrahlung doses beyond the size of the phantom. It should be noted that the range of the ^{90}Y emitted beta particles in lung is ~ 35 mm. The geometry of the lung phantom used in this experiment therefore could not have deposited all emitted energies. However, as the goal was to measure the deposited absorbed dose in the range of (0.1 -10) Gy (linear range of the film) and for this dose range, the lung phantom geometry was sufficient. The 0.1 Gy lower limit is well-within the boundaries of the phantom size used. The GATE Monte Carlo simulations of the experimental geometry with a larger phantom radius were performed to separate the beta and bremsstrahlung doses, as shown in **Figure 27**. The Monte Carlo simulation show that a radial distance of 10 mm in low-density polyethylene is sufficient to account for the entirety of the pure beta absorbed doses. The beta dose function is higher than that of the bremsstrahlung dose by more than three orders of magnitude at 1 mm in low-density polyethylene. As the distances increase, this ratio decreases to near unity, however, as one approaches to 10 mm. The bremsstrahlung dose predominates beyond the cut-off of the beta dose component showing its importance to tissues in this distance interval. As the ratio of the bremsstrahlung dose and beta dose close to the origin is negligible, the experimental bremsstrahlung dose scored in **Figure 26(A-C)** is insignificant for the purposes of absorbed dose validation.

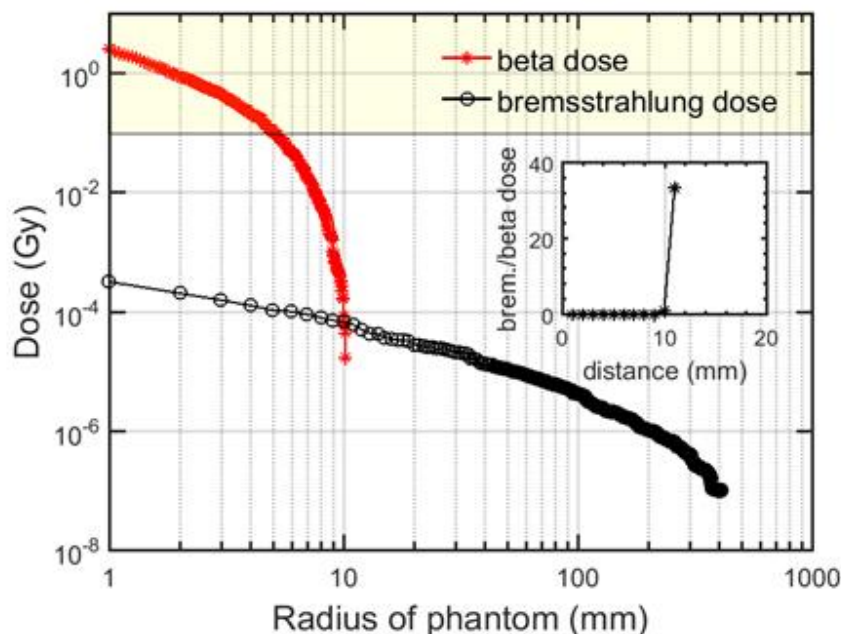


Figure 27: Monte Carlo simulation of absorbed dose distribution from beta and bremsstrahlung radiation of the decay scheme of ^{90}Y as a function of distance from a line source of activity 5.18 MBq in a plastic cylinder of wall thickness of 0.21 mm and internal diameter of 0.42 mm using the same line source and similar Monte Carlo setup but with the larger low-density polyethylene geometry of radius of 42 cm. Acquisition time in simulation was 4 hr. The voxel size used for betas simulation was 0.05 mm, whereas for bremsstrahlung simulation was 1 mm. The yellowish shaded region in the plot represents the sensitive region of the EBT3 film.

The emission of moderate-energy beta β^- particles from the ^{177}Lu decay as well as low-energy gamma photons results in a relatively low absorbed dose as shown in measured dose data in **Figure 26(D)**. However, only beta absorbed doses were included in the small phantom volume in the Monte Carlo measurement. Comparison between the two is valid, however, because the photonic contribution of the decay can be ignored, since the photon contribution to absorbed dose is typically $>1000\text{X}$ smaller than the beta dose in the small geometry of the phantom.

From **Figure 26**, it is evident that the results are in close conformance with the GATE Monte Carlo simulation results. The average difference between measured data using the EBT3 film and MC simulation is observed to be below 6%. Several factors including lack of uniform

exposure to the calibration film during the photon irradiation, film drilling artifacts, phantom drilling process, scanner artifacts, the probability of film scratches during the experiment (measurement noise), and noise in Monte Carlo simulations might cause errors in the spatial dose shifts between two distributions.

5.3.5. Comparison of measured and simulated dose distributions

The 1D local gamma evaluation was performed to compare the simulated and measured beta dose distributions using **Equation (16)**. The Gamma index was calculated in absolute dose values using 10%/1mm gamma evaluation criteria for each material type. The gamma calculation search radius was set to the value where absorbed dose was 0.1 Gy.

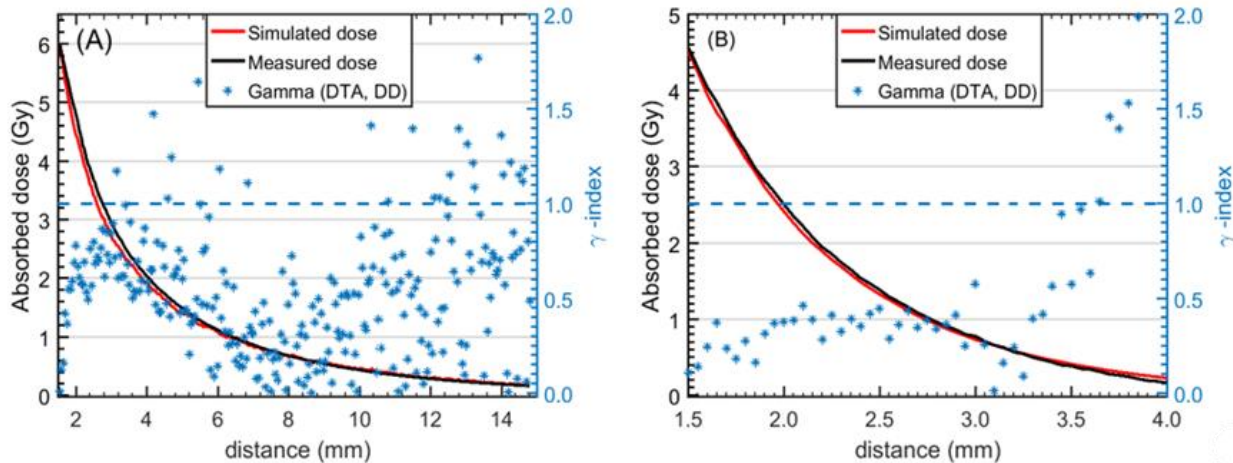


Figure 28: 1D gamma analysis calculations for ^{90}Y simulation and experimental absorbed dose comparisons in (A) lung and (B) cortical bone for 16-hour exposures. The dashed line in plot is the boundary of the pass-fail region.

First, 16-hour exposure data using ^{90}Y sources in lung tissue up to radial distances of 1.5-15 mm was analyzed. The maximum value of γ was 1.75, corresponding to the maximum value of the dose difference (12.7%). The average value of γ in higher dose gradient region 1.5-5 mm was 0.65. Percentage of points passing the 10%/1 mm gamma criterion in 1.5-5 mm region was

94.36%, while in the region 5-15 mm the passing percentage was 90%. The average passing rate was 94.0%. The γ - index and the measured and simulated absorbed doses are presented in **Figure 28**.

In addition, 16-hour exposure in cortical bone up to a distance of 4 mm from the line source was analyzed. Up to the distance of 3.5 mm, all comparison points passed the gamma test, and beyond 3.5 mm, calculation points failed the test as can be seen in **Figure 28(B)**. The maximum value of gamma in 3.5-4 mm distance corresponds to the maximum dose difference (14.5%). The percentage of points passing the 10%/1 mm gamma criterion in 1.5-3.5 mm region is 100%, while in the region (1.5-4) mm average passing rate is 90.9%, which is as expected. For ^{90}Y in polyethylene, using 4-hour exposure time the gamma passing rate calculated was 95.5%, up to a distance of 4.5 mm. Furthermore, for ^{177}Lu in lung using the 38-hour exposure time, gamma passing rate was 92.3 %, up to the radius of 2 mm.

In summary, the gamma passing rate for ^{90}Y in low-density polyethylene, cortical bone, and lung were 95.5%, 90.9% and 94.0% respectively. Additionally, the gamma passing rate for ^{177}Lu in lung was 93.6%. The percentage of points satisfying the constraint $\gamma < 1$ shows a minimal difference between different tissue types. Overall, the percentage of points passing the preset tolerances of 10%/1 mm in absorbed dose, averaged over all tests was 93.5%. The 1D gamma index analysis suggests that the measured dose distribution is in close agreement with the simulated dose distribution. These results compare favorably with the gamma passing rates in IMRT, where passing rates are typically around ~ 95%, using the standard gamma criteria of 3%/3mm.

5.4. Discussion and Conclusions

Radionuclides such as ^{90}Y , and ^{177}Lu are being increasingly used in targeted radionuclide therapies. Internal emitter dosimetry has been an area of growing importance in targeted radionuclide therapy, due to the potential to improve therapeutic outcomes under a dosimetry-guided treatment paradigm. Various methods are available to calculate the absorbed dose distributions. In patient-specific dosimetry, the DPKs are gaining popularity and are implemented in 3D image-based dosimetry.

The analytic or discretized radionuclide-specific DPKs convolved with the activity map of the organ of the patient and combined with density information from the CT scan can result in quantitative dose rate distributions. Extensive tabulations of the dose point kernels in water, and tissue-specific kernels are also available [8-11, 50, 160]. However, only a few dose distributions have been validated experimentally, and up until now the beta radiation dose distributions have been excluded from validation experiments [162-164]. In this work, we experimentally measured the ^{90}Y beta absorbed doses in low-density polyethylene, cortical bone, lung, and ^{177}Lu doses in lung using radiochromic film and tissue-equivalent phantoms. Measured absorbed doses using the film were assessed by comparing to the corresponding Monte Carlo simulations.

Radiochromic EBT3 film appears to be appropriate for the measurement of beta absorbed doses in this experiment because of its minimal absorbed dose rate ($\sim 1\%$) [167, 183] and energy dependency [184-186]. Studies suggest that the film energy response changes are reasonably constant ($\sim 1\%$) between 100 keV and 10 MeV. Below 100 keV, the film response can vary substantially as a function of energy (20-30) % [184, 185]. The almost uniform energy dependence suggests that the EBT3 film can be calibrated using a 6 MV photon beam and used for quantitative measurements of absorbed dose in mixed photon and electron radiation fields in energy ranges relevant to this work.

In this work, only beta absorbed dose from ^{90}Y and ^{177}Lu were considered. The choice to investigate ^{90}Y was made for two reasons: (1) is its relatively common usage in radionuclide therapy, and (2) it has a relatively long range in soft tissues and bone. Furthermore, ^{90}Y is almost pure β -emitter, the very low abundance of γ emissions (<0.01%) combined with the low contribution to absorbed dose by bremsstrahlung interactions of the β^- emissions as explained in section 3.3 avoids significant gamma contribution to the measurement. For ^{177}Lu , approximately 17% of the decays involve the emission of low-energy gamma photons [$E_\gamma = 113$ keV (6.23 %) and 208 keV (10.41 %)] in addition to the betas with an $E_{\beta(\text{max})}$ of 496.8 keV (79.44 %), 383.9 keV (8.89%), and 175.5 keV (11.66%) [187], which may slightly increase absorbed dose within the range of beta energy deposition. For the phantom radius of 2 mm, the ^{177}Lu photons are expected to contribute approximately ~1% to the overall energy deposition [11]. Our decision to measure absorbed dose from ^{177}Lu in only the lung-equivalent material was due to the longer range of betas in lung (~ 8 mm) compared to other tissue-equivalent materials.

Advantages of the proposed method with respect to state of the art are severalfold. Firstly, this experiment with EBT3 film can be used to perform high-resolution dosimetry of β^- particles of few other beta-emitting radionuclides with end-point ranges of approximately > 5 mm. Additionally, our results indicate that EBT3 film could be effectively used to obtain experimental 2D absorbed dose measurements within activity-filled phantoms. The dynamic range of the Gafchromic EBT3 film is 0.1 – 10 Gy [188], and the dynamic range of LiF-based microcube TLDs of dimension 1 mm³ is 10 μGy – 1 Gy [189]. Therefore, one could also use the TLDs to measure the beta absorbed doses in certain radial distances. However, one cannot perform the high-resolution dosimetry of β^- particles using the microcube TLDs as they are dimensionally larger than, for example, the beta range of ^{177}Lu . In addition, microcube TLDs pose experimental

limitations relating to phantom construction, accurate positioning of the dosimeter, and air/phantom interfaces, thus potentially limiting the measurement accuracy and inter-investigator agreement. Many isotopes such as ^{177}Lu and ^{131}I have significant gamma emissions that contribute to absorbed dose. Therefore, a combination of film and TLDs in larger phantoms may be appropriate to characterize these dosimetric components.

Although laser cutting parameters were optimized to minimize de-lamination near the line source, the first 1-2 mm of radius was still impacted by delamination. This limitation of the measurement technique made it challenging to accurately measure beta absorbed dose deposition from ^{177}Lu , which has a much smaller maximum beta range. Differences between the experimental absorbed dose and simulated dose in the film was primarily attributed to the curve fitting process, activity measurements and the experimental irradiations. Several other reasons such as the difficulty in precisely locating the origin of the film, laser film drilling artifacts, noise on the films during the experiment setup, and statistical errors in Monte Carlo simulations additionally contributed a small portion. It is important to highlight that the selection of the origin of experimental films has a large influence on the result. During the data analysis, the origin was selected using the MATLAB *getpts* function. This function lets the user manually select points within the image. The final origin position within all films was determined by using the mean of six different measurements. The estimated precision of this approach, as estimated by inter-measurement variability, was ± 0.03 mm.

Our validation experiments have shown that it is feasible to measure the beta absorbed dose experimentally using radiochromic film-based dosimetry. Good agreement was observed between measured absorbed dose distributions and Monte Carlo simulations for all isotopes and phantom materials. This result (1) provides experimental evidence regarding the accuracy of existing Monte

Carlo codes and (2) provides an upper bound on the systematic error from Monte Carlo calculations in the context of radionuclide dosimetry.

In summary, we have presented a novel, inexpensive, and high-resolution experimental method for validation of beta decay dosimetry. Good agreement was observed between the experimental beta absorbed doses compared with the GATE Monte Carlo simulations for line sources of radioactivity in tissue-equivalent materials. Future work will expand these absorbed dose validation methods to other radionuclides and measurement geometries that include gamma dose contributions at larger radii.

6.1. Introduction

Alpha-emitting radionuclides have been of great interest in nuclear medicine due to their suitable physical properties for eradicating small volume lesions or to treat minimal residual disease to prevent recurrence or progression. Therapeutic α -radiation carries energies in excess of several MeV, and its associated high linear energy transfer (LET) leads to highly effective cell killing via DNA double-strand break, which is largely independent of cell cycle and oxygenation status [34, 190]. Targeted alpha therapy (TAT) is the most rapidly developing option for cancer treatment in the TRT space [191]. The only FDA-approved drug for TAT is Xofigo (radium-223 chloride) and has demonstrated the clinical feasibility of alpha-based therapy with increasing degrees of success [192-195]. Currently there are a number of clinical trials in the NCI intramural program that investigate the therapeutic benefit of radionuclides such as ^{225}Ac , ^{227}Th , ^{224}Ra , ^{212}Pb , and ^{211}At in a variety of malignancies including prostate cancer, neuroendocrine tumors, and hepatocellular carcinoma [196-198]. One additional factor that enhances the potential for cancer cell killing is that most of these alpha emitting radionuclides initiate a decay chain with several additional high-energy alphas being emitted within seconds to minutes of the initial decay.

There is a growing interest in developing methods to calculate the patient-specific internal absorbed dose distributions undergoing cancer therapy with radiopharmaceuticals. Current research shows that the dosimetry post radionuclide therapy enables us to personalize the radiopharmaceutical injected dose to the patient. The most accurate technique for performing the dosimetry is by utilizing voxel-wise dosimetry using dose point kernels. Our previous work investigated the impact of tissue types on dose point kernels (DPKs) for β -emitting radionuclides, and we observed that tissue-specific density-based scaling is sufficient for β -dosimetry [1, 50].

Besides the β - and γ -emitters, the study on dosimetric aspects of therapeutic α -emitting radionuclides is also necessary as it deposits the much larger absorbed dose compared to β - and γ -emitters. Recently, Khan et al. studied a few α -emitting radionuclides such as ^{227}Th , ^{225}Ac , and ^{223}Ra using Geant4 simulation [199]. Graves et al. simulated a large database of radionuclides, but their work ignored the α -particle emissions because of its short-range compared to β 's and γ 's [11]. The first aim of this work was to provide a comprehensive study on α -emitting radionuclides for the purposes of its (1) micro-dosimetric calculations for dose point kernels generation and (2) to study their Bragg peaks. The scale of alpha particle ranges functionally precludes DPK implementation on nuclear imaging (very simple local deposition techniques will likely succeed), but implementation on a micro/cellular scale may lead to meaningful insight.

To accomplish this aim, Monte Carlo simulations were performed in this study to simulate simple decay schemes of mono-energetic α -radiations (3-9) MeV and a complex decay scheme of therapeutic α -emitting radionuclides ^{227}Th , ^{227}Ac , ^{223}Ra , ^{224}Ra , ^{212}Pb , ^{211}At , ^{212}Bi , and ^{213}Bi in several tissue types to generate its DPKs. In addition, this study also investigates the correlation between the number of Bragg peaks and the number of α -particles emitted from the full decay chain of these radionuclides. The choice to simulate these clinically relevant therapeutic α -emitters is motivated by the fact that many relevant radionuclides do not currently have complete DPKs in literature.

There has been a significant interest in Fibroblast Activation Protein (FAP), which is highly expressed in cancer-associated fibroblasts (CAFs) of the tumor stroma [200, 201]. Recent studies have demonstrated that CAFs have emerged as important regulators of the anti-tumor immune response. Literature suggests that these cells are present in high density at the invasive front of the tumor stroma and have lower expression in the tumor center [202, 203]. The possibility of

radiotherapeutic FAP-targeting compounds is being actively investigated. The unique situation where FAP radiotherapeutics target not cancer cells themselves, but CAFs distributed in and around the macroscopic tumor mass, it begs the question as to whether relatively short-range alpha-emitting radioisotopes are an appropriate therapeutic tool. The second aim of this work was to use the kernels generated in this work to assess the potential of therapeutic α -emitting radionuclides to be used in FAP-targeted compounds. This was achieved by using the histological slides showing FAP expression and α -dose point kernels.

6.2. Materials and Methods

The geometry of simulations consisted of a spherical homogeneous phantom with a point source centered at the origin. The radius of the phantom was set based on the simulated ranges of α -particles in tissues. Choice of tissues was made based on our previous simulation work using β -emitting radionuclides [1, 50]. Monte Carlo modeling of radiation transport was performed using the GATE Monte Carlo simulation toolkit (v 9.0) [51, 53, 96]. The coupled transport of charged particles and photons were evaluated for α -emitting radionuclides to simulate the range of α -particles in several tissues and their DPKs. The production cuts of 1 mm were set in the simulation, and the step-limiters of 1 μm were set for α - and electrons in the phantom volume. The particle energy losses were tallied with the complete decay spectra of each radionuclide, including daughters in various α -decay schemes, using the *DoseActor* in GATE. The mean absorbed dose in voxels was computed by averaging the deposited energy in all voxels and dividing by the total mass of the voxel. The mean average radial absorbed dose (Gy) was computed by averaging the absorbed dose in all voxels at each 1 μm interval. It is important to note that we are primarily divorcing this work from nuclear imaging voxels and are migrating toward theoretical voxels much smaller than even individual cells.

In all simulations, the *EmStandard_opt4* electromagnetic physics list was simulated with enabling the *RadioactiveDecay* process to ensure the full decay chain and its associated emission. In addition, *FTFP_BERT_EMZ* physics lists were added, and the atomic deexcitation was included, and subsequently, fluorescence x-rays, Auger cascade emissions, and particle-induced x-ray emissions (PIXE) were turned on in all simulations performed herein. Fifty million decays were simulated in all simulations. This number of decays was chosen because preliminary commissioning of the simulation showed that this number is sufficient to obtain good statistics. A total of 90 simulations were performed. Statistical uncertainties were less than 1% for all 1 μm voxels.

6.2.1. Dose Point Kernels

The DPKs are scaled using the density of tissues, range of alpha particles in different tissues, and average energy of alphas from the radioactive decay as given by **Equation (18)**:

$$J\left(\frac{r}{R_\alpha}\right) = 4\pi \times r^2 \times \rho \times D(r) \times \left(\frac{R_\alpha}{E_{ave}}\right) \quad (18)$$

where, J is the DPK as a function of the scaled distance, R_α is the range of alpha particles, $D(r)$ is the absorbed dose per decay, r is the radial distance from the point source, ρ is the density of the tissue, and E_{ave} is the average α -particle energy released initially during the decay chain. The scaled DPKs represented by J in **Equation (18)** is a dimensionless quantity. The R_α used in **Equation (18)** was estimated from the simulation itself.

6.2.2. Monoenergetic α -particles simulations

α -Particles with monoenergetic energies of (3 – 9) MeV were simulated in different tissues. Tissues such as water, adipose, blood, red marrow, lung, and compact bone were used. The densities and elemental compositions of these tissues were taken from our previous work [1].

Mono-energy α -DPKs were obtained by scaling the radial distance and dose point kernels by the range of α 's at the Bragg peak by using the **Equation (18)**.

6.2.3. Simulations of α -emitting radionuclides

Included in this part were eight therapeutic α -emitting radionuclides summarized in **Table 8**. Data tabulated in **Table 8** were taken from NuDat 2.8 database [204]. The energy deposition in several tissue phantoms were tallied based on the full radioactive decay of these radionuclides including their progenies or descendants. A full radioactive decay chain was simulated for all radionuclides. By Default, GATE follows the complete decay chain until isotope stability. GATE simulates the whole decay chain in one event. A simplified decay chain of ^{225}Ac and ^{213}Bi is shown in **Figure 29**.

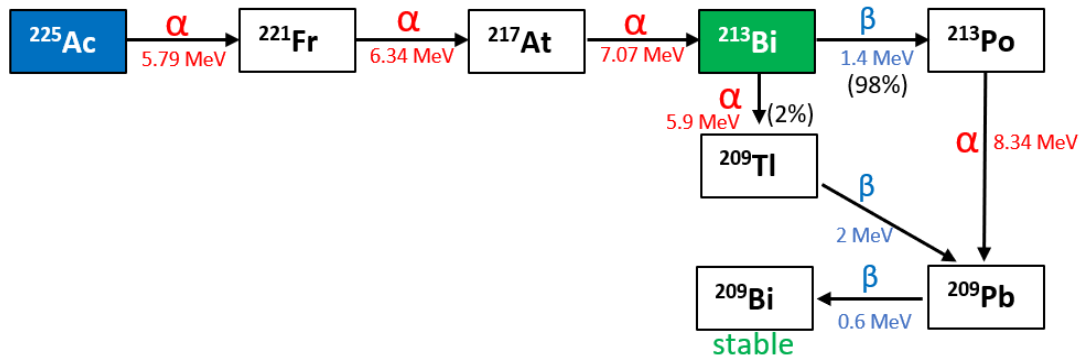


Figure 29: Simplified decay chains of ^{225}Ac and ^{213}Bi radionuclides.

Table 8: Summary of radionuclides simulated in this work. Full decay chain was simulated for all radionuclides.

	Radionuclide	Half life	Max. α energy (MeV)	Emissions per decay	Branching ratio (α)
1	^{227}Th	18.68 d	6.146	$5\alpha, 2\beta$	100%
2	^{224}Ra	3.66 d	5.788	$5\alpha, 2\beta$	100%
3	^{223}Ra	11.43 d	5.979	$4\alpha, 2\beta$	100%
4	^{225}Ac	10.0 d	5.935	$4\alpha, 2\beta$	100%
5	^{211}At	7.214 d	5.982, 0.785	$1\alpha, 1EC$	41.80%, 58.20%

6	^{212}Pb	10.622 h	6.0, 8.8	$1\alpha, 2\beta$	36%
7	^{212}Bi	1 h	6.10	$1\alpha, 1\beta$	36%
8	^{213}Bi	46 m	8.34	$1\alpha, 2\beta$	2%

6.2.4. Application of alpha dose point kernels

As there is an increasing interest in labelling FAPI compounds with therapeutic α -emitters, we assess its potential to be used in FAPI compounds by convolving the alpha dose point kernels with the histological slides stained to elucidate FAP expression. The resulting dose maps were assessed to estimate whether the α -emitting radionuclide ^{225}Ac is useful for use in FAPI-targeting tracers for targeting various cancer types.

Histological images used in this work is shown in **Figure 30**. **Figure 30(A)** shows relatively uniform FAP expression in the histological slide compared to **Figure 30(B)**. FAP staining shows a brown-stained area around the tumor cells suggestive of fibroblast exhibiting FAP expression. The size of both images are $2\text{ mm} \times 1.4\text{ mm}$, and the pixel size is $0.243\ \mu\text{m}$.

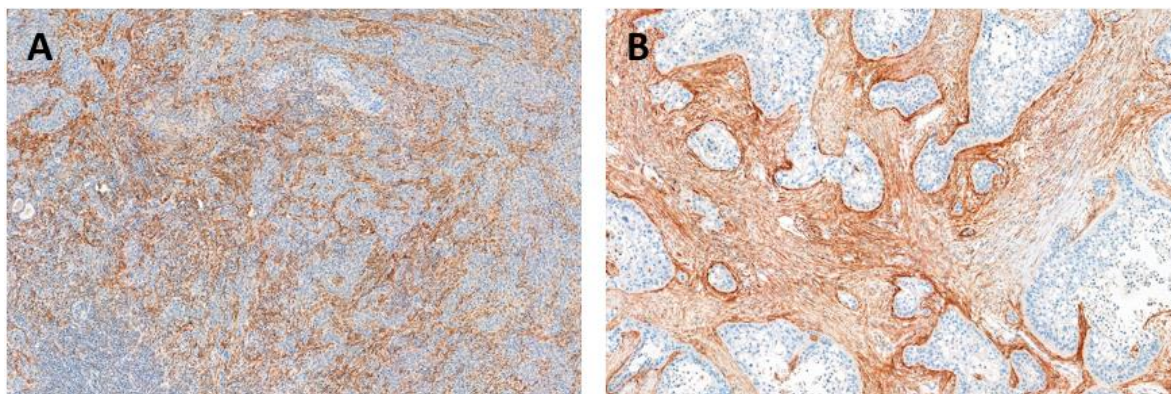


Figure 30: Histological slides showing the FAP (A) uniform expression and (B) irregularly shaped expression.

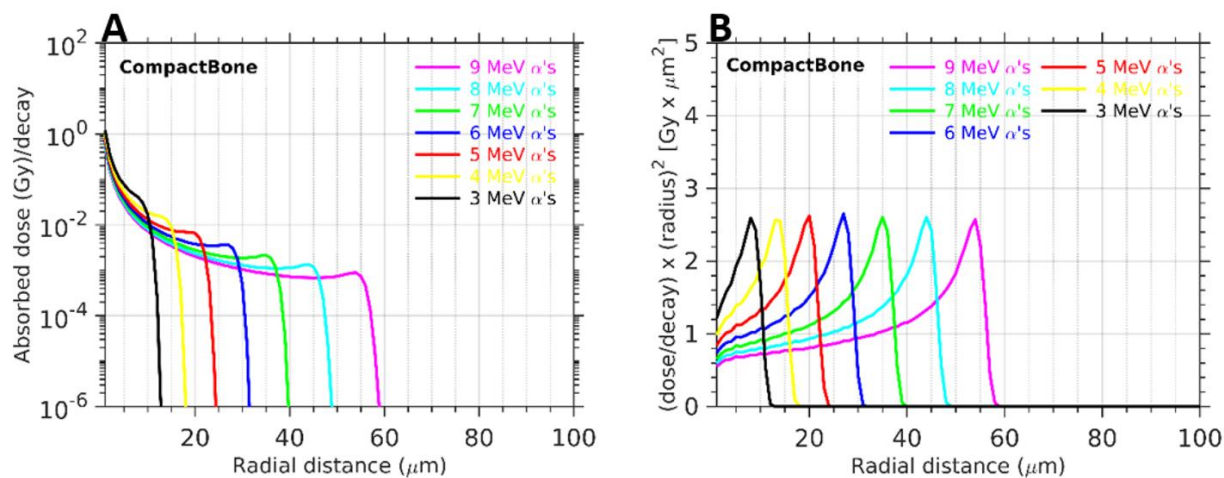
Images were inverted before further processing. Image inversion was performed because the FAP expression would have higher radioactivity uptake values compared to the minimal activity uptake in peripheral cells. The inverted images were convolved with the dose point kernels of

^{225}Ac to assess its suitability to be used as a therapeutic in FAPI compounds. Image convolution was performed in MATLAB using its *convn* function.

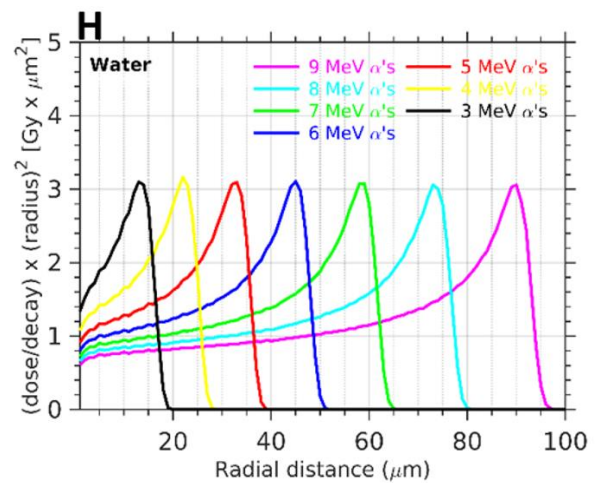
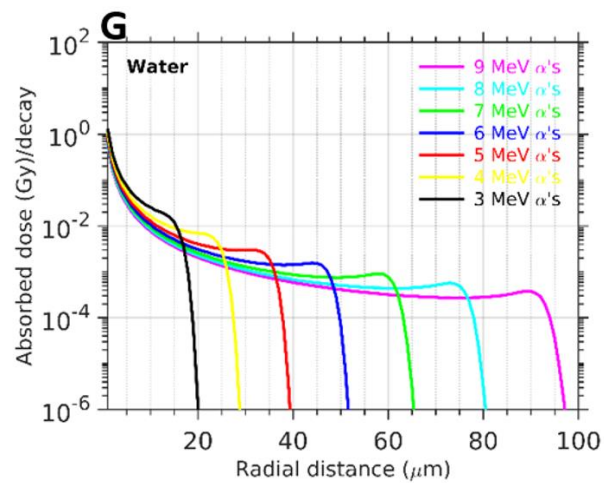
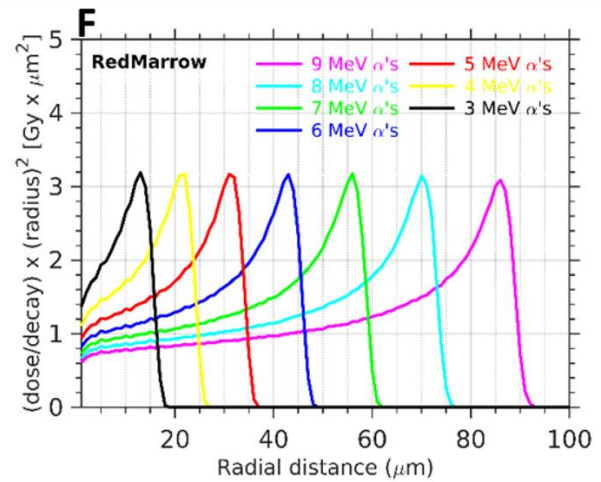
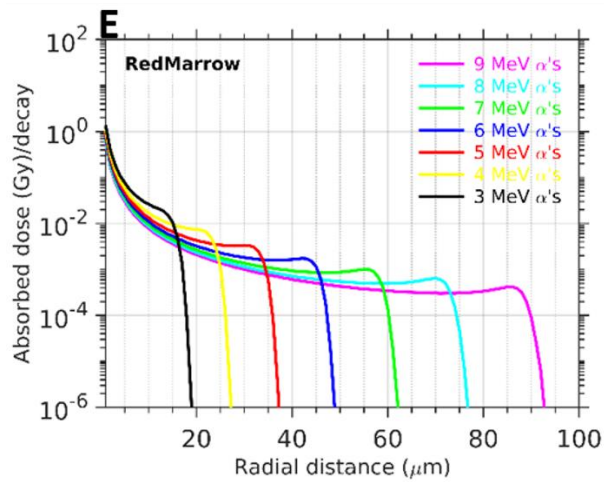
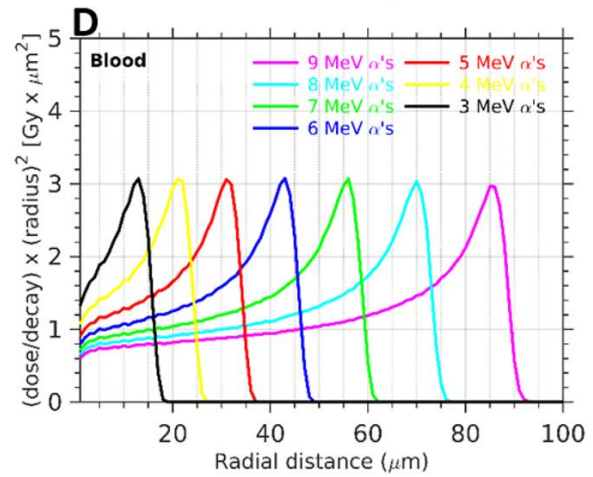
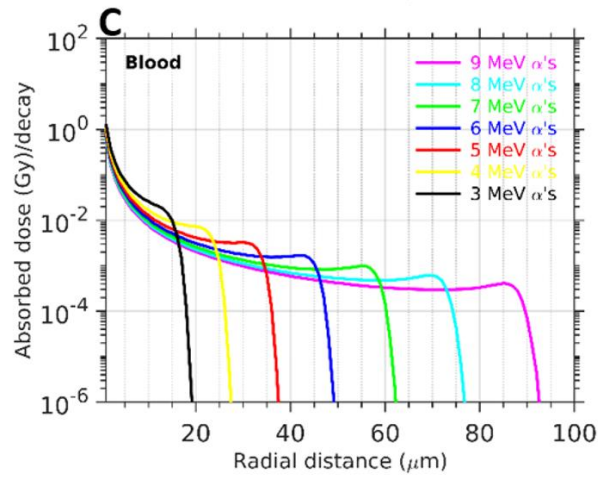
6.3. Results

6.3.1. Monoenergetic α -particles simulations

The radial absorbed dose deposition profiles of a mono-energetic α -particle of energy 3 - 9 MeV as a function of distance from the center of the source were plotted in **Figure 31** for all mono-energetic α 's simulated herein. The x-axis of these plots, i.e., the radial distance, represents the radius of spherical shells where the energy deposition occurred during the simulation. In another words, this radial distance represents the maximum penetration distance that α 's would penetrate in tissues.



continued



continued

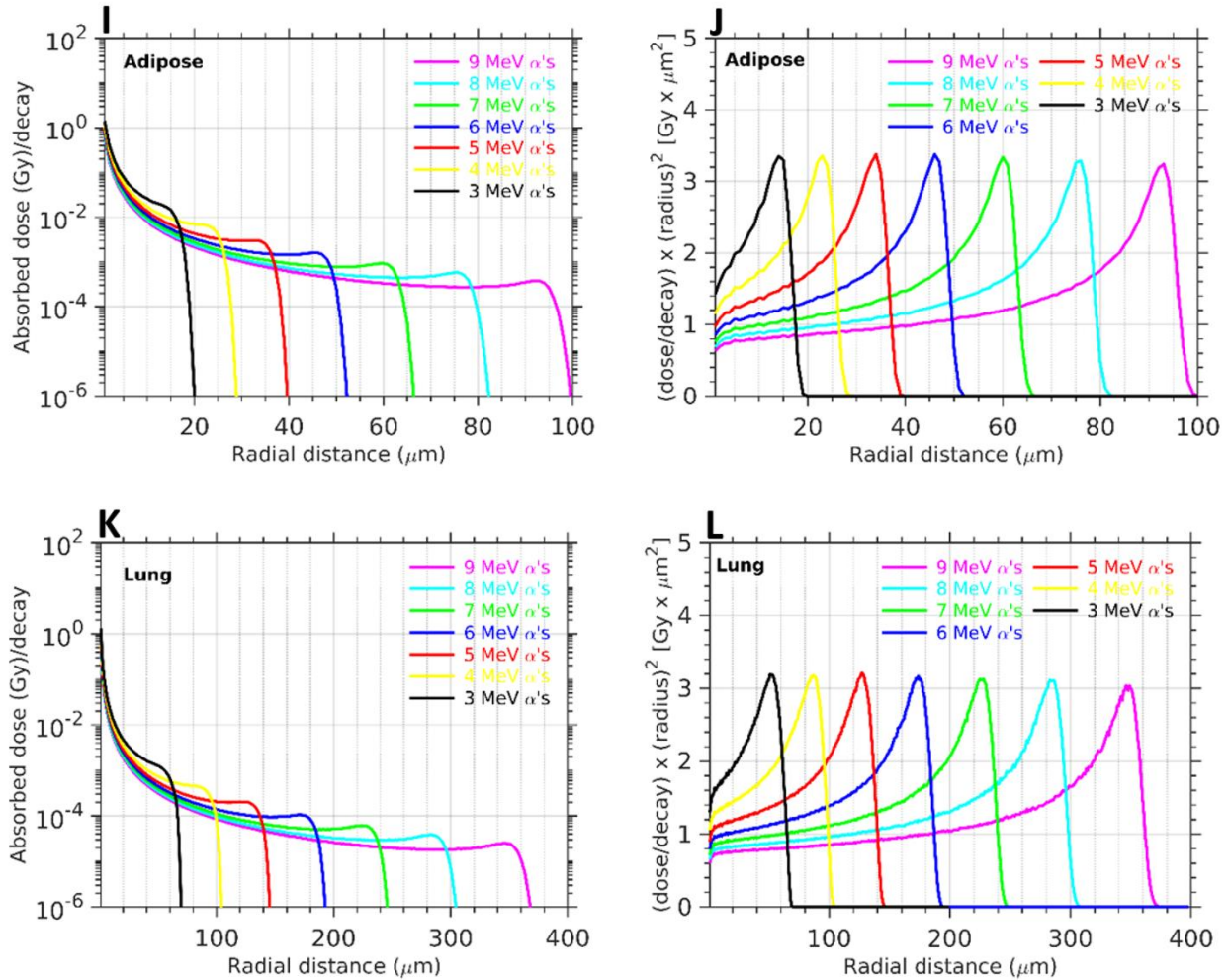
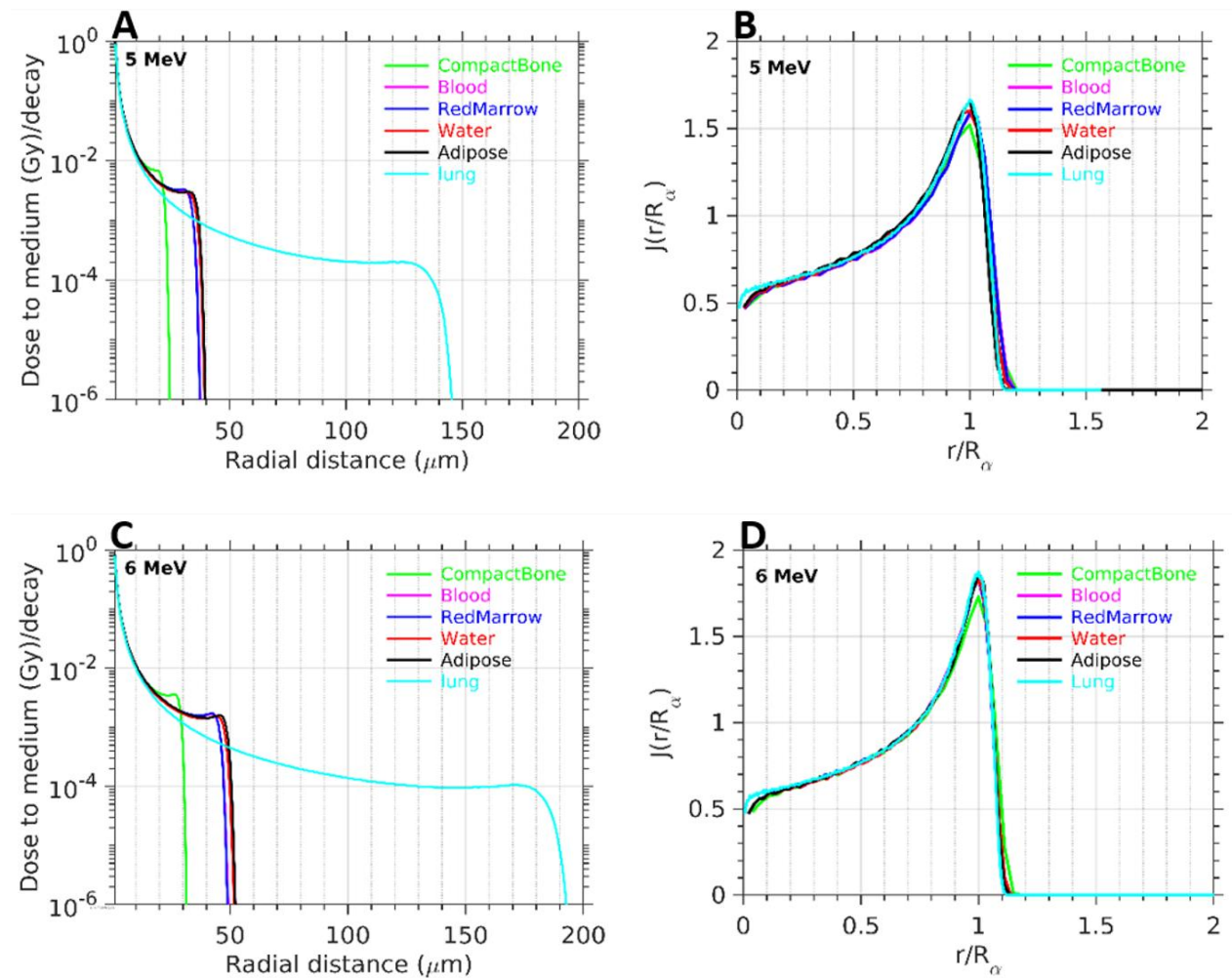


Figure 31: Simulation of mono-energetic α 's in several tissues. (A, C, E, G, I, K) Plot of absorbed dose per decay vs the radial distance and (B, D, F, H, J, L) plot of Bragg peak at different energies. Plots are arranged in terms of decreasing density of tissues for ease of comparison.

As shown in **Figure 31**, the Bragg peaks have the same height regardless of the α -energies at the same tissue. A similar trend of Bragg peaks were also seen when data from ICRU 49 was plotted [34, 205]. However, the height of Bragg peaks was found to be slightly different in different tissues. Due to the high LET, the α -particles lose the maximum energy close to the Bragg peak at the end of their track, as shown in **Figure 31**. Abscissa and ordinates are taken to be the same for ease of comparison except for the lung tissue.

6.3.1.1. Dose point kernels of mono-energetic α -particles and comparison against different tissues

Between the scaled distance of 0.2 to 0.8 r/R_α , the absolute percentage difference is less than 5% for all mono-energetic α 's simulations performed in this work. The discrepancy of $\sim 6\%$ was observed at the Bragg peak when tissue-specific DPKs were compared to water kernels. However compact bone DPKs show the greatest difference of $\sim 10\%$ at the Bragg peak for all mono-energetic α 's compared to water kernels. After the scaled distance of unity ($r/R_\alpha > 1$), the dose fall-off regions show a maximum difference of up to 100% (Figure 32).



continued

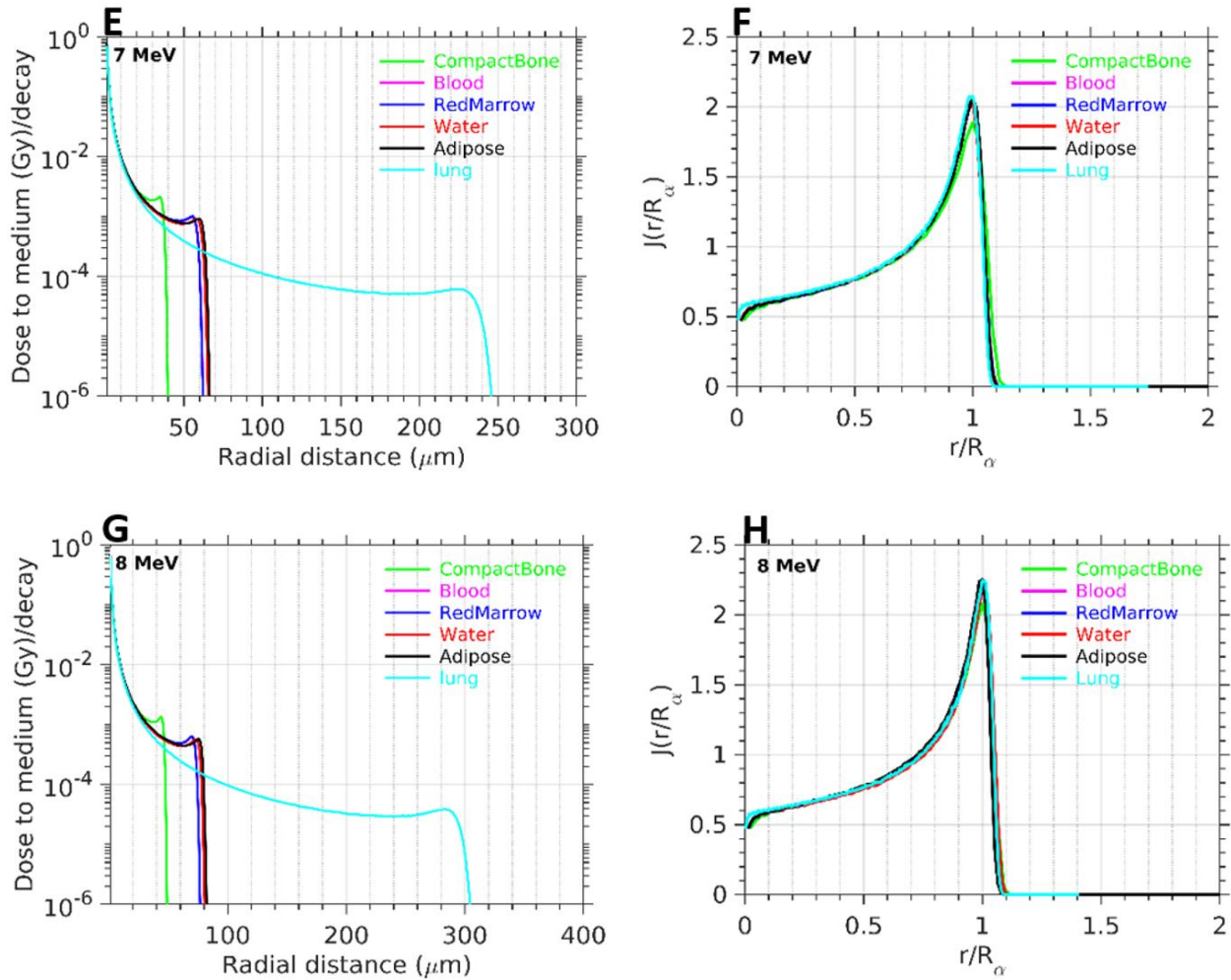
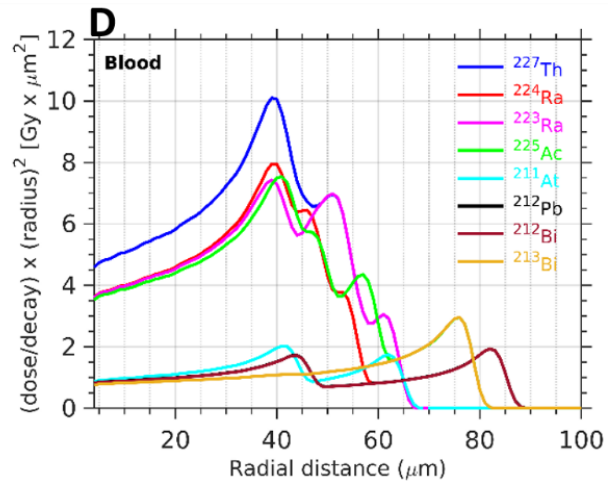
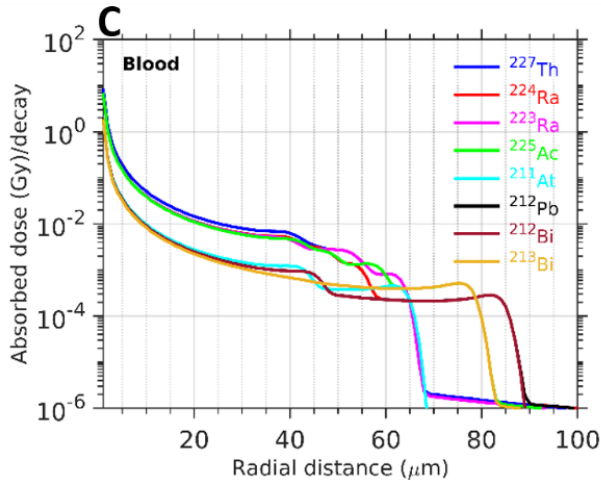
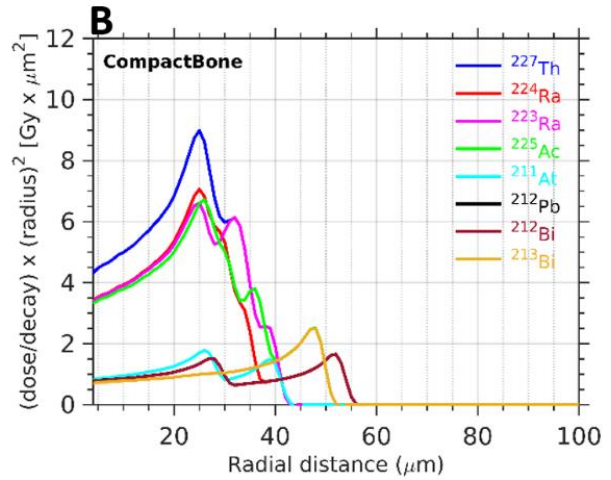
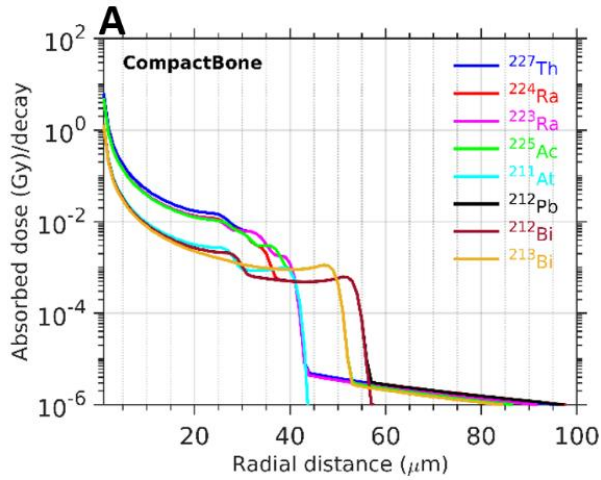


Figure 32: (A, C, E, G) Dose point kernels of mono-energetic α 's (5-8) MeV in several tissue types. (B, D, F, H) Comparison of tissue-specific dose point kernels of mono-energetic α 's in several tissues.

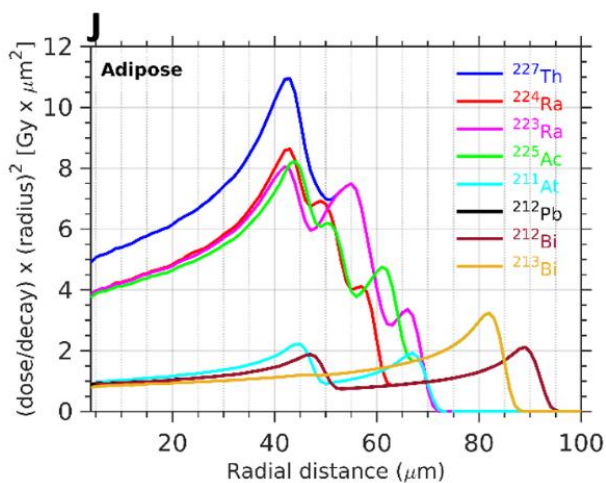
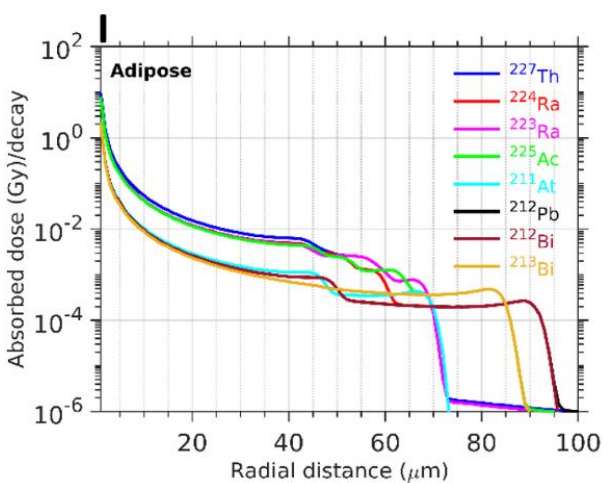
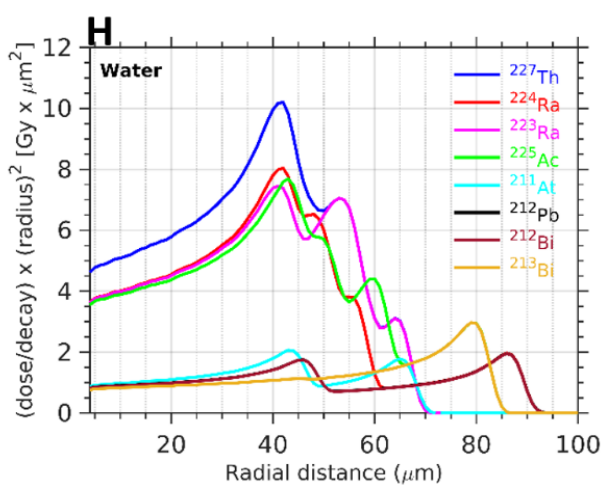
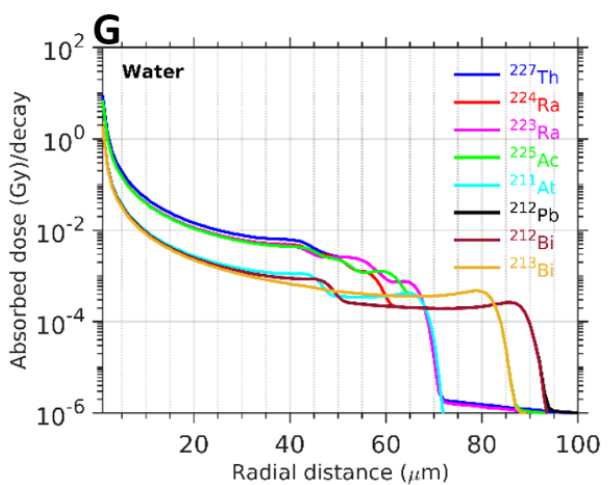
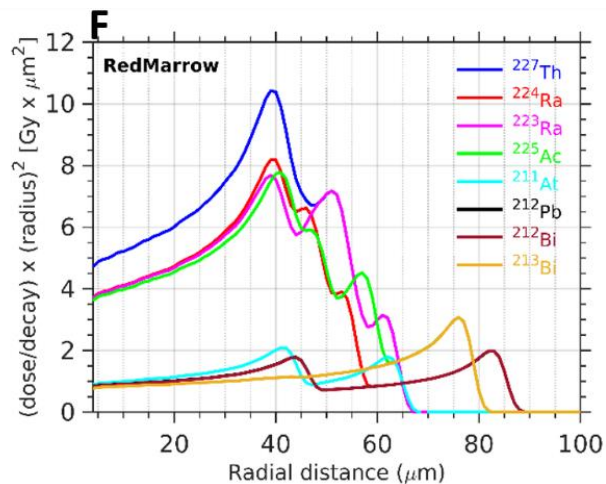
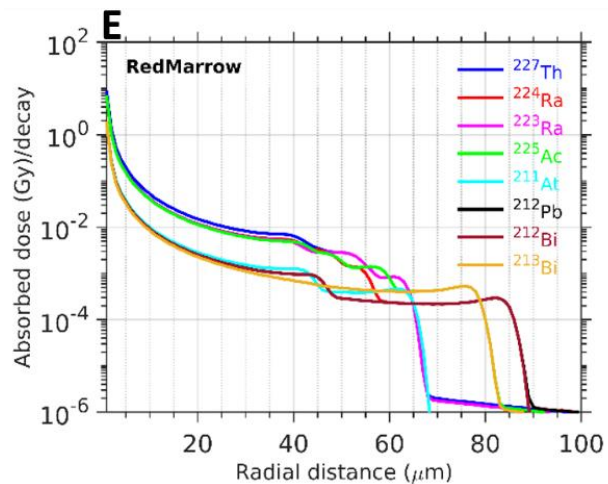
6.3.2. α -Emitting radionuclides in different tissues

Figure 33 shows that the absorbed dose per decay curves overlap for ^{227}Th and ^{223}Ra decay after 50 μm radial distance in water; this is because they are in the same decay chain. Radionuclide ^{223}Ra is a descendant of ^{227}Th decay. Likewise, ^{212}Pb is a descendant of the ^{224}Ra decay chain; therefore, the decay curves in the plots were found to overlap after 62 μm in water, and similar trends are observed in other tissues simulated herein. Radionuclide ^{212}Bi is a descendant of ^{212}Pb decay, but it exhibited a very comparable dose level as ^{212}Pb , as shown in **Figure 33**. This is not surprising because ^{212}Pb decays to ^{212}Bi with the emission of β -radiation, and the absorbed dose

from β -radiation yields a contribution of less than 1% compared to the total absorbed dose per full decay. That is why their spectrum seems to overlap with each other fully. All the simulated decay chains are summarized in the APPENDIX C. Comparisons of the Bragg peaks of all the simulated radionuclides were also made in all tissue types.



continued



continued

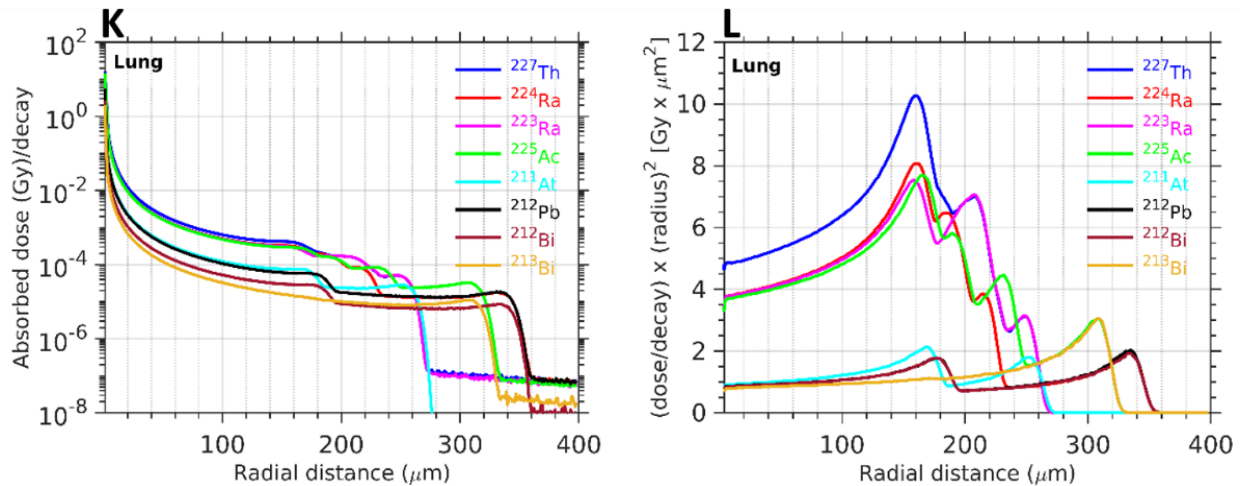


Figure 33: (A-L) α -Emitting radionuclides ^{227}Th , ^{224}Ra , ^{223}Ra , ^{225}Ac , ^{211}At , ^{212}Pb , ^{212}Bi and ^{213}Bi in compact bone, blood, red marrow, water, adipose and lung tissues.

The absorbed dose distribution profiles can be compared for different radionuclides using the data presented in **Figure 33 (A-L)**. ^{227}Th deposited the greatest amount of absorbed dose per decay compared to all other radionuclides simulated. For example, a comparison of absorbed dose profiles at a radial distance of 42 μm in water **Figure 33 (H)** reveals that absorbed dose deposition from ^{227}Th decay is the greatest, which is about (1.3 - 1.4) times larger than the absorbed dose per decay due to ^{224}Ra , ^{223}Ra , and ^{225}Ac and (5 - 9) times compared to absorbed dose deposition due to the decay of ^{211}At , ^{212}Pb , ^{212}Bi , and ^{213}Bi .

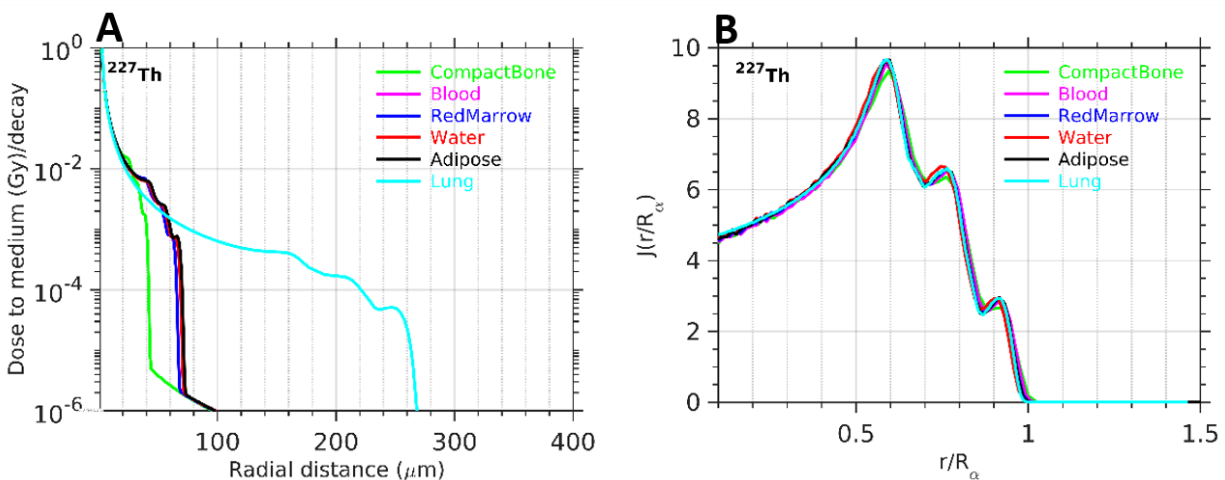
6.3.2.1. Comments on multiple Bragg-peaks

Table 9: Number of Brags peaks observed in simulations.

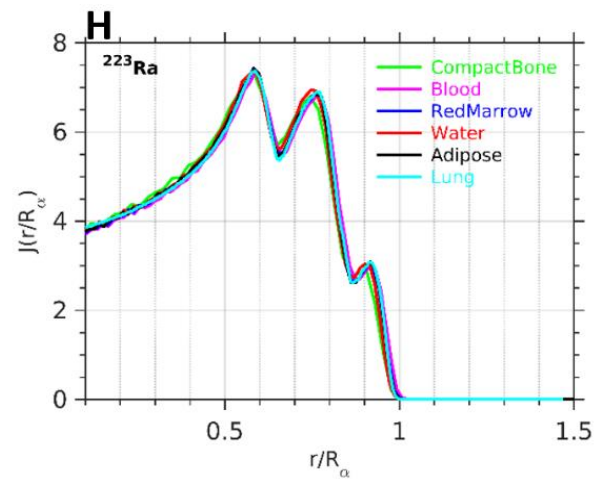
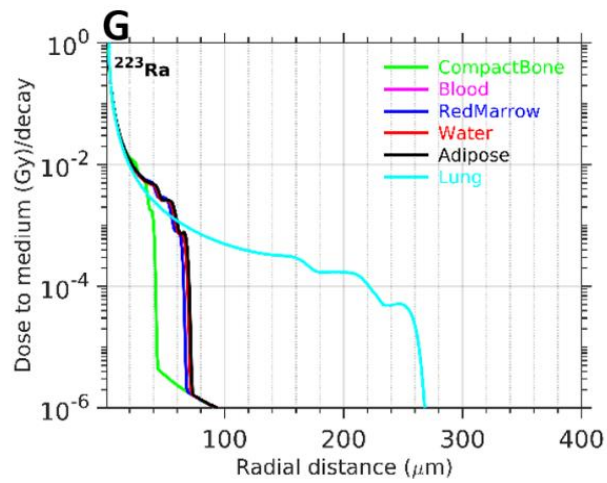
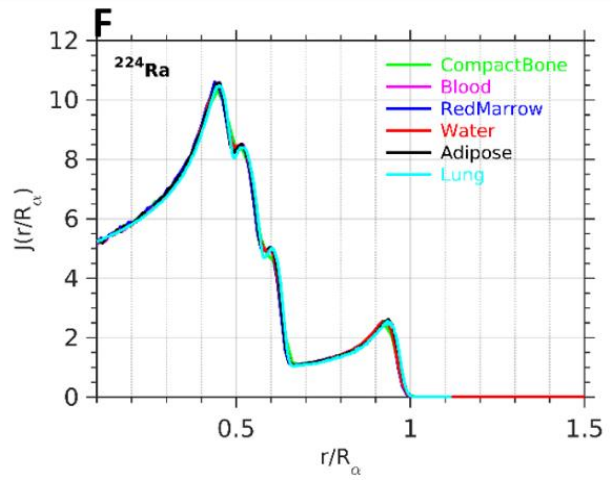
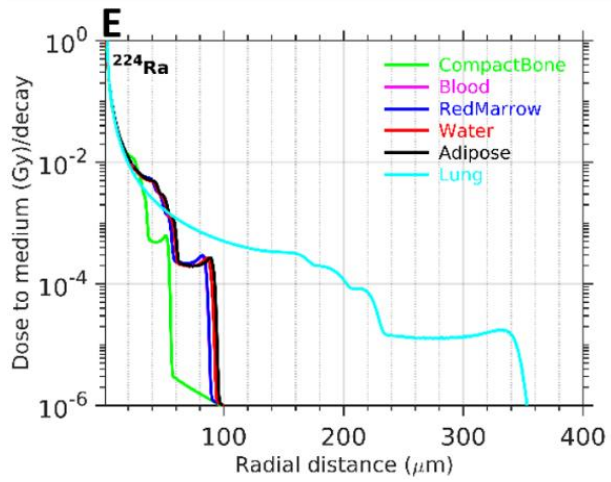
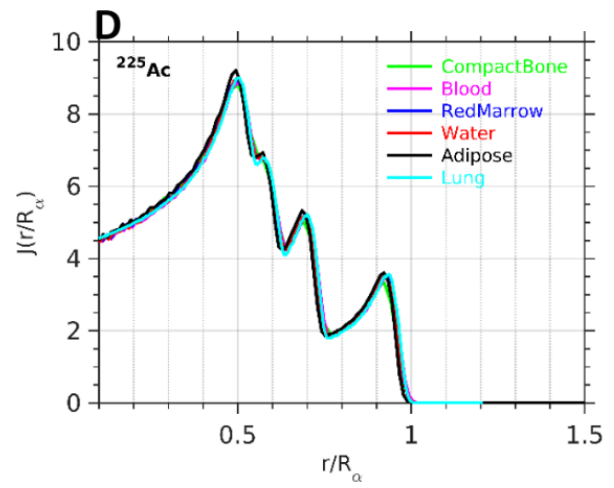
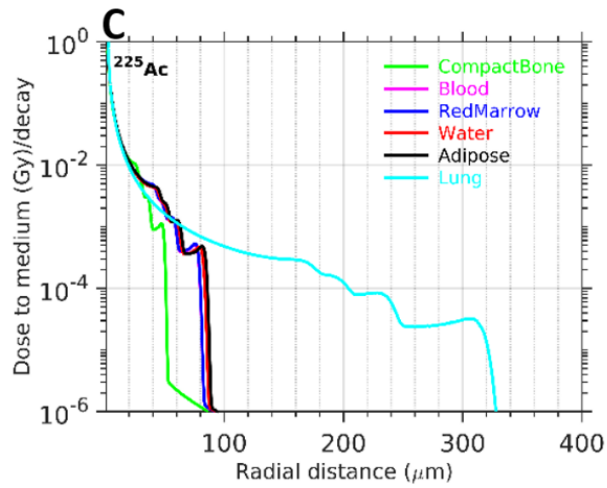
	Radionuclide	# of emitted α 's	# of Bragg peaks observed
1	^{227}Th	5α	3
2	^{224}Ra	5α	4
3	^{223}Ra	4α	3
4	^{225}Ac	4α	4
5	^{211}At	1α	2
6	^{212}Pb	1α	2
7	^{212}Bi	1α	2
8	^{213}Bi	1α	1

Multiple Bragg peaks were observed for seven simulated α -emitting radionuclides due to their different decay characteristics. Khan et al. had also observed multiple Bragg peaks for ^{223}Ra and ^{225}Ac radionuclides [199]. In this work, although ^{227}Th full decay spectrum had emitted 5α 's, we observed only the three Bragg peaks for ^{227}Th radionuclide. As for ^{225}Ac and ^{224}Ra , four Bragg peaks were observed, however, their decay chains have 4α 's and 5α 's for these radionuclides. In the case of ^{223}Ra decay, three Bragg peaks were observed, and for ^{212}Pb , ^{211}At , and ^{212}Bi , two Bragg peaks were observed. In addition, for ^{213}Bi decay, only one Bragg peak was observed. The number of Bragg peaks observed is summarized in **Table 9**.

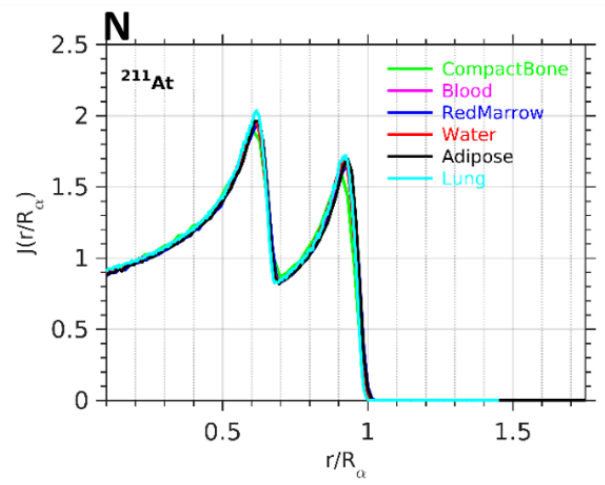
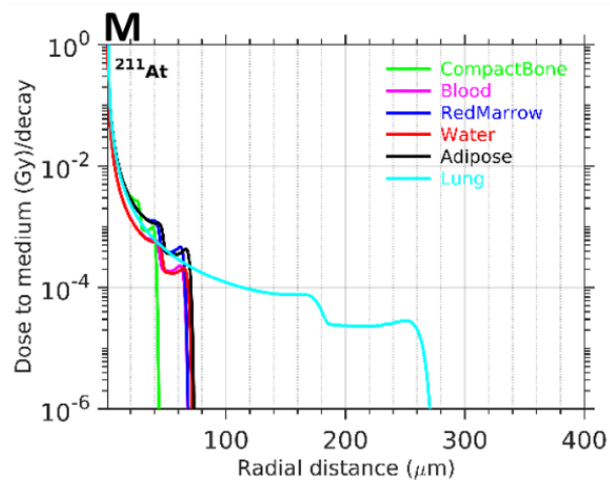
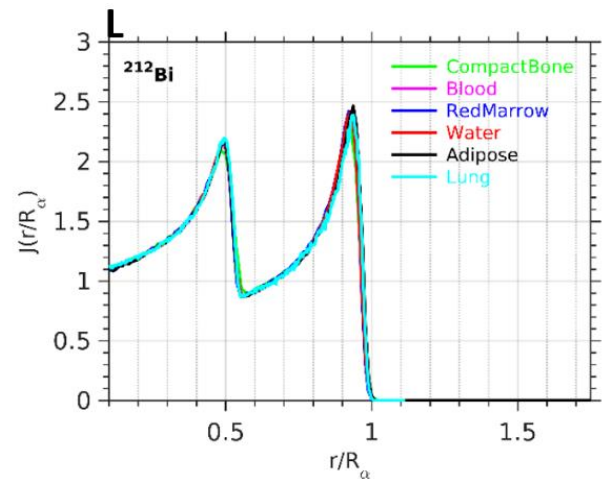
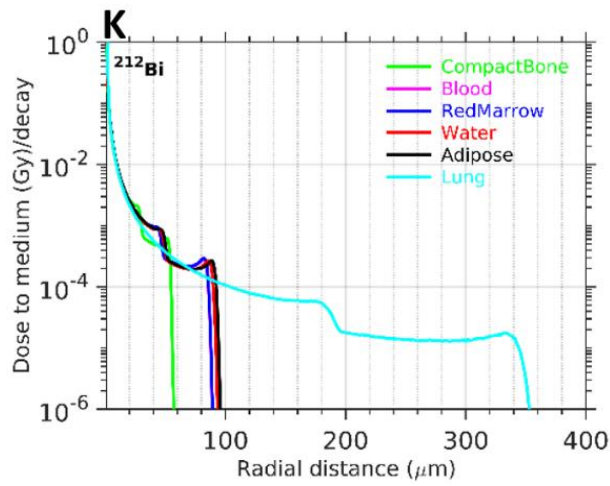
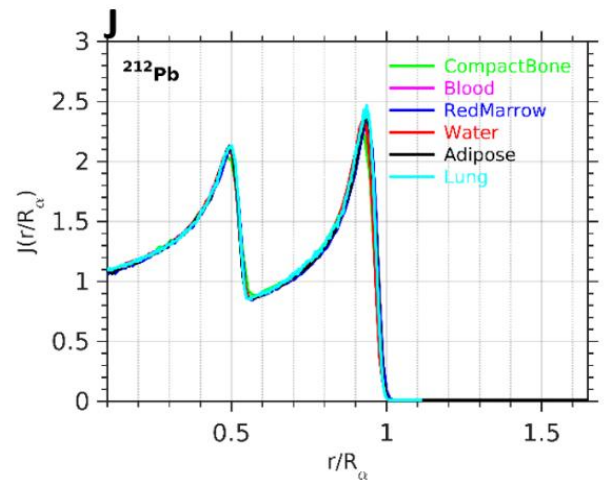
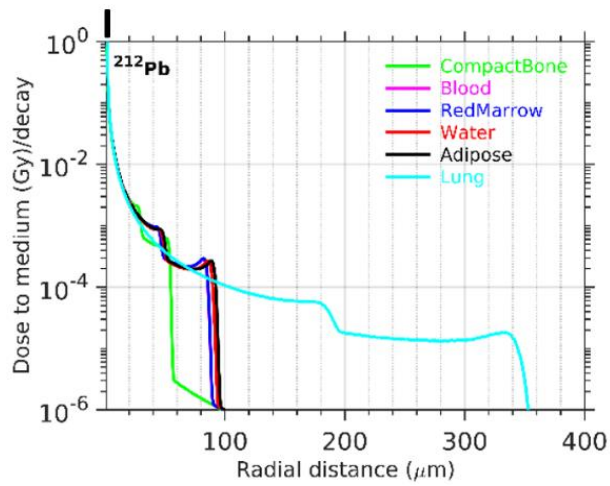
6.3.3. Dose point kernels comparison against different tissues



continued



continued



continued

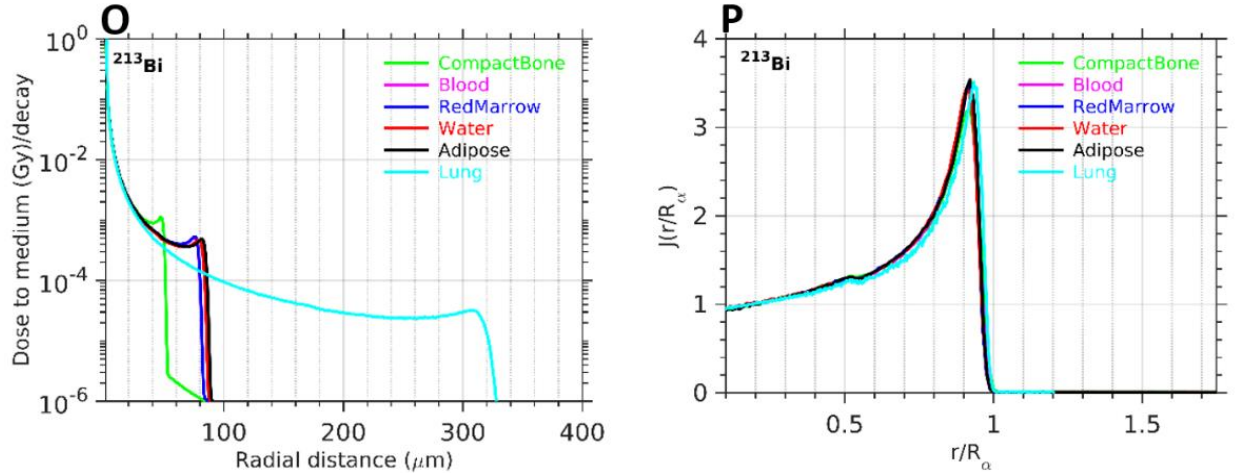


Figure 34 (A-P): Dose point kernels of α -emitting radionuclides ^{227}Th , ^{225}Ac , ^{224}Ra , ^{223}Ra , ^{212}Pb , ^{211}At , ^{212}Bi , and ^{213}Bi in several tissues and their DPKs comparisons.

Discrepancies among the DPKs plotted in **Figure 34(B, D, F, H, J, L, N, P)** were quantified for scaled distances $(r/R_\alpha) < 1$. The DPKs in water were compared to other tissue-specific kernels. For the radionuclide ^{227}Th , the mean percent differences in DPKs up to a scaled distance (r/R_α) of 0.6, i.e., up to the first Bragg peak, is $\sim 5\%$. At the first Bragg peak, the average difference of less than 8% was observed. Maximum discrepancies up to 20% was observed at the rapid dose fall-off region immediately after the second and third Bragg peaks.

For ^{225}Ac , the mean percent differences in DPKs are $\sim 3\%$ up to the scaled distance (r/R_α) of 0.6 for all tissues compared to water DPKs. This region also included the first three Bragg peaks; however, the dose fall-off region after the third peak exhibited a difference of up to 20%. Similarly, immediately after the fourth Bragg peak dose fall-off region, significant differences of up to 22% were observed.

The mean percent differences in DPKs for ^{224}Ra up to a scaled distance (r/R_α) of 0.6, i.e., just after the third Bragg peak, is $\sim 5\%$. After the third peak, a percent difference of up to 10% was seen at the dose fall-off region. Moreover, the highest difference of 23% was observed when DPKs of the lung were compared to the water kernels close to the scaled distance of 1, i.e., the dose-fall

off region of the fourth Bragg peak. However, other tissues such as red marrow, blood, and adipose tissue were found to have a good agreement, i.e., less than 10% in this region.

For ^{223}Ra , the mean percent differences in DPKs up to a scaled distance (r/R_α) of 0.9 is 5%. However, the discrepancies were up to 10% at the dose fall-off region after the third Bragg peak. All tissue-specific DPKs have similar differences of an average of 5% up to the scaled distance of 0.9. In addition, for ^{211}At , mean percent differences in DPKs up to a scaled distance (r/R_α) of 0.9 is about 4%; however, the dose fall-off region after the second Bragg peak appears to have a maximum percent difference of up to 10%. Similar discrepancies were observed for all tissue-specific DPKs.

For ^{212}Pb , the mean percent differences in DPKs up to a scaled distance (r/R_α) of unity is less than 3%. However, a difference of up to 10% was observed in the dose fall-off region just after the first Bragg peak. Similarly, maximum differences of up to 20% were observed in the second dose fall-off region after the second Bragg region. Moreover, for ^{212}Bi , the mean percent differences in DPKs up to a scaled distance (r/R_α) of unity is less than 3%, and similar differences were observed as that of ^{212}Pb in the two dose fall-off regions. Furthermore, the tissue-specific kernels for ^{213}Bi show a mean percent difference of ~4% compared to water DPKs. Up to a scaled distance (r/R_α) of 0.9, the mean difference was ~3%. However, the discrepancies were found to be greater in the dose fall-off region of about 10%.

As would be predicted, the highest discrepancies were observed for lung and compact bone tissues compared to the water kernels. This highest degree of disparity in lung and compact bone DPKs is due to their low and high density compared to water. Of all the other tissues investigated, blood, red marrow, and adipose DPKs were found to have the closest agreements with water kernels. Similar conclusions were made by Khan et al [199], but their comparison neglected the

dose fall-off region close to the scaled distance of unity. However, this work included all the Bragg peaks in DPK and their dose fall-off regions in the DPK spectrum.

6.3.4. Convolution of dose point kernels with histological slides for microdosimetry

The results of convolution of ^{225}Ac dose point kernels and histological slides showing the FAP expression is shown in **Figure 35**. Visual assessment of dose map (**Figure 35 (E and F)**) shows that alpha radiations emitting from the ^{225}Ac decay irradiated all pixels in the vicinity of FAP expression. However, the unit of dose map obtained after the convolution step is arbitrary.

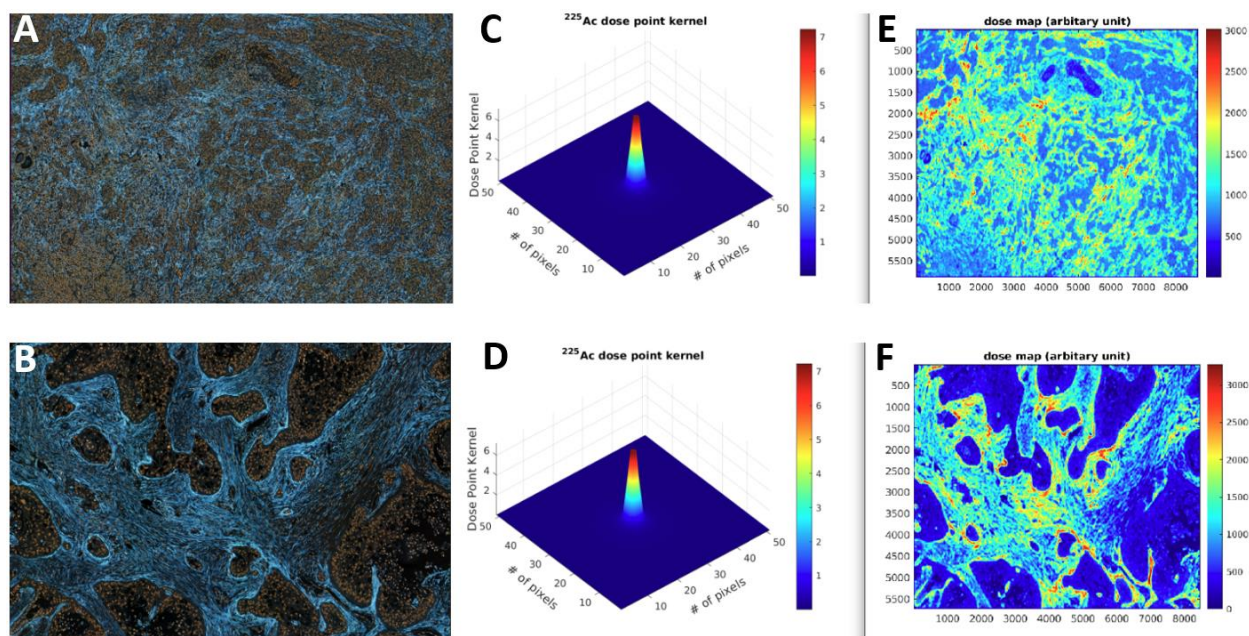


Figure 35: (A) and (B) are inverted images of the original images, (C) and (D) are ^{225}Ac dose point kernels, and (E) and (F) are the results of convolution, i.e., the dose map.

6.4. Discussion and Conclusions

Here we have presented the Monte Carlo simulations of eight therapeutic α -emitting radionuclides of interest for the field of TRT. A simple geometry of spherical tissue volume was simulated to generate the α -DPKs of radionuclides and mono-energetic α -particles of energy (3-9)

MeV. This study shows how would the DPKs look like even at the highly localized absorbed dose due to the rapid fall-off of the radiation field with the radial distance from the point source. To our knowledge, this is the first time where many clinically relevant α -emitting radionuclides are studied for their dosimetric evaluation and to explore their Bragg peaks.

The mean percentage deviation of tissue-specific kernels compared with water kernels was ~5% for all radionuclides. However, it is important to remark that uncertainties in computed absorbed dose values are high with differences up to ~23% in the dose fall-off region after the Bragg peak of the α -radiation. This significant difference was observed for ^{227}Th water kernel compared to the lung DPKs. The results of this simulation work are also aligned with the results published by Khan et al [199]. Similar to β -DPKs, the tissue density appears to be a more critical variable that dramatically impacts DPKs shapes, as expected.

Owing to the complex decay scheme of α -emitting radionuclides, the simulations were more computationally intensive than the β -emitting radionuclides simulations. As a reference, the simulation took 98 h of computation time for ^{227}Th radionuclide in water. For ^{225}Ac , ^{224}Ra , and ^{223}Ra simulation spent 44 h, 31 h, and 54 h, respectively. In addition, radionuclides ^{211}At , ^{212}Pb , ^{212}Bi , ^{213}Bi that have comparatively simple decay schemes took 17 h, 38 h, 39 h, and 34 h of computation time using the water phantom. All simulations were conducted on a high-performance computing cluster at the University of Iowa but without making parallel simulations by assigning two cores per simulation with a virtual memory of 8GB (Intel Xeon Gold 6230, 2.1GHz).

One of the challenging aspects of α -emitting radionuclides is their experimental validation. Due to the short-range of α 's, it is extremely difficult to experimentally validate these kernels. However, for the β -emitting radionuclides, the situation is different because of their relatively long

ranges in tissues. Our previous work has validated the simulated dose point kernels using the radiochromic (EBT3) films for β -particle dosimetry [2].

We have found that, in general, there is a linear relationship between the number of α -emitted from the radionuclide decay chain and the number of Bragg peaks. The number of Bragg peaks was found to be less than that of a number of α 's from the decay chain for ^{227}Th , ^{224}Ra , and ^{223}Ra radionuclides. However, the decay of ^{225}Ac shows the same number of Bragg peaks as that of the number of α 's emitted. Interestingly, the decay of ^{211}At , ^{212}Pb , and ^{212}Bi show more Bragg peaks than the number of α 's emitted from the decay.

Application of α - dose point kernels for microdosimetry using histological slides showing FAP expression appears to be useful to evaluate the suitability of therapeutic α -emitters to be used in FAP-targeted compounds. However, more histological slides needed to be studied to get a more definitive answer of whether the α -emitting radionuclides have potential to be used in FAPI compounds. The dose map obtained in this work has arbitrary units. The quantification of the absorbed dose map in each single pixels would give us more confidence to use these α -emitters in FAP-tracers.

In conclusion, we have studied eight clinically relevant α -emitting radionuclides and mono-energetic α -particles (3-9) MeV. Dose point kernels were generated, and their Bragg peaks were evaluated. Multiple Bragg peaks were observed for seven radionuclides simulated in this work. Comparison of water DPKs to other tissue-specific DPKs demonstrated an average difference of 5%, except at the higher dose gradient (i.e., the dose fall-off) regions after the Bragg peak where discrepancy up to 23% were observed. This is in line with the results published by Khan et al [199]. This higher degree of discrepancies was observed for lung and compact bone DPKs compared to water DPKs. Of all the other tissues investigated, blood, red marrow, and adipose

DPKs were found to have the closest agreements with water DPKs. The potential of ^{225}Ac radionuclide was evaluated using the histological slides showing the FAP expression for its suitability to be used in FAP-targeted tracers. Our results shows that ^{225}Ac radionuclide may be useful in targeting the FAP expressions in various cancer types. Other therapeutic α -emitting radionuclides can also be assessed using the methodology presented in this work.

CHAPTER 7: MONTE CARLO SIMULATION OF GE DISCOVERY MI PET SCANNER AND EVALUATION OF LONG AXIAL FIELD-OF-VIEW SCANNER USING ITS FRONT-END ARCHITECTURE

7.1. Introduction

There has been a significant interest in developing long axial field-of-view (LAFOV) PET scanners to enhance the geometric sensitivity of PET systems. The latest standard geometry commercial silicon photomultiplier (SiPM)-based clinical PET scanners typically have an axial field-of-view (AFOV) of 15-30 cm [206-208]. However, several limitations are associated with a limited AFOV, such as low photon detection efficiency [75, 76, 78, 209], longer scanning time, the requirement of higher radioactivity injections, and difficulty in large field of view parametric and pharmacokinetic PET imaging [210-214]. Significant efforts have been made recently developing a total-body and LAFOV PET scanner that can image the patient using only a single bed position in a relatively short scanning time with lower injected activity [69, 74]. In addition, the LAFOV scanners can extend the imaging to multisystem diseases by implementation of multi-organ multi-parametric PET combining Standardized Uptake Value (SUV) PET with kinetic modeling [215-218], and even thorax breath-hold imaging [219].

To date, three platforms have been developed, including the uEXPLORER [68-70], PennPET EXPLORER [71, 72], and the Siemens Biograph Vision Quadra [73, 74, 220]. The uEXPLORER uses the similar detector as the United Imaging Healthcare's uMI 550 and 780 PET/CT scanners, however the LYSO crystal depth is more by ~2 mm. In addition, the PennPET Explorer is based on the Philips detector technology and detector geometry used in the Vereos scanner [75]. The Biograph Vision Quadra uses the same technology as the digital Biograph Vision 600 PET/CT system (Siemens Healthineers) [73]. All these scanners use a modern SiPM technology instead of traditional photomultipliers. First human studies on the uEXPLORER total-

body PET scanner have already been performed while utilizing substantially lower administered activity (~25 MBq as compared to more typical 370 MBq) and a short total acquisition time of ~1 min [76, 77]. The PennPET EXPLORER group recently reported their development of a whole-body imager currently with an active 64 cm AFOV and indicated that the optimal axial length of the scanner could be in the range of (1.0 -1.4 m) [71].

The scanner architecture of Phillips Vereos PET scanner [71, 221] and United Imaging Healthcare's uMI scanner [69] have been studied for the total-body PET scanner design both through Monte Carlo simulation and downstream physical testing. Similarly, the front-end scanner architecture of Biograph Vision 600 PET/CT has been implemented in Biograph Vision Quadra [74]. Monte Carlo simulation of the Discovery STE PET/CT scanner and its reduced and extended AFOV has been performed using the SimSET toolkit [222]. In addition, Monte Carlo studies of the Siemens Biograph mCT scanner were performed in 2012 using the GATE (Geant4 Application for Tomographic Emission) simulation toolkit [79]. Their study suggested that the extended axial coverage of 2 m with 20 mm thick LSO crystals yields a relative performance gain of (25 – 31) times higher Noise Equivalent Count Rate (NECR) [79]. In another simulation study, Surti et al. simulated imaging at activity levels as low as 1/20th of that typically injected for routine ¹⁸F-FDG studies using the EGS4 code with a scanner AFOV of 72 cm [223].

Monte Carlo simulations have been used for assessing the performance of hypothetical LAFOV PET systems adopted from existing clinical PET systems but with sparse detector geometries to reduce the manufacturing and purchasing cost of such scanners thus facilitating their wider clinical adoption. Specifically, Monte Carlo studies have been performed comparing the NEMA performance of existing clinical PET systems with compact detector configurations against those adapting sparse detector configurations with either (i) same detector ring diameter and

AFOV but only half the detectors [224] or (ii) same detector ring diameter and number of detectors but spaced out to cover twice the original AFOV [84, 85, 225-227]. The validated Monte Carlo model proposed in this study could also be used in future to expand knowledge in this area for hypothetical sparse detector configurations based on commercial GE PET scanner geometries.

To our knowledge, the investigation into the imaging properties of a hypothetical extended axial field-of-view GE Healthcare Discovery MI (DMI) scanner system architecture has not been performed. This is of particular interest because the LYSO detector thickness in DMI is more than 20% longer than the aforementioned systems, which suggests potentially even more substantial sensitivity gains than other systems. The DMI PET scanner is currently available in 3, 4, and 5-ring configurations that provides a 15, 20, and 25 cm AFOV. In this study, our goal was to explore and understand the potential of the DMI architecture for a total-body scanner by looking at the performance gain with increasing AFOV through simulation. First, to validate our Monte Carlo model of the DMI detection system, we simulated the front-end architecture of the GE Discovery MI PET 4-ring scanner using the GATE toolkit and compared against published NEMA measurements from DMI 4 ring system [206]. After validation, we gradually added the scanner rings to the AFOV up to 2 meters. NEMA performance results were obtained for the hypothetical extended AFOV scanners with several configurations, between 4 and 40 rings. The axial sensitivity, spatial resolution, count rates, scatter fraction, and Noise Equivalent Count Rates (NECR) were measured according to the modified NEMA protocols as implemented by Spencer et al. [69] using modified NEMA phantoms. These modified phantoms were necessary given that NEMA designed phantoms and methods never contemplated the LAFOV geometry.

7.2. Methodologies

7.2.1. Monte Carlo simulations

The GEANT4 Application for Tomographic Emission (GATE) is a Monte Carlo toolkit for nuclear imaging [51, 53, 120], radiotherapy, and dosimetry [1, 2, 50, 96]. GATE version 8.1 with Geant4 10.4.1 [52] was used to model the Discovery MI scanner and simulate particle propagation. The physics list of *emstandard_opt4* was used in all simulations, as this model has previously been shown to be appropriate for medical applications involving electromagnetic effects [106, 228]. This list includes all the relevant physical processes for photons and electrons interactions (i.e., photoelectric effect, Compton scattering, Rayleigh scattering, ionization, bremsstrahlung, multiple scattering, and positron annihilation). The decay of ^{18}F were simulated by β^+ sources with energy spectra parametrized according to the Landolt-Börnstein tables [53]. Range production cuts were set to 0.1 mm for electrons and photons in the whole geometry. Variance reduction techniques were not used. The number of primary particles was adapted for all simulations according to the NEMA guidelines regarding activity and acquisition time. Optical processes of light emission and transport were not included in the simulations, as these processes substantially increase the simulation time.

7.2.2. Discovery MI 4-ring scanner geometry

The Discovery MI scanner used in this work is the latest generation of PET/CT scanners developed by GE Healthcare utilizing the silicon photomultiplier (SiPM) based technology [206, 229]. The scanner system has been integrated with 64 slice x-ray computed tomography system and a 4-ring PET geometry with LightBurst digital detectors providing a 20 cm AFOV and a 70 cm transaxial field of view, i.e., the scanner bore diameter. Each ring consists of 34 detector modules, each containing 4 axial and 4 transaxial blocks, for a total of 544 detector blocks. Each

detector block is 16 mm (transaxial) \times 48 mm (axial) and contains a 4 (transaxial) \times 9 (axial) crystal array, with crystals placed on three 3 \times 2 arrays of SiPM detectors, for a total of 19,584 crystals and 9,792 SiPM channels. The SiPM signal readout electronics are implemented as an application-specific integrated circuit. The output energy is digitized by an external analog-to-digital converter (ADC) and the timing signal by an external time-to-digital converter. The size of each crystal used is 3.95 mm (transaxial) \times 5.3 mm (axial) \times 25 mm (depth), with several crystals connected to light guides that optimize light collection and improve sensitivity and resolution. The crystals themselves are slightly radioactive due to the very long half-life, naturally occurring lutetium isotope ^{176}Lu that comprises 2.6% of natural lutetium [204].

Table 10: Specifications of the Discovery MI used in the simulation for 4-ring scanner.

Crystal material	LYSO
Number of major rings	4
Axial crystal rings	36
Transaxial crystals per ring	544
Size of crystals (mm ³)	3.95 \times 5.3 \times 25
Total number of crystals	19,584
Axial FOV (mm)	200
Bore diameter (mm)	700
Coincidence window width (ns)	4.9
Energy resolution	12% at 511 keV
Timing resolution (ps)	375
Lower energy threshold (keV)	425
Upper energy threshold (keV)	625

7.2.3. GATE Modelling of Discovery MI scanner

The cylindrical PET scanner architecture was defined by a set of hierarchically arranged elements with four different depth levels. First level was a detector module. Each module was repeated in a ring-like manner 34 times and each module was composed of an array of 4 (transaxial) \times 4 (axial) blocks (second depth level). The blocks were divided into a grid of 4 (transaxial) \times 9 (axial) array, this is the third level of the system. Each grid finally housed a LYSO

crystal of size $3.95 \times 5.3 \times 25 \text{ mm}^3$ (fourth level). GATE repeaters were utilized so that every crystal did not have to be added manually. The crystal was repeated 36 times in each block, 4 in the y-direction and 9 in the z-direction. The blocks were then repeated 4 times in y and z-direction inside the detector module. Since the crystals were already repeated in the block, and the block was repeated in its entirety, all the module sub-volumes accompanied the repeated module. The extended AFOV scanners for 8, 20, 30, and 40 rings were modeled by repeating the scanner module 8, 20, 30, and 40 times respectively, while keeping the other geometry the same. The total number of detector elements for the (4 - 40) ring consists of (19,584 - 195,840) LYSO crystals. In addition, the attenuating materials locating at the front face of the crystals were simulated (0.7 mm thick plastic polycarbonate, 0.1 mm thick metalized mylar and mylar window of 1.5 mm thickness) based on the information provided by the GE through private communication.

Scintillation photons were digitized in GATE using the *digitizer module*. The digitizer is composed of several signal processing operations that mimic the photon detection process. The signal processing chain start with adding the *hits* (individual photons interactions) into *pulses*, converting them into singles, and sorting them into final *coincidences*. Several parameters were defined along the digitizer chain, such as crystal energy resolution at 511 keV, timing resolution, lower and upper-level energy discriminators, and the coincidence window as tabulated in **Table 10**. However, for extended axial FOV scanners, the coincidence timing window was estimated based on the empirical formula available in the literature to account for the relatively large difference in maximum time-of-flight values between the direct and oblique lines of response [79, 230]. The optimal coincidence timing window for extended AFOV scanners were calculated according to the **Equation (19)**:

$$\tau = \frac{FOV_{trans}\sqrt{1 + (\tan(\alpha))^2}}{c} + 3\Delta t \quad (19)$$

where FOV_{trans} is the transaxial FOV (70 cm), α is the acceptance angle, Δt is the coincidence timing resolution (375 ps), and c is the speed of light in a vacuum. The acceptance angles for 4-, 8-, 20-, 30-, and 40-ring scanners are $\pm 15^\circ$, $\pm 30^\circ$, $\pm 55^\circ$, $\pm 65^\circ$, and $\pm 70^\circ$ respectively.

The simulated scanner deadtime, however, was heuristically and necessarily tuned to match the experimental count-rate measurements. The scanner's non-paralysable deadtime of 200 ns was found to mimic the measurements closely. In GATE digitizer the *setDepth* value of 2 was used based on the preliminary simulation results. In addition, the non-paralysable deadtime was applied on the singles before the coincidence sorter at the depth level of detector module. The coincidence policy was set to *takeAllGoods* for all simulations in the coincidence sorter settings as it is recommended for the single window method and to accept all possible coincidences within the geometric limits set by the scanner [231].

7.2.3.1. Intrinsic Activity in LYSO crystals

Lutetium contains about ~2.6% of ^{176}Lu , which decays by β -emission (E_{\max} 593 keV) with a cascade of three γ -ray emissions (88 keV, 202 keV, and 307 keV) [204, 232]. Using the simulated density of LYSO (7.11 gm/cm^3), molar mass ($\text{Lu}_{1.8}\text{Y}_{0.2}\text{SiO}_5\text{:Ce}$), and half-life of ^{176}Lu (3.6×10^{10} y)[233], an intrinsic detector activity of 268.85 Bq/mL was calculated. This isotope emits 88 keV, 202 keV, and 307 keV gammas and two betas (E_{\max} 192 keV, 0.4% and E_{\max} 593 keV, 99.6%) [204]. The emitted gamma energies are outside the PET acquisition's energy window (425 – 625 keV). Decays of ^{176}Lu were included in Monte Carlo simulations. This intrinsic activity within the LYSO crystals was simulated as a ^{176}Lu ion source, which is the most accurate method to simulate the radioactive decay [52]. The intrinsic activity source encompassed the whole scanner, and the activity (ion source) was confined to the LYSO scintillation crystals [101]. To quantify the impact

of intrinsic activities, scanner performance was simulated with and without intrinsic activities. The count rate curves for DMI 4-ring configuration with and without ^{176}Lu background intrinsic activities are generated for visual inspection, and the ratio of NECR with and without intrinsic activity is estimated. This ratio quantifies the factor by which the ^{176}Lu background degrades the emission data.

7.2.4. System Performance

The GATE model of the Discovery MI 4-ring scanner was validated by comparing the sensitivity, spatial resolution, and NECR results of the NEMA acceptance measurements performed by Hsu et al. at Stanford University [206]. Other measurement results are also available [234, 235]. The NEMA sensitivity phantom, scatter phantom, and spatial resolution phantoms defined by NEMA NU 2-2018 protocols [236] were accurately modeled to measure the simulated DMI PET scanner performance. The tests outlined in these procedures have been mainly devised to provide a comprehensive description of typical clinical scanners' performance.

7.2.4.1. Spatial resolution

Monte Carlo modeling of spatial resolution measurements was performed according to the NEMA NU-2 2018 procedure using ^{18}F point sources. The point sources are capillary glass tubes of length 1 mm, wall thickness of 0.4 mm, and internal diameter of 1 mm. The activity per source was 0.15 kBq, about ~ 190 kBq/cc for all point sources. Simulations using 4-ring scanner were performed with sources placed at 1 and 10 cm radial offset vertically from the center of the FOV to compare the simulation result with measurement data. In addition, to understand the effects of parallax error, spatial resolution was simulated with sources placed at 0, 1, 5, 10, 15, and 20 cm radial offset vertically from the center of the scanner FOV in air using all (4 - 40) scanner ring configurations. Simulation was performed such that the total coincidences were greater than

100,000 per point source. The simulation output data were reconstructed using the filter back projection (FBP) algorithm with a voxel size of $2 \times 2 \times 3.5 \text{ mm}^3$, without any smoothing, as specified in the NEMA procedure using the STIR [237] reconstruction platform. The full width at half maximum (FWHM) and full width at tenth maximum (FWTM) of the point source response function were evaluated by plotting one-dimensional response functions along with line profiles through the peak of the distribution of each point source using ImageJ [238]. System axial, tangential, and radial spatial resolutions were obtained as per NEMA specification [236]. See **Table 11** and **Figure 36** for results.

7.2.4.2. Sensitivity

The NEMA PET Sensitivity Phantom was simulated to measure the sensitivity of the scanner. The purpose of this test is to measure the ability of the GATE DMI scanner system to detect the true coincidence events per second per unit of radioactivity in the FOV. The sensitivity phantom consists of five concentric 700 mm long aluminum tubes with a polyethylene tube filled inside the smallest of the concentric aluminum tubes. The innermost polyethylene (density 0.96 g/cm^3) tube has a fillable volume with an internal diameter of 2 mm and wall thickness of 0.6 mm. All tubes were modeled in GATE for sensitivity measurements. Aluminum tubes (density 2.7 g/cm^3) were subsequently added one at a time for simulation, as per NEMA specification. The decay of radiouclide was simulated using the F-18 positron emission source, and decay correction was performed for subsequent simulations to mimic physical measurements. A standard 70 cm long line source with an outer and inner diameter of 3.2 mm and 2 mm was simulated for a line source insert for the 4 and 8-ring scanners. In addition, a 200 cm long cylindrical line source, in aluminum sleeves of varying thickness, with the same diameter was simulated in all scanner configurations (4, 8, 20, 30 and 40-ring) for sensitivity comparison. 4 MBq ^{18}F sources were used in all cases.

The sensitivity phantoms were simulated for thirty seconds to minimize statistical uncertainty. Trues-only sensitivity was simulated by subtracting random events, and negligible scatter events from prompt coincidence events. All simulations had true counts of more than 100,000 coincidences. Random events were estimated using the singles rate method. For each added sleeve, the total number of true coincidences per slice was calculated using single-slice rebinning and normalized by source activity and total acquisition time. Sensitivity for each aluminum tube was computed, and the sensitivity without attenuation was determined by extrapolation to zero thickness (see **Figure 38(A-B)**).

7.2.4.3. Count rates, scatter fraction, and Noise Equivalent Count Rates

The NEMA scatter phantom is a right circular cylinder of a polyethylene material of density of 0.96 g/cm³, with an outside diameter of 20.3 cm and length of 70 cm [236]. A line source is a hollow cylindrical tube with an inner diameter of 3.2 mm. It is inserted in a hole of diameter 6.4 mm drilled at a radial offset of 45 mm parallel to the phantom's central axis. The line source is also polyethylene. Two versions of scatter phantoms were simulated, one with the phantom of length of 70 cm, as recommended by NEMA, and the other with a length of 200 cm for count rates, scatter fraction (SF) and the NECR evaluation of longer than 8-ring PET geometries. Data were acquired using sufficient particles such that statistical uncertainties in simulations are less than 2%. Simulations were performed in the high-performance computing cluster at the University of Iowa. The scatter fraction and NECR were calculated by **Equations (20)** and **(21)**:

$$SF = \frac{Scatter}{Trues + Scatter} \quad (20)$$

and

$$NECR = \frac{T^2}{T + S + k.R} \quad (21)$$

where T, S, and R are trues, scatter, and randoms coincidence rates, respectively. The scatter fraction is calculated using the true and scatter coincidence events estimated directly in the simulation. Randoms coincidences were measured using the singles-based method. The k value was set to 1 on the assumption that a low variance estimate of randoms is used. Finally, the NECR was computed as a function of activity concentration in the phantom because the PET scanners are often compared based on the peak NECR values. For the comparison of NECR peak values, scanners with rings 4, 8, 20, 30, and 40 were simulated with a scatter phantom of length 200 cm.

i. Simulation using scatter phantom of length 70 cm

The line source was filled with an activity of 1, 2, 5, 10, 20, 40, 60, 80, 100, 200, 300, 400, 500, 600, 700, and 800 MBq ^{18}F , this corresponds to an activity concentration of (0.05 – 36.36) kBq/mL. Scatter phantom volume (~22,000 mL) was used to calculate the activity concentrations.

ii. Simulation using scatter phantom of length 200 cm

The line source in a 200 cm long scatter phantom was filled with an activity of 1, 2, 5, 10, 20, 40, 60, 80, 100, 200, 300, 400, 500, 600, 700, and 800 MBq ^{18}F . Using the phantom volume of ~62,800 mL, the activity concentrations in the phantom were (0.02 – 12.74) kBq/mL.

iii. Count rates curves using NEMA guidelines

First, the GATE simulation output root file's coincidence tree was read in ROOT software [239] to sort the sinogram data, i.e., its SinogramS and SinogramTheta. The data analysis was then performed in MATLAB for 2D sinogram generations to estimate the trues, randoms, and scatter coincidences. Next, per NEMA [236], the sinogram data were transformed into a 2D histogram with 640 projection bins (-320 to 320 mm from the center of FOV) for the x-axis and 320 bins (0 to π) vertical y-axis. A Gaussian filter was then applied to account for the effect of the detector's limited spatial resolution. Subsequently, the NEMA analysis of Monte Carlo results with randoms

from singles rate was performed. An illustration of the NEMA protocols for count rates estimation is shown in **Figure 36**. Once the trues, randoms, and scatters were estimated for different activity levels, the corresponding count rate curves and NECR can be estimated. It should be noted that the same protocols were applied for the extended AFOV scanners as well, although the data were acquired with the extended version of the phantoms.

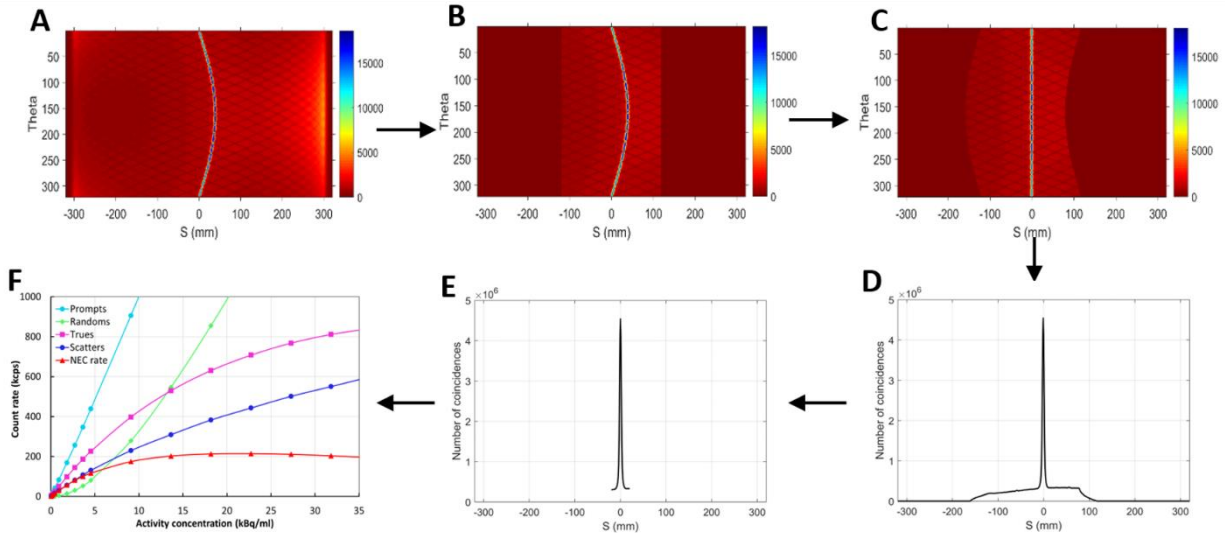


Figure 36: Count rates estimation using the NEMA protocol [236]. The activity of 800 MBq was used in the scatter phantom to generate this figure using the 4-ring scanner. (A) Sinograms of coincidences obtained from GATE root output (B) Sinogram after inserting Gaussian filter and setting pixels farther than 12 cm from the center of FOV to zero (C) Sinogram after alignment according to maximum values for each projection angle (D) Sum of all projection angles of the sinogram (E) Selecting the central 40 mm strip to estimate the scatters and randoms (F) plot of count rates curves and NECR. A sinogram-based analysis was performed to estimate the coincidence event rates.

7.3. Results

7.3.1. Quantification of contribution from Intrinsic Activity from LYSO crystals

The natural radiation from the LYSO crystals have shown only minor impacts on PET imaging performance due to the relatively low energy of gamma emissions from ^{176}Lu decay. The cascaded γ -emissions from ^{176}Lu have energy below the lower DMI scanner energy window threshold as tabulated in **Table 10**. Simulations suggest that in the clinical activity range (5-15

kBq/ml), the impact of the intrinsic activity on count rates is less than 1%; please refer to **Figure 41**. As its impact is statistically low, we did not include the intrinsic activities for all extended LAFOV scanners. In addition, intrinsic activities were not simulated in spatial resolution and sensitivity estimations as it would, in turn, increase the computation cost without impact on results.

7.3.2. Spatial resolution

Table 11 shows the spatial resolution results in terms of FWHM (mm) for two radial positions in both simulation and measurements. Data show agreement between measured and simulated DMI scanner data, lending confidence to the validity of GATE simulation. The spatial resolution values obtained using the 4-ring simulated scanner model are within (3.20 - 7.97)% of the published measurement results. Simulated FWHMs are consistently demonstrate a better resolution than experimentally measured values. This could be due to the absence of modeling within GATE of the process of light spreading and light sharing between the SiPM arrays. The spatial resolution in the center of the transverse field of view is about 4 mm, with an expected radial resolution loss at increased radii.

The transverse resolution, the average of radial and tangential resolutions, at the center of imaging system for different scanner ring configurations is shown in **Figure 37(A)**. Results show that transverse resolution is relatively constant (very small degradation) with extended scanner ring configurations at the center of the scanner FOV. In addition, the results show a degradation in axial resolution when extending the scanner ring configurations up to 30-ring ($\alpha \pm 65^\circ$) and a minimal change in axial resolution was found when further extending the scanner to 40-ring ($\alpha \pm 70^\circ$). We found that the axial resolution degrades from 4.40 mm to 5.45 mm at the center of the scanner FOV when extending the 4-ring ($\alpha \pm 15^\circ$) scanner configuration to 40-ring configuration ($\alpha \pm 70^\circ$). In addition, the transverse resolution as a function of position radially offset from the

center of the scanner FOV is characterized. A comparison of transverse resolution between 4, 8, 20, 30, and 40-ring scanner configurations is presented in **Figure 37(B)**.

Table 11: Spatial resolution results for different radial, tangential and axial positions for simulated and measured point sources at two radial positions: (0, 1, 0) cm and (0, 10, 0) cm within the scanner FOV. The mean values of the three different reconstructed images are reported. Measurement performed at Stanford University from Hsu et al.[206] are also reported for comparison.

	GATE simulations (this work)		Measurement (Stanford)	
	FWHM	FWTM	FWHM	FWTM
(0, 1, 0) cm				
Radial	3.94	8.87	4.17	9.14
Tangential	4.10	8.68	4.40	9.17
Axial	4.41	9.79	4.57	10.38
(0, 10, 0) cm				
Radial	5.29	9.78	5.65	10.36
Tangential	4.89	9.24	4.74	9.68
Axial	5.90	11.52	6.39	12.34

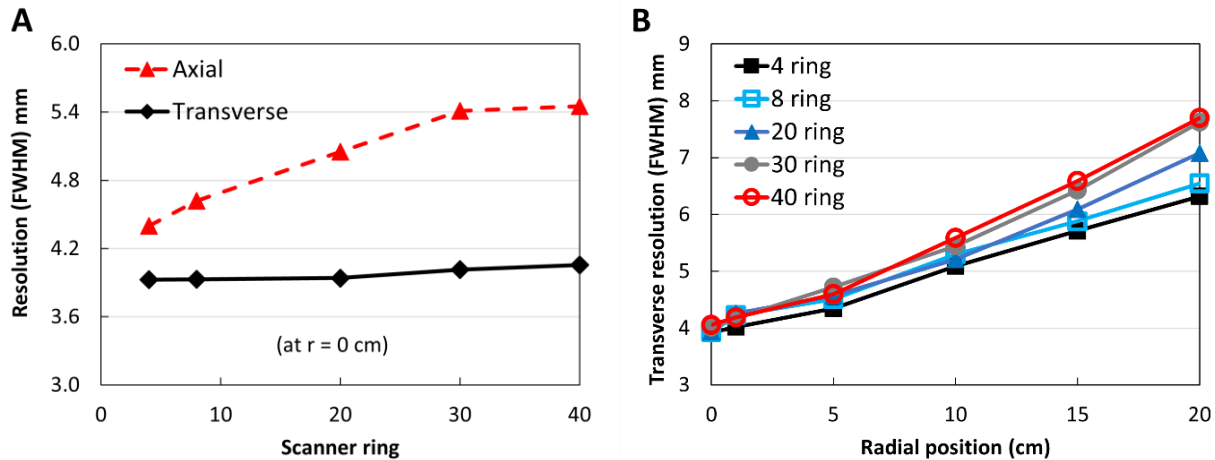


Figure 37: (A) Spatial resolution along the axial and transverse (average of radial and tangential) direction for different scanner rings (B) Transverse resolution for six-point sources with varying radial offsets (at 0, 1, 5, 10, 15, and 20 cm) in the center of the axial FOV for five scanner geometries.

The results obtained in this work are similar as the simulation result presented by Schmall et al. using a 4 x 4 x 20 mm³ LSO crystals [240]. Unlike this work, they simulated the point sources

in a warm background in the center of the scanner FOV and they utilized the iterative OSEM algorithm. As this work has followed the NEMA procedures, the results of spatial resolution might have suffered from re-binning and interpolating process of simulated data during the analytic reconstruction.

7.3.3. Sensitivity

The literature reported sensitivity of the Discovery MI 4-ring scanner was 14.0 cps/kBq [206], while our simulation produced a sensitivity of 14.86 cps/kBq at the center of the field-of-view of the scanner using a 70 cm NEMA sensitivity phantom. This is ~5.95% difference between the measurement and simulation results (**Figure 38A**). The simulated sensitivities using the sensitivity phantom of 200 cm length for 4, 8, 20, 30, and 40-ring scanners were 5.20, 20.84, 109.36, 207.31, and 313.78 cps/kBq respectively. Increase in sensitivity agrees with calculations based on geometry and solid angle. The attenuation-free sensitivities for 4, 8, 20, 30, and 40-ring scanner configurations are presented in **Figure 38 (B)**. **Figure 38 (B)** shows the quadratic (second-order polynomial) increase in sensitivity with axial FOV, as expected [222]. In all simulations, random rates were less than 3%, and scatters were less than 0.5% of the total coincidence events.

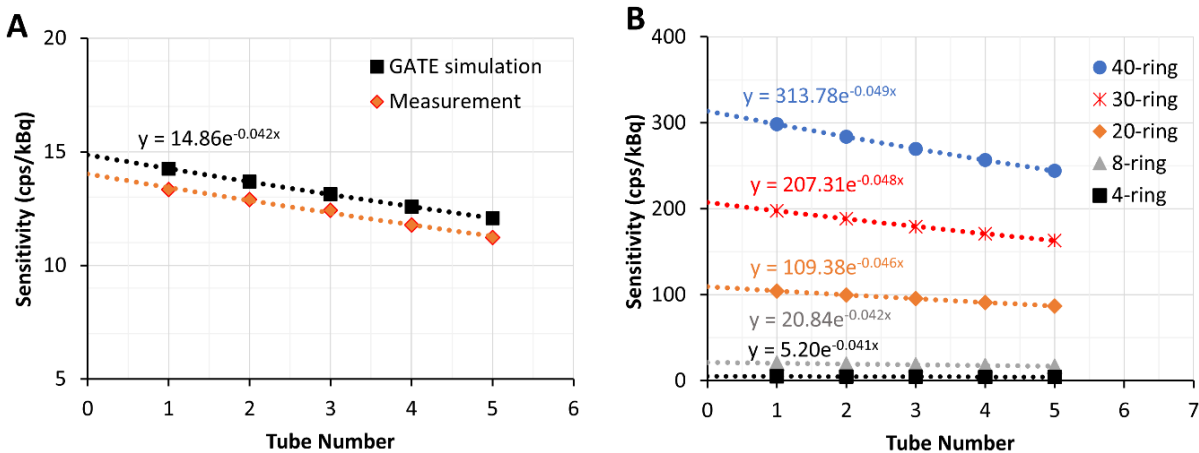


Figure 38: (A) Figure shows a comparison of simulated and measured absolute attenuation free sensitivity for the DMI 4-ring scanner. There is a 6.41% difference between simulation and

measurement [206] data points. Exponential regression of the true count rates was used for attenuation-free sensitivity estimation. (B) Comparison of attenuation-free sensitivities for 4, 8, 20, 30, and 40-ring scanners.

It should be noted that sensitivities for 4-ring scanner were simulated using the standard 70 cm long line source for comparison with measurement data. In addition, to suitably compare the sensitivity of 4-ring scanner to extended AFOV scanners, a 200 cm long line source was simulated in (4 - 40)-ring scanners. Monte Carlo suggests that simulations of 70 cm standard sensitivity phantom in all ring configurations give a sensitivity enhancement up to ~27 times compared to the sensitivity of the 4-ring clinical DMI scanner. Furthermore, sensitivity simulations using a long line source of 200 cm in all scanner configurations performed herein resulted in a sensitivity gain of ~60-fold using a 40-ring scanner compared to the 4-ring scanner. This is illustrated in **Figure 39 (B)**; the area under the axial profile for the 40-ring scanner (red curve) is ~60 times larger compared to the area under the axial profile for the 4-ring scanner (black curve).

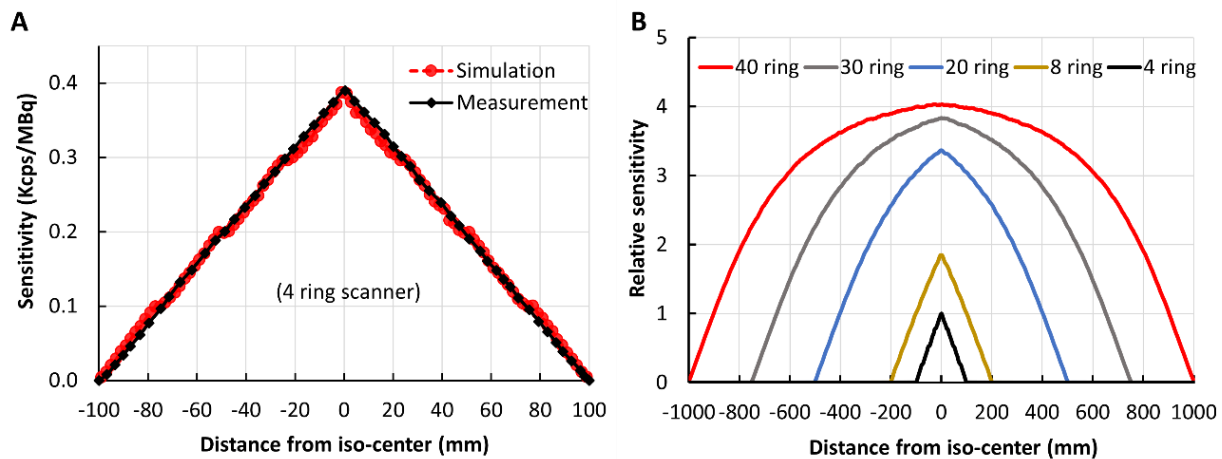


Figure 39: (A) Axial sensitivity profile of contiguous axial slices from the center of the scanner for 4-ring scanner. (B) Axial sensitivity profiles for 4, 8, 20, 30, and 40-ring scanner configurations. Acceptance angles were not restricted for these profiles as the Discovery MI scanner accepts all oblique lines. Sensitivity profiles were obtained using simulation of a 200 cm long 3.2 mm diameter line source with 4 MBq ^{18}F activity.

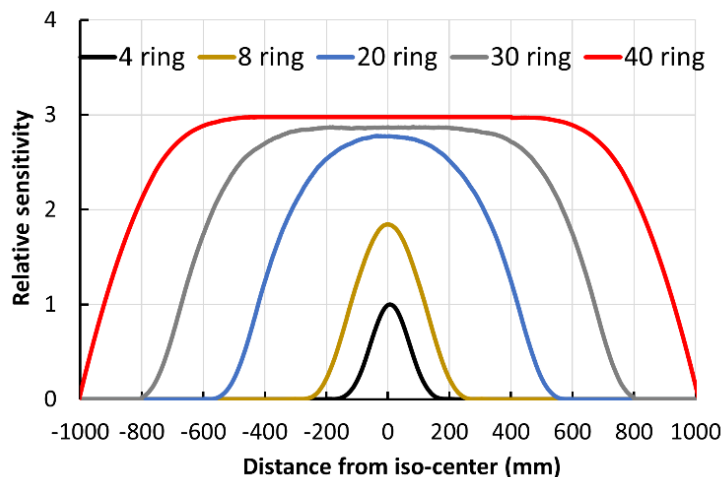


Figure 40: Relative sensitivity profiles for a line source of 200 cm length in a 30 cm diameter, 200 cm long cylindrical phantom, for scanners with 4-ring, 8-ring, 20-ring, 30-ring, and 40-ring configurations. Line source had a same diameter as in NEMA sensitivity phantom. Similar sets of sensitivity profiles were seen in simulations performed by Surti et al [75].

The sensitivity profile in the 3D PET was triangular for a 4-ring scanner, as shown in **Figure 39 (A)**, with a peak at the center of the field of view, as expected. However, for extended AFOV scanners, sensitivity profiles are no- longer triangular, as shown in **Figure 39 (B)**, due to the larger solid angle acceptance. The sensitivity profiles shown in **Figure 39 (B)** will be much different if we simulated a line source in the presence of attenuation medium [223, 241]. To understand the impact of attenuation to the sensitivity profiles, a 200 cm long phantom with 30 cm diameter including a line source of 200 cm was simulated for (4-40) ring configurations and the results are presented in **Figure 40**, however, this is not a NEMA test. This is included because the NEMA test does not have the sensitivity test for higher attenuation scenarios as in patient imaging for sensitivity profile comparisons. Sensitivity profiles are relatively uniform in the central 80 cm for 30-ring (1.5 m) scanner and central 120 cm for a 40-ring (2 m) scanner with less than 8% change, as shown in **Figure 40**. This suggests that a single bed position is sufficient for imaging a 80 cm and a 120 cm long object in a 30-ring and 40-ring scanners [223]. The extended AFOV

scanners shows the relatively uniform axial profiles at the center of the scanner FOV because the attenuation is greater for oblique lines of response and the center of the scanner FOV contribute more oblique lines of response [241]. This explains the differences in sensitivity between the different ring configurations in almost attenuation free (**Figure 39B**) and higher attenuation (**Figure 40**) scenarios.

7.3.4. Count rate performance

Count rate results were acquired up to 35 kBq/mL, although clinical FDG studies are typically performed with activity concentrations of less than 15 kBq/mL. Count rates were obtained for the 4-ring scanner using 20 cm diameter 70 cm long phantom are displayed in **Figure 42**. The simulated results included the effects of modeled deadtime. Different types of simulated coincidence count rates as a function of increasing activity concentration are shown in the figure. At first, contributions from crystal's intrinsic activities were estimated by simulating the count rates curve with and without intrinsic activities.

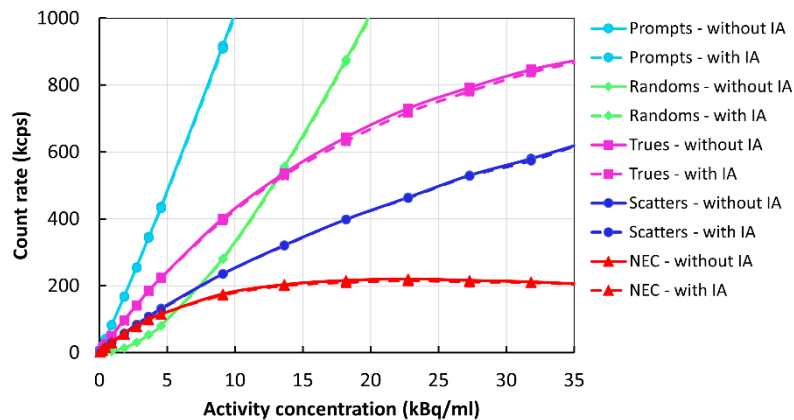


Figure 41: Count rates comparison between simulation with and without intrinsic activities (IA). The volume of the scatter phantom was considered for the activity concentration calculations. The impact of intrinsic activities was found to be < 1% in the clinical activity range. Therefore, intrinsic activities in LYSO crystals are not included in all simulations performed herein to save the computation burden.

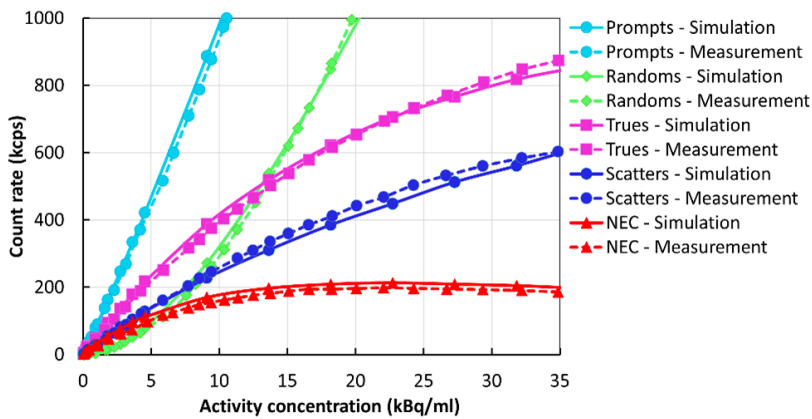


Figure 42: Comparison of count rates curve between simulation and measurement performed at Stanford University for DMI 4-ring scanner [206]. The volume of the scatter phantom (~22 L) was considered for the activity concentration calculations. The maximum deviation in activity concentration measurements was 2.43%.

The comparison of simulation with literature measurements resulted in excellent agreement within the measurement uncertainties, in the range of activities practically used in clinical and research scans. The NECR continues to increase slowly beyond the point at which true count rates are equal to the random count rates. For the 4-ring scanner, the measured NECR peak was 201.1 ($\pm 3.14\%$) kcps at 22.1 ($\pm 3\%$) kBq/mL with a scatter fraction of 40.4% [206], while the simulated peak NECR was 212.92 ($\pm 2\%$) kcps at 22.7 kBq/mL with a scatter fraction of 38.9%. Comparing the NECR peak count rates between simulation and measurements gives a percent difference of ~5.71%. It should be noted that the count rates error compared against the Stanford data [206] was ~3%, and the statistical uncertainties in simulations were < 2.0% for count rate curve estimations. The summary of count rates, scatter fractions and comparisons of NECR peak values for scanners with rings 4, 8, 20, 30, and 40 with a scatter phantom of length 200 cm are plotted in **Figure 43 - Figure 45**.

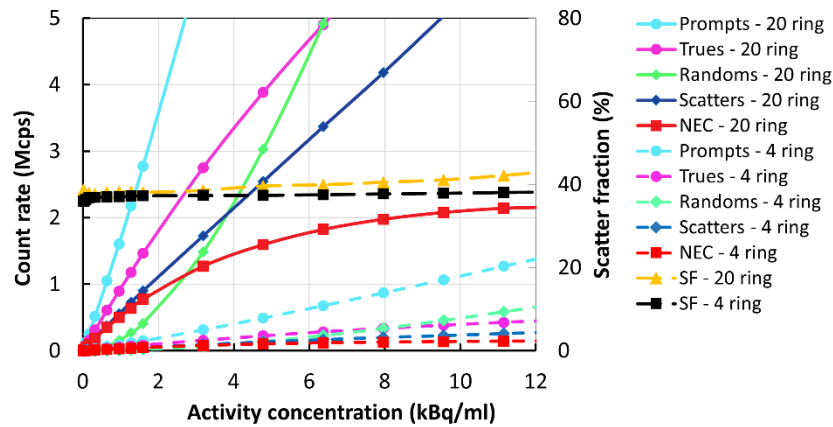


Figure 43: Count rate curves and NECR for 4-ring (AFOV 20 cm) and 20-ring (1 m AFOV) scanner. Count rate curves for the 4-ring scanner lies at the bottom of the plot. For comparison with 4 and 20 ring scanner NECR, a 200 cm long scatter phantom was simulated in both ring configurations. A gain of 15 times can be expected when comparing the NECR peak values.

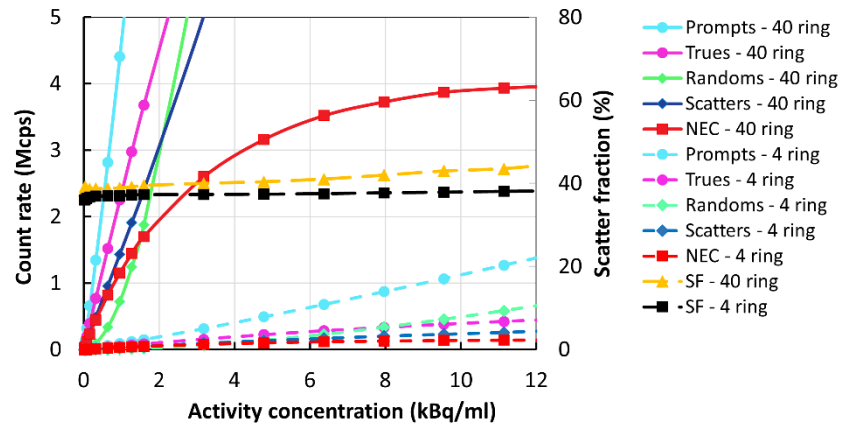


Figure 44: Count rate curves and NECR for 4-ring (AFOV 20 cm) and 40-ring (2 m AFOV) scanner. Count rate curves for the 4-ring scanner lies at the bottom of the plot. For comparison, 200 cm long scatter phantom was simulated in both ring configurations. A gain of 28 times can be expected when comparing the NECR peak values.

We did not find a clear NECR peak up to 12 kBq/mL for 20, and 40-ring scanner simulations at the activity concentrations simulated. All simulations are based on a non-paralysable deadtime of 200-ns per detector block. The NECR comparison of 4-ring vs. 40-ring gives a performance enhancement of 28-fold, whereas comparison of 4-ring vs. 20-ring gives a

performance of 15-fold using the 200 cm long scatter phantom in all simulations. The comparison of NECR peak values for 4-40 ring scanners is tabulated in **Table 12**.

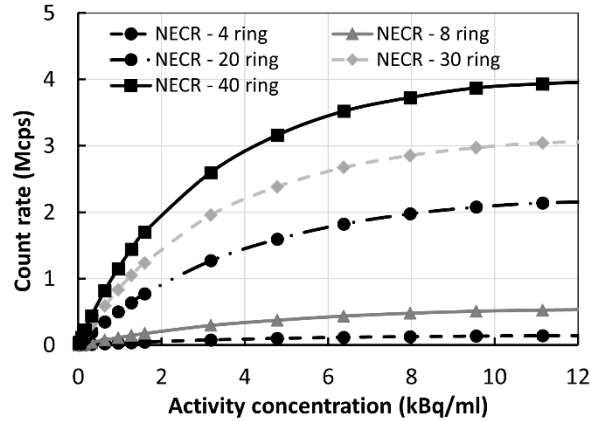


Figure 45: The increase in NECR as a function of axial length for 4, 8, 20, 30, and 40-ring scanners. Note that for this comparison, all scanners were simulated with 200 cm long scatter phantom with an activity concentration range of (0.02 – 12.74) kBq/mL.

Table 12: Comparison of NECR peak values for 4 - 40 ring scanners. The NECR peak value for 4-ring scanner using a 200 cm long scatter phantom is compared to 8, 20, 30, and 40-ring scanner configurations.

	NECR peak (Mcps)	NECR Gain
4 - ring	0.143	1
8 - ring	0.536	3.75
20 - ring	2.162	15.12
30 - ring	3.066	21.44
40 - ring	3.975	27.80

7.4. Discussion and Conclusions

The objectives of this work were to first, develop a Monte Carlo model of the Discovery MI PET scanner and validate its accuracy against published measurement values. Once the Monte Carlo model was validated for the standard PET system, we expanded the axial extent of the simulated scanner architecture to study performance as a function of AFOV. We simulated all NEMA tests to characterize the performance of our model of the Discovery MI 4-ring scanner.

Subsequently, after validation of a 4-ring Discovery MI scanner Monte Carlo model, we characterize the performance of extended AFOV scanners, using NEMA tests for spatial resolution, sensitivity, count rate, and scatter fraction to estimate the sensitivity and NECR gain. LAFOV scanner sensitivity and NECR gain increase significantly with axial length. The NEMA testing of the different ring configurations up to 2 m reveals the performance gain of ~ (28-60) times relative to the 4-ring Discovery MI PET scanner as defined by the sensitivity and NECR peak values.

Validation of the Monte Carlo model of the 4-ring scanner appeared successful. The estimation of spatial resolution was in a close agreement between simulation and measurement data, with less than a 8% difference. Spatial resolutions were better in radial and tangential direction than in the axial direction for both the measured and simulated data. Spatial resolution simulations in extended AFOV scanners suggest that the maximum degradation in the axial resolution is ~23.8% compared to the Discovery MI 4-ring scanner. However, the transverse resolution is relatively constant, with very small degradation was observed when increasing the axial acceptance angle up to $\pm 70^\circ$. The results obtained in this work compared well with the results presented by Schmall et al. [240].

The simulated model reproduced the experimental counting rates curves with less than 6% relative errors over the range of clinical activity concentrations found in (2-6 kBq/mL) and less than 8% up to 25 kBq/mL. Also, a comparison of the measured and simulated NECR peak was within ~6% of actual 4-ring scanner. The sensitivity profiles for scanners with AFOV greater than 1 m (20-ring) using the 200 cm long scatter phantom reveals the uniform sensitivity profile at the central part, as shown in **Figure 40**. **Figure 40** tells us that if we want to image major organs, from head to pelvis, with the peak sensitivity then an AFOV of 1.5 m (30-ring) appears sufficient

because this configuration shows a relatively uniform profile in the central 80 cm, which covers most of the major organs.

It should be noted that several parameters were not simulated in this study. First, the scanner bed was not considered in this study as its material composition was not known. Second, the crystals' casing materials (light shield) are also not accounted for in simulations as its material and compositions were unknown. The impact of natural radioactivity from LYSO crystals was studied first and found that impact is minimal, < 1%, this is because virtually all the cascaded γ -emissions have energy below the lower threshold of the DMI energy window. Due to this, at clinical activity concentrations, background noise from electronics and natural radioactivity from crystals are often considered negligible. Therefore, we did not include LYSO intrinsic activities in all simulations. However, care should be taken when simulating low activity using the extended AFOV scanners and for low count rate imaging applications.

Another limitation of this study is the choice of scanner deadtime in simulations. The dead time digitizer settings have a certain degree of uncertainty since these values were not provided by the manufacturer. The scanner's deadtime was heuristically tuned to match the physical measurements and then applied to other simulations. This could have contributed a few percent in differences between the simulation and measurement results in higher activity concentration simulations.

The simulations show a substantial NECR peak enhancement of ~28 times relative to the 4-ring Discovery MI PET scanner for a 2 m long AFOV with 25 mm LYSO crystals thickness. This is aligned with the study performed by Poon et al. using the simulation of the Siemens Biograph mCT with LSO crystals [79]. These performance enhancements are in-line with those measured on the uEXPLORER [69] and Siemens Biograph Vision Quadra [74]. However, the

NECR peak obtained in this work for the 40-ring scanner configuration is about a factor 2 times higher than the NECR peak reported by Spencer et al.[69] using the uEXPLORER scanner. In retrospect, this is not surprising because the LYSO crystal thickness used in uEXPLORER is lower (18.1 mm) [70] than crystals used in Discovery MI geometry (25 mm) and they used a scatter phantom of 175 cm length [206]. The sensitivity of the Discovery MI scanner dramatically decreases, by a factor of (1.30-1.45) when we simulated (4-40)-ring configurations using a crystal thickness of (18.1-20) mm. In addition, the uEXPLORER does not accept all oblique lines of response as they imposed a maximum axial angle of acceptance of $\pm 57^\circ$ [69, 70]. As the 4-ring DMI scanner uses all oblique lines, we did not restrict the axial angle of acceptance in all extended axial FOV simulations performed herein. This increases the true events however a higher proportion of the oblique events contribute more scatter events, and it increases the attenuation in the scatter phantom **Figure 43 - Figure 44**. The scanners used in this work hence collect the data using the maximum axial angle of acceptance of $\pm 15^\circ$, $\pm 55^\circ$, and $\pm 70^\circ$ for 4, 20, and 40-ring scanners, as these are the unrestricted acceptance angles for each of these geometries. The NECR peak that we estimated for a 20-ring (1 m) scanner is close to that of uEXPLORER.

The clinical performance of the long axial field of view Biograph Vision Quadra (106 cm) scanner was recently published [74]. However, their report does not have any suitable data for comparison with this work. Prenosil et al. recently reported the NECR peak of 2.956 Mcps (using maximum full ring difference MRD of 322 with an acceptance angle of $\pm 52^\circ$) using Siemens Biograph Vision Quadra [220] which is close to the simulated NECR peak of 3.066 Mcps using 30-ring DMI scanner as tabulated in **Table 12** in the results section although the NECR peak was obtained at the different activity concentrations.

High sensitivity and extended AFOV PET systems can enable short-duration imaging, low-dose imaging [76, 242], single bed position scanning, whole-body dynamic and parametric imaging studies [210, 211, 213, 215, 243] such as radiotracer kinetics throughout the entire body. This would further enable applications for PET in the field of low count imaging applications, such as ^{90}Y imaging, ^{89}Zr monoclonal antibody imaging, and theragnostic applications [244], pediatric imaging [245], screening of patients at risk [246], and possibly many others [68, 78, 209].

In conclusion, we modeled the 4-ring Discovery MI PET scanner based on data available in the literature and provided from the manufacturer. The simulation models were validated against experimental measurements in the literature using the 4-ring Discovery MI PET scanner. Following the scanner validation, more scanner rings were added to simulate the hypothetical long AFOV scanners up to an axial length of 2 meter. In addition to the standard NEMA NU 2-2018 protocol, a new set of simulations based on extending NEMA phantoms were utilized to characterize the physical performance of the scanners. Spatial resolution, sensitivity, count rates, scatter fraction, and noise equivalent counting rates were evaluated. Overall, the longest AFOV of 2 meter and 25 mm thick LYSO crystals resulted in expected significant performance gains relative to the current 4-ring Discovery MI PET scanner architecture.

CHAPTER 8: PET PHANTOM DEVELOPMENT

8.1. Introduction

Accuracy of image-based dosimetry is entirely dependent upon the accuracy of PET or SPECT scanning systems in quantitatively mapping radionuclide concentrations (Bq/mL) *in vivo*. The challenge is that we have no non-invasive way to validate the accuracy of that measurement in the human body. To circumvent this limitation, so-called “phantoms” are used. Imaging phantoms are artificial test-objects that contain known concentrations of radioactivity that are used as stand-ins for a patient to ensure that imaging systems are accurately measuring radioactivity concentrations. Phantoms ideally should challenge and measure the imaging system’s ability to accurately perform standard corrections like scatter correction, attenuation correction, and dead time correction, while at the same time measuring inherent imaging properties like spatial resolution and uniformity. Phantoms are routinely used to calibrate scanners, to perform various quantitative scanner performance measures, and for quality control purposes. In more advanced applications, phantom testing can be used to verify performance measurements of new imaging protocols, testing performance characteristics of reconstruction methods, generating scanner harmonization data, and even generating image quality metrics. Phantoms are used not just in nuclear medicine, but in a wide variety of imaging modalities such as computed tomography (CT), magnetic resonance imaging (MRI), and ultrasound. Numerous modality-specific phantoms have been designed to examine different aspects of the imaging system performance.

Phantom imaging provides the opportunity for a ground-truth measurement. In PET and SPECT applications only a few phantom designs are in common use. They include a simple cylindrical phantom of diameter ~20 cm, the ACR 20 cm diameter Jaszczak phantom with both hot and cold features, a slightly larger and body-shaped NEMA IEC Image Quality (IQ) phantom

with six spheres of different sizes, and a Society of Nuclear Medicine and Molecular Imaging Clinical Trials Network (CTN) chest phantom as shown in **Figure 46**.

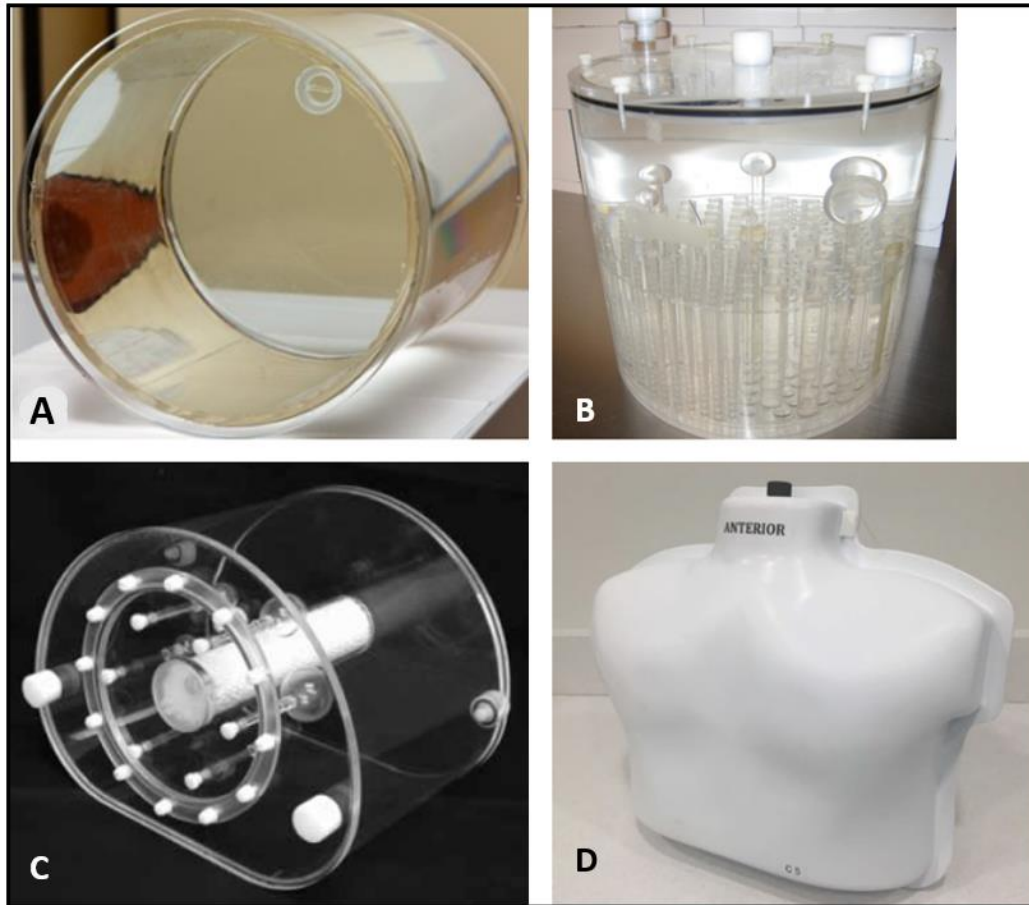


Figure 46: Commonly used phantoms in nuclear medicine PET and SPECT applications. (A) Cylindrical (B) Jaszczak (C) NEMA image quality and (D) CTN chest phantom.

Different phantoms have different abilities to provide information about various critical scanner performance metrics, including accuracy of calibration, uniformity, image resolution, noise, contrast recovery coefficient performance, and lesions detectability. **Table 13** summarizes which phantoms perform which of these functions well.

Table 13: Comparison of different phantoms.

	Phantom	Use case
1	Cylindrical Phantom	Scanner calibration accuracy (QC and QA), reconstructed resolution, noise, and uniformity
2	ACR Jaszczak	Spatial resolution, lesion detectability, calibration
3	NEMA IQ	Image quality, calibration, noise, generate recovery coefficient curve
4	CTN Chest phantom	Image quality, calibration, noise, generate recovery coefficient curve

The partial volume effect is an issue for the absolute quantification of the uptake in small objects. This effect is significant when the object of investigation is 2-3x smaller than the system's FWHM, as it is in almost all brain structures, small tumors, and the myocardial wall. This results in large biases when tracer uptake is measured. This effect arises from the two different mechanisms due to the (a) finite resolution of the PET scanner (b) image sampling [247]. Because of the finite resolution of the PET scanners (4-5 mm), the image of a small source object appears to be larger but dimmer, and the activities are also found outside of the object, called as "spills out" effect. Furthermore, in PET, the radiotracer distribution is sampled on a voxel grid in the image space, as a result of that voxels do not match the actual contours of the tracer distribution. Thus, only inner voxels will have a true activity, but voxels located within the source object's boundaries will have partial activities. In other words, objects will have their activity concentration distorted near their edges and will be blurred out into the surrounding region. Therefore, the partial volume effect due to image sampling is also a concern in high-resolution imaging such as CT and MRI.

Multiple techniques exist for partial volume correction, such as deconvolution (used for image restoration), the correction applied at the voxel-level including kinetic modeling, and the

correction applied at a region of interest level such as using the recovery coefficients (RC) with the aim of improving PET quantitative accuracy. The simple and commonly used method frequently used in PET tumor imaging for partial volume correction is the use of RC values. Usually, the pre-calculated RC value for an object is used to approximate the true activities in smaller objects or tumors. This method is very simple and usually yields robust results in the case of phantom imaging. However, this method may not be suitable for patient imaging, where the tumor uptake is not uniform throughout the tumor.

The recovery coefficient (RC) value for each sphere size in the phantom is defined as a ratio of PET measured radioactivity to true injected radioactivity concentration in the spheres without surrounding activity.

$$RC = \frac{\text{measured radioactivity}}{\text{known sphere activity}} \quad (22)$$

For ideal quantization, the RC coefficient value is 1. In the presence of background activity:

$$RC = \frac{\text{measured sphere radioactivity} - \text{measured background activity}}{\text{known sphere activity} - \text{known background activity}} \quad (23)$$

The RC is also referred as contrast recovery coefficient (CRC) when in the presence of background activity, which accounts for the contrast at which the data is acquired in the presence of the background activity. These values are usually estimated by drawing the region of interests (ROIs) in the reconstructed image slices. The percent contrast recovery for the hot spheres as defined by the NEMA guidelines for each hot sphere is [236, 248] is given by **Equation (24)**:

$$Q_{H,i} = \frac{\left(\frac{C_{H,i}}{C_{B,i}} - 1\right)}{\left(\frac{a_H}{a_B} - 1\right)} \times 100 \% \quad (24)$$

where, $C_{H,i}$ is the average counts in the ROI for spheres i , $C_{B,i}$ is the average of homogeneous background ROI counts for sphere i , a_H is the activity concentration in the spheres and a_B is the activity concentration in the background.

The background variability (coefficient of variation) as a measure of image noise or image roughness is defined by using the **Equation (25)**:

$$N_i = \frac{SD_i}{C_B} \times 100 \% \quad (25)$$

where, SD_i is the standard deviation of the background ROI counts for sphere i and C_B is the average background ROI counts for sphere i . For the ideal case, $N_i = 0\%$. The background signal-to-noise ratio (SNR) is reciprocal of the image noise or the background variability.

The uniform phantom is a 20 cm long cylindrical phantom with a 20 cm diameter with a phantom casing material of polyethylene. It was designed such it can be filled with a uniform activity concentration. This phantom is particularly helpful when measuring the image uniformity and for scanner calibration. Image uniformity can be assessed using the ROI drawn over the imaging data of the phantom and it can be assessed in either radial or axial directions. Using the method developed by Lodge et al, an accurate and reproducible measurement of spatial resolution can be achieved by imaging the uniform phantom at a slightly oblique angle [249]. The periodic scanning of the uniform phantom provides valuable information to a PET/CT quality control program.

The American College of Radiology (ACR) PET phantom is the next most commonly used phantom in PET. It is a cylinder with an internal radius of 10.8 cm. For its use in PET, the upper faceplate has 4 fillable thin-walled cylinders (8, 12, 16, and 25 mm in diameter), two additional 25 mm cylinders (to simulate air and bone). The lower part of this phantom consists of 6 sets of acrylic rods arranged in a pie-shaped pattern with 4.8, 6.4, 7.9, 9.5, 11.1, and 12.7-mm diameter

respectively. For its use in SPECT, the middle portion of this phantom contains 6 solid spheres (Figure 46 (B) and Figure 47). This phantom is used to assess the scanner image uniformity and scanner calibration. In addition, this phantom is particularly useful for high image contrast resolution measurements, and even assessing image quality metrics for PET imaging. This phantom can also be useful in SPECT imaging for performance evaluations such as collimator, calibration, reconstruction parameters, and quality control.

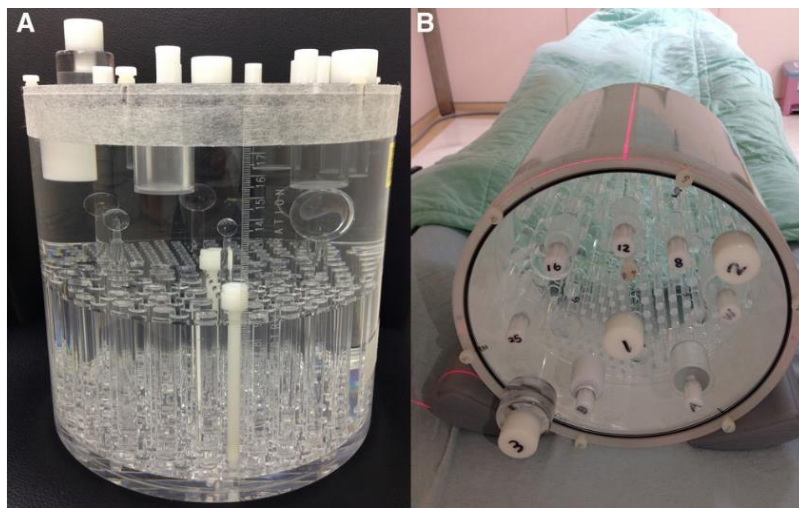


Figure 47: The ACR PET phantom (A) side view of the phantom shows upper faceplate, middle portion with spheres (for use in SPECT), and lower part with six different sizes of rods arranged in a 6 pie-shaped pattern (B) top view of the phantom.

The NEMA IQ geometric phantom was developed by NEMA (National Electrical Manufacturers' Association) has been in use since 2001 [236]. It consists of six different sized fillable spheres as inserts (10, 13, 17, 22, 28, and 37 mm), with a central inner cylinder used to mimic the human lung and measure the effectiveness of scanner correction. The main tank holds ~9.5 liters of water. The NEMA instructions published in 2018 requires filling all spheres with the hot (with activity) solution, with a lower concentration of activity in the background to create a 4:1 contrast ratio, although studies can be performed at any contrast. The NEMA IQ phantom is

designed to generate the recovery coefficient curves that quantify partial volume effects of imaging systems through the imaging of different sized spheres. The recovery coefficient curve is a standard measure of the partial volume effects of the PET scanner using the chosen reconstruction. In addition, the background variability, i.e., a coefficient of variation, can be measured from several regions of the uniform background. The primary limitation of the phantom is the limited number of spheres and the range of sphere sizes, which are no longer representative of lesion sizes currently visualizable by modern PET systems with new clinical radiopharmaceuticals. It is a relatively symmetric phantom with a small amount of imaging complexity with the central cylinder of a different electron density than the rest of the phantom.

The original version of the CTN (Clinical Trials Network) anthropomorphic chest phantom, consisted of 6 spherical objects in an anthropomorphic-shaped torso that was designed and manufactured by SNMMI [250]. More than 200 PET imaging sites have collected the data generated using this older version of the phantom to compare and validate imaging protocols, including quantitation depending on the image reconstruction parameters [251]. In 2016 the CTN phantom was redesigned to include 12 spheres, with NEMA-sized spheres (10, 13, 17, 22, 28, and 37 mm) so data generated could be meaningfully compared with NEMA image quality phantom data [252]. These sphere sizes were chosen to match the NEMA image quality (IQ) phantom spheres. An additional small sphere of 7 mm is used to challenge the imaging system's lesion detection capability. Two narrow-bore tubing circuits are used to fill all the spheres. The phantom has a single 7 mm diameter sphere located in the mediastinum, two 10 mm spheres separated by 1 mm placed in the lung fields to characterize the lesion separation, a 10 mm sphere in an area corresponding to an axillary lymph node, a single 15 mm diameter sphere in the left shoulder, and

a single 22 mm diameter sphere in the right lung field. Two larger spheres of size 28 and 37 mm are in the lower mediastinum.

Recently efforts have been made by SNMMI to standardize analysis of all of the above described phantoms through the design and launch of an automated cloud-based phantom analysis tool [253]. The main goal of this tool is to facilitate PET scanner quality control programs by providing a simple and reproducible calculation tool to measure the scanner performance [252]. A tutorial for the optimal utilization of this cloud-based analysis tool is available for PET/CT quality control [254, 255]. Several approaches to design and assess lesion detectability in PET imaging have been previously performed [256].

However, there is increasing need for more realistic human-simulation phantoms designed to challenge PET (and SPECT) imaging systems with geometries and features that more realistically simulate actual complex clinical imaging situations. As a first step, we have modified the NEMA IQ phantom to be more relevant to lesion sizes currently imageable with PET systems, and with more spheres to better characterize recovery coefficient behavior. We have also developed a prototype large anthropomorphic chest phantom in this work to better sample the contrast recovery coefficient curve in a more challenging, realistic, and complex attenuation and scatter environment. These phantom developments will improve measures of quantitative scanner performance under complex but clinically relevant geometries. These phantoms will help to fully characterize a particular PET/CT scanner model's (a) noise properties (b) reconstructed resolution (c) recovery coefficient and (d) image quality.

8.2. Methods

The NEMA IEC phantom, the ACR phantom, and the CTN phantom described above were designed quite some time ago, and they no longer meaningfully test performance characteristics

and limits of modern PET systems, signaling a need for new phantoms designed for the newer higher performance scanners, and new imaging agents.

Given the rapid development of new PET and SPECT scanners with enhanced imaging capabilities, the development of radiopharmaceuticals with a wide range of count statistic challenges, a new range of pharmacologic distributions and contrasts, and the absolute need for accurate quantitation for dosimetry, there is a need for a more anthropomorphically realistic phantom that is able to simulate the very real imaging challenges encountered in our current clinical environment. We need to be able to simulate realistically complex attenuation and scatter conditions. We need to be able to simulate physiologically complex and challenging radionuclide distributions and be able to assess a PET or SPECT imaging system's ability to cope with these challenges.

Two phantoms described below have been developed in this work. Additionally, we have ongoing effort to design and manufacture the abdomen and pelvis phantom for PET imaging that are not discussed here.

8.2.1. Modified NEMA phantom

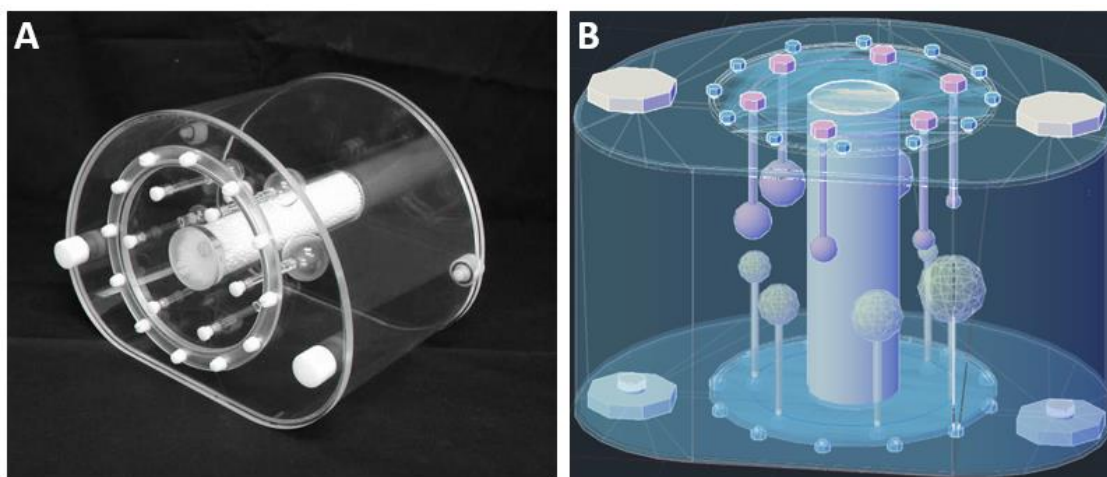


Figure 48: (A) NEMA phantom with 6 spheres. (B) CAD drawing of modified NEMA spheres with 12 spheres.

The NEMA IQ phantom was redesigned to insert additional spherical objects inside the phantom to better sample the recovery coefficient curve. The two limitations that are addressed in the modified phantom are: 1) Objects below 10 mm have been added to generate recovery coefficient data into a region commonly imaged with current PET/CT systems. 2) Current advanced iterative reconstruction algorithms generate difficult to predict ring artifacts that add heretofore unseen structure to the recovery coefficient curve in the region between 10 mm and 17 mm that requires characterization. as shown in **Figure 48**. **Figure 48 (A)** and **(B)** show the NEMA IQ phantom with six spheres and the modified NEMA phantom, now with 12 spherical objects. The added spheres sizes located at the lower half of the NEMA IQ phantom are not the same as the standard NEMA size spheres. The additional sphere sizes are designed to be roughly mid-way between existing standard sized NEMA spheres, while also extending below the current minimum sized sphere. Manufacturing of the phantom was done by exploiting 3D printed spheres for scalability of production and lesion positioning. All spheres are fillable, and the phantom was filled according to guidelines set by NEMA. The new spheres sizes had diameters of 32.5, 25, 19.5, 15, 11.5, and 8.5 mm.

8.2.2. Large anthropomorphic phantom design

The SNMMI CTN chest phantom was redesigned from the ground-up to make a larger chest phantom that more closely mimics the average American adult (male) chest. A total of 16 spheres were placed inside the phantom torso. The design includes 12 NEMA-sized spheres (37, 28, 22, 22, 17, 17, 13, 13, 10, 10, 10, and 7 mm) and additionally 19, 15.5, 11.5, and 8.5-mm spheres that were designed to be the same size as those in the modified NEMA IEC IQ phantom described above. These dimensions are the interior diameter of the spheres. All spheres, and interior platform of the phantom were 3D printed. The shell thickness of each sphere is 1 mm. The

12 NEMA-size spheres are placed approximately in the same relative positions as that in the CTN chest phantom. The lung cavities consist of spongy materials that closely mimic the lung tissue of density $\sim 0.3 \text{ g/cm}^3$. The total volume occupied by the lungs in this phantom is $\sim 6.038 \text{ L}$ and is filled with Styrofoam pellets, but is contiguous with the rest of the phantom so that water can fill the intervening spaces between pellets.

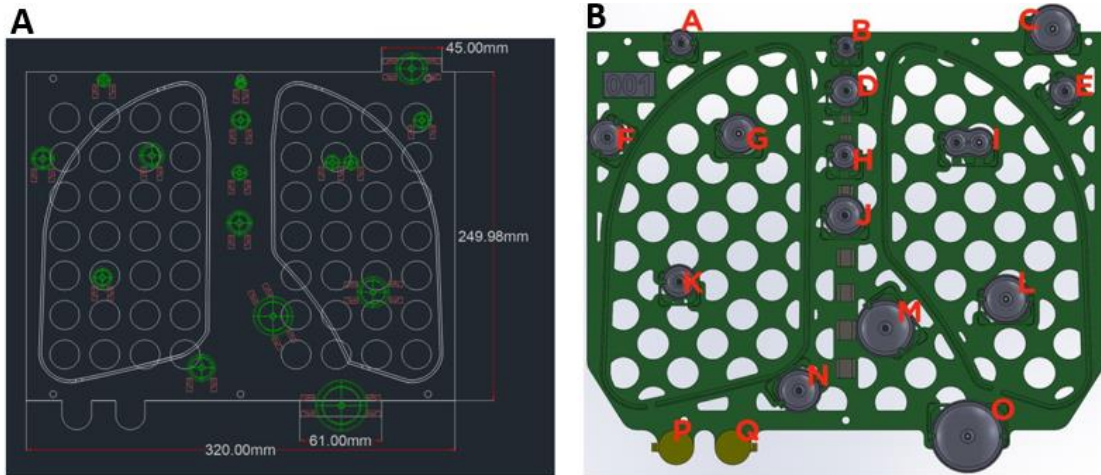


Figure 49: (A) Drawing of the inner platform support of the phantom. (B) Inner tubing circuitry path.

As in CTN Oncology chest phantom, we implemented two independent capillary tubing circuit paths to fill the phantom spheres. Specifically, spheres are filled serially through narrow bore tubing that enters the bottom of a sphere, fills the sphere, exits through the top of the sphere to tubing that is then connected to the bottom of the next sphere in the circuit. **Figure 49** shows the spheres labeling (A, B, ..., P, Q). Where, I is two 10 mm contiguous spheres and P and Q are overflow containers for two circuit paths. Fluid path 1 has a sphere volume of $\sim 42.5 \text{ ml}$ and fills the spheres (B- \rightarrow D- \rightarrow H- \rightarrow J- \rightarrow M- \rightarrow O- \rightarrow Q) and fluid path 2 has a sphere volume of $\sim 22.5 \text{ ml}$ and fills the spheres (C- \rightarrow E- \rightarrow I- \rightarrow L- \rightarrow A- \rightarrow F- \rightarrow G- \rightarrow K- \rightarrow N- \rightarrow P). A total of $\sim 80 \text{ ml}$ radioactive solution is needed to fill all the spheres and tubing volume (path 1: 50 ml, path 2: 25 ml, with additional volume for tubing and overflow to assure full filling of the spheres).

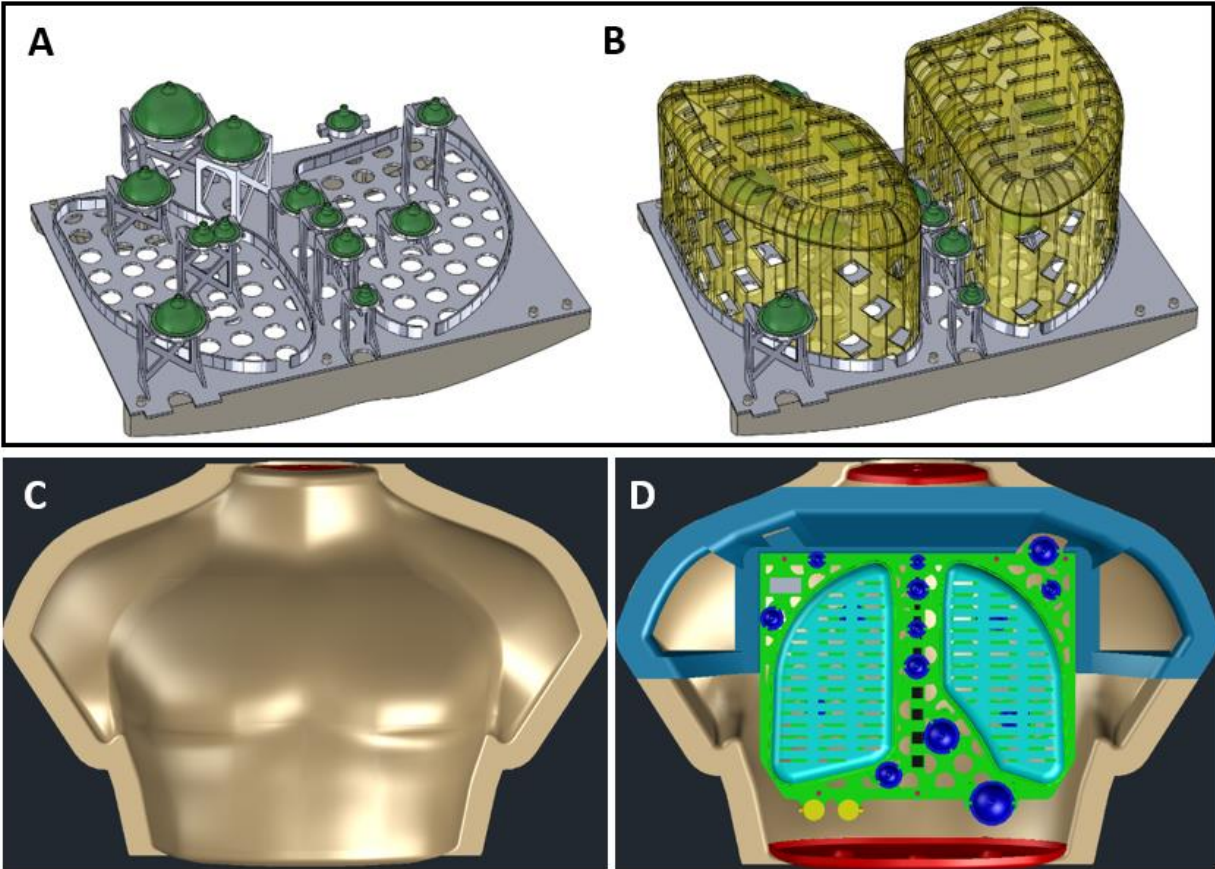


Figure 50: (A-D) CAD drawings of the large CTN chest phantom showing its interior parts.

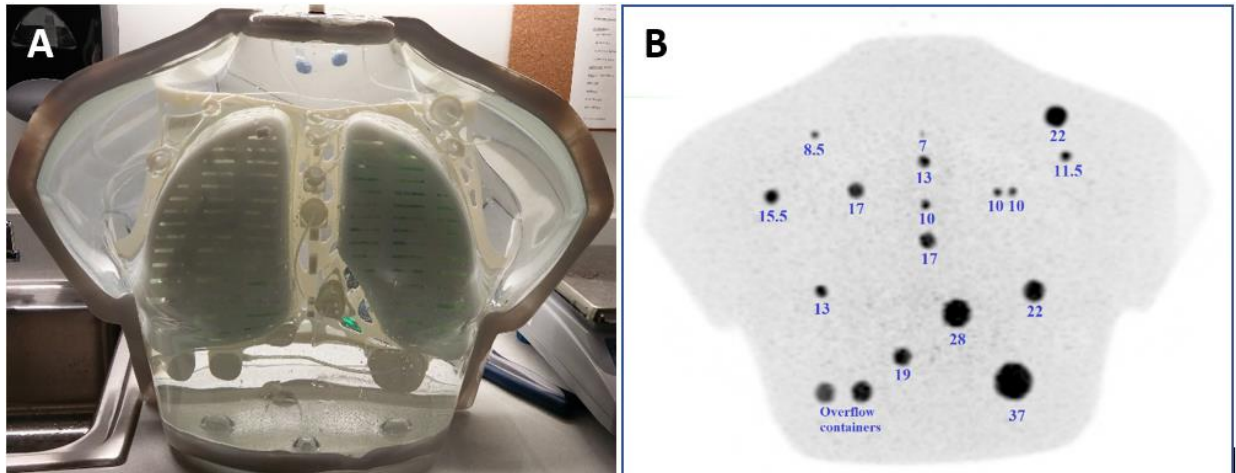


Figure 51: (A) Final product of large CTN chest anthropomorphic phantom. (B) PET MIP image of the final product showing the different sized spheres.

The dry weight of the phantom is ~3.5 kg and fillable background volume of ~23 Liter. Thus, the total weight of the phantom after filling is ~26.5 kg. All spheres and background volume of the phantom were filled with a radioactivity solution of radioactivity according to the SNMMI-CTN Oncology filling guidelines.

8.2.3. Phantom fill and image acquisition

PET imaging of both the modified NEMA phantom and the large anthropomorphic phantom was performed to generate recovery coefficient curves using the GE Discovery MI PET/CT scanner. Both phantoms contain the same sized spheres, and so should generate similar recovery coefficient curves under similar imaging and reconstruction conditions. The PET scanner system consists of a 64 slices CT system and a 4-ring scanner system with SiPM detectors providing 20 cm AFOV and 70 cm Transaxial FOV. The phantom was filled according to the recently updated NEMA guidelines (2018) and SNMMI PET/CT CTN Oncology Phantom filling instructions to create a lesion to background ratio of ~4:1. All activities were measured in dose calibrators calibrated to a NIST traceable 511 keV source. The phantom filling time, activity concentration both in spheres and background volume, the weight of the background fill volume, and the image acquisition time were all recorded. Image reconstructions were performed such that it covers the full spectrum of clinical range of reconstruction parameters (VPFX, VPFX SharpIR), including advanced reconstructions (Q.Clear). Where, the VPFX mode incorporates the Ordered Subsets Expectation Maximization (OSEM) algorithm with Time-of-Flight (TOF) information, VPFXS (SharpIR) incorporates VPFX with point-spread-function (PSF) and Q.Clear incorporate the advanced Bayesian Penalized Likelihood reconstruction algorithm. The standard corrections such as attenuation, random, scatter, dead time, decay, and normalization were included in the reconstruction.

Table 14: PET/CT acquisition and reconstruction parameters.

Time per bed position	15 min (Modified NEMA) 10 min (Chest phantom)
Reconstruction	VPFX, SharpIR, Q.Clear
Iterations/subsets	2i4ss, 3i8ss, 4i16ss, 6i16ss
Post filter	6 - 1 mm (FWHM)
Matrix Size	192x192x192(Modified NEMA) 192x192x233 (Chest phantom)
Voxel size	2.6x2.6x2.79 mm (both)
X-ray CT	120 kV, 100 mA (Helical CT)

Different reconstruction settings were utilized to (1) compare the RC values, (2) compare iterative updates, (3) analyze the action of Gaussian blurring in reconstructions, and (4) understand the impact of different β -values in Q.Clear reconstructions. The post smoothing filter sizes and penalization factor (β) was chosen based on the clinical recommendations. Reconstructed images were evaluated by both visual and quantitative methods. Recovery coefficients of the spherical lesions and background variability were calculated and used as a quantitative measurement to evaluate the performance of different image reconstruction algorithms. RC curves were generated using all spheres included in both the modified NEMA phantom and the large chest anthropomorphic phantom using high statistics data, 15 min/bed, 2 bed position for the modified NEMA phantom and 3 bed position for the large anthropomorphic chest phantom. Commonly used CT protocol in clinical scans were used for CT settings tabulated in **Table 14**. The phantom data were analyzed using the MIM software.

8.3. Results

8.3.1. Imaging of modified NEMA phantom

Phantom was carefully filled to minimize the air bubbles in the spheres. CT images were used to verify whether the spheres were uniformly filled without bubbles.

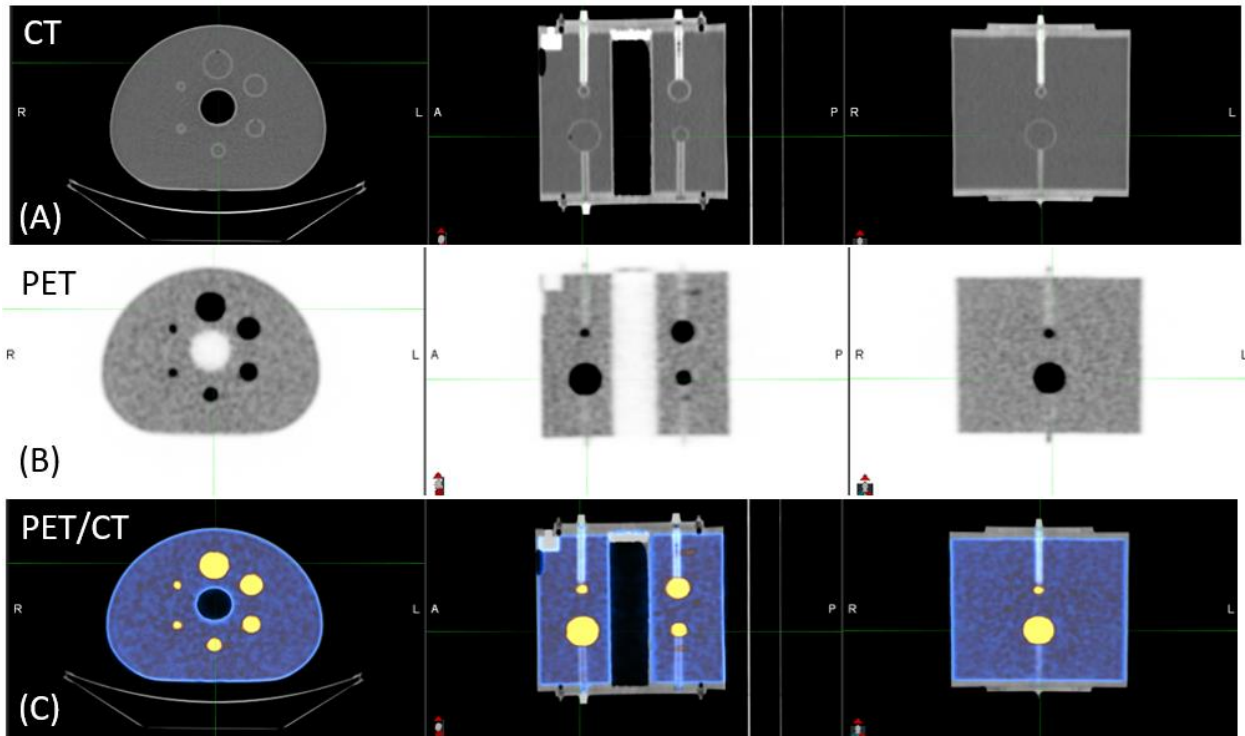


Figure 52: PET/CT maging of modified NEMA phantom with 12 spheres showing the spheres in the upper and lower part of the phantom (A) CT scan (B) PET scan and (C) fused PET and CT slices.

The RC of all spheres used in phantom were calculated where spill-out counts were present and when partial volume correction is required. To use the sphere RC, the physical size of the sphere is needed. The RC of the spheres were calculated by drawing ROIs on the image data as shown in **Figure 53**. ROIs sizes were defined by the inner diameter of the spheres. The 3D spherical brush tool was used to create the 3D ROIs equivalent in volume and positioned in space to precisely overlap the spherical activity space. To minimize the calculation variability and speed up the calculations, all ROIs drawn on one data set were copied to all other data sets. For the

modified NEMA phantom, a transverse image centered on the hot spheres were used in the calculations.

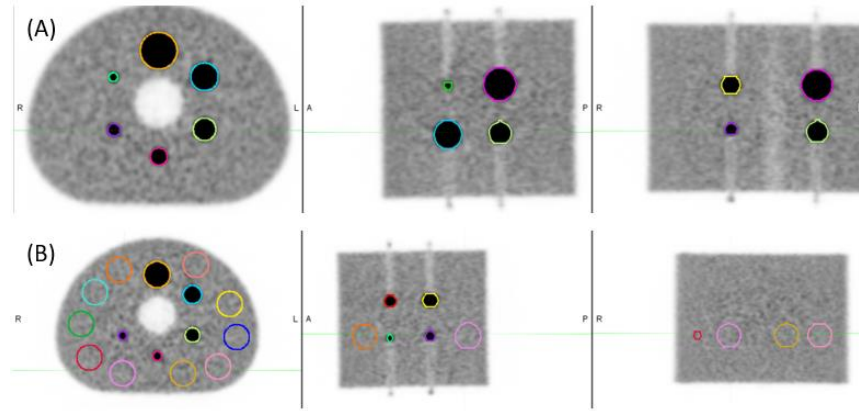


Figure 53: ROIs based (A) recovery coefficient calculations and (B) the background activity calculations of modified NEMA 12 spheres phantom. 3D spherical ROI were drawn for analysis.

Table 15: Visual comparison of reconstructed images using three different reconstruction algorithms with variable filter (6, 5, 4, 3, and 2 mm) and penalization factors ($\beta = 450, 400, 350, 300, \text{ and } 250$).

	6 mm	5 mm	4 mm	3 mm	2 mm
VPFX 4i16ss					
VPFXS 4i16ss					
	$\beta = 450$	$\beta = 400$	$\beta = 350$	$\beta = 300$	$\beta = 250$
QCFXS					

All spheres in the NEMA modified phantom (8.5 – 37 mm) were visible at all acquisitions.

Visual assessment of reconstructed images tabulated in **Table 15** shows that the image quality has

been substantially improved using the Q.Clear regularized reconstruction. Moving from OSEM (VPFX and VPFXS) to Q.Clear reconstruction reduces the background noise and smaller lesions appears more clearly and with more distinct boundaries.

The RCs are strongly dependent on the size of the sphere or lesion. The different combinations of the iteration and subsets with the same iterative updates resulted in the same recovery coefficients. To control the loss of image quality, it is recommended to set the number of subsets of moderate value (12-16 or fewer) in image reconstructions [257].

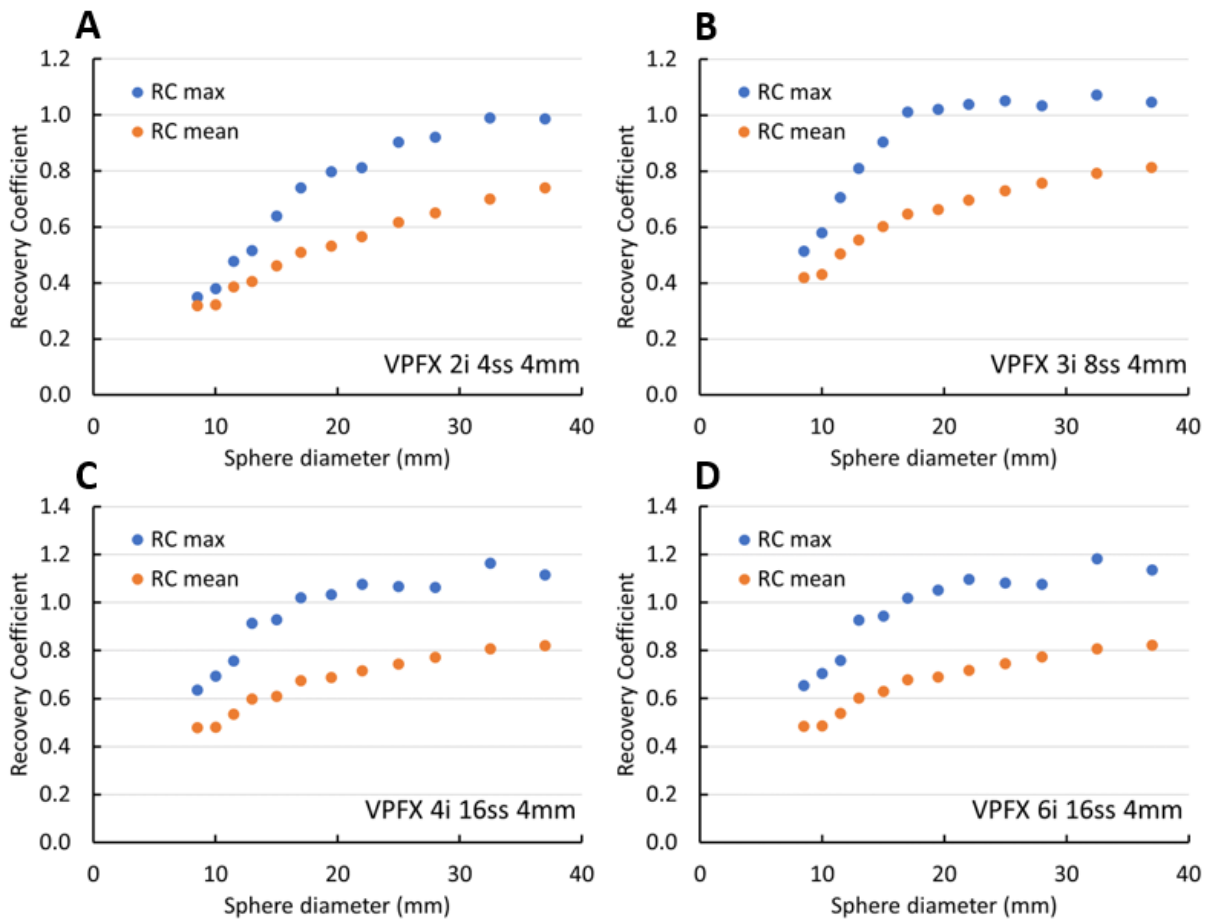


Figure 54(A-D): VPFX reconstructions with different iterative updates and post reconstruction filter.

Figure 54 (A-D) shows the impact of iterative updates (defined by the product of number iterations times the number of subsets) on the recovery coefficients using the same post-reconstruction filter width. Lower iterative updates resulted in lower recovery coefficients and using the more iterative updates greater is the convergence. However, as we go with more iterative updates, a more significant amount of noise is present in the image, resulting in a non-smooth recovery coefficient (max) curve, as shown in **Figure 54 (C-D)**.

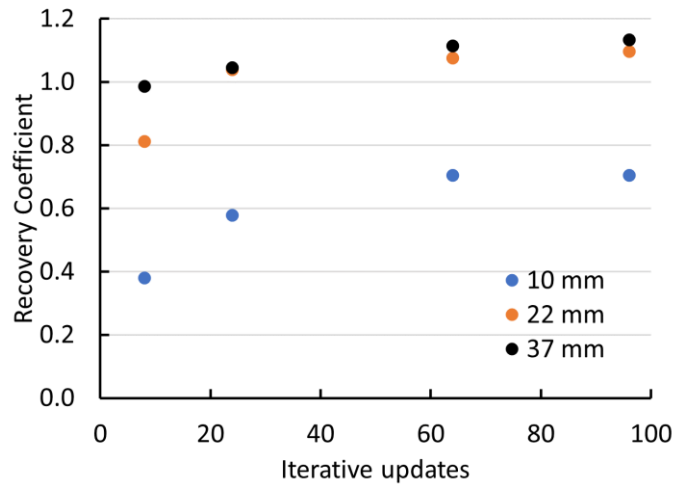


Figure 55: Impact of iterative updates on the recovery coefficients of spherical lesions.

The recovery coefficients for spheres sizes of 10, 22, and 37 mm data were plotted with iterative updates obtained from different reconstruction settings used in **Figure 54 (A-D)** to understand the impact of iterative updates on recovery coefficients. As shown in **Figure 55**, the recovery coefficients likely reached the convergence for iterative updates > 60.

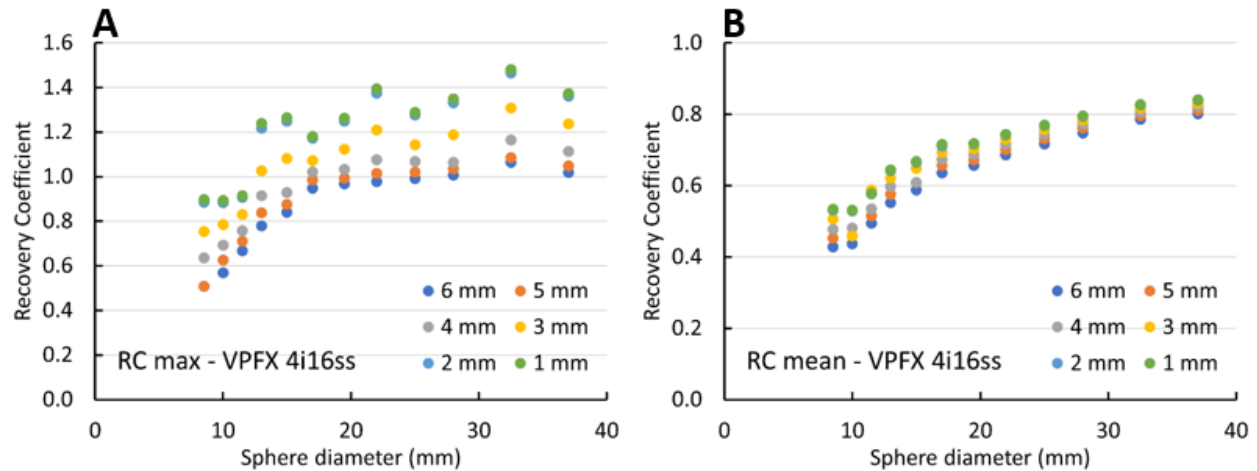


Figure 56: Impact of post-reconstruction filter size is shown for two different combinations.

Impact of post-reconstruction filter width is shown in **Figure 56 (A-B)**. Use of the post filter suppresses the image noise as shown in **Table 15**. It suppresses noise by averaging adjacent pixels by using a convolving Gaussian filter of user-defined width with the reconstructed image. The trend of recovery coefficient curve (max) is not smooth for smaller filter sizes (1-3) mm compared to (4-6) mm. However, the curve using the recovery coefficient mean data, for obvious reasons, is smoother than with the max data where a single spurious voxel can cause a spike in the curve. Here, the max and mean are the maximum and mean activity concentration in the VOI and the unit of pixel values are Bq/ml. Recovery coefficients curves were obtained with a sphere or lesion to background ratio of 4:1.

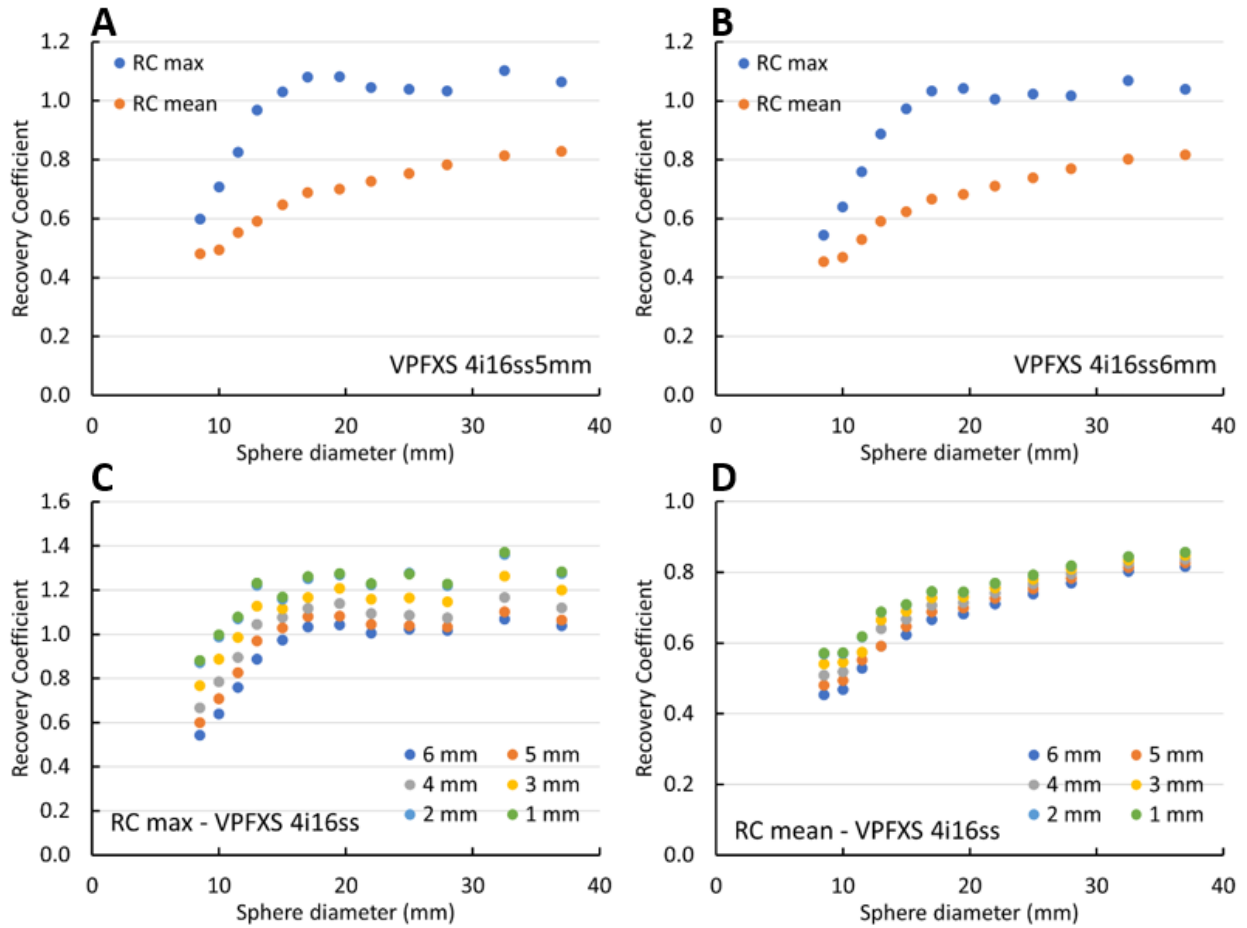


Figure 57: VPFXS (SharpIR) reconstructions using 4 iteration and 16 subsets (A) using post filter of 5 mm (B) 6 mm filter (C) RC max values using different filters and (D) RC mean values with variable filter sizes.

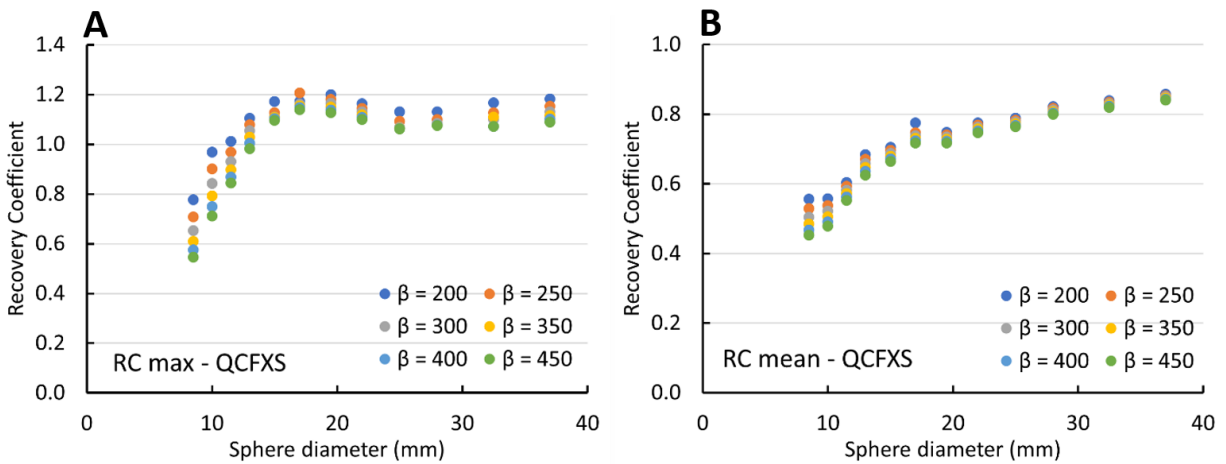


Figure 58: RC curves (A) RC max and (B) RC mean values obtained using QCFXS (Q.Clear) reconstructions for different penalization factors.

The modified NEMA phantom data were further assessed using the SharpIR and Q.Clear algorithms with variable post Gaussian filter and with different β values. The recovery coefficient curves using these reconstructions are shown in **Figure 57** and **Figure 58**. As expected, RC coefficients with Q.Clear reconstruction modes showed slightly higher values compared to other two reconstruction modes (**Figure 58**). This result is expected because the reconstruction iterates through hundreds of iterative updates, and this gives smaller objects time to fully converge.

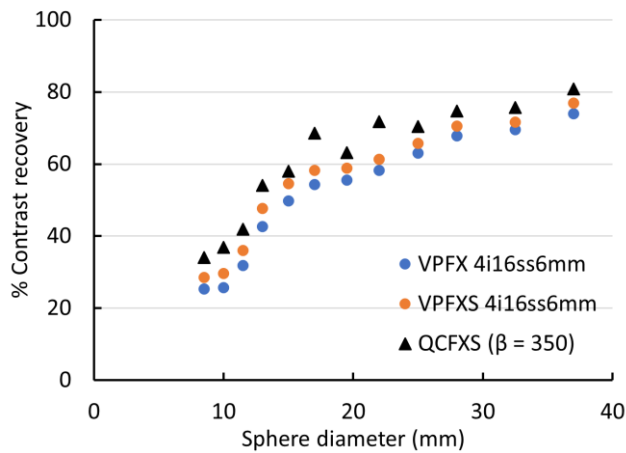


Figure 59: Comparison of percentage contrast recovery (mean) using three different reconstructions.

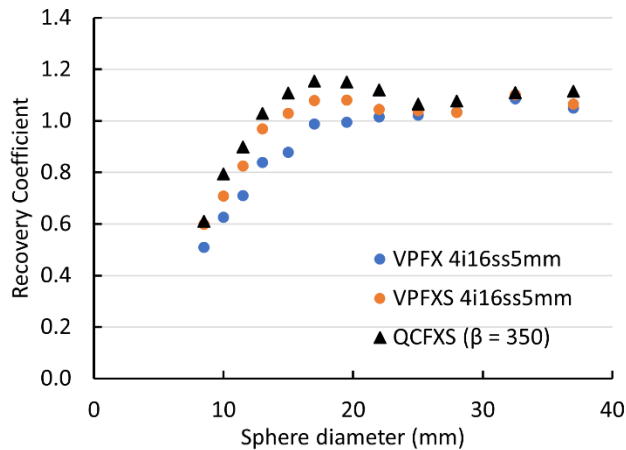


Figure 60: Comparison of recovery coefficients using three different reconstructions.

Plots **Figure 59** and **Figure 60** shows that the contrast recovery (%) and RC increased gradually in the order from VPFX (OSEM+TOF), SharpIR (OSEM+TOF+PSF) to Q.Clear (Bayesian Penalized Likelihood). The average RC of spheres from 8.5 mm to 28 mm using the Q.Clear reconstruction algorithm were substantially higher than those of other reconstructions. However, the spheres larger than 28 mm showed only a minimal difference among reconstruction methods. This is because partial volume effects, from the standpoint of max values (and to a lesser extent mean values) are close to non-existent when the objects is approximately 2-3X the reconstructed resolution. Unlike VPFX reconstructions, VPFXS and QCFXS reconstructions shows the bump in recovery coefficient curve, which is likely due to the inclusion of PSF in these reconstructions.

8.3.2. Imaging of large anthropomorphic chest phantom

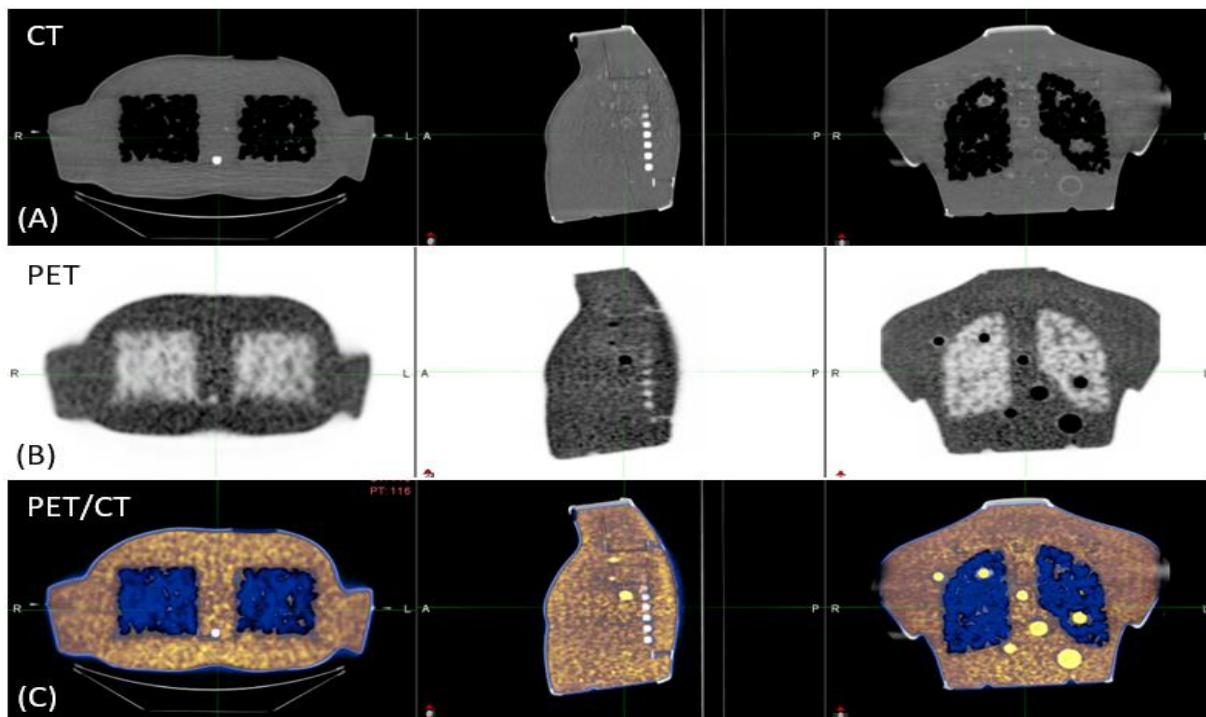


Figure 61: PET/CT imaging of large anthropomorphic chest phantom. Transverse, sagittal, and coronal slices of the phantom are shown. (A) CT scan (B) PET scan and (C) fused PET/CT slices.

The large CTN anthropomorphic chest phantom closely simulates the clinical scan of adult (male) chest. Fill volume of the anthropomorphic chest phantom is more than two times the volume of the NEMA phantom. Photons emitted from the spheres or lesions located in the deep region of the phantom such as in mediastinum suffers higher attenuation. Thus, a higher noise in data is expected compared to the NEMA phantom data, at least in this region. The results of a PET/CT scan of the phantom is shown in **Figure 61**. A comparison of the three reconstructed images using the recommended clinical reconstruction settings is provided in **Table 16**.

Table 16: Comparison of three different reconstructed images of large andromorphic chest phantom.

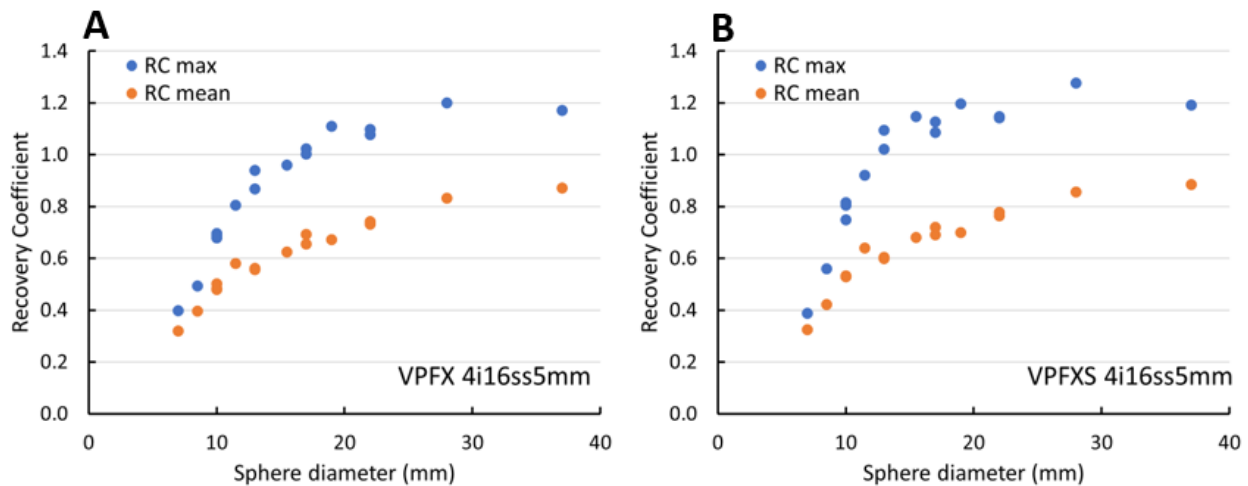
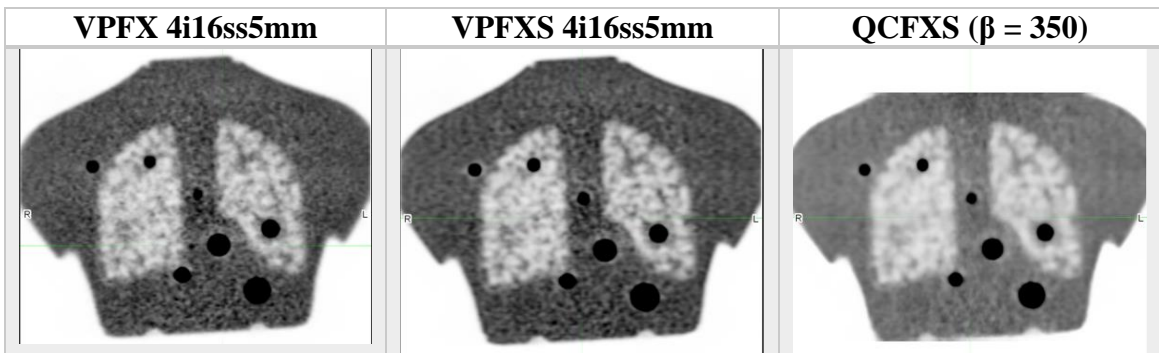


Figure 62: Recovery coefficient curves of the large anthropomorphic chest phantom spherical lesions using (A) VPFX and (B) VPFXS (Sharp IR) reconstructions.

The recovery coefficient curve for spherical lesions using the large chest anthropomorphic phantom is shown in **Figure 62**. As in the NEMA phantom, RC curve were generated using the max and mean values. In **Figure 62**, recovery coefficients of spheres located in mediastinum region of the phantom are slightly larger than the same size spheres located in other regions. Three spheres are located in mediastinum (10, 13, and 17 mm). The RC curves using the mean values are relatively smoother than using the max values as expected. The RC curves are noisier than the modified NEMA phantom. This is primarily due to the fact that the large chest phantom has substantially more attenuation and thus the photons will scatter more compared to the modified NEMA phantom, therefore the images are formed from substantially fewer detected coincident events.

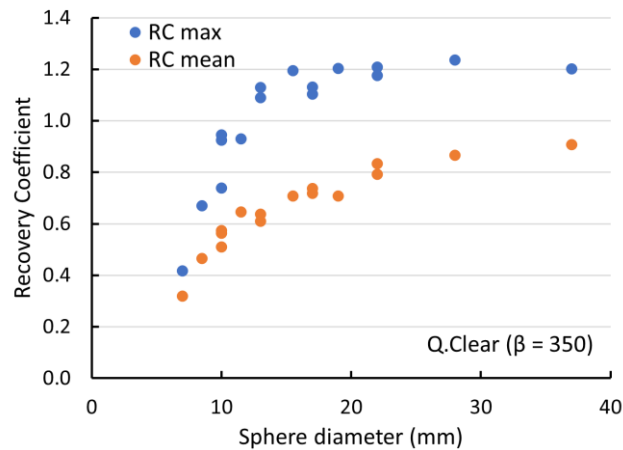


Figure 63: RC curve using the Q.Clear reconstruction using $\beta = 350$.

Comparison of the three reconstructions settings using the RC max and mean calculations is shown in **Figure 64**. Recovery coefficients of spherical lesions are greater when using the Q.Clear reconstructions, as expected. However, for larger spheres (28 and 37 mm) recovery coefficients are closely matched with each other, which means that the impact of reconstructions is minimal as

in modified NEMA phantom data. All spheres (7 - 37 mm) were visible in reconstructed images, however the RC value for 7 mm sphere is only ~40% using (RC max) all reconstructions.

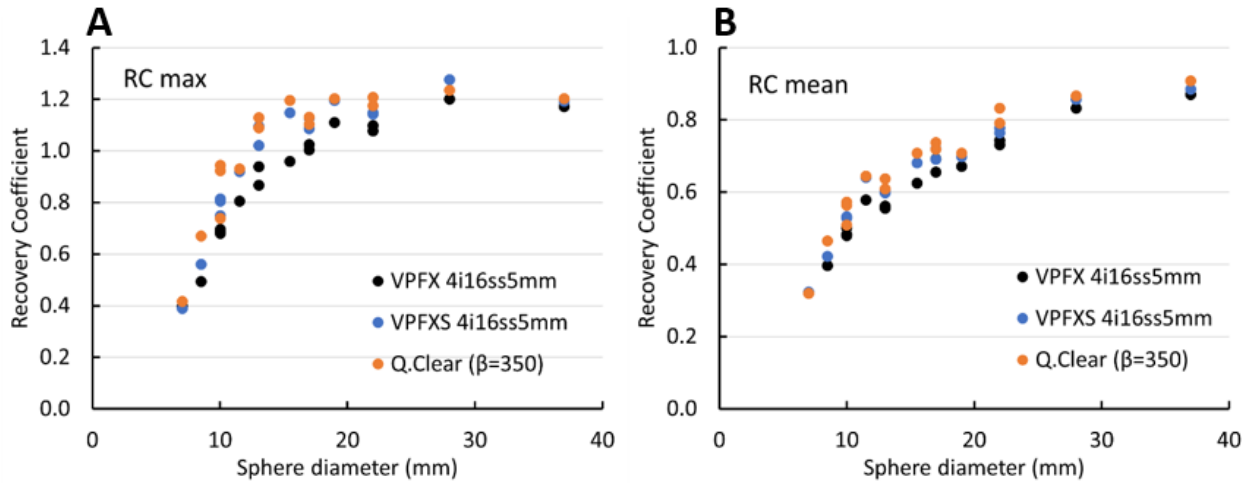


Figure 64: Comparison of recovery coefficient curves of three reconstructions using (A) RC max and (B) RC mean values.

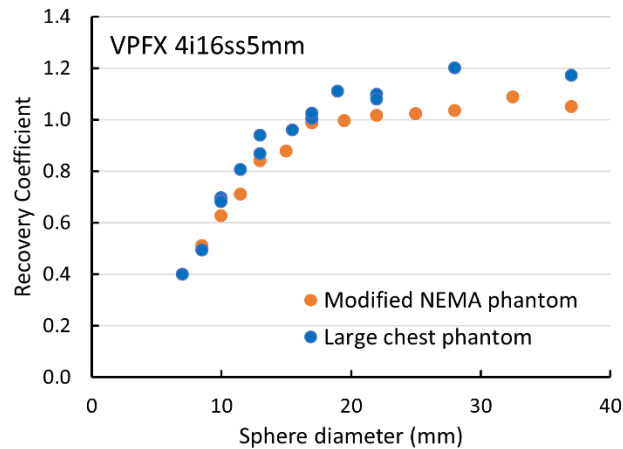


Figure 65: Comparison of recovery coefficient (RC max) curves for two different phantoms developed in this work.

The visual comparison of the recovery coefficients data obtained from two different phantoms developed in this work is shown in **Figure 65**. Note that the recovery coefficients data were generated using the same reconstruction settings (VPFX with 4 iteration, 16 subsets and 5 mm post filter width) for this comparison. The recovery coefficients of spherical lesions available

in the large anthropomorphic chest phantom are slightly larger than the recovery coefficients of spheres in the modified NEMA phantom. It is primarily due to the greater attenuation of photons in the large anthropomorphic chest phantom (~26 L) compared to the modified NEMA phantom (~10 L).

8.4. Discussion and Conclusions

Molecular imaging continues to experience rapid technological development in PET scanner design enhancing its sensitivity, and in image reconstruction approaches enhancing reconstructed resolution, minimizing noise, and improving contrast recovery characteristics. The evolution of PET phantoms is necessary to meaningfully measure these improved performance metrics. However, the field has been slow to respond with new and more challenging phantoms. This work represents a first step towards the modernization of PET phantoms for use in PET, and even SPECT imaging. Application of these improved phantoms will benefit quantitative imaging, in general, but also accurate measurement of radionuclide concentrations for use in quantitative dosimetry.

Phantoms have been proven to be useful, and in fact necessary tools for nuclear PET and SPECT imaging, and for validating dosimetry measurements. In this work, we developed a prototype of large chest anthropomorphic phantom and additionally the NEMA IQ phantom was modified. The large chest phantom was first designed in AutoCAD 3D modeling software. Subsequently, AutoCAD files were sent to the manufacturer to construct the phantom. The phantom outer shells were manufactured using a thermoforming molding technique. The internal structures were 3D printed. The NEMA phantom modification was done with the help of machine shop located at the University of Iowa Hospitals and Clinics and all added spheres and their filling ports were 3D printed.

The currently available CTN oncology chest phantom developed by SNMMI is small and does not closely resemble the adult chest in size, which somewhat limits its utility. Thus, the main motivation of developing a prototype anthropomorphic chest phantom was to mimic the imaging situation of chest of the adult American male (40-year). The phantoms described in this work has the advantage of providing RCs for a large range of sphere sizes as mentioned in the methods section. The RCs are used for partial volume corrections. Accurate partial volume effect measurement is the main challenge in PET quantification. Therefore, these phantoms may be invaluable for its use in accreditation programs attempting to harmonize the image quality, activity quantification, and it may also be suitable for lesion detectability performance measurements. As described by Sunderland et al., phantoms are not only useful for the scanner performance measurements but also for the PET scanners validation at different sites [251]. These phantoms developed in this work may also be useful to generate the large number of datasets to be used as input in artificial intelligence studies to analyze images, reconstruction algorithms, and correction techniques used in PET.

The prototype chest phantom developed in this work has demonstrated numerous benefits. The size of the phantom closely mimics the adult human chest. The phantom shell was made transparent to clearly visualize the interior of the phantom help detect defects. This phantom has been tested and sent to multiple imaging sites for characterization of new imaging systems. This phantom is currently being used at the University of Iowa, University of Pennsylvania, and Royal Prince Alfred Hospital in Australia. However, one drawback of this design used in this work was that the phantom filling is quite challenging and may take up to an hour to complete. Furthermore, the phantom is not customization friendly at this stage. We are working to make it customizable so that we may simulate multiple clinical scenarios in the future. It is worth mentioning that the

development and manufacture and characterization of this prototype took a significant amount of time and initial investment of around \$10,000.

The development of anthropomorphic PET phantoms using tissue equivalent materials has been an active field of research over the last decade with an increasing focus on reproducible manufacture and materials characterization. As of the writing of this thesis, there is no total-body PET phantom available for mimicking the imaging properties of a full human body. As PET scanners are continuously evolving, the anthropomorphic chest phantom including the development of abdomen and pelvis phantom should be a next step. We have initiated this step but due to the time constraints, we were unable to complete that task. Therefore, future work is required to continue working in these areas to finish the ongoing project on abdomen and pelvis phantom development.

CHAPTER 9: DISCUSSION

The rapid development of targeted radiopharmaceutical therapy and its accompanying image-based quantitative dosimetry component elucidates nicely the potential marriage of nuclear imaging and therapy. In this thesis, we have studied several aspects of radiopharmaceutical dosimetry science and nuclear imaging. First, we generated new tissue specific DPKs for common beta-emitting therapeutic radionuclides and followed this with careful experimental validation of the DPKs using a novel radiochromic film method. We followed this work with a series of novel DPK generation for up-and-coming therapeutic alpha-emitting radionuclides. The short range of the alpha particles pointed to application to dosimetry on a cellular level, rather than through nuclear imaging. Monte Carlo simulation of a clinical PET scanner, extended to its potential as a long AFOV total-body PET scanner was also performed. This was followed by development and testing of novel next-generation PET phantoms, including the modified NEMA and large chest anthropomorphic phantom. These phantoms will be useful in various ways including the understanding of, and tools for, quantitative PET and SPECT imaging for use in both diagnostic and therapeutic applications. The additional work investigating some of the currently less well-understood or investigated aspects of dosimetry were designed to develop and validate methodologies that will improve the workflow and accuracy of radionuclide dosimetry in clinical environments.

The motivation of the first project of the thesis, i.e., the Monte Carlo simulations of dose point kernels, was that it serves as a computationally efficient method to compute the absorbed dose distributions post radiopharmaceutical therapy as an improvement over the MIRD organ-based approach. The voxel-wise or voxel-level approach using DPKs is gaining significant interest in the RPT dosimetry paradigm. Our first project studied the impact of tissue types on dose point

kernels using the six different tissue types such as lung, adipose, soft tissue, blood, red marrow, and bone. The Monte Carlo simulations that we performed in this work suggest that the impact of tissue types is minimal for the purposes of dosimetry if we carefully take into account the tissue density. Tissue density was found to be the major player in the variability of the DPKs. This finding both simplifies and adds credence to dosimetry calculations that take into account different tissue-types.

DPKs are historically based upon careful Monte Carlo simulations. The increased interest in DPK usage in dosimetry calculations in both academic and commercial dosimetry software brings the obvious question of actual experimental validation of DPKs to the forefront. Due to the relatively short range of β - particles, the high-resolution measurement of dose deposition has been problematic, and not yet achieved, until this work. The physical experiments in this thesis were conducted to validate the Monte Carlo simulation results. Two radionuclides ^{90}Y and ^{177}Lu were used in the experiments. These two radionuclides are among the most commonly used in RPT. Recently, ^{177}Lu has been gaining more attention compared to ^{90}Y because ^{90}Y appears to show greater normal toxicity at equivalent doses. Three tissue equivalent materials such as polyethylene (soft-tissue equivalent), lung, and bone were utilized in the experiment. Because of the larger ranges of ^{90}Y emitted beta particles, absorbed dose was measured in all three phantom materials. However, for ^{177}Lu only lung equivalent material was used for absorbed dose measurement because of the suitable range of ^{177}Lu emitted beta particles in lung. Both ^{90}Y and ^{177}Lu sources were obtained from the nuclear medicine clinic at University of Iowa. In the case of ^{90}Y , the source was available as SIR-spheres in a vial. For our purposes, we first dissolve the SIR-spheres and made the source homogeneous in liquid to be used in the actual experimental exposures. For absorbed dose measurements, radiochromic EBT3 film was exploited. Radiochromic film was

found to be excellent dosimeter for the beta particle absorbed dose measurements. High resolution (508 dpi or 0.05 mm pixel size) dosimetry calculations were performed by suitably scanning the experimentally exposed films using flatbed scanners.

Absorbed dose quantification of the EBT3 film was done carefully by calibrating the film using the 6 MV photons beam using the Siemens Oncor linear accelerator at the Department of Radiation Oncology, University of Iowa. A range of monitor units (0 – 2000 MU) were used in the calibration; later the MUs were converted to absorbed dose in units of cGy. Subsequently, films were exposed using line sources of ^{90}Y and ^{177}Lu for different time periods up to 24 hrs for ^{90}Y and 38 hrs for ^{177}Lu . Monte Carlo simulation of corresponding experimental set ups were performed to compare with the physical measurements. The detailed uncertainties estimations in experiment were calculated and found to be ~8%, which consists of overall uncertainty in the experimental work including uncertainty in optical density measurements in each channel, activity measurements, dose calibrator, and exposure time uncertainties. The results of these measurements matched Monte Carlo simulations closely, and suggests that the GATE Monte Carlo results are robust, and we can confidently use GATE Monte Carlo derived dose point kernels in radiopharmaceutical dosimetry.

α -emitting radionuclides are a new and exciting addition to the RPT landscape, as they appear to show potential for dramatic enhancement of RPT treatment efficacy. To add to the existing library of DPKs, the dosimetry of eight therapeutic α -emitting radionuclides were studied including monoenergetic alpha particles (3 MeV – 9 MeV) in silico exploiting Monte Carlo simulations in several tissue types. Although at this stage the direct applicability of α -DPKs is not meaningful in the context of nuclear imaging-based dosimetry, these kernels are useful in assessing the microdosimetric properties of metastasized tumors on the cellular level. In particular, there is

a significant interest in studying the previously unstudied potential of therapeutic α -emitters in Fibroblast Activation Protein Inhibitor (FAPI) compounds, which is used as a vector molecule to target the Cancer Associated Fibroblasts (CAFs) cells in tumor microenvironment. These CAFs cells are overexpressed in more than 90% of epithelial carcinomas, including pancreatic, colon, breast and ENT (ear, nose, and throat) cancers [258]. Application of α -emitting DPKs is currently ongoing in research work with industry and UCSF collaborators.

In nuclear PET quantitative imaging, GATE Monte Carlo studies were utilized and carefully simulated the current clinical GE Discovery MI PET scanner. Monte Carlo simulation results were validated against published measurements data. NEMA performance measurements were utilized to validate the scanner as it is the standard practice to compare the performance of the scanners and is used as a tool to validate the clinical PET scanners. All NEMA metrics except the image quality were evaluated thoroughly, including the spatial resolution, sensitivity, count rates, scatter fraction, and the NECR peak values. Validating the Monte Carlo simulation performance of the current commercially available GE Discovery MI PET scanner was a necessary first step before moving to the actual goal of the study, which was to evaluate the performance of hypothetical long AFOV scanners based on the GE Discovery MI scanner front-end architecture. The geometry of the GE Discovery MI scanner was of particular interest as it exploits the thicker crystals (25 mm) compared to other clinically available PET systems, and simulations of performance of a long AFOV scanner based upon GE Discovery MI have not, to date, been performed.

After the validation of the clinical 4-ring GE Discovery MI scanner, AFOV of 20 cm, we gradually added scanner rings up to an AFOV of 2 m by keeping other geometries the same including the detector crystal size and scanner deadtime. The data digitization scheme in all

scanner models were slightly varied as the coincidence timing windows necessarily differ as the size of the system grows from a small AFOV to large AFOV. We performed the simulations using the 4 (20 cm), 8 (40 cm), 20 (100 cm), 30 (150 cm), and 40-ring (200 cm) scanner configurations. Different ring configurations were simulated as they each represent different potential scanner systems, and it helps answer which scanner configurations will have what performance level and also potentially address the question of optimal scanner AFOV length. The simulated model presented reproduced physical measurement counting rates curves with less than 6% relative errors in the clinical activity concentrations range (2-6 kBq/ml).

As in the 4-ring system, all NEMA metrics were estimated for each ring configuration, including the effects of parallax errors in large AFOV scanners. Importantly, effects of parallax errors were found to be minimal without significant degradations to spatial resolution of the scanner, even at largest AFOVs. The results of the comparison of the scanner 4-ring system with large AFOV scanners are detailed in **Chapter 7**. Overall, the sensitivity simulations using a line source of 200 cm in all scanner configurations performed herein resulted in a sensitivity gain of ~60-fold using a 40-ring scanner compared to the 4-ring scanner. Furthermore, the NECR peak comparison of 4-ring versus 40-ring gives a performance enhancement of 28-fold, whereas comparison of 4-ring versus 20-ring gives a performance of 15-fold using the 200 cm long scatter phantom. These performance gains are in-line with those measured on the uEXPLORER and Siemens Biograph Vision Quadra.

In addition, the author of this PhD thesis has contributed to a few other manuscripts and abstracts presented to conferences at SNMMI and AAPM. The lists of the manuscripts and abstracts are included at the appendix of this thesis.

CHAPTER 10: CONCLUDING REMARKS AND FUTURE DIRECTIONS

Radiopharmaceutical therapy (RPT) based on the concept of delivering cytotoxic levels of ionizing radiation to cancer sites while minimizing radiation exposure to healthy cells is one of the burgeoning fields of nuclear medicine. Compared to conventional external beam therapy (EBRT), RPT targets cancer at the cellular level rather than on a gross anatomical level. A few examples of RPTs include the treatment of bony metastases resulting from castrate-resistant prostate cancer with $^{223}\text{RaCl}_2$ (Xofigo), the treatment of neuroendocrine tumors (NETs) with ^{177}Lu -DOTATATE (Lutathera), thyroid ablation with the administration of ^{131}I , and treatment of synovitis and liver cancer with ^{90}Y microspheres (SIR-spheres). Due to recent FDA approvals and astounding commercial success of these approved RPTs, new RPTs are being developed, where radionuclides are incorporated into new systemic targeted therapies. New molecularly-based targeting mechanisms are being developed using prostate specific membrane antigen (PSMA) for prostate cancer and fibroblast activation protein inhibitor (FAPI) for a variety of different solid cancer types. These are just two of many, many molecular targets under active investigation and commercial development. To make sure that RPT is optimally implemented, advances in targeting mechanism need to be matched with advances in quantitative nuclear imaging and dosimetry methods. Typically, RPTs are administered intravenously, and the treatment planning has typically been implemented as in chemotherapy, where the activity administered is either fixed or adjusted based on a patient's body weight. Recently results of phase III clinical trials using ^{177}Lu -DOTATATE (NETTER I) [30] and ^{177}Lu -PSMA-617 (VISION) [31] were published. In each of these cases, the clinical trials showed a substantial survival benefit even without patient-specific injection dose optimization. That means these clinical trials were based on fixed amount of radiopharmaceutical activities independent of patient-specific factors. In addition, phase II

randomized trial of ^{177}Lu -PSMA-617 (TheraP) also did not incorporate dosimetry guided injected activity [259]. However, it is clear that the patients in these clinical trials are being systematically “underdosed”, as patients, at large are not experiencing dose limiting (or even serious) toxicities in most cases. Quantitative imaging combined with image-based dosimetry calculations with DPKs provides an achievable approach to measure the radiation dose to normal organs as well as tumors, which in turn would allow a patient specific dosing regimen designed to optimize dose to the tumor, while at the same time avoiding normal tissue toxicities. The incorporation of patient-specific dosimetry guided treatment into the clinical trials is hypothesized to dramatically improve the therapeutic index, i.e., the ratio of survival benefit to side effects after therapy. Which would accelerate the use of personalized RPT treatments in the clinic.

The dosimetry in RPTs can be performed in two general ways: (1) organ-based (MIRD) and (2) voxel-level 3D dosimetry approach. With the increasing therapeutic application of radiopharmaceuticals and the need for greater accuracy and efficacy in treatments, dosimetry in nuclear medicine is evolving from organ-based approach to the voxel-level approach. Increased attention is being paid to the computationally-efficient DPK-based voxel-level dosimetry due to its resulting 3D absorbed dose distributions which have demonstrated results close full Monte Carlo simulation calculations (the current gold standard in dosimetry). The recent ^{177}Lu dosimetry challenge program conducted by the Society of Nuclear Medicine and Molecular Imaging (SNMMI) shows that the voxel-level dosimetry method in absorbed dose calculations was used by more than 60% of the challenge participants [33]. In silico studies were performed in this PhD thesis to help advance the field of voxel-wise dosimetry by performing Monte Carlo simulations of DPKs, including the β - and α -DPKs, and studying the impact of tissue types on kernels. We further experimentally verified the Monte Carlo generated β absorbed dose distributions for the

first time. The experimental measurement work suggests us that we should now be comfortable with β -DPKs to be used as an input for voxel-wise dosimetry. However, in the case of α -DPKs, the implementation is not straightforward as the spatial resolution and voxel sizes used in nuclear imaging is much larger than the ranges of α -particles emitted from therapeutic α -emitting radionuclides. That being said, we are continuing our research on α -particles dosimetry at the cellular level using microscopic pathology slides of various kinds of cancer.

Personalized RPT therapy through the implementation of image-guided dosimetry in clinics would provide the foundation of treatment planning to maximize efficacy. This will also reduce the short or long-term toxicity based on patient's molecular profile. Monte Carlo simulations of dose point kernels provides foundational information to be inserted in patient specific absorbed dose calculations help optimize or modulate the injection activity dose, hence the treatment. Monte Carlo studies are found to be very useful in advancing translational research. Ongoing advances in nuclear molecular imaging including SPECT and PET and radiopharmaceutical therapy will be very likely to be fruitful in advancing cancer treatment. Our understanding of personalized dosimetry will facilitate optimization of the therapeutic index for RPTs, with delivery of targeted high ionizing radiation dose to tumors with maximal sparing of normal tissues.

The SNMMI ^{177}Lu Dosimetry Challenge program launched in 2021 has demonstrated that SNMMI is a strong advocate for personalized dosimetry-based treatment planning, which is expected to become standard procedure in the near future with a demand for qualified physicians and medical physicists to supervise and apply these methodologies. In addition, other regulatory bodies such as ASTRO, AAPM, ICRU and NCI are also the strong supporter of personalized dosimetry for RPT. Still the dosimetry of therapeutic β -emitting radionuclides is not in common

use, and dosimetry using α -emitting radionuclides is challenging due to their highly localized absorbed dose distributions and hence are not fully mature and for widespread use.

There are a number of caveats of using image-based dosimetry. Image artefacts and noise may easily influence the absorbed dose calculations. Thus, detailed assessment of administered activity, imaging both pretherapy and post therapy, scan parameters, image reconstruction, and partial volume corrections methods are essential components in this process. Each of these steps is important to ensure the most accurate quantification is achieved. The pretherapy imaging helps define the location of the target and potentially serves as a source for quantification uptake and provides input data for 3D voxel-wise dosimetry. Using the post therapy scans we can calculate the absorbed dose to both tumor and normal organs in an individual patient. This data will provide the ability to retrospectively estimate the absorbed dose for future therapy consideration and for correlation with therapy response and toxicity.

In addition, a number of other technical considerations impact the accuracy of image-based dosimetry. These include the impact of VOI delineation, accuracy of both attenuation, and scatter corrections in the image acquisition and reconstruction chain. Furthermore, the impact of numerical integration method (mono exponential fit, trapezoidal integration, or combination of these 2 methods), and number of imaging time points still needs to be investigated thoroughly.

Current dosimetry practices use the multiple time point imaging data over the course of several days, but it is putting burden on patients, requiring multiple clinic visits and hospital resources. In addition, patients may be reluctant to return for multiple dosimetry scanning at several time points, particularly when they are located far away from the clinic. Therefore, the interest in dosimetry using a single time point imaging is on the rise. This approach uses a single SPECT scan data combined with planar gamma-images or population imaging pharmacokinetic

data [41]. However, simplified dosimetry using a single time point method has been questioned and challenged in some studies. Thus, moving forward a rigorous validation of this method is necessary.

Due to the limited axial coverage (AFOV) of current PET clinical scanners larger amounts of radiopharmaceutical injection are required, and 10-30 min are needed for a high statistical quality patient scan. To minimize these limitations there has been a significant interest in the development of total-body PET/CT scanners. A total-body PET scanner covers the entire human body and thus imaging requires a single bed position (or two based on scanner AFOV), this would significantly reduce the scan time, potentially down to just several minutes. More detector crystals capture a higher proportion of the emitted coincidence photons, therefore this significantly enhances the sensitivity of the scanner and provides enhanced signal-to-noise ratio and therefore the better image quality. As of writing this thesis, three total-body PET scanners have been developed, uEXPLORER (194 cm) [68, 69], PennPET EXPLORER (64 cm, 140 cm planned) [71, 72] and Biograph Vision Quadra (106 cm) [74, 220]. The performance of these scanners showed a significant performance gain in terms of system sensitivity and NECR peak values. Excessively higher cost of these scanners is restricting their use in clinics. Therefore, Monte Carlo simulation studies have been performed to estimate the optimal AFOV of the scanner with the goal of potential cost reduction.

Monte Carlo simulations appears to be an invaluable tool for the study of PET scanners and for the performance projections of hypothetical long-AFOV scanners [3, 107]. Many studies have used the Monte Carlo simulations to study the PET scanners using sparse detector geometries to understand the possibility of reducing the cost of a total-body PET scanner and to increase the research boundaries. In those studies, simulations were designed using the existing clinical scanner

systems with the (1) same detector ring diameter and AFOV but with only half of the detectors [83] and (2) same detector ring diameter and number of detectors but spaced out to cover the original AFOV [85, 225]. In addition, a total-body modular PET scanner using plastic scintillator detector has also been simulated using GATE and their NEMA characteristics are also available [260].

PET imaging sensitivity has been substantially improved with a longer AFOV and 3D imaging. It is expected that the implementation of digital SiPM based detectors can improve the TOF of the PET systems, enhancing signal to noise even further. If we further narrow down the time resolution, that is, the detection times of two photons from the same coincidence event then that will substantially improve the depth resolution. For example, the time resolution of 40 ps corresponding to the depth resolution of 6 mm, where there might not even the need of tomographic image reconstruction step. We can estimate this number by a simple formula $\Delta d = (\Delta t \times c)/2$, where c is the velocity of light, Δd and Δt are depth resolution and timing resolutions respectively. Thus, moving forward research in the improvement of coincidence electronics may be a significant next step. Recently, Kwon et al performed an experiment using a new form of direct position emission imaging (dPEI) that can produces 3D PET images without a need for an image reconstruction [261]. They achieved a timing resolution of 32 ps, corresponds to spatial precision of 4.8 mm, by detecting Cerenkov photons with the application of convolutional neural networks.

To understand the potential of a total-body PET scanners the development of PET phantoms that closely mimic the human body may also be helpful. In this work, we developed the anthropomorphic adult chest size phantom. The development of phantoms that mimic the abdomen and pelvis areas is a next step. The addition of challenging features such as non-regular geometric

objects in the phantom may help characterize the scanners and their lesion detectability. Providing an opportunity to study common challenging PET and SPECT clinical imaging situations (hot bladder near small positive lymph nodes, or low count immunotherapy lesion detectability scenarios) are a job for next generation phantoms. Phantom-based measurements are often considered as the gold standard in PET imaging to characterize and compare quantitative characteristics of the PET systems, but previous phantoms have been largely overly simplistic and geometric in design. Current 3D printing advances are creating opportunities for more realistic anthropomorphic phantoms for a new generation of phantoms. The use of these large phantoms in different imaging centers would facilitate and simplify PET standardization and harmonization efforts if used with automated lesion detection algorithms, and potential applications in deep learning based training of detection and segmentation of lesions.

In summary, the role of total-body PET imaging in the future could be applicable in many areas such as in simultaneous dynamic imaging of multiple organs with increased sensitivity, real-time tracking of blood flow, respiratory and cardiovascular motion-frozen imaging, and low activity imaging. Furthermore, the long AFOV total-body scanners can also provide the better therapy monitoring and may be useful to perform downstream the dosimetry studies as multiple time point imaging is the gold standard in dosimetry. Thus, total-body PET systems are likely to be a game changer in aforementioned applications. Therefore, it will be at the front-front of the future PET scanner developments and likely leading to further developments in performance and more cost-effective solutions.

APPENDIX

In this section, we present GATE simulation scripts, and the data analysis tools (MATLAB and ROOT scripts) that were developed during this thesis work.

A. Dose point kernels GATE simulation scripts

A.1 50 keV monoenergetic electrons

```
#-----#
#          V E R B O S I T Y          #
#-----#
/gate/verbose Physic      0
/gate/verbose Cuts       0
/gate/verbose SD         0
/gate/verbose Actions    0
/gate/verbose Actor     0
/gate/verbose Step       0
/gate/verbose Error      0
/gate/verbose Warning    0
/gate/verbose Output     0
/gate/verbose Beam       0
/gate/verbose Volume     0
/gate/verbose Image      0
/gate/verbose Geometry   0
/gate/verbose Core       0
/run/verbose              2
/event/verbose            2
/tracking/verbose        2

/gate/geometry/setMaterialDatabase GateMaterials.db

#-----#
#          W O R L D          #
#-----#
/gate/world/geometry/setXLength      2 cm
/gate/world/geometry/setYLength      2 cm
/gate/world/geometry/setZLength      2 cm
/gate/world/setMaterial              Water

#-----#
#          P H A N T O M   G E O M E T R Y          #
#-----#
/gate/world/daughters/name           my_phantom
/gate/world/daughters/insert         sphere
```

```

/gate/my_phantom/setMaterial          Water
/gate/my_phantom/geometry/setRmax    0.12454 mm
/gate/my_phantom/geometry/setRmin    0. mm
/gate/my_phantom/vis/forceSolid
/gate/my_phantom/vis/setColor        grey
/gate/my_phantom/placement/setTranslation 0 0 0 mm
/gate/my_phantom/attachPhantomSD

#-----#
#           A C T O R S           #
#-----#
/gate/actor/addActor DoseActor        dosimetry
/gate/actor/dosimetry/attachTo        my_phantom
/gate/actor/dosimetry/stepHitType     post
/gate/actor/dosimetry/setResolution   400 400 400
/gate/actor/dosimetry/setVoxelSize    0.0006227 0.0006227 0.0006227 mm
#/gate/actor/dosimetry/setSize        0.24908 0.24908 0.24908 mm
/gate/actor/dosimetry/setPosition     0 0 0 mm
/gate/actor/dosimetry/enableDose      false
/gate/actor/dosimetry/enableEdep      true
/gate/actor/dosimetry/enableUncertaintyEdep true
/gate/actor/dosimetry/enableSquaredEdep true
/gate/actor/dosimetry/save            output/2e7_50keV_water.mhd
/gate/actor/dosimetry/saveEveryNSeconds 30

/gate/actor/addActor                  SimulationStatisticActor stat
/gate/actor/stat/save                 output/2e7_50keV_water_post_stats.txt
/gate/actor/stat/saveEveryNSeconds    30

#-----#
#           P H Y S I C S         #
#-----#
/gate/physics/addPhysicsList emstandard_opt3

#-----#
#           E L E C T R O M A G N E T I C   O P T I O N S           #
#-----#
/gate/physics/setEMin                 0.1 keV
/gate/physics/setEMax                 10 GeV
/gate/physics/setDEDXBinning          220
/gate/physics/setLambdaBinning        220

/gate/physics/Gamma/SetCutInRegion    world 0.1 mm
/gate/physics/Electron/SetCutInRegion world 0.0054 mm
/gate/physics/Gamma/SetCutInRegion    my_phantom 0.1 mm
/gate/physics/Electron/SetCutInRegion my_phantom 0.003 mm
/gate/physics/SetMaxStepSizeInRegion  my_phantom 0.0006227 mm

```

```

/gate/physics/ActivateStepLimiter          e-
/gate/physics/processes/ElectronIonisation/setStepFunction e- 0.0001 0.001 mm

#-----#
#           INITIALIZE                       #
#-----#
/gate/run/initialize
/gate/physics/displayCuts
/gate/physics/processList      Enabled
/gate/physics/processList      Initialized

#-----#
#           SOURCE DEFINITION                #
#-----#
/gate/source/addSource monoenergetic_electron      gps
/gate/source/monoenergetic_electron/gps/particle  e-
/gate/source/monoenergetic_electron/gps/energytype Mono
/gate/source/monoenergetic_electron/gps/ene/mono  50. keV
/gate/source/monoenergetic_electron/gps/angtype   iso
/gate/source/monoenergetic_electron/gps/centre   0. 0. 0. mm
/gate/source/monoenergetic_electron/gps/type     Point
/gate/source/monoenergetic_electron/attachTo     my_phantom
/gate/source/monoenergetic_electron/visualize    100 yellow 2
/gate/source/list

#-----#
#           VISUALIZATION                    #
#-----#
/vis/disable
/vis/open OGLSQt
/vis/viewer/reset
/vis/viewer/set/viewpointThetaPhi 30 60
/vis/viewer/zoom 5
/vis/viewer/set/style wireframe
/vis/drawVolume
/vis/viewer/flush
/vis/scene/add/trajectories
/tracking/storeTrajectory 1
/vis/scene/add/hits
/vis/scene/endOfEventAction accumulate 10

#-----#
#           RANDOM GENERATOR                 #
#-----#
/gate/random/setEngineName MersenneTwister
/gate/random/setEngineSeed auto

```

```

#-----#
#          S T A R T   S I M U L A T I O N          #
#-----#
/gate/application/setTotalNumberOfPrimaries 2e7
/gate/application/start

#-----#
#          E N D   S I M U L A T I O N          #
#-----#

```

All other monoenergetic electrons simulation scripts and MATLAB analysis scripts are available in GitHub repository: https://github.com/ashok-tiwari/Beta_dose_point_kernels

A.2 Simulation scripts of ^{186}Re β -emitter

```

#-----#
#          V E R B O S I T Y          #
#-----#
# The verbosity settings were the same as in Appendix A.1.
/gate/geometry/setMaterialDatabase GateMaterials.db

#-----#
#          W O R L D          #
#-----#
/gate/world/geometry/setXLength    5 cm
/gate/world/geometry/setYLength    5 cm
/gate/world/geometry/setZLength    5 cm
/gate/world/setMaterial             Water

#-----#
#          P H A N T O M   G E O M E T R Y          #
#-----#
/gate/world/daughters/name          my_phantom
/gate/world/daughters/insert        sphere--
/gate/my_phantom/setMaterial        Water
/gate/my_phantom/geometry/setRmax   6.7743 mm
/gate/my_phantom/geometry/setRmin   0. mm
/gate/my_phantom/vis/forceSolid
/gate/my_phantom/vis/setColor       grey
/gate/my_phantom/placement/setTranslation 0 0 0 mm
/gate/my_phantom/attachPhantomSD

#-----#
#          A C T O R S          #
#-----#
/gate/actor/addActor               DoseActor    dosimetry

```

```

/gate/actor/dosimetry/attachTo      my_phantom
/gate/actor/dosimetry/stepHitType   random
#/gate/actor/dosimetry/setResolution 351 351 351
/gate/actor/dosimetry/setPosition    0 0 0 mm
/gate/actor/dosimetry/setSize        13.5486 13.5486 13.5486 mm
/gate/actor/dosimetry/setVoxelSize   0.0386 0.0386 0.0386 mm
/gate/actor/dosimetry/enableDose     true
/gate/actor/dosimetry/enableEdep     true
/gate/actor/dosimetry/enableUncertaintyEdep true
/gate/actor/dosimetry/enableSquaredEdep true
/gate/actor/dosimetry/save           output/2e7_Re186_water.mhd
/gate/actor/dosimetry/saveEveryNSeconds 60

```

```

/gate/actor/addActor                SimulationStatisticActor stat
/gate/actor/stat/save               output/2e7_Re186_water.txt
/gate/actor/stat/saveEveryNSeconds 60

```

```

#-----#
#          P H Y S I C S   D E S C R I P T I O N          #
#-----#

```

```

/gate/physics/addPhysicsList        emstandard_opt3
# For ion source simulation add radioactive decay
/gate/physics/addProcess RadioactiveDecay

```

```

#-----#
#          E L E C T R O M A G N E T I C   O P T I O N S          #
#-----#

```

```

/gate/physics/setEMin                0.1 keV
/gate/physics/setEMax                10 GeV
/gate/physics/setDEDXBinning         220
/gate/physics/setLambdaBinning       220
/gate/physics/Gamma/SetCutInRegion   world 0.1 mm
/gate/physics/Electron/SetCutInRegion world 0.01 mm
/gate/physics/Gamma/SetCutInRegion   my_phantom 0.1 mm
/gate/physics/Electron/SetCutInRegion my_phantom 0.005 mm
/gate/physics/SetMaxStepSizeInRegion my_phantom 0.0386 mm
/gate/physics/ActivateStepLimiter    e-
/gate/physics/processes/ElectronIonisation/setStepFunction e- 0.0001 0.001 mm

```

```

#-----#
#          I N I T I A L I Z E          #
#-----#

```

```

/gate/run/initialize
/gate/physics/displayCuts
/gate/physics/processList    Enabled

```


The visualization settings were the same as in Appendix A.1.

```
#-----#  
#   R A N D O M   G E N E R A T O R   #  
#-----#  
/gate/random/setEngineName MersenneTwister  
/gate/random/setEngineSeed auto  
/gate/random/verbose 2  
  
#-----#  
#   S T A R T   S I M U L A T I O N   #  
#-----#  
/gate/application/setTotalNumberOfPrimaries 2e7  
/gate/application/start  
  
#-----#  
#   E N D   S I M U L A T I O N   #  
#-----#
```

All other β -emitting radionuclides simulation scripts are available in the GitHub repository:
https://github.com/ashok-tiwari/Beta_dose_point_kernels

B. Validation experiment simulation setup in GATE using ^{177}Lu line source

```
#-----#  
#   V E R B O S I T Y   #  
#-----#  
# Verbosity settings were the same as in A.1.  
/gate/geometry/setMaterialDatabase GateMaterials.db  
  
#-----#  
#   W O R L D   #  
#-----#  
/gate/world/geometry/setXLength      300 mm  
/gate/world/geometry/setYLength      300 mm  
/gate/world/geometry/setZLength      300 mm  
/gate/world/setMaterial              Air  
  
#-----#  
#   P H A N T O M   G E O M E T R Y   #  
#-----#  
/gate/world/daughters/name           my_cylinder1  
/gate/world/daughters/insert         cylinder  
/gate/my_cylinder1/setMaterial       Polyethylene
```

```

/gate/my_cylinder1/placement/setTranslation 0 0 -5.139 mm # 5+(0.278/2) = 5.139
/gate/my_cylinder1/geometry/setRmax 20. mm # radius = 2 cm
/gate/my_cylinder1/geometry/setRmin 0.44 mm
/gate/my_cylinder1/geometry/setHeight 10. mm
/gate/my_cylinder1/vis/forceSolid
/gate/my_cylinder1/vis/setColor blue
/gate/my_cylinder1/attachPhantomSD

```

```

/gate/world/daughters/name my_cylinder2
/gate/world/daughters/insert cylinder
/gate/my_cylinder2/setMaterial Polyethylene
/gate/my_cylinder2/placement/setTranslation 0 0 5.139 mm
/gate/my_cylinder2/geometry/setRmax 20. mm # radius = 2 cm
/gate/my_cylinder2/geometry/setRmin 0.44 mm
/gate/my_cylinder2/geometry/setHeight 10. mm
/gate/my_cylinder2/vis/forceSolid
/gate/my_cylinder2/vis/setColor magenta
/gate/my_cylinder2/attachPhantomSD

```

```

# define Gafchromic film (polyester + active layer + polyester)
/gate/world/daughters/name Gafchromic_film
/gate/world/daughters/insert cylinder
/gate/Gafchromic_film/setMaterial Air
/gate/Gafchromic_film/placement/setTranslation 0 0 0 mm
/gate/Gafchromic_film/geometry/setRmax 21. mm
/gate/Gafchromic_film/geometry/setRmin 0.44 mm
/gate/Gafchromic_film/geometry/setHeight 0.278 mm
/gate/Gafchromic_film/vis/forceWireframe
/gate/Gafchromic_film/vis/setColor white
/gate/Gafchromic_film/attachPhantomSD

```

```

# define polyester top layer of Gafchromic film
/gate/Gafchromic_film/daughters/name polyester_top
/gate/Gafchromic_film/daughters/insert cylinder
/gate/polyester_top/setMaterial Polyester
/gate/polyester_top/placement/setTranslation 0 0 -0.0765 mm
/gate/polyester_top/geometry/setRmax 21. mm
/gate/polyester_top/geometry/setRmin 0.44 mm
/gate/polyester_top/geometry/setHeight 0.125 mm
/gate/polyester_top/vis/forceSolid
/gate/polyester_top/vis/setColor green
/gate/polyester_top/attachPhantomSD

```

```

# define active layer in between two polyester base
/gate/Gafchromic_film/daughters/name active_layer
/gate/Gafchromic_film/daughters/insert cylinder

```

```

/gate/active_layer/setMaterial          Gafchromicactive
/gate/active_layer/placement/setTranslation 0 0 0 mm
/gate/active_layer/geometry/setRmax      21. mm
/gate/active_layer/geometry/setRmin      0.44 mm
/gate/active_layer/geometry/setHeight    0.028 mm
/gate/active_layer/vis/forceSolid
/gate/active_layer/vis/setColor          white
/gate/active_layer/attachPhantomSD

# define polyester bottom layer of Gafchromic film
/gate/Gafchromic_film/daughters/name     polyester_bot
/gate/Gafchromic_film/daughters/insert   cylinder
/gate/polyester_bot/setMaterial          Polyester
/gate/polyester_bot/placement/setTranslation 0 0 0.0765 mm # (0.125/2+0.028/2) offset
/gate/polyester_bot/geometry/setRmax     21. mm
/gate/polyester_bot/geometry/setRmin     0.44 mm
/gate/polyester_bot/geometry/setHeight   0.125 mm
/gate/polyester_bot/vis/forceSolid
/gate/polyester_bot/vis/setColor         green
/gate/polyester_bot/attachPhantomSD

# define line source
/gate/my_cylinder1/daughters/name        source_cylinder
/gate/my_cylinder1/daughters/insert      cylinder
/gate/source_cylinder/setMaterial        Plastic
/gate/source_cylinder/placement/setTranslation 0 0 5.139 mm
/gate/source_cylinder/geometry/setRmax   0.44 mm
/gate/source_cylinder/geometry/setRmin   0.21 mm
/gate/source_cylinder/geometry/setHeight 120. mm
/gate/source_cylinder/vis/forceSolid
/gate/source_cylinder/vis/setColor       white
/gate/source_cylinder/attachPhantomSD

#-----#
#           A C T O R S           #
#-----#
/gate/actor/addActor      DoseActor      dosimetry
/gate/actor/dosimetry/attachTo      Gafchromic_film
/gate/actor/dosimetry/stepHitType    random
#/gate/actor/dosimetry/setVoxelSize   0.05 0.05 0.278 mm
/gate/actor/dosimetry/setResolution   760 760 1
/gate/actor/dosimetry/setSize         38 38 0.278 mm # 0.278 is thickness of film
/gate/actor/dosimetry/setPosition     0. 0. 0. mm
/gate/actor/dosimetry/enableEdep      true
/gate/actor/dosimetry/enableDose      false
/gate/actor/dosimetry/enableUncertaintyEdep      false

```

```

/gate/actor/dosimetry/enableSquaredEdep          false
/gate/actor/dosimetry/save                       output/Lu177_6hr_poly_508dpi.mhd
/gate/actor/dosimetry/saveEveryNSeconds         30

/gate/actor/addActor SimulationStatisticActor     stat
/gate/actor/stat/save                           output/Lu177_6hr_poly_508dpi_stats.txt
/gate/actor/stat/saveEveryNSeconds             30

#-----#
#           P H Y S I C S   D E S C R I P T I O N           #
#-----#
/gate/physics/addPhysicsList emstandard_opt3
# For ion source simulation add radioactive decay
/gate/physics/addProcess RadioactiveDecay

/gate/physics/setEMin                          0.1 keV
/gate/physics/setEMax                          10 GeV
/gate/physics/setLambdaBinning                 220
/gate/physics/Gamma/SetCutInRegion             world 2 mm
/gate/physics/Electron/SetCutInRegion          world 2 mm
/gate/physics/Positron/SetCutInRegion          world 2 mm
/gate/physics/SetMaxStepSizeInRegion           my_cylinder1 0.05 mm
/gate/physics/SetMaxStepSizeInRegion           my_cylinder2 0.05 mm
/gate/physics/SetMaxStepSizeInRegion           polyester_top 0.05 mm
/gate/physics/SetMaxStepSizeInRegion           active_layer 0.05 mm
/gate/physics/SetMaxStepSizeInRegion           polyester_bot 0.05 mm
/gate/physics/ActivateStepLimiter              e-
/gate/physics/processes/eMultipleScattering/setGeometricalStepLimiterType e- distanceToBoundary
/gate/physics/processes/eMultipleScattering/setGeometricalStepLimiterType e+ distanceToBoundary

#-----#
#           I N I T I A L I Z E                               #
#-----#
/gate/run/initialize
/gate/physics/displayCuts
/gate/physics/processList Enabled
/gate/physics/processList Initialized

#-----#
#           L u 1 7 7   -   S O U R C E                       #
#-----#
/gate/source/addSource                         Lu177Source
/gate/source/Lu177Source/gps/particle          ion
/gate/source/Lu177Source/gps/ion              71 177 0 0
/gate/source/Lu177Source/gps/energytype       Mono
/gate/source/Lu177Source/gps/monoenergy       0. keV
/gate/source/Lu177Source/setForcedUnstableFlag true

```

```

/gate/source/Lu177Source/useDefaultHalfLife
/gate/source/Lu177Source/setActivity          0.1103 mCi
/gate/source/Lu177Source/gps/type           Volume
/gate/source/Lu177Source/gps/shape          Cylinder
/gate/source/Lu177Source/gps/radius          0.21 mm
/gate/source/Lu177Source/gps/halfz          60.0 mm
/gate/source/Lu177Source/gps/angtype         iso
/gate/source/Lu177Source/gps/mintheta        0. deg
/gate/source/Lu177Source/gps/maxtheta        180. deg
/gate/source/Lu177Source/gps/minphi          0. deg
/gate/source/Lu177Source/gps/maxphi          360. deg
/gate/source/Lu177Source/attachTo            source_cylinder
/gate/source/Lu177Source/gps/centre          0. 0. 0. cm
/gate/source/Lu177Source/gps/number          1
/gate/source/list
/gate/output/verbose 2

```

```

#-----#
#          VISUALIZATION          #
#-----#
# The visualization settings were the same as in A.1.

```

```

#-----#
# MONTE CARLO PSEUDO - RANDOM NUMBER GENERATOR #
#-----#
/gate/random/setEngineName    MersenneTwister
/gate/random/setEngineSeed    auto
/gate/random/verbose          2

```

```

#-----#
#          START SIMULATION          #
#-----#
/gate/application/setTimeSlice  1. s
/gate/application/setTimeStart  0. s
/gate/application/setTimeStop   10. s
/gate/application/start

```

```

#-----#
#          END SIMULATION          #
#-----#

```

C. Decay chains of simulated α -emitting radionuclides

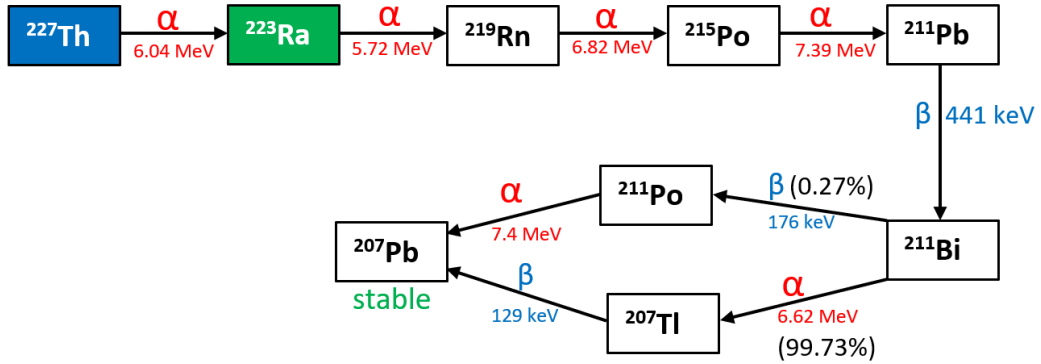


Figure C1: Simplified decay chains of ^{227}Th and ^{223}Ra radionuclides.

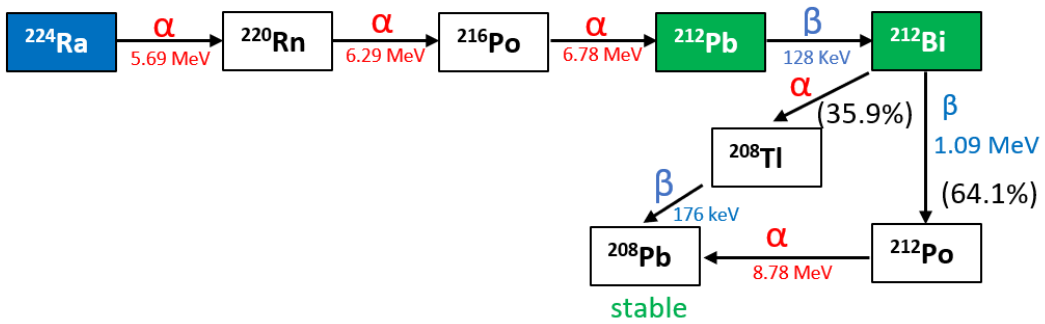


Figure C2: Simplified decay chains of ^{224}Ra , ^{212}Pb and ^{212}Bi radionuclide.

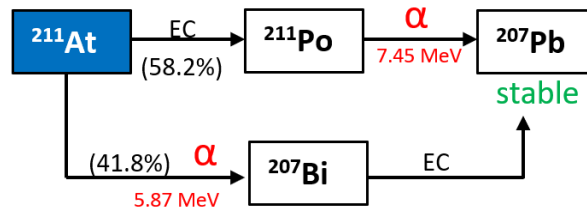


Figure C3: Simplified decay chain of ^{211}At radionuclide.

D. Dose point kernels simulation scripts of ^{225}Ac α -emitter

```
#-----#
#           V E R B O S I T Y           #
#-----#
# The verbosity settings were the same as in A.1.
/gate/geometry/setMaterialDatabase GateMaterials.db

#-----#
#           W O R L D                   #
#-----#
/gate/world/geometry/setXLength 1 mm
/gate/world/geometry/setYLength 1 mm
/gate/world/geometry/setZLength 1 mm
/gate/world/setMaterial          Water

#-----#
#           P H A N T O M   G E O M E T R Y           #
#-----#
/gate/world/daughters/name          my_phantom
/gate/world/daughters/insert        sphere
/gate/my_phantom/setMaterial        Adipose
/gate/my_phantom/geometry/setRmax   210 um
/gate/my_phantom/geometry/setRmin   0 um
/gate/my_phantom/vis/forceSolid
/gate/my_phantom/vis/setColor       grey
/gate/my_phantom/placement/setTranslation 0 0 0 um
/gate/my_phantom/attachPhantomSD

#-----#
#           P H Y S I C S                 #
#-----#
/gate/physics/addPhysicsList emstandard_opt4
/gate/physics/addProcess RadioactiveDecay

### FTFP - Precompound Fritof Parton Model FTF
### BERT - Bertini Intranuclear Cascade Model
### HP - High Precision Neutron Package Model
/gate/physics/addPhysicsList FTFP_BERT_HP_EMZ
# suffix EMZ represent the highest precision electromagnetic physics models

# Add Atomic-Deexcitation for fluorescence and Auger emission including Auger cascades
/gate/physics/addAtomDeexcitation

# Activate fluorescence x-rays
/process/em/fluo true
```

```
# Activate Auger electron cascades simulation and particle induced X-ray emission (PIXE)
/process/em/auger true
/process/em/augerCascade true
/process/em/pixe true
```

```
#-----#
#      ELECTROMAGNETIC OPTIONS      #
#-----#
```

```
/gate/physics/setEMin          1 keV
/gate/physics/setEMax          10 GeV
/gate/physics/setDEDXBinning    220
/gate/physics/setLambdaBinning 220
```

```
/gate/physics/Gamma/SetCutInRegion world 1 mm
/gate/physics/Electron/SetCutInRegion world 1 mm
/gate/physics/Positron/SetCutInRegion world 1 mm
/gate/physics/Proton/SetCutInRegion world 1 mm
/gate/physics/displayCuts
```

```
/gate/physics/SetMaxStepSizeInRegion my_phantom 1 um
/gate/physics/ActivateStepLimiter    e-
/gate/physics/ActivateStepLimiter    alpha
```

```
#-----#
#      A C T O R S      #
#-----#
```

```
/gate/actor/addActor      DoseActor      dosimetry
/gate/actor/dosimetry/attachTo my_phantom
/gate/actor/dosimetry/stepHitType post
/gate/actor/dosimetry/setSize 400 400 400 um
/gate/actor/dosimetry/setVoxelSize 1 1 1 um
/gate/actor/dosimetry/setPosition 0 0 0 mm
/gate/actor/dosimetry/enableDose false
/gate/actor/dosimetry/enableEdep true
/gate/actor/dosimetry/enableUncertaintyEdep false
/gate/actor/dosimetry/enableSquaredEdep false
/gate/actor/dosimetry/save Adipose/Ac225_Adipose_5e7.mhd
/gate/actor/dosimetry/saveEveryNSeconds 30
```

```
/gate/actor/addActor      SimulationStatisticActor stat
/gate/actor/stat/save      Adipose/stat_Ac225_Adipose_5e7.txt
/gate/actor/stat/saveEveryNSeconds 30
```

```
#-----#
#      I N I T I A L I Z E      #
#-----#
```

```

/gate/run/initialize
/gate/physics/displayCuts
/gate/physics/processList    Enabled
/gate/physics/processList    Initialized

```

```

#-----#
#          SOURCE DEFINITION          #
#-----#

```

```

/gate/source/addSource          IonSource
/gate/source/IonSource/gps/type Point
/gate/source/IonSource/gps/centre 0.0 0.0 0.0 cm
/gate/source/IonSource/gps/particle ion
/gate/source/IonSource/gps/ion    89 225 0 0
/gate/source/IonSource/setForcedUnstableFlag true
/gate/source/IonSource/useDefaultHalfLife
/gate/source/IonSource/gps/ene/type Mono
/gate/source/IonSource/gps/monoenergy 0. MeV
/gate/source/IonSource/gps/number 1
/gate/source/IonSource/gps/angtype iso
/gate/source/IonSource/gps/mintheta 0. deg
/gate/source/IonSource/gps/maxtheta 180. deg
/gate/source/IonSource/gps/minphi 0. deg
/gate/source/IonSource/gps/maxphi 360. deg
/gate/source/IonSource/attachTo my_phantom
/gate/source/IonSource/visualize 1000 yellow 10
/gate/source/list

```

```

#-----#
#          RANDOM GENERATOR          #
#-----#

```

```

/gate/random/setEngineName MersenneTwister
/gate/random/setEngineSeed auto

```

```

#-----#
#          START SIMULATION          #
#-----#

```

```

/gate/application/setTotalNumberOfPrimaries 5e7
/gate/application/start

```

```

#-----#
#          END SIMULATION            #
#-----#

```

E. Simulation scripts of Discovery MI 4-ring scanner with a scatter phantom

```
#-----#
#          V E R B O S I T Y          #
#-----#
# The verbosity settings are the same as in A.1.
/gate/geometry/setMaterialDatabase GateMaterials.db

#-----#
#          W O R L D                   #
#-----#
/gate/world/geometry/setXLength      300. cm
/gate/world/geometry/setYLength      300. cm
/gate/world/geometry/setZLength      300. Cm
/gate/world/setMaterial               Air

#-----#
#          S C A N N E R   G E O M E T R Y          #
#-----#
/gate/world/daughters/name           cylindricalPET
/gate/world/daughters/insert         cylinder
/gate/cylindricalPET/setMaterial     Air
/gate/cylindricalPET/placement/setTranslation 0.0 0.0 0.0 mm
/gate/cylindricalPET/geometry/setRmax 380. mm
/gate/cylindricalPET/geometry/setRmin 350. mm
/gate/cylindricalPET/geometry/setHeight 200. mm
/gate/cylindricalPET/vis/setVisible 1
/gate/cylindricalPET/vis/forceWireframe

# ROTATIONAL SECTOR
/gate/cylindricalPET/daughters/name  my_rsector
/gate/cylindricalPET/daughters/insert box
/gate/my_rsector/placement/setTranslation 368.0 0.0 0.0 mm
/gate/my_rsector/geometry/setXLength 25.0 mm
/gate/my_rsector/geometry/setYLength 64.5 mm
/gate/my_rsector/geometry/setZLength 200.0 mm
/gate/my_rsector/setMaterial         Air
/gate/my_rsector/vis/forceSolid
/gate/my_rsector/vis/setVisible      1
/gate/my_rsector/vis/setColor        magenta

# REPEAT RSECTOR
/gate/my_rsector/repeaters/insert     ring
/gate/my_rsector/ring/setRepeatNumber 34

# MODULE
/gate/my_rsector/daughters/name       my_module
```

```

/gate/my_rsector/daughters/insert          box
/gate/my_module/placement/setTranslation    0.0 0.0 0.0 mm
/gate/my_module/geometry/setXLength         25.0 mm
/gate/my_module/geometry/setYLength         64.5 mm
/gate/my_module/geometry/setZLength         47.84 mm
/gate/my_module/setMaterial                 Air
/gate/my_module/vis/forceSolid
/gate/my_module/vis/setColor                gray

# REPEAT MODULE
/gate/my_module/repeaters/insert            cubicArray
/gate/my_module/cubicArray/setRepeatNumberX 1
/gate/my_module/cubicArray/setRepeatNumberY 1
/gate/my_module/cubicArray/setRepeatNumberZ 4 # 4- ring system #
/gate/my_module/cubicArray/setRepeatVector  0. 0. 50.64 mm

# SUBMODULE
/gate/my_module/daughters/name              my_submodule
/gate/my_module/daughters/insert            box
/gate/my_submodule/placement/setTranslation 0.0 0.0 0.0 mm
/gate/my_submodule/geometry/setXLength      25.0 mm
/gate/my_submodule/geometry/setYLength      15.9 mm
/gate/my_submodule/geometry/setZLength      47.84 mm
/gate/my_submodule/setMaterial              Air
/gate/my_submodule/vis/setVisible           1
/gate/my_submodule/vis/forceSolid
/gate/my_submodule/vis/setColor             blue

# REPEAT SUBMODULE
/gate/my_submodule/repeaters/insert          cubicArray
/gate/my_submodule/cubicArray/setRepeatNumberX 1
/gate/my_submodule/cubicArray/setRepeatNumberY 4
/gate/my_submodule/cubicArray/setRepeatNumberZ 1
/gate/my_submodule/cubicArray/setRepeatVector 0.0 16.125 0.0 mm

# CRYSTAL
/gate/my_submodule/daughters/name            my_crystal
/gate/my_submodule/daughters/insert          box
/gate/my_crystal/placement/setTranslation     0.0 0.0 0.0 mm
/gate/my_crystal/geometry/setXLength          25.0 mm
/gate/my_crystal/geometry/setYLength          3.95 mm
/gate/my_crystal/geometry/setZLength          5.30 mm
/gate/my_crystal/setMaterial                  Air
/gate/my_crystal/vis/setVisible               0
/gate/my_crystal/vis/forceSolid
/gate/my_crystal/vis/setColor                 gray

```

REPEAT CRYSTAL

```
/gate/my_crystal/repeaters/insert cubicArray
/gate/my_crystal/cubicArray/setRepeatNumberX 1
/gate/my_crystal/cubicArray/setRepeatNumberY 4
/gate/my_crystal/cubicArray/setRepeatNumberZ 9
/gate/my_crystal/cubicArray/setRepeatVector 0.0 3.975 5.3155 mm
```

PLACE LYSO crystals

```
/gate/my_crystal/daughters/name LYSO
/gate/my_crystal/daughters/insert box
/gate/LYSO/placement/setTranslation 0.0 0.0 0.0 mm
/gate/LYSO/geometry/setXLength 25.0 mm
/gate/LYSO/geometry/setYLength 3.95 mm
/gate/LYSO/geometry/setZLength 5.3 mm
/gate/LYSO/setMaterial LYSO
/gate/LYSO/vis/setColor red
```

ATTACH SYSTEM

```
/gate/systems/cylindricalPET/rsector/attach my_rsector
/gate/systems/cylindricalPET/module/attach my_module
/gate/systems/cylindricalPET/submodule/attach my_submodule
/gate/systems/cylindricalPET/crystal/attach my_crystal
/gate/systems/cylindricalPET/layer0/attach LYSO
```

ATTACH LAYER SD

```
/gate/LYSO/attachCrystalSD
/gate/systems/cylindricalPET/describe
```

Attenuating materials between the front face of the crystals and patient bore

Plastic Polycarbonate cover 0.7 mm thick

```
/gate/world/daughters/name layer1
/gate/world/daughters/insert cylinder
/gate/layer1/setMaterial Polycarbonate
/gate/layer1/geometry/setRmax 352.7 mm
/gate/layer1/geometry/setRmin 352 mm
/gate/layer1/geometry/setHeight 200. mm
/gate/layer1/vis/forceSolid
/gate/layer1/vis/setVisible 1
/gate/layer1/vis/setColor white
```

Mylar 1.5 mm thick patient scanner window

```
/gate/world/daughters/name layer2
/gate/world/daughters/insert cylinder
/gate/layer2/setMaterial Mylar
/gate/layer2/geometry/setRmax 354.2 mm
```

```

/gate/layer2/geometry/setRmin      352.7 mm
/gate/layer2/geometry/setHeight    200. mm
/gate/layer2/vis/forceSolid
/gate/layer2/vis/setVisible        1
/gate/layer2/vis/setColor          red

```

```

# Metalized Mylar 0.1 mm
/gate/world/daughters/name         layer3
/gate/world/daughters/insert       cylinder
/gate/layer3/setMaterial           mMylar
/gate/layer3/geometry/setRmax      354.3 mm
/gate/layer3/geometry/setRmin      354.2 mm
/gate/layer3/geometry/setHeight    200. mm
/gate/layer3/vis/forceSolid
/gate/layer3/vis/setVisible        1
/gate/layer3/vis/setColor          white
/gate/layer1/attachPhantomSD
/gate/layer2/attachPhantomSD
/gate/layer3/attachPhantomSD

```

```

#-----#
#   PHANTOM GEOMETRY   #
#-----#

```

Phantom is cylinder of 20.3 cm diameter, 200 cm long and has a line source insert

```

/gate/world/daughters/name         scatter_phantom
/gate/world/daughters/insert       cylinder
/gate/scatter_phantom/setMaterial   Polyethylene
/gate/scatter_phantom/placement/setTranslation 0.0 0.0 0.0 cm
/gate/scatter_phantom/geometry/setRmax 10.15 cm
/gate/scatter_phantom/geometry/setRmin 0. cm
/gate/scatter_phantom/geometry/setHeight 200.0 cm
/gate/scatter_phantom/vis/setVisible 1
/gate/scatter_phantom/vis/forceWireframe
/gate/scatter_phantom/vis/setColor  red

```

```

# Daughter of phantom, hole inside the scatter phantom
/gate/scatter_phantom/daughters/name  hole
/gate/scatter_phantom/daughters/insert cylinder
/gate/hole/setMaterial                 Air
/gate/hole/geometry/setRmax           3.2 mm
/gate/hole/geometry/setRmin           0. mm
/gate/hole/geometry/setHeight         200.0 cm
/gate/hole/placement/setTranslation  0.0 -45.0 0.0 mm
/gate/hole/vis/setVisible              1
/gate/hole/vis/forceWireframe

```

```

/gate/hole/vis/setColor blue

# For line source tube inside air hole
/gate/hole/daughters/name sourceinsert_tube
/gate/hole/daughters/insert cylinder
/gate/sourceinsert_tube/setMaterial Polyethylene
/gate/sourceinsert_tube/geometry/setRmin 1.6 mm
/gate/sourceinsert_tube/geometry/setRmax 2.4 mm
/gate/sourceinsert_tube/geometry/setHeight 200.0 cm
/gate/sourceinsert_tube/placement/setTranslation 0.0 0.0 0.0 mm
/gate/sourceinsert_tube/vis/setVisible 1
/gate/sourceinsert_tube/vis/forceWireframe
/gate/sourceinsert_tube/vis/setColor white

/gate/sourceinsert_tube/daughters/name linesourcevolume
/gate/sourceinsert_tube/daughters/insert cylinder
/gate/linesourcevolume/setMaterial Water
/gate/linesourcevolume/geometry/setRmax 1.6 mm
/gate/linesourcevolume/geometry/setRmin 0.0 mm
/gate/linesourcevolume/geometry/setHeight 200.0 cm
/gate/linesourcevolume/placement/setTranslation 0.0 0.0 0.0 mm
/gate/linesourcevolume/vis/setVisible 0
/gate/linesourcevolume/vis/forceSolid
/gate/linesourcevolume/vis/setColor white
/gate/scatter_phantom/attachPhantomSD
/gate/hole/attachPhantomSD
/gate/sourceinsert_tube/attachPhantomSD
/gate/linesourcevolume/attachPhantomSD

#-----#
# SIMULATION STATISTICS #
#-----#
/gate/actor/addActor SimulationStatisticActor stat
/gate/actor/stat/save output/stat_{activity}_MBq.txt
/gate/actor/stat/saveEveryNSeconds 30

#-----#
# PHYSICS LIST & CUTS #
#-----#
/gate/physics/addPhysicsList emstandard_opt4
# For ion sources
/gate/physics/addProcess RadioactiveDecay

/gate/physics/setEMin 1 keV
/gate/physics/setEMax 1 GeV
/gate/physics/setDEDX Binning 220

```

```

/gate/physics/setLambdaBinning          220
/gate/physics/Gamma/SetCutInRegion     world 1 mm
/gate/physics/Electron/SetCutInRegion  world 1 mm
/gate/physics/Positron/SetCutInRegion  world 1 mm
/gate/physics/Gamma/SetCutInRegion     scatter_phantom 0.1 mm
/gate/physics/Electron/SetCutInRegion  scatter_phantom 0.1 mm
/gate/physics/Positron/SetCutInRegion  scatter_phantom 0.1 mm
/gate/physics/Gamma/SetCutInRegion     LYSO 0.1 mm
/gate/physics/Electron/SetCutInRegion  LYSO 0.1 mm
/gate/physics/Positron/SetCutInRegion  LYSO 0.1 mm

```

```

#-----#
#   INITIALIZE                               #
#-----#

```

```

/gate/run/initialize
/gate/physics/displayCuts
/gate/physics/processList   Enabled
/gate/physics/processList   Initialized

```

```

#-----#
#   DIGITIZER SETTINGS                       #
#-----#

```

```

/gate/digitizer/Singles/insert          adder
/gate/digitizer/Singles/insert          readout
/gate/digitizer/Singles/readout/setDepth 2

/gate/digitizer/Singles/insert          blurring
/gate/digitizer/Singles/blurring/setResolution 0.12
/gate/digitizer/Singles/blurring/setEnergyOfReference 511 keV

/gate/digitizer/Singles/insert          timeResolution
/gate/digitizer/Singles/timeResolution/setTimeResolution 375 ps

/gate/digitizer/Singles/insert          deadtime
/gate/digitizer/Singles/deadtime/setDeadTime 200. ns
/gate/digitizer/Singles/deadtime/setMode nonparalysable
/gate/digitizer/Singles/deadtime/chooseDTVolume my_module

/gate/digitizer/Singles/insert          thresholder
/gate/digitizer/Singles/thresholder/setThreshold 425 keV
/gate/digitizer/Singles/insert          upholder
/gate/digitizer/Singles/upholder/setUphold 650 keV
/gate/digitizer/Singles/describe

/gate/digitizer/Coincidences/setWindow 2.45 ns
/gate/digitizer/Coincidences/minSectorDifference 3

```

```

/gate/digitizer/Coincidences/MultiplesPolicy      takeAllGoods
/gate/digitizer/Coincidences/describe

#/gate/digitizer/name                            delay
#/gate/digitizer/insert                          coincidenceSorter
#/gate/digitizer/delay/setWindow                 2.45 ns
#/gate/digitizer/delay/setOffset                 500. ns
#/gate/digitizer/delay/MultiplesPolicy           takeAllGoods
#/gate/digitizer/delay/describe

```

```

#-----#
#          SOURCE DEFINITION          #
#-----#

```

```

/gate/source/addSource          F18
/gate/source/F18/setActivity    {activity}. MBq
/gate/source/F18/gps/particle  e+
/gate/source/F18/setForcedUnstableFlag true
/gate/source/F18/setForcedHalfLife 6586.2 s
/gate/source/F18/gps/energytype  Fluor18
/gate/source/F18/gps/type        Volume
/gate/source/F18/gps/shape        Cylinder
/gate/source/F18/gps/radius        1.6 mm
/gate/source/F18/gps/halfz         100.0 cm
/gate/source/F18/gps/angtype       iso
/gate/source/F18/gps/centre        0. -45. 0. mm
/gate/source/F18/gps/Forbid        scatter_phantom
/gate/source/F18/dump              1
/gate/source/list

```

```

#-----#
#          OUTPUT          #
#-----#

```

```

/gate/output/root/enable
/gate/output/root/setFileName      output/scat_{activity}_MBq
/gate/output/root/setRootHitFlag    0
/gate/output/root/setRootSinglesAdderFlag 0
/gate/output/root/setRootSinglesReadoutFlag 0
/gate/output/root/setRootSinglesFlag  0
/gate/output/root/setRootCoincidencesFlag 1
#/gate/output/root/setRootdelayFlag    1
/gate/output/root/setRootNtupleFlag    0

```

```

#-----#
#          VISUALIZATION          #
#-----#

```

```

# This part of code is same as in A.1.

```

```

#-----#
#   RANDOM GENERATOR   #
#-----#
/gate/random/setEngineName MersenneTwister
/gate/random/setEngineSeed auto
/gate/random/verbose 1

#-----#
#   START SIMULATION   #
#-----#
/gate/application/setTimeSlice      1 s
/gate/application/setTimeStart      0. s
/gate/application/setTimeStop       1 s
/gate/application/startDAQ
exit

#-----#
#   END SIMULATION     #
#-----#

```

All other scanner simulations scripts, including different phantoms scripts and data analysis tools written in MATLAB and ROOT, are available in the GitHub repository:

<https://github.com/ashok-tiwari/PET-scanners-simulations>

F. List of publications

- **Tiwari A**, Graves SA, Sunderland J. The Impact of Tissue Type and Density on Dose Point Kernels for Patient-Specific Voxel-Wise Dosimetry: A Monte Carlo Investigation. *Radiat Res.* 2020;193(6):531-42.
- **Tiwari A**, Sunderland J, Graves SA, Strand S, Flynn R. Absorbed dose distributions from beta-decaying radionuclides: Experimental validation of Monte Carlo tools for radiopharmaceutical dosimetry. *Med Phys.* 2020;47(11):5779-90.
- **Tiwari A**, Merrick M, Graves SA, Sunderland J. Monte Carlo evaluation of hypothetical long axial field-of-view PET scanner using GE Discovery MI PET front-end architecture. *Med Phys.* 2022;49:1139-1152.

- Merrick MJ, Rotsch DA, **Tiwari A**, Nolen J, Brossard T, Song J, Wadas TJ, Sunderland JJ, and Graves SA. Imaging and Dosimetric Characteristics of ^{67}Cu . *Phys Med Biol* 66, 035002, 2021.
- Merrick MJ, Rotsch DA, **Tiwari A**, Nolen J, Brossard T, Song J, Wadas TJ, Sunderland JJ, and Graves SA. Half-Life of ^{67}Cu , *J Phys Commun*. 5 085007, 2021.
- Graves S, Martin M, **Tiwari A**, Merrick M, and Sunderland JJ. SIR-Spheres® activity measurements reveal systematic miscalibration, *J Nucl Med.*, (doi:10.2967/jnumed.121.262650) 2021.

G. List of peer reviewed abstracts

- Measurements of dose point kernels using GATE Monte Carlo toolkit for personalized convolution dosimetry. **Tiwari A**, Graves S, Sunderland J. *Journal of Nuclear Medicine* 60 (supplement 1), 274-274, (SNMMI Annual Meeting, 2019), Anaheim, California, USA.
- Impact of Kernel Truncation On ^{177}Lu -DOTATATE and ^{131}I -MIBG Voxelwise Dosimetry. Graves S, **Tiwari A**, Hyer D, Flynn R, Buatti J, Sunderland J. *MEDICAL PHYSICS* 46 (6), E316-E316, (AAPM Annual Meeting, 2019).
- Toward best practice voxel-wise ^{177}Lu dosimetry: kernel generation, scanner characterization, and convolution-based dose calculation. Graves S, **Tiwari A**, Menda Y, Madsen M, and Sunderland J. *Journal of Nuclear Medicine* 60 (supplement 1), 119, (SNMMI Annual Meeting, 2019), California, USA.
- Experimental validation of Monte Carlo-generated beta absorbed doses for 3D voxelwise dosimetry. **Tiwari A**, Graves S, Strand S, and Sunderland J. *Journal of Nuclear Medicine* May 2020, 61 (supplement 1) 533, (SNMMI Annual Meeting 2020).
- Monte Carlo validation of convolution-based voxelwise dosimetry. Graves S, **Tiwari A**, Kruzer A, Nelson A, Mirando D, Dewaraja Y, and Sunderland J, *Journal of Nuclear Medicine* May 2020, 61 (supplement 1) 1019, (SNMMI Annual Meeting 2020).
- Collapsed-cone convolution superposition for improved accuracy of voxelwise dosimetry. Graves S, **Tiwari A**, and Sunderland J. *Journal of Nuclear Medicine* May 2020, 61 (supplement 1) 535, (SNMMI Annual Meeting 2020).
- Production, SPECT Imaging, and Initial Evaluation of ^{67}Cu for Theranostic Applications. Merrick MJ, Rotsch D, **Tiwari A**, Nolen J, Brossard T, Song J, Wadas TJ, Sunderland JJ, and Graves SA. (AAPM Annual Meeting, 2020).

- Monte Carlo simulation of 4-ring Discovery MI PET/CT scanner and its extended axial field-of-view to 2 m. **Tiwari A**, Merrick MJ, Graves SA, and Sunderland J. Journal of Nuclear Medicine May 2021, 62 (supplement 1) 1150, (SNMMI Annual Meeting, 2021).
- Evaluation of a scalable qSPECT calibration method for radiopharmaceutical dosimetry. Graves S, Merrick M, **Tiwari A**, and Sunderland J. Journal of Nuclear Medicine, May 2021, 62 (supplement 1) 143, (SNMMI Annual meeting, 2021).
- A Comprehensive PET-CT scanner characterization performance assessment paradigm and database. Sunderland J and **Tiwari A**, Journal of Nuclear Medicine, May 2021, 62 (supplement 1) 1398, (SNMMI Annual meeting, 2021).
- Longitudinal PET/CT Imaging of ^{64}Cu for Radiopharmaceutical Therapy Dosimetry. Merrick M, Dunnwald L, **Tiwari A**, Sunderland J, and Graves S. (AAPM Annual Meeting 2021).
- Evaluation of therapeutic alpha emitters for their potential to be used in FAPI compounds. **Tiwari A**, Graves SA, Merrick MJ, and Sunderland J. (SNMMI 2022 Annual Meeting), Vancouver, Canada.

REFERENCES

1. Tiwari A, Graves SA, Sunderland J. The Impact of Tissue Type and Density on Dose Point Kernels for Patient-Specific Voxel-Wise Dosimetry: A Monte Carlo Investigation. *Radiat Res.* 2020;193(6):531-42.
2. Tiwari A, Sunderland J, Graves SA, Strand S, Flynn R. Absorbed dose distributions from beta-decaying radionuclides: Experimental validation of Monte Carlo tools for radiopharmaceutical dosimetry. *Med Phys.* 2020;47(11):5779-90.
3. Tiwari A, Merrick M, Graves SA, Sunderland J. Monte Carlo evaluation of hypothetical long axial field-of-view PET scanner using GE Discovery MI PET front-end architecture. *Med Phys.* 2022;49(2):1139-52.
4. Fischer-Valuck BW, Rao YJ, Michalski JM. Intensity-modulated radiotherapy for prostate cancer. *Transl Androl Urol.* 2018;7(3):297-307.
5. Ludwike WMvK, Esmee CAvdS, Arthur JATB, Bart dK, Marnix GEHL. Lutetium-177-PSMA therapy for prostate cancer patients - a brief overview of the literature. *Tijdschr Urol.* 2020;10:141-6.
6. Sanli Y, Simsek DH, Sanli O, Subramaniam RM, Kendi AT. (177)Lu-PSMA Therapy in Metastatic Castration-Resistant Prostate Cancer. *Biomedicines.* 2021;9(4).
7. Khreish F, Ebert N, Ries M, Maus S, Rosar F, Bohnenberger H, et al. (225)Ac-PSMA-617/(177)Lu-PSMA-617 tandem therapy of metastatic castration-resistant prostate cancer: pilot experience. *Eur J Nucl Med Mol Imaging.* 2020;47(3):721-8.
8. Bolch WE, Bouchet LG, Robertson JS, Wessels BW, Siegel JA, Howell RW, et al. MIRD pamphlet No. 17: The dosimetry of nonuniform activity distributions - Radionuclide S values at the voxel level. *Journal of Nuclear Medicine.* 1999;40(1):11s-36s.
9. Lanconelli N, Pacilio M, Lo Meo S, Botta F, Di Dia A, Aroche AT, et al. A free database of radionuclide voxel S values for the dosimetry of nonuniform activity distributions. *Phys Med Biol.* 2012;57(2):517-33.
10. Papadimitroulas P, Loudos G, Nikiforidis GC, Kagadis GC. A dose point kernel database using GATE Monte Carlo simulation toolkit for nuclear medicine applications: comparison with other Monte Carlo codes. *Med Phys.* 2012;39(8):5238-47.
11. Graves SA, Flynn RT, Hyer DE. Dose point kernels for 2,174 radionuclides. *Med Phys.* 2019;46(11):5284-93.
12. Sgouros G, Bodei L, McDevitt MR, Nedrow JR. Radiopharmaceutical therapy in cancer: clinical advances and challenges. *Nat Rev Drug Discov.* 2020;19(9):589-608.

13. Ku A, Facca VJ, Cai Z, Reilly RM. Auger electrons for cancer therapy - a review. *EJNMMI Radiopharm Chem.* 2019;4(1):27.
14. Kiess AP, Minn I, Chen Y, Hobbs R, Sgouros G, Mease RC, et al. Auger Radiopharmaceutical Therapy Targeting Prostate-Specific Membrane Antigen. *J Nucl Med.* 2015;56(9):1401-7.
15. Bloomer WD, McLaughlin WH, Adelstein SJ, Wolf AP. Therapeutic applications of Auger and alpha emitting radionuclides. *Strahlentherapie.* 1984;160(12):755-7.
16. Behr TM, Behe M, Lohr M, Sgouros G, Angerstein C, Wehrmann E, et al. Therapeutic advantages of Auger electron- over beta-emitting radiometals or radioiodine when conjugated to internalizing antibodies. *Eur J Nucl Med.* 2000;27(7):753-65.
17. Kassis AI, Sastry KS, Adelstein SJ. Kinetics of uptake, retention, and radiotoxicity of ¹²⁵IUdR in mammalian cells: implications of localized energy deposition by Auger processes. *Radiat Res.* 1987;109(1):78-89.
18. Kassis AI, Fayad F, Kinsey BM, Sastry KS, Taube RA, Adelstein SJ. Radiotoxicity of ¹²⁵I in mammalian cells. *Radiat Res.* 1987;111(2):305-18.
19. Rebeschung C, Hoffmann D, Stefani L, Desruet MD, Wang K, Adelstein SJ, et al. First human treatment of resistant neoplastic meningitis by intrathecal administration of MTX plus (¹²⁵I)UdR. *Int J Radiat Biol.* 2008;84(12):1123-9.
20. Macapinlac HA, Kemeny N, Daghighian F, Finn R, Zhang J, Humm J, et al. Pilot clinical trial of 5-[¹²⁵I]iodo-2'-deoxyuridine in the treatment of colorectal cancer metastatic to the liver. *J Nucl Med.* 1996;37(4 Suppl):25S-9S.
21. Behr TM, Sgouros G, Vougiokas V, Memtsoudis S, Gratz S, Schmidberger H, et al. Therapeutic efficacy and dose-limiting toxicity of Auger-electron vs. beta emitters in radioimmunotherapy with internalizing antibodies: evaluation of ¹²⁵I- vs. ¹³¹I-labeled CO17-1A in a human colorectal cancer model. *Int J Cancer.* 1998;76(5):738-48.
22. Wessels BW, Rogus RD. Radionuclide selection and model absorbed dose calculations for radiolabeled tumor associated antibodies. *Med Phys.* 1984;11(5):638-45.
23. Dewaraja YK, Chun SY, Srinivasa RN, Kaza RK, Cuneo KC, Majdalany BS, et al. Improved quantitative (90) Y bremsstrahlung SPECT/CT reconstruction with Monte Carlo scatter modeling. *Med Phys.* 2017;44(12):6364-76.
24. Tafti BA, Padia SA. Dosimetry of Y-90 Microspheres Utilizing Tc-99m SPECT and Y-90 PET. *Semin Nucl Med.* 2019;49(3):211-7.
25. Bayly RJ, Peacegood JA, Peake SC. ⁹⁰Y ferric hydroxide colloid. *Ann Rheum Dis.* 1973;32 Suppl 6:Suppl:10.

26. Roncali E, Taebi A, Foster C, Vu CT. Personalized Dosimetry for Liver Cancer Y-90 Radioembolization Using Computational Fluid Dynamics and Monte Carlo Simulation. *Ann Biomed Eng.* 2020;48(5):1499-510.
27. Yue J, Mauxion T, Reyes DK, Lodge MA, Hobbs RF, Rong X, et al. Comparison of quantitative Y-90 SPECT and non-time-of-flight PET imaging in post-therapy radioembolization of liver cancer. *Med Phys.* 2016;43(10):5779.
28. Bodei L, Mueller-Brand J, Baum RP, Pavel ME, Horsch D, O'Dorisio MS, et al. The joint IAEA, EANM, and SNMMI practical guidance on peptide receptor radionuclide therapy (PRRNT) in neuroendocrine tumours. *Eur J Nucl Med Mol Imaging.* 2013;40(5):800-16.
29. Kratochwil C, Fendler WP, Eiber M, Baum R, Bozkurt MF, Czernin J, et al. EANM procedure guidelines for radionuclide therapy with (177)Lu-labelled PSMA-ligands ((177)Lu-PSMA-RLT). *Eur J Nucl Med Mol Imaging.* 2019;46(12):2536-44.
30. Strosberg J, El-Haddad G, Wolin E, Hendifar A, Yao J, Chasen B, et al. Phase 3 Trial of (177)Lu-Dotatate for Midgut Neuroendocrine Tumors. *N Engl J Med.* 2017;376(2):125-35.
31. Sartor O, de Bono J, Chi KN, Fizazi K, Herrmann K, Rahbar K, et al. Lutetium-177-PSMA-617 for Metastatic Castration-Resistant Prostate Cancer. *N Engl J Med.* 2021;385(12):1091-103.
32. Wahl RL, Sunderland J. Radiopharmaceutical Dosimetry for Cancer Therapy: From Theory to Practice. *J Nucl Med.* 2021;62(Suppl 3):1S-2S.
33. Uribe C, Peterson A, Van B, Fedrigo R, Carlson J, Sunderland J, et al. An International Study of Factors Affecting Variability of Dosimetry Calculations, Part 1: Design and Early Results of the SNMMI Dosimetry Challenge. *J Nucl Med.* 2021;62(Suppl 3):36S-47S.
34. Sgouros G, Roeske JC, McDevitt MR, Palm S, Allen BJ, Fisher DR, et al. MIRD Pamphlet No. 22 (abridged): radiobiology and dosimetry of alpha-particle emitters for targeted radionuclide therapy. *J Nucl Med.* 2010;51(2):311-28.
35. Sgouros G. Dosimetry, Radiobiology and Synthetic Lethality: Radiopharmaceutical Therapy (RPT) With Alpha-Particle-Emitters. *Semin Nucl Med.* 2020;50(2):124-32.
36. Lassmann M, Eberlein U, Gear J, Konijnenberg M, Kunikowska J. Dosimetry for Radiopharmaceutical Therapy: The European Perspective. *J Nucl Med.* 2021;62(Suppl 3):73S-9S.
37. Flux G, Bardies M, Monsieurs M, Savolainen S, Strands SE, Lassmann M, et al. The impact of PET and SPECT on dosimetry for targeted radionuclide therapy. *Z Med Phys.* 2006;16(1):47-59.

38. Hanscheid H, Lassmann M. Will SPECT/CT Cameras Soon Be Able to Display Absorbed Doses? Dosimetry from Single-Activity-Concentration Measurements. *J Nucl Med.* 2020;61(7):1028-9.
39. Hanscheid H, Lapa C, Buck AK, Lassmann M, Werner RA. Dose Mapping After Endoradiotherapy with (177)Lu-DOTATATE/DOTATOC by a Single Measurement After 4 Days. *J Nucl Med.* 2018;59(1):75-81.
40. Madsen MT, Menda Y, O'Dorisio TM, O'Dorisio MS. Technical Note: Single time point dose estimate for exponential clearance. *Med Phys.* 2018;45(5):2318-24.
41. Jackson PA, Hofman MS, Hicks RJ, Scalzo M, Violet J. Radiation Dosimetry in (177)Lu-PSMA-617 Therapy Using a Single Posttreatment SPECT/CT Scan: A Novel Methodology to Generate Time- and Tissue-Specific Dose Factors. *J Nucl Med.* 2020;61(7):1030-6.
42. Bolch WE, Eckerman KF, Sgouros G, Thomas SR. MIRDO Pamphlet No. 21: A Generalized Schema for Radiopharmaceutical Dosimetry-Standardization of Nomenclature. *Journal of Nuclear Medicine.* 2009;50(3):477-84.
43. Dewaraja YK, Frey EC, Sgouros G, Brill AB, Roberson P, Zanzonico PB, et al. MIRDO pamphlet No. 23: quantitative SPECT for patient-specific 3-dimensional dosimetry in internal radionuclide therapy. *J Nucl Med.* 2012;53(8):1310-25.
44. Ljungberg M, Celler A, Konijnenberg MW, Eckerman KF, Dewaraja YK, Sjogreen-Gleisner K, et al. MIRDO Pamphlet No. 26: Joint EANM/MIRD Guidelines for Quantitative Lu-177 SPECT Applied for Dosimetry of Radiopharmaceutical Therapy. *Journal of Nuclear Medicine.* 2016;57(1):151-62.
45. Stabin MG. MIRDOSE: personal computer software for internal dose assessment in nuclear medicine. *J Nucl Med.* 1996;37(3):538-46.
46. Stabin MG, Sparks RB, Crowe E. OLINDA/EXM: the second-generation personal computer software for internal dose assessment in nuclear medicine. *J Nucl Med.* 2005;46(6):1023-7.
47. Andersson M, Johansson L, Eckerman K, Mattsson S. IDAC-Dose 2.1, an internal dosimetry program for diagnostic nuclear medicine based on the ICRP adult reference voxel phantoms. *EJNMMI Res.* 2017;7(1):88.
48. Kesner A, Olguin E, Zanzonico P, Bolch W. MIRDCalc V 1.0-A community spreadsheet tool for organ-level radiopharmaceutical absorbed dose calculations. *Journal of Nuclear Medicine.* 2018;59.
49. Bolch WE, Jokisch D, Zankl M, Eckerman KF, Fell T, Manger R, et al. ICRP Publication 133: The ICRP computational framework for internal dose assessment for reference adults: specific absorbed fractions. *Ann ICRP.* 2016;45(2):5-73.

50. Tiwari A, Graves S, Sunderland J. Measurements of dose point kernels using GATE Monte Carlo toolkit for personalized convolution dosimetry. *Journal of Nuclear Medicine*. 2019;60.
51. Strul D, Santin G, Lazaro D, Breton V, Morel C. GATE (Geant4 Application for Tomographic Emission): a PET/SPECT general-purpose simulation platform. *Nucl Phys B-Proc Sup*. 2003;125:75-9.
52. Allison J, Amako K, Apostolakis J, Arce P, Asai M, Aso T, et al. Recent developments in Geant4. *Nuclear Instruments and Methods in Physics Research Section A: Accelerators, Spectrometers, Detectors and Associated Equipment*. 2016;835:186-225.
53. Jan S, Santin G, Strul D, Staelens S, Assie K, Autret D, et al. GATE: a simulation toolkit for PET and SPECT. *Phys Med Biol*. 2004;49(19):4543-61.
54. Taschereau R, Chatziioannou AF. Monte Carlo simulations of absorbed dose in a mouse phantom from 18-fluorine compounds. *Med Phys*. 2007;34(3):1026-36.
55. Mauxion T, Barbet J, Suhard J, Pouget JP, Poirot M, Bardies M. Improved realism of hybrid mouse models may not be sufficient to generate reference dosimetric data. *Med Phys*. 2013;40(5):052501.
56. Parach AA, Rajabi H, Askari MA. Assessment of MIRD data for internal dosimetry using the GATE Monte Carlo code. *Radiat Environ Biophys*. 2011;50(3):441-50.
57. Snyder WS, Fisher HL, Jr., Ford MR, Warner GG. Estimates of absorbed fractions for monoenergetic photon sources uniformly distributed in various organs of a heterogeneous phantom. *J Nucl Med*. 1969:Suppl 3:7-52.
58. Gupta A, Lee MS, Kim JH, Park S, Park HS, Kim SE, et al. Preclinical voxel-based dosimetry through GATE Monte Carlo simulation using PET/CT imaging of mice. *Phys Med Biol*. 2019;64(9):095007.
59. DOSIsoft software, <https://www.dosisoft.com/products/planet-dose/>. Accessed May 20, 2020.
60. Kupitz D, Wetz C, Wissel H, Wedel F, Apostolova I, Wallbaum T, et al. Software-assisted dosimetry in peptide receptor radionuclide therapy with ¹⁷⁷Lutetium-DOTATATE for various imaging scenarios. *PLoS One*. 2017;12(11):e0187570.
61. MIM Software, https://www.mimsoftware.com/molecular_radiotherapy/sureplanmrt. Accessed May 15, 2020.
62. Grassi E, Fioroni F, Ferri V, Mezzenga E, Sarti MA, Paulus T, et al. Quantitative comparison between the commercial software STRATOS((R)) by Philips and a homemade software for voxel-dosimetry in radiopeptide therapy. *Phys Med*. 2015;31(1):72-9.

63. Capala J, Graves SA, Scott A, Sgouros G, James SS, Zanzonico P, et al. Dosimetry for Radiopharmaceutical Therapy: Current Practices and Commercial Resources. *J Nucl Med.* 2021;62(Suppl 3):3S-11S.
64. Conti M, Eriksson L. Physics of pure and non-pure positron emitters for PET: a review and a discussion. *EJNMMI Phys.* 2016;3(1):8.
65. Muller C, Zhernosekov K, Koster U, Johnston K, Dorrer H, Hohn A, et al. A unique matched quadruplet of terbium radioisotopes for PET and SPECT and for alpha- and beta-radionuclide therapy: an in vivo proof-of-concept study with a new receptor-targeted folate derivative. *J Nucl Med.* 2012;53(12):1951-9.
66. Eiber M, Fendler WP, Rowe SP, Calais J, Hofman MS, Maurer T, et al. Prostate-Specific Membrane Antigen Ligands for Imaging and Therapy. *J Nucl Med.* 2017;58(Suppl 2):67S-76S.
67. Vandenberghe S, Moskal P, Karp JS. State of the art in total body PET. *EJNMMI Phys.* 2020;7(1):35.
68. Cherry SR, Badawi RD, Jones T. EXPLORER: Changing the molecular imaging paradigm with total-body PET/CT. *Proc Spie.* 2016;9783.
69. Spencer BA, Berg E, Schmall JP, Omidvari N, Leung EK, Abdelhafez YG, et al. Performance evaluation of the uEXPLORER Total-body PET/CT scanner based on NEMA NU 2-2018 with additional tests to characterize long axial field-of-view PET scanners. *J Nucl Med.* 2020.
70. Zhang X, Xie Z, Berg E, Judenhofer MS, Liu W, Xu T, et al. Total-Body Dynamic Reconstruction and Parametric Imaging on the uEXPLORER. *J Nucl Med.* 2020;61(2):285-91.
71. Karp JS, Viswanath V, Geagan MJ, Muehllehner G, Pantel AR, Parma MJ, et al. PennPET Explorer: Design and Preliminary Performance of a Whole-Body Imager. *J Nucl Med.* 2020;61(1):136-43.
72. Pantel AR, Viswanath V, Daube-Witherspoon ME, Dubroff JG, Muehllehner G, Parma MJ, et al. PennPET Explorer: Human Imaging on a Whole-Body Imager. *J Nucl Med.* 2020;61(1):144-51.
73. Siemens Healthineers 2021 [Available from: <https://www.siemens-healthineers.com/molecular-imaging/pet-ct/biograph-vision-quadra>].
74. Alberts I, Hunermund JN, Prenosil G, Mingels C, Bohn KP, Viscione M, et al. Clinical performance of long axial field of view PET/CT: a head-to-head intra-individual comparison of the Biograph Vision Quadra with the Biograph Vision PET/CT. *Eur J Nucl Med Mol Imaging.* 2021;48(8):2395-404.

75. Surti S, Pantel AR, Karp JS. Total Body PET: Why, How, What for? *IEEE Trans Radiat Plasma Med Sci.* 2020;4(3):283-92.
76. Badawi RD, Shi H, Hu P, Chen S, Xu T, Price PM, et al. First Human Imaging Studies with the EXPLORER Total-Body PET Scanner. *J Nucl Med.* 2019;60(3):299-303.
77. Sui X, Liu G, Hu P, Chen S, Yu H, Wang Y, et al. Total-Body PET/Computed Tomography Highlights in Clinical Practice: Experiences from Zhongshan Hospital, Fudan University. *PET Clin.* 2021;16(1):9-14.
78. Cherry SR, Badawi RD, Karp JS, Moses WW, Price P, Jones T. Total-body imaging: Transforming the role of positron emission tomography. *Sci Transl Med.* 2017;9(381).
79. Poon JK, Dahlbom ML, Moses WW, Balakrishnan K, Wang W, Cherry SR, et al. Optimal whole-body PET scanner configurations for different volumes of LSO scintillator: a simulation study. *Phys Med Biol.* 2012;57(13):4077-94.
80. Zhang X, Zhou J, Cherry SR, Badawi RD, Qi J. Quantitative image reconstruction for total-body PET imaging using the 2-meter long EXPLORER scanner. *Phys Med Biol.* 2017;62(6):2465-85.
81. Surti S, Werner ME, Karp JS. Study of PET scanner designs using clinical metrics to optimize the scanner axial FOV and crystal thickness. *Phys Med Biol.* 2013;58(12):3995-4012.
82. Moskal P, Rundel O, Alfs D, Bednarski T, Bialas P, Czerwinski E, et al. Time resolution of the plastic scintillator strips with matrix photomultiplier readout for J-PET tomograph. *Phys Med Biol.* 2016;61(5):2025-47.
83. Zhang J, Knopp MI, Knopp MV. Sparse Detector Configuration in SiPM Digital Photon Counting PET: a Feasibility Study. *Mol Imaging Biol.* 2019;21(3):447-53.
84. Zein SA, Karakatsanis NA, Issa M, Haj-Ali AA, Nehmeh SA. Physical performance of a long axial field-of-view PET scanner prototype with sparse rings configuration: A Monte Carlo simulation study. *Med Phys.* 2020;47(4):1949-57.
85. Zein SA, Karakatsanis NA, Conti M, Nehmeh SA. Monte Carlo Simulation of the Siemens Biograph Vision PET With Extended Axial Field of View Using Sparse Detector Module Rings Configuration. *Ieee T Radiat Plasma.* 2021;5(3):331-42.
86. Buck AK, Nekolla S, Ziegler S, Beer A, Krause BJ, Herrmann K, et al. Spect/Ct. *J Nucl Med.* 2008;49(8):1305-19.
87. Fahey FH, Grogg K, El Fakhri G. Use of Monte Carlo Techniques in Nuclear Medicine. *J Am Coll Radiol.* 2018;15(3 Pt A):446-8.
88. Hissoiny S, Ozell B, Bouchard H, Despres P. GPUMCD: A new GPU-oriented Monte Carlo dose calculation platform. *Med Phys.* 2011;38(2):754-64.

89. Jia X, Gu X, Sempau J, Choi D, Majumdar A, Jiang SB. Development of a GPU-based Monte Carlo dose calculation code for coupled electron-photon transport. *Phys Med Biol.* 2010;55(11):3077-86.
90. Jahnke L, Fleckenstein J, Wenz F, Hesser J. GMC: a GPU implementation of a Monte Carlo dose calculation based on Geant4. *Phys Med Biol.* 2012;57(5):1217-29.
91. Briesmeister JF. MCNP—A general Monte Carlo N-particle transport code. LA-13181. 1997.
92. Kawrakow I, Mainegra-Hing E., D.W.O.R., Tessier F., Walters B.R.B. The EGSnrc code system: Monte Carlo simulation of electron and photon transport. NRCC Report PIRS-701 2018.
93. Sempau J, Sanchez-Reyes A, Salvat F, ben Tahar HO, Jiang SB, Fernandez-Varea JM. Monte Carlo simulation of electron beams from an accelerator head using PENELOPE. *Phys Med Biol.* 2001;46(4):1163-86.
94. Bahreyni Toossi MT, Islamian JP, Momennezhad M, Ljungberg M, Naseri SH. SIMIND Monte Carlo simulation of a single photon emission CT. *J Med Phys.* 2010;35(1):42-7.
95. Muhammad W, Ullah A, Mahmood K, Matiullah. Assessment of national dosimetry quality audits results for teletherapy machines from 1989 to 2015. *J Appl Clin Med Phys.* 2016;17(2):145-52.
96. Sarrut D, Bardies M, Boussion N, Freud N, Jan S, Letang JM, et al. A review of the use and potential of the GATE Monte Carlo simulation code for radiation therapy and dosimetry applications. *Med Phys.* 2014;41(6).
97. Staelens S, Strul D, Santin G, Vandenberghe S, Koole M, D'Asseler Y, et al. Monte Carlo simulations of a scintillation camera using GATE: validation and application modelling. *Phys Med Biol.* 2003;48(18):3021-42.
98. Lazaro D, Buvat I, Loudos G, Strul D, Santin G, Giokaris N, et al. Validation of the GATE Monte Carlo simulation platform for modelling a CsI(Tl) scintillation camera dedicated to small-animal imaging. *Phys Med Biol.* 2004;49(2):271-85.
99. Schmidtlein CR, Kirov AS, Nehmeh SA, Erdi YE, Humm JL, Amols HI, et al. Validation of GATE Monte Carlo simulations of the GE Advance/Discovery LS PET scanners. *Med Phys.* 2006;33(1):198-208.
100. Lamare F, Turzo A, Bizais Y, Le Rest CC, Visvikis D. Validation of a Monte Carlo simulation of the Philips Allegro/GEMINI PET systems using GATE. *Phys Med Biol.* 2006;51(4):943-62.
101. McIntosh B, Goertzen AL. Validation of Gate Simulations of the (Lu)-L-176 Intrinsic Activity in Lso Detectors. *Ieee Nucl Sci Conf R.* 2009:3426-+.

102. Zagni F, D'Ambrosio D, Spinelli AE, Cicoria G, Fanti S, Marengo M. Accurate modeling of a DOI capable small animal PET scanner using GATE. *Appl Radiat Isot.* 2013;75:105-14.
103. Aklan B, Jakoby BW, Watson CC, Braun H, Ritt P, Quick HH. GATE Monte Carlo simulations for variations of an integrated PET/MR hybrid imaging system based on the Biograph mMR model. *Phys Med Biol.* 2015;60(12):4731-52.
104. Bretin F, Bahri MA, Luxen A, Phillips C, Plenevaux A, Seret A. Monte Carlo simulations of the dose from imaging with GE eXplore 120 micro-CT using GATE. *Med Phys.* 2015;42(10):5711-9.
105. Kowalski P, Wislicki W, Shopa RY, Raczynski L, Klimaszewski K, Curcenau C, et al. Estimating the NEMA characteristics of the J-PET tomograph using the GATE package. *Phys Med Biol.* 2018;63(16):165008.
106. Salvadori J, Labour J, Odille F, Marie PY, Badel JN, Imbert L, et al. Monte Carlo simulation of digital photon counting PET. *EJNMMI Phys.* 2020;7(1):23.
107. Tiwari A, Merrick M, Graves S, Sunderland J. Monte Carlo simulation of 4-ring Discovery MI PET/CT scanner and its extended axial field-of-view to 2 m. *Journal of Nuclear Medicine.* 2021(62).
108. Viswanath V, Daube Witherspoon ME, Werner M, Surti S, Trindade A, Rodrigues P, et al., editors. GATE simulations to study extended axial FOVs for the PennPET Explorer scanner. *IEEE Nuclear Science Symposium and Medical Imaging Conference (NSS/MIC); 2017; Atlanta, GA, USA: IEEE.*
109. Ferrer L, Chouin N, Bitar A, Lisbona A, Bardies M. Implementing dosimetry in GATE: dose-point kernel validation with GEANT4 4.8.1. *Cancer Biother Radiopharm.* 2007;22(1):125-9.
110. Khazaei Moghadam M, Kamali Asl A, Geramifar P, Zaidi H. Evaluating the Application of Tissue-Specific Dose Kernels Instead of Water Dose Kernels in Internal Dosimetry: A Monte Carlo Study. *Cancer Biother Radiopharm.* 2016;31(10):367-79.
111. Kostou T, Papadimitroulas P, Loudos G, Kagadis GC. A preclinical simulated dataset of S-values and investigation of the impact of rescaled organ masses using the MOBY phantom. *Phys Med Biol.* 2016;61(6):2333-55.
112. Chauvin M, Borys D, Botta F, Bzowski P, Dabin J, Denis-Bacelar AM, et al. OpenDose: Open-Access Resource for Nuclear Medicine Dosimetry. *J Nucl Med.* 2020;61(10):1514-9.
113. Thiam CO, Breton V, Donnarieix D, Habib B, Maigne L. Validation of a dose deposited by low-energy photons using GATE/GEANT4. *Physics in Medicine and Biology.* 2008;53(11):3039-55.

114. Benhalouche S, Visvikis D, Le Maitre A, Pradier O, Boussion N. Evaluation of clinical IMRT treatment planning using the GATE Monte Carlo simulation platform for absolute and relative dose calculations. *Med Phys*. 2013;40(2):021711.
115. Bouzid D, Bert J, Dupre PF, Benhalouche S, Pradier O, Boussion N, et al. Monte-Carlo dosimetry for intraoperative radiotherapy using a low energy x-ray source. *Acta Oncol*. 2015;54(10):1788-95.
116. Grevillot L, Bertrand D, Dessy F, Freud N, Sarrut D. A Monte Carlo pencil beam scanning model for proton treatment plan simulation using GATE/GEANT4. *Phys Med Biol*. 2011;56(16):5203-19.
117. Grevillot L, Frisson T, Maneval D, Zahra N, Badel JN, Sarrut D. Simulation of a 6 MV Elekta Precise Linac photon beam using GATE/GEANT4. *Phys Med Biol*. 2011;56(4):903-18.
118. Didi S, Moussa A, Yahya T, Mustafa Z. Simulation of the 6 MV Elekta Synergy Platform linac photon beam using Geant4 Application for Tomographic Emission. *J Med Phys*. 2015;40(3):136-43.
119. Scikit-hep/uproot:3.10.12(3.10.12). Zenodo. [Internet]. 2019. Available from: <https://doi.org/10.5281/zenodo.3543691>.
120. Sarrut D, Bala M, Bardies M, Bert J, Chauvin M, Chatzipapas K, et al. Advanced Monte Carlo simulations of emission tomography imaging systems with GATE. *Phys Med Biol*. 2021;66(10).
121. Prise KM, O'Sullivan JM. Radiation-induced bystander signalling in cancer therapy. *Nat Rev Cancer*. 2009;9(5):351-60.
122. Dieudonne A, Hobbs RF, Bolch WE, Sgouros G, Gardin I. Fine-Resolution Voxel S Values for Constructing Absorbed Dose Distributions at Variable Voxel Size. *Journal of Nuclear Medicine*. 2010;51(10):1600-7.
123. Grimes J, Celler A. Comparison of internal dose estimates obtained using organ-level, voxel S value, and Monte Carlo techniques. *Medical Physics*. 2014;41(9).
124. Huizing DMV, de Wit-van der Veen BJ, Verheij M, Stokkel MPM. Dosimetry methods and clinical applications in peptide receptor radionuclide therapy for neuroendocrine tumours: a literature review. *Ejnm Research*. 2018;8.
125. Berger MJ. Improved point kernels for electron and beta-ray dosimetry. US Atomic Energy Commission. 1973.
126. Botta F, Mairani A, Battistoni G, Cremonesi M, Di Dia A, Fasso A, et al. Calculation of electron and isotopes dose point kernels with FLUKA Monte Carlo code for dosimetry in nuclear medicine therapy. *Medical Physics*. 2011;38(7):3944-54.

127. Champion C, Incerti S, Perrot Y, Delorme R, Bordage MC, Bardies M, et al. Dose point kernels in liquid water: An intra-comparison between GEANT4-DNA and a variety of Monte Carlo codes. *Applied Radiation and Isotopes*. 2014;83:137-41.
128. Furhang EE, Sgouros G, Chui CS. Radionuclide photon dose kernels for internal emitter dosimetry. *Medical Physics*. 1996;23(5):759-64.
129. Prestwich WV, Nunes J, Kwok CS. Beta dose point kernels for radionuclides. *Journal of Nuclear Medicine*. 1989;30:1036-46.
130. Simpkin DJ, Mackie TR. Egs4 Monte-Carlo Determination of the Beta-Dose Kernel in Water. *Med Phys*. 1990;17(2):179-86.
131. Uusijarvi H, Chouin N, Bernhardt P, Ferrer L, Bardies M, Forssell-Aronsson E. Comparison of Electron Dose-Point Kernels in Water Generated by the Monte Carlo Codes, PENELOPE, GEANT4, MCNPX, and ETRAN. *Cancer Biother Radio*. 2009;24(4):461-7.
132. Seltzer SM. Electron Photon Monte-Carlo Calculations - the Etran Code. *Appl Radiat Isotopes*. 1991;42(10):917-41.
133. Graves SA, Flynn RT, Hyer DE. Dose point kernels for 2,174 radionuclides. *Med Phys*. 2019.
134. Collaboration O. GATE Users Guide Version 8.0 2004 [Available from: <http://www.opengatecollaboration.org/sites/default/files/GATE-UsersGuideV8.0.pdf>].
135. Jan S, Santin G, Strul D, Staelens S, Assie K, Autret D, et al. GATE: a simulation toolkit for PET and SPECT. *Physics in Medicine and Biology*. 2004;49(19):4543-61.
136. Visvikis D, Bardies M, Chiavassa S, Danford C, Kirov A, Lamare F, et al. Use of the GATE Monte Carlo package for dosimetry applications. *Nucl Instrum Meth A*. 2006;569(2):335-40.
137. Ferrer L, Chouin N, Bitar A, Lisbona A, Bardies M. Implementing dosimetry in GATE: Dose-point kernel validation with GEANT4 4.8.1. *Cancer Biotherapy and Radiopharmaceuticals*. 2007;22(1):125-9.
138. Maigne L, Perrot Y, Schaart DR, Donnarieix D, Breton V. Comparison of GATE/GEANT4 with EGSnrc and MCNP for electron dose calculations at energies between 15 keV and 20 MeV. *Physics in Medicine and Biology*. 2011;56(3):811-27.
139. Marcatili S, Villoing D, Mauxion T, McParland BJ, Bardies M. Model-based versus specific dosimetry in diagnostic context: Comparison of three dosimetric approaches. *Med Phys*. 2015;42(3):1288-96.
140. Kawashima H. Radioimmunotherapy: a specific treatment protocol for cancer by cytotoxic radioisotopes conjugated to antibodies. *ScientificWorldJournal*. 2014;2014:492061.

141. ICRU. Photon, Electron, Proton and Neutron Interaction Data for Body Tissues. ICRU Report 46, Bethesda, MD. 1992.
142. Agostinelli S, Allison J, Amako K, Apostolakis J, Araujo H, Arce P, et al. Geant4—a simulation toolkit. *Nuclear Instruments and Methods in Physics Research Section A: Accelerators, Spectrometers, Detectors and Associated Equipment*. 2003;506(3):250-303.
143. Berger MJ, Coursey JS, Zucker MA. ESTAR, PSTAR, and ASTAR: computer programs for calculating stopping-power and range tables for electrons, protons, and helium ions (version 1.21). Tech. rep.; 1999.
144. Cross WG, Freedman NO, Wong PY. Beta-Ray Dose Distributions from Point Sources in an Infinite Water Medium. *Health Physics*. 1992;63(2):160-71.
145. Mainegra-Hing E, Rogers DWO, Kawrakow I. Calculation of photon energy deposition kernels and electron dose point kernels in water. *Med Phys*. 2005;32(3):685-99.
146. Stabin MG, Siegel JA, Hunt J, Sparks R, Lipsztein J, Eckerman KF. Radar: The radiation dose assessment resource. An online source of dose information for nuclear medicine and occupational radiation safety. *Journal of Nuclear Medicine*. 2001;42(5):243p-p.
147. Laboratory NNDCBN. NuDat (Nuclear Structure and Decay Data) 2008 [Available from: <https://www.nndc.bnl.gov/nudat2/>].
148. Hamby DM, Mangini CD, Caffrey JA, Tang M. VARSKIN 5: a computer code for skin contamination dosimetry. 2014.
149. Mayles P, Nahum A, Rosenwald JC. *Handbook of radiotherapy physics: theory and practice*. 1st Edition ed. New York: Taylor & Francis; 2007.
150. Knapp FF, Dash A. *Radiopharmaceuticals for Therapy*: Springer; 2016.
151. Garske-Roman U, Sandstrom M, Baron KF, Lundin L, Hellman P, Welin S, et al. Prospective observational study of Lu-177-DOTA-octreotate therapy in 200 patients with advanced metastasized neuroendocrine tumours (NETs): feasibility and impact of a dosimetry-guided study protocol on outcome and toxicity. *Eur J Nucl Med Mol I*. 2018;45(6):970-88.
152. Sanchez-Garcia M, Gardin I, Lebtahi R, Dieudonne A. A new approach for dose calculation in targeted radionuclide therapy (TRT) based on collapsed cone superposition: validation with Y-90. *Phys Med Biol*. 2014;59(17):4769-84.
153. Huizing DMV, de Wit-van der Veen BJ, Verheij M, Stokkel MPM. Dosimetry methods and clinical applications in peptide receptor radionuclide therapy for neuroendocrine tumours: a literature review. *EJNMMI Res*. 2018;8(1):89.

154. Flux GD, Sjogreen Gleisner K, Chiesa C, Lassmann M, Chouin N, Gear J, et al. From fixed activities to personalized treatments in radionuclide therapy: lost in translation? *Eur J Nucl Med Mol Imaging*. 2018;45(1):152-4.
155. Dieudonne A, Hobbs RF, Lebtahi R, Maurel F, Baechler S, Wahl RL, et al. Study of the impact of tissue density heterogeneities on 3-dimensional abdominal dosimetry: comparison between dose kernel convolution and direct Monte Carlo methods. *J Nucl Med*. 2013;54(2):236-43.
156. Berger MJ. Distribution of absorbed dose around point sources of electrons and beta particles in water and other media. *J Nucl Med*. 1971;Suppl 5:-23.
157. Prestwich WV, Nunes J, Kwok CS. Beta-Dose Point Kernels for Radionuclides of Potential Use in Radioimmunotherapy. *J Nucl Med*. 1989;30(6):1036-46.
158. Furhang EE, Sgouros G, Chui CS. Radionuclide photon dose kernels for internal emitter dosimetry. *Med Phys*. 1996;23(5):759-64.
159. Botta F, Mairani A, Battistoni G, Cremonesi M, Di Dia A, Fasso A, et al. Calculation of electron and isotopes dose point kernels with FLUKA Monte Carlo code for dosimetry in nuclear medicine therapy. *Med Phys*. 2011;38(7):3944-54.
160. Tiwari A, Graves SA, Sunderland J. The Impact of Tissue Type and Density on Dose Point Kernels for Patient-Specific Voxel-Wise Dosimetry: A Monte Carlo Investigation. *Radiat Res*. 2020.
161. Wessels BW, Griffith MH. Miniature thermoluminescent dosimeter absorbed dose measurements in tumor phantom models. *J Nucl Med*. 1986;27(8):1308-14.
162. Giap HB, Macey DJ, Bayouth JE, Boyer AL. Validation of a dose-point kernel convolution technique for internal dosimetry. *Phys Med Biol*. 1995;40(3):365-81.
163. Wilderman SJ, Dewaraja YK. Method for fast CT/SPECT-based 3D Monte Carlo absorbed dose computations in internal emitter therapy. *Ieee T Nucl Sci*. 2007;54(1):146-51.
164. Gardin I, Bouchet LG, Assie K, Caron J, Lisbona A, Ferrer L, et al. Voxeldose: a computer program for 3-D dose calculation in therapeutic nuclear medicine. *Cancer Biother Radiopharm*. 2003;18(1):109-15.
165. Gear JJ, Charles-Edwards E, Partridge M, Flux GD. Monte Carlo verification of polymer gel dosimetry applied to radionuclide therapy: a phantom study. *Phys Med Biol*. 2011;56(22):7273-86.
166. Reinhardt S, Hillbrand M, Wilkens JJ, Assmann W. Comparison of Gafchromic EBT2 and EBT3 films for clinical photon and proton beams. *Med Phys*. 2012;39(8):5257-62.

167. Casanova Borca V, Pasquino M, Russo G, Grosso P, Cante D, Sciacero P, et al. Dosimetric characterization and use of GAFCHROMIC EBT3 film for IMRT dose verification. *J Appl Clin Med Phys*. 2013;14(2):4111.
168. Mukherjee B, Gholami YH, Bhonsle U, Hentschel R, Khachan J. A unique alpha dosimetry technique using Gafchromic EBT3 (R) film and feasibility study for an activity calibrator for alpha-emitting radiopharmaceuticals. *Brit J Radiol*. 2015;88(1056).
169. Oare C, Wilke C, Ehler E, Mathew D, Sterling D, Ferreira C. Dose calibration of Gafchromic EBT3 film for Ir-192 brachytherapy source using 3D-printed PLA and ABS plastics. *3D Print Med*. 2019;5(1):3.
170. Fox RA, Barker P, Smart G. The use of GAFchromic film to determine the absolute activity of beta emitters. *Phys Med Biol*. 1999;44(4):833-42.
171. Ashland™ Gafchromic radiotherapy films. [Available from: <http://www.gafchromic.com/gafchromic-film/radiotherapy-films/EBT/index.asp>].
172. Callens MB, Crijns W, Depuydt T, Haustermans K, Maes F, D'Agostino E, et al. Modeling the dose dependence of the vis-absorption spectrum of EBT3 GafChromic films. *Med Phys*. 2017;44(6):2532-43.
173. Niroomand-Rad A, Blackwell CR, Coursey BM, Gall KP, Galvin JM, McLaughlin WL, et al. Radiochromic film dosimetry: Recommendations of AAPM Radiation Therapy Committee Task Group 55. *Med Phys*. 1998;25(11):2093-115.
174. Huet C, Dagois S, Derreumaux S, Trompier F, Chenaf C, Robbes I. Characterization and optimization of EBT2 radiochromic films dosimetry system for precise measurements of output factors in small fields used in radiotherapy. *Radiat Meas*. 2012;47(1):40-9.
175. Papaconstadopoulos P, Hegyi G, Seuntjens J, Devic S. A protocol for EBT3 radiochromic film dosimetry using reflection scanning. *Medical Physics*. 2014;41(12).
176. Lourenco V, Bobin C, Chiste V, Lacour D, Rigoulay F, Tapner M, et al. Primary standardization of SIR-Spheres based on the dissolution of the (90)Y-labeled resin microspheres. *Appl Radiat Isot*. 2015;97:170-6.
177. Devic S, Tomic N, Soares CG, Podgorsak EB. Optimizing the dynamic range extension of a radiochromic film dosimetry system. *Med Phys*. 2009;36(2):429-37.
178. van der Merwe D, Van Dyk J, Healy B, Zubizarreta E, Izewska J, Mijnheer B, et al. Accuracy requirements and uncertainties in radiotherapy: a report of the International Atomic Energy Agency. *Acta Oncol*. 2017;56(1):1-6.
179. Devic S, Seuntjens J, Hegyi G, Podgorsak EB, Soares CG, Kirov AS, et al. Dosimetric properties of improved GafChromic films for seven different digitizers. *Med Phys*. 2004;31(9):2392-401.

180. Eckerman KF, Endo A. MIRD: Radionuclide Data and Decay Schemes. 2nd ed: Society of Nuclear Medicine; 2008.
181. Low DA, Harms WB, Mutic S, Purdy JA. A technique for the quantitative evaluation of dose distributions. *Med Phys*. 1998;25(5):656-61.
182. Low DA, Dempsey JF. Evaluation of the gamma dose distribution comparison method. *Med Phys*. 2003;30(9):2455-64.
183. Arjomandy B, Tailor R, Anand A, Sahoo N, Gillin M, Prado K, et al. Energy dependence and dose response of Gafchromic EBT2 film over a wide range of photon, electron, and proton beam energies. *Med Phys*. 2010;37(5):1942-7.
184. Sutherland JG, Rogers DW. Monte Carlo calculated absorbed-dose energy dependence of EBT and EBT2 film. *Med Phys*. 2010;37(3):1110-6.
185. Bekerat H, Devic S, DeBlois F, Singh K, Sarfehnia A, Seuntjens J, et al. Improving the energy response of external beam therapy (EBT) GafChromic™ dosimetry films at low energies (≤ 100 keV). *Med Phys*. 2014;41(2):022101.
186. Sipila P, Ojala J, Kaijaluoto S, Jokelainen I, Kosunen A. Gafchromic EBT3 film dosimetry in electron beams - energy dependence and improved film read-out. *J Appl Clin Med Phys*. 2016;17(1):360-73.
187. National Nuclear Data Center NuDat (Nuclear Structure and Decay Data). 2008 [Available from: <https://www.nndc.bnl.gov/nudat2/>].
188. Lewis D, Micke A, Yu X, Chan MF. An efficient protocol for radiochromic film dosimetry combining calibration and measurement in a single scan. *Med Phys*. 2012;39(10):6339-50.
189. Thermo Scientific Harshaw TLD Materials and Dosimeters. 2019 [Available from: <https://assets.thermofisher.com/TFS-Assets/LSG/Catalogs/Dosimetry-Materials-Brochure.pdf>].
190. Wulbrand C, Seidl C, Gaertner FC, Bruchertseifer F, Morgenstern A, Essler M, et al. Alpha-particle emitting ^{213}Bi -anti-EGFR immunoconjugates eradicate tumor cells independent of oxygenation. *PLoS One*. 2013;8(5):e64730.
191. Allen BJ. Future prospects for targeted alpha therapy. *Curr Radiopharm*. 2011;4(4):336-42.
192. Parker C, Nilsson S, Heinrich D, Helle SI, O'Sullivan JM, Fossa SD, et al. Alpha emitter radium-223 and survival in metastatic prostate cancer. *N Engl J Med*. 2013;369(3):213-23.
193. Parker C, Heidenreich A, Nilsson S, Shore N. Current approaches to incorporation of radium-223 in clinical practice. *Prostate Cancer Prostatic Dis*. 2018;21(1):37-47.

194. Etchebehere E, Brito AE, Rezaee A, Langsteger W, Beheshti M. Therapy assessment of bone metastatic disease in the era of (223)radium. *Eur J Nucl Med Mol Imaging*. 2017;44(Suppl 1):84-96.
195. Dandapani SV, Wong J, Twardowski P. Review of Radium-223 and Metastatic Castration-Sensitive Prostate Cancer. *Cancer Biother Radiopharm*. 2020;35(7):490-6.
196. Ballal S, Yadav MP, Sahoo RK, Tripathi M, Dwivedi SN, Bal C. (225) Ac-PSMA-617-targeted alpha therapy for the treatment of metastatic castration-resistant prostate cancer: A systematic review and meta-analysis. *Prostate*. 2021;81(9):580-91.
197. Meredith RF, Torgue JJ, Rozgaja TA, Banaga EP, Bunch PW, Alvarez RD, et al. Safety and Outcome Measures of First-in-Human Intraperitoneal alpha Radioimmunotherapy With 212Pb-TCMC-Trastuzumab. *Am J Clin Oncol*. 2018;41(7):716-21.
198. Andersson H, Cederkrantz E, Back T, Divgi C, Elgqvist J, Himmelman J, et al. Intraperitoneal alpha-particle radioimmunotherapy of ovarian cancer patients: pharmacokinetics and dosimetry of (211)At-MX35 F(ab')₂--a phase I study. *J Nucl Med*. 2009;50(7):1153-60.
199. Khan AU, DeWerd LA. A Monte Carlo Investigation of Dose Point Kernel Scaling for alpha-Emitting Radionuclides. *Cancer Biother Radiopharm*. 2021;36(3):252-9.
200. Hamson EJ, Keane FM, Tholen S, Schilling O, Gorrell MD. Understanding fibroblast activation protein (FAP): substrates, activities, expression and targeting for cancer therapy. *Proteomics Clin Appl*. 2014;8(5-6):454-63.
201. Zi F, He J, He D, Li Y, Yang L, Cai Z. Fibroblast activation protein alpha in tumor microenvironment: recent progression and implications (review). *Mol Med Rep*. 2015;11(5):3203-11.
202. Sandberg TP, Stuart M, Oosting J, Tollenaar R, Sier CFM, Mesker WE. Increased expression of cancer-associated fibroblast markers at the invasive front and its association with tumor-stroma ratio in colorectal cancer. *BMC Cancer*. 2019;19(1):284.
203. Coto-Llerena M, Ercan C, Kancherla V, Taha-Mehlitz S, Eppenberger-Castori S, Soysal SD, et al. High Expression of FAP in Colorectal Cancer Is Associated With Angiogenesis and Immunoregulation Processes. *Front Oncol*. 2020;10:979.
204. National Nuclear Data Center, NuDat (Nuclear Structure and Decay Data) 2008 [Available from: <https://www.nndc.bnl.gov/nudat2/>].
205. ICRU. ICRU 49, Stopping Powers and Ranges for Protons and Alpha Particles. 49. 1993. Bethesda, MD, ICRU.
206. Hsu DFC, Ilan E, Peterson WT, Uribe J, Lubberink M, Levin CS. Studies of a Next-Generation Silicon-Photomultiplier-Based Time-of-Flight PET/CT System. *J Nucl Med*. 2017;58(9):1511-8.

207. Rausch I, Ruiz A, Valverde-Pascual I, Cal-Gonzalez J, Beyer T, Carrio I. Performance Evaluation of the Vereos PET/CT System According to the NEMA NU2-2012 Standard. *J Nucl Med.* 2019;60(4):561-7.
208. van Sluis J, de Jong J, Schaar J, Noordzij W, van Snick P, Dierckx R, et al. Performance Characteristics of the Digital Biograph Vision PET/CT System. *J Nucl Med.* 2019;60(7):1031-6.
209. Cherry SR, Jones T, Karp JS, Qi J, Moses WW, Badawi RD. Total-Body PET: Maximizing Sensitivity to Create New Opportunities for Clinical Research and Patient Care. *J Nucl Med.* 2018;59(1):3-12.
210. Karakatsanis NA, Lodge MA, Tahari AK, Zhou Y, Wahl RL, Rahmim A. Dynamic whole-body PET parametric imaging: I. Concept, acquisition protocol optimization and clinical application. *Phys Med Biol.* 2013;58(20):7391-418.
211. Karakatsanis NA, Lodge MA, Zhou Y, Wahl RL, Rahmim A. Dynamic whole-body PET parametric imaging: II. Task-oriented statistical estimation. *Phys Med Biol.* 2013;58(20):7419-45.
212. Dimitrakopoulou-Strauss A, Pan L, Sachpekidis C. Kinetic modeling and parametric imaging with dynamic PET for oncological applications: general considerations, current clinical applications, and future perspectives. *Eur J Nucl Med Mol Imaging.* 2021;48(1):21-39.
213. Rahmim A, Lodge MA, Karakatsanis NA, Panin VY, Zhou Y, McMillan A, et al. Dynamic whole-body PET imaging: principles, potentials and applications. *Eur J Nucl Med Mol Imaging.* 2019;46(2):501-18.
214. Zaidi H, Karakatsanis N. Towards enhanced PET quantification in clinical oncology. *Br J Radiol.* 2018;91(1081):20170508.
215. Karakatsanis NA, Zhou Y, Lodge MA, Casey ME, Wahl RL, Zaidi H, et al. Generalized whole-body Patlak parametric imaging for enhanced quantification in clinical PET. *Phys Med Biol.* 2015;60(22):8643-73.
216. Karakatsanis NA, Casey ME, Lodge MA, Rahmim A, Zaidi H. Whole-body direct 4D parametric PET imaging employing nested generalized Patlak expectation-maximization reconstruction. *Phys Med Biol.* 2016;61(15):5456-85.
217. Karakatsanis N, Lodge M, Zhou Y, Casey M, Wahl R, Subramaniam R, et al. Novel multi-parametric SUV/Patlak FDG-PET whole-body imaging framework for routine application to clinical oncology. *Journal of Nuclear Medicine* 56 (supplement 3) 625. 2015.
218. Feng T, Zhao Y, Shi H, Li H, Zhang X, Wang G, et al. Total-Body Quantitative Parametric Imaging of Early Kinetics of (18)F-FDG. *J Nucl Med.* 2021;62(5):738-44.

219. Meirelles GS, Erdi YE, Nehmeh SA, Squire OD, Larson SM, Humm JL, et al. Deep-inspiration breath-hold PET/CT: clinical findings with a new technique for detection and characterization of thoracic lesions. *J Nucl Med*. 2007;48(5):712-9.
220. Prenosil GA, Sari H, Furstner M, Afshar-Oromieh A, Shi K, Rominger A, et al. Performance Characteristics of the Biograph Vision Quadra PET/CT system with long axial field of view using the NEMA NU 2-2018 Standard. *J Nucl Med*. 2021.
221. Viswanath V, Daube Witherspoon ME, Karp JS, Surti S. Numerical observer study of lesion detectability for a long axial field-of-view whole-body PET imager using the PennPET Explorer. *Phys Med Biol*. 2020;65(3):035002.
222. MacDonald LR, Harrison RL, Alessio AM, Hunter WC, Lewellen TK, Kinahan PE. Effective count rates for PET scanners with reduced and extended axial field of view. *Phys Med Biol*. 2011;56(12):3629-43.
223. Surti S, Karp JS. Impact of detector design on imaging performance of a long axial field-of-view, whole-body PET scanner. *Phys Med Biol*. 2015;60(13):5343-58.
224. Zhang J, Knopp MI, Knopp MV. Sparse Detector Configuration in SiPM Digital Photon Counting PET: a Feasibility Study. *Mol Imaging Biol*. 2019;21(3):447-53.
225. Yamaya T, Yoshida E, Inadama N, Nishikido F, Shibuya K, Higuchi M, et al. A Multiplex "OpenPET" Geometry to Extend Axial FOV Without Increasing the Number of Detectors. *Ieee T Nucl Sci*. 2009;56(5):2644-50.
226. Karakatsanis NA, Zein SA, Nehmeh SA. Evaluation of Image Quality and Quantitation in a Clinical PET Scanner with a Uniformly Sparse Detector Rings Configuration. *IEEE Nuclear Science Symposium and Medical Imaging Conference Proceedings*. 2018:1-9.
227. Karakatsanis NA, Zein SA, Nehmeh SA. Positron Emission Tomography with Sparse Block Rings and Continuous Bed Motion. *2019 Ieee Nuclear Science Symposium and Medical Imaging Conference (Nss/Mic)*. 2019.
228. Beaudoux V, Blin G, Barbrel B, Kantor G, Zacharatou C. Geant4 physics list comparison for the simulation of phase-contrast mammography (XPulse project). *Phys Med*. 2019;60:66-75.
229. Baratto L, Park SY, Hatami N, Davidzon G, Srinivas S, Gambhir SS, et al. ¹⁸F-FDG silicon photomultiplier PET/CT: A pilot study comparing semi-quantitative measurements with standard PET/CT. *PLoS One*. 2017;12(6):e0178936.
230. Berg E, Zhang X, Bec J, Judenhofer MS, Patel B, Peng Q, et al. Development and Evaluation of mini-EXPLORER: A Long Axial Field-of-View PET Scanner for Nonhuman Primate Imaging. *J Nucl Med*. 2018;59(6):993-8.

231. Moraes ER, Poon JK, Balakrishnan K, Wang WL, Badawi RD. Towards component-based validation of GATE: Aspects of the coincidence processor. *Phys Medica*. 2015;31(1):43-8.
232. Browne E, Junde H. Nuclear Data Sheets for A = 176. *Nucl Data Sheets*. 1998;84(2):337-486.
233. Kossert K, Jorg G, Gostomski CLV. Experimental half-life determination of Lu-176. *Appl Radiat Isotopes*. 2013;81:140-5.
234. Chicheportiche A, Marciano R, Orevi M. Comparison of NEMA characterizations for Discovery MI and Discovery MI-DR TOF PET/CT systems at different sites and with other commercial PET/CT systems. *EJNMMI Phys*. 2020;7(1):4.
235. Wagatsuma K, Miwa K, Sakata M, Oda K, Ono H, Kameyama M, et al. Comparison between new-generation SiPM-based and conventional PMT-based TOF-PET/CT. *Phys Medica*. 2017;42:203-10.
236. NEMA NU 2-2018 Performance Measurements of Positron Emission Tomograph (PET). Rosslyn, VA; 2018.
237. Thielemans K, Tsoumpas C, Mustafovic S, Beisel T, Aguiar P, Dikaios N, et al. STIR: software for tomographic image reconstruction release 2. *Phys Med Biol*. 2012;57(4):867-83.
238. Schindelin J, Rueden CT, Hiner MC, Eliceiri KW. The ImageJ ecosystem: An open platform for biomedical image analysis. *Mol Reprod Dev*. 2015;82(7-8):518-29.
239. Brun R, Rademakers F. ROOT — An object oriented data analysis framework. *Nuclear Instruments and Methods in Physics Research Section A: Accelerators, Spectrometers, Detectors and Associated Equipment*. 1997;389(1-2):81-6.
240. Schmall JP, Karp JS, Werner M, Surti S. Parallax error in long-axial field-of-view PET scanners—a simulation study. *Phys Med Biol*. 2016;61(14):5443-55.
241. Daube-Witherspoon ME, Viswanath V, Werner ME, Karp JS. Performance Characteristics of Long Axial Field-of-View PET Scanners with Axial Gaps. *IEEE Trans Radiat Plasma Med Sci*. 2021;5(3):322-30.
242. Zhang YQ, Hu PC, Wu RZ, Gu YS, Chen SG, Yu HJ, et al. The image quality, lesion detectability, and acquisition time of (18)F-FDG total-body PET/CT in oncological patients. *Eur J Nucl Med Mol Imaging*. 2020;47(11):2507-15.
243. Fahrni G, Karakatsanis NA, Di Domenicantonio G, Garibotto V, Zaidi H. Does whole-body Patlak (18)F-FDG PET imaging improve lesion detectability in clinical oncology? *Eur Radiol*. 2019;29(9):4812-21.

244. Wright CL, Zhang J, Tweedle MF, Knopp MV, Hall NC. Theranostic Imaging of Yttrium-90. *Biomed Res Int*. 2015;2015:481279.
245. Zhao YM, Li YH, Chen T, Zhang WG, Wang LH, Feng J, et al. Image quality and lesion detectability in low-dose pediatric (18)F-FDG scans using total-body PET/CT. *Eur J Nucl Med Mol Imaging*. 2021;48(11):3378-85.
246. Lennon AM, Buchanan AH, Kinde I, Warren A, Honushefsky A, Cohain AT, et al. Feasibility of blood testing combined with PET-CT to screen for cancer and guide intervention. *Science*. 2020;369(6499).
247. Soret M, Bacharach SL, Buvat I. Partial-volume effect in PET tumor imaging. *J Nucl Med*. 2007;48(6):932-45.
248. Kessler RM, Ellis JR, Jr., Eden M. Analysis of emission tomographic scan data: limitations imposed by resolution and background. *J Comput Assist Tomogr*. 1984;8(3):514-22.
249. Lodge MA, Leal JP, Rahmim A, Sunderland JJ, Frey EC. Measuring PET Spatial Resolution Using a Cylinder Phantom Positioned at an Oblique Angle. *J Nucl Med*. 2018;59(11):1768-75.
250. Christian P. Use of a precision fillable clinical simulator phantom for PET/CT scanner validation in multi-center clinical trials: The SNM Clinical Trials Network (CTN) Program. *Journal of Nuclear Medicine*. 2012;53.
251. Sunderland JJ, Christian PE. Quantitative PET/CT scanner performance characterization based upon the society of nuclear medicine and molecular imaging clinical trials network oncology clinical simulator phantom. *J Nucl Med*. 2015;56(1):145-52.
252. Sunderland J, Muzic R, Lodge M, Nye J, Zimmermann L, Burrell L, et al. Design, construction, and testing of an anthropomorphic oncology phantom for PET/CT scanner characterization. *Journal of Nuclear Medicine*. 2018;59.
253. SNMMI Phantom Analysis Toolkit (PAT), <https://www.snmmi.org/PAT> Accessed June 10, 2021.
254. Sunderland J, Clarke B. Tutorial for optimal utilization of SNMMI fully automated cloud-based PET Phantom Analysis Tool for PET/CT Quality Control. *Journal of Nuclear Medicine*. 2020;61.
255. Sunderland J, Tiwari A. A comprehensive PET-CT scanner characterization performance assessment paradigm and database. *Journal of Nuclear Medicine*. 2021;62.
256. Wollenweber SD, Alessio AM, Kinahan PE. A phantom design for assessment of detectability in PET imaging. *Med Phys*. 2016;43(9):5051.
257. Morey AM, Kadrmas DJ. Effect of varying number of OSEM subsets on PET lesion detectability. *J Nucl Med Technol*. 2013;41(4):268-73.

258. Brennen WN, Isaacs JT, Denmeade SR. Rationale behind targeting fibroblast activation protein-expressing carcinoma-associated fibroblasts as a novel chemotherapeutic strategy. *Mol Cancer Ther.* 2012;11(2):257-66.
259. Hofman MS, Emmett L, Sandhu S, Iravani A, Joshua AM, Goh JC, et al. [(177)Lu]Lu-PSMA-617 versus cabazitaxel in patients with metastatic castration-resistant prostate cancer (TheraP): a randomised, open-label, phase 2 trial. *Lancet.* 2021;397(10276):797-804.
260. Moskal P, Kowalski P, Shopa RY, Raczynski L, Baran J, Chug N, et al. Simulating NEMA characteristics of the modular total-body J-PET scanner-an economic total-body PET from plastic scintillators. *Phys Med Biol.* 2021;66(17).
261. Kwon SI, Ota R, Berg E, Hashimoto F, Nakajima K, Ogawa I, et al. Ultrafast timing enables reconstruction-free positron emission imaging. *Nature Photonics.* 2021;15:914 - 8.